Molecular Self-Assembly, Nucleation Kinetics and Cluster Formation Associated with Solution Crystallisation

by

Thomas Daniel Turner

A dissertation submitted in accordance with the requirements

for the degree of

DOCTOR OF PHILOSOPHY

(Chemical Engineering)

UNIVERSITY OF LEEDS

Institute of Particle Science & Engineering

School of Chemical and Process Engineering

September 2015

The candidate confirms that the work submitted is his/her own, except where work which has formed part of jointly authored publications has been included. The contribution of the candidate and the other authors to this work has been explicitly indicated below. The candidate confirms that appropriate credit has been given within the thesis where reference has been made to the work of others.

Publication: *Towards an understanding of the nucleation of alpha-para amino benzoic acid from ethanolic solutions: a multi-scale approach*

D. Toroz, I. Rosbottom, T. D. Turner, D. M. C. Corzo, R. B. Hammond, X. Lai and K. J. Roberts, Faraday Discuss., 2015, 179, 79

This publication contains data/results which will be presented in Chapters **4**, **6** and **7** of this thesis.

Work in this publication which is attributable to the author of this thesis;

Abstract summary of results in 3.4 and 3.5

Methodology sections;

2.3. Poly-thermal and isothermal turbidometric measurements.

Experimental details including theory regarding the data analysis procedure for poly-thermal and isothermal methods.

2.4. Small angle X-ray scattering studies.

Experimental details including theory regarding the data analysis procedure for application of the Unified fit model and form factor fitting to scattering data.

Results Sections

3.4. PABA nucleation kinetics from ethanolic solutions.

Details of poly-thermal and isothermal studies to derive nucleation kinetics from turbidometric measurements. Identification of the nucleation mechanism and critical cluster size of the alpha form of para amino benzoic acid in ethanolic solutions. D. M. C. Corzo, R. B. Hammond, X. Lai and K. J. Roberts contributed to this section with

helpful discussions on fundamental nucleation theory and solution thermodynamics. D. M. C. Corzo provided helpful advice on the application of the polythermal method for deriving nucleation kinetics. I. Rosbottom provided useful discussions for linking derived growth exponents from the kinetic studies with measured growth rate data of para amino benzoic acid single crystals grown from ethanolic solutions.

3.5. Small angle X-ray scattering studies of alpha-PABA in ethanolic solutions during cooling crystallisation.

Details of small angle x-ray scattering studies which were used to obtain Nano-scale structural information regarding the nucleation process of alpha para amino benzoic acid crystallising from ethanol. Details of pre-nucleation cluster formation and also solution structure as a function of cooling are provided. X.Lai contributed to this work with experimental support in collecting the data at the synchrotron and also provided invaluable discussions regarding small angle scattering analysis and its application to nucleation theory. D. Toroz provided helpful discussions regarding the solution state structure explored in these experiments and linking this to the molecular dynamics simulations in sections 3.2 and 3.3.

Conclusions of the results sections 3.4 and 3.5

Publication: *The influence of solution environment on the nucleation kinetics and crystalisability of para-aminobenzoic acid*

T.D. Turner, D.M. C. Corzo, D. Toroz, A. Curtis, R.B. Hammond, X. Lai, K.J. Roberts, submitted to PCCP (Physical Chemistry Chemical Physics) 10/07/2015 under review at time of thesis submission.

This publication contains data/results which will be presented in Chapters **5** and **6** of this thesis

Work in this publication which is attributable to the author of this thesis;

All sections of this publication are attributable to the author with the exception of section 2.4 which details results of solvation free energy calculations performed by Dr Robert Hammond and Dr Dimitrios Toroz.

The Results section 3.1 details results of the solvation free energy calculations performed by Dr Dimitrios Toroz and Dr Robert Hammond. Results sections 3.1, 3.3

and 3.5 were supported by experimental support from Andrew Curtis and Marriana Mello Dos Santos. Diana Camacho Corzo, Prof. Kevin Roberts and Dr Xiaojun Lai provided helpful discussion and guidance relating to all aspects of the nucleation kinetics determination and calculations.

'People say to me, "Are you looking for the ultimate laws of physics?" No, I'm not. I'm just looking to find out more about the world, and if it turns out there is a simple ultimate law that explains everything, so be it. That would be very nice to discover. If it turns out it's like an onion with millions of layers, and were sick and tired of looking at layers, then that's the way it is….. My interest in science is to simply find out more about the world, and the more I find out, the better it is. I like to find out'

Richard Feynman

Acknowledgements

Abstract

The structural pathway from a single molecule to clustering through to nucleation during a crystallisation process is not fully understood. As such the solution state structure, nucleation kinetics and phase transformation kinetics of p-Aminobenzoic (PABA) acid are probed using a combination of *in-situ* crystallisation characterisation techniques and nucleation kinetic analysis methods.

The solubility of alpha PABA is measured in a number of solvents where van't Hoff analysis shows that solute-solute interactions are probable in all solvents. Solution state FTIR studies reveal the presence of a distribution of solvated monomer and carboxylic acid dimer species in acetonitrile solutions. This provides a link between solution state structural synthons and the carboxylic acid dimer structural synthon of the alpha PABA solid phase.

Isothermal nucleation kinetic analysis reveals that calculated interfacial tension, γ_{eff}, values are found to be low for an organic material; where γ_{eff} values are $0.85 - 1.31$ mJ/m^2 in ethanol and $2.36 - 2.60$ mJ/m^2 in water. Due to this the critical cluster sizes are in the region of $0.48 - 1.98$ nm. Poly-thermal kinetic analysis reveals a nucleation mechanism change from instantaneous to progressive as a function of decreasing solubility in ethanol, acetonitrile and water. This is caused by an increase in attachment frequency due to decreasing de-solvation free energy of PABA found from molecular dynamics simulations, this in combination with increasing γ_{eff} causes the thermodynamic component of the nucleation rate to become limiting.

Isothermal and poly-thermal X-ray scattering studies of PABA nucleation reveal the formation of large liquid-like clusters of PABA, >40nm, in the under-saturated state. These Nano-scale assemblies increase in size and structural ordering, indicated by an increase in fractal dimensionality from $1 - 2$ as a function of driving force. The Guinier region of the high q structures is found to increase from $R_g = 0.46$nm to 0.53 nm which indicates a population of monomers and dimers of PABA in the supersaturated state. This was confirmed as the carboxylic acid dimer structure from form factor fitting of known structural synthons of the alpha phase.

In-situ XRD studies of the polymorphic phase transformation of the beta-alpha phase, indicates that the dissolution and growth processes are consistent with zero

order nucleation kinetics and first and zero order kinetics respectively with the latter seemingly temperature dependant. UV/Vis analysis in combination with the XRD data reveal the transformation is a dissolution controlled process explained by particle morphology. The transformation temperature was also estimated from the growth and dissolution rate constants as 22.8 – 23.6 °C.

Table of Contents

List of Figures

List of Tables

List of Symbols

A	Pre-exponential factor
A	Crystal surface area (m^2)
A	Amplitude (m)
A_0	Fixed needle cross sectional area (m^2)
A_b	Absorbance
a	Dimensionless molecular latent heat of crystallisation
α	activity
$α_{det}$	Detectable fraction of crystallised volume
b	Dimensionless thermodynamic parameter
b	Path length (m)
B	Porod pre-factor
C	Number of components
C	Solubility (mol/L)
C*	Equilibrium solubility (mol/L)
C_e	Equilibrium solution concentration (m^{-3})
C_0	Concentration of instantaneously nucleated crystallites (m^{-3})
$ΔC_p$	Specific heat capacity (J / K)
c_r	Solubility of particle with radius r
Δc	Supersaturation driving force
c	Concentration (mol / dm^3)
c	Speed of light
D	Diffusion coefficient (m^2/s)
D_s	Surface fractal dimension
D_{crit}	radius of a critical nucleus (nm)

d	Dimensionality of crystallite growth
d	d spacing of lattice planes (nm or Å)
δ	Stagnant layer thickness (m)
ε_p,	Photon Frequency (Hz)
ε	Molar extinction coefficient $Lmol^{-1}cm^{-1}$
E_{latt}	Lattice energy (KJ/mol)
ΔE	Energy difference (J)
f^*	Attachment frequency
F	Degrees of freedom
G	Guinier prefactor
ΔG	Free energy (KJ/mol)
ΔG_s	Free energy difference of particle surface and particle bulk (KJ/mol)
ΔG_v	Free energy difference of a single molecule and infinitely large particle in solution (KJ/mol)
ΔG_{solv}	Free energy of solvation (KJ/mol)
ΔG_{diss}	Free energy of dissolution (KJ/mol)
ΔH_{fus}	Enthalpy of fusion (KJ/mol)
ΔH_{diss}	Enthalpy of dissolution (KJ/mol)
ΔH_{solv}	Enthalpy of solvation (KJ/mol)
ΔH_{sub}	Enthalpy of sublimation (KJ/mol)
i^*	Number of molecules in critical nucleus
I_e	Scattering factor for a single electron
$I(q)$	Scattering function
I_0	Scattering intensity at zero scattering angle (counts)
I	Intensity of radiation after absorption
I_0	Incident intensity

$J_{(t)}$	Nucleation Rate ($m^{-3}\ s^{-1}$)
k	Boltzmann constant ($J\ K^{-1}$)
k_m	coefficient of mass transfer (m/s)
K_G	Growth rate constant $m^{(1/m)}\ s^{-1}$
K_J	Nucleation rate constant ($m^{-3}\ s^{-1}$)
k_n	Nucleus numerical shape factor
k_v	Crystallite growth shape factor (m^{3-d})
k_d	Diffusion rate constant
k_r	Adsorption rate constant
KE	Kinetic energy (J)
M	Mass of component (g)
M	Molecular mass (g / mol)
m, n	Crystallite growth exponents
m	Mass of electron (g)
N_{det}	Detectable number of crystallites
n	Nucleation order
n	Refractive index
n	Order of diffraction
n	Number of electrons
N_p	Scattering volume (m^{-3})
P	Number of Phases
P	Pressure (Pa)
ρ	Density of component
ρ	Electron density (e.u/nm^{-3})
$\rho_{(r)}$	Pair-distance distribution function

q	Heat flow (J m^2)
q	Cooling rate (K s^{-1})
q	Scattering vector (nm^{-1} / Å^{-1})
q_0	Parameter in the uc (q) dependence for both PN and IN (K s^{-1})
r*	Critical nucleus radius (m)
r	radius (m)
R	Gas constant
R_g	Radius of gyration (nm)
S	Supersaturation ratio
S	Entropy
S(q)	Structure factor
ΔS_{fus}	Entropy of fusion (kJ/ K^{-1} mol^{-1})
ΔS_{diss}	Entropy of dissolution (kJ/ K^{-1} mol^{-1})
σ	Surface energy of solid (n / m)
σ	Relative supersaturation
τ	Induction time (s)
t_r	relaxation time (s)
t_n	nucleation time (s)
t_g	growth time (s)
T	Temperature (K)
T_0	Temperature at which crystallites are instantaneously nucleated (K)
T_{crys}	Crystallisation temperature (K)
T_{dis}	Dissolution temperature (K)
T_c	Equilibrium crystallisation temperature (K)
T_e	Equilibrium dissolution temperature (K)

ΔT_c	Critical undercooling for crystallisation (K)
T_m	Melting point (K)
θ	Bragg angle
U	Internal energy (J)
u	Relative undercooling
u_c	Relative critical undercooling for crystallisation
μ	Chemical potential (J/mol)
μ_0	Standard potential (J/mol)
v_0	Volume of solute molecule in crystal (m^3)
V_m	Molar volume (Dm^3/mol)
V	Volume of solution (m^3)
V	Voltage (V)
v	Velocity (m/s)
v	Frequency of radiation (Hz)
$\bar{v}$	Wavenumber (cm^{-1})
v_{max}	Largest frequency of radiation produced
x_{ideal}	Ideal solubility
x_{real}	Real solubility
x	molar solubility (mol / dm^3)
x	Molar fraction concentration
x_i	Molar fraction in liquid state
X	Mole fraction of component
λ	Molecular latent heat of crystallisation (J)
λ	Wavelength (m)
γ	Activity coefficient

γ_{eff} Effective interfacial tension of crystal nucleus (mJ m^{-2})

z Zeldovich factor

z_i Molar fraction in solid state

List of Abbreviations

ACN   Acetonitrile

ATR   Attenuated Total Reflectance

BCF   Burton Cabrera Frank

CNT   Classical Nucleation Theory

PABA   Para Amino Benzoic Acid

EtOH   Ethanol

FTIR   Fourier Transform Infrared

IN   Instantaneous nucleation

PN   Progressive nucleation

SD   Standard deviation

KHBR   Kashchiev–Borissova–Hammond–Roberts approach

MSZW   Metastable zone width

vdW   van der Waals

H-bonding   Hydrogen bonding

MD   Molecular dynamics

SAXS   Small Angle X-ray Scattering

UV/Vis   Ultraviolet / Visible

XRD   X-ray Diffraction

Chapter 1 Introduction

The key scientific background and current research in the field is outlined together with the research aims and objectives, how these aims will be met experimentally will be discussed, finally the project management and structure of this thesis is presented at the end of the chapter.

1.1 Research Background

Crystallisation is the aggregation of single solute molecules in solution to form clusters through nucleation, followed by growth into macromolecular crystals. The process is fundamental in almost all industries; materials, fine chemicals, food and pharmaceuticals and is used as a technique for isolation of a target material [1]. Crystallisation is both the formation of a product and also purification of that product from unreacted starting materials and by-products. The process of crystallisation has a key role in pharmaceutical product design and manufacture, with almost 90% of pharmaceuticals containing crystalline phases either as part of the synthesis or the target molecular phase. The ability to engineer a crystallisation process requires an understanding of how molecular interactions drive molecular self-assembly during nucleation which ultimately leads to a new crystalline phase with desired physical properties[2, 3].

Nucleation as a process is fundamental in crystallisation and occurs through the formation of molecular clusters from a supersaturated solution. This process has been a major topic of research in crystallisation science since Ostwald, 1897, proposed his rule of stages in order to explain crystallisation and metastability, indicating the presence of multiple crystal forms and the idea of crystallisation kinetics[4]. The work which followed, by Volmer, 1929, was the first theory on nucleation which led to multiple researchers developing this into a formalism to explain nucleation as a kinetic process of molecular packing from solution[5, 6].

This theory has become known as classical nucleation theory (CNT) which generally describes nucleation as density fluctuations in a supersaturated solution with respect to the solute which leads to the formation of molecular clusters[5]. These clusters must have the same crystalline packing as the resultant macromolecular crystal structure and all polymorphic forms are represented to some degree in solution[7], highlighted in Figure 1-1.

CNT, originally developed to explain the kinetic phenomena of condensation from a vapour, has its flaws for the modern day application to nucleation. CNT goes someway to explain nucleation as an aggregation of solute molecules which leads to the growth of a crystalline phase, however much research has seen a disagreement

with theoretical calculation and experimental result. A study into the crystallisation of Lysozyme has shown a disagreement of the nucleation rate, J, of 10 orders of magnitude between experimental and CNT prediction[8]. CNT seems to fail on a number of assumptions made regarding nucleation from solution; for example clusters are assumed spherical and molecular packing in the cluster is identical to that in the extended crystalline phase. Recently a number of studies of protein systems have revealed evidence of a 2 step model (Figure 1-1) with large liquid-like clusters of protein molecules forming prior to crystallisation[9,10,11,12].
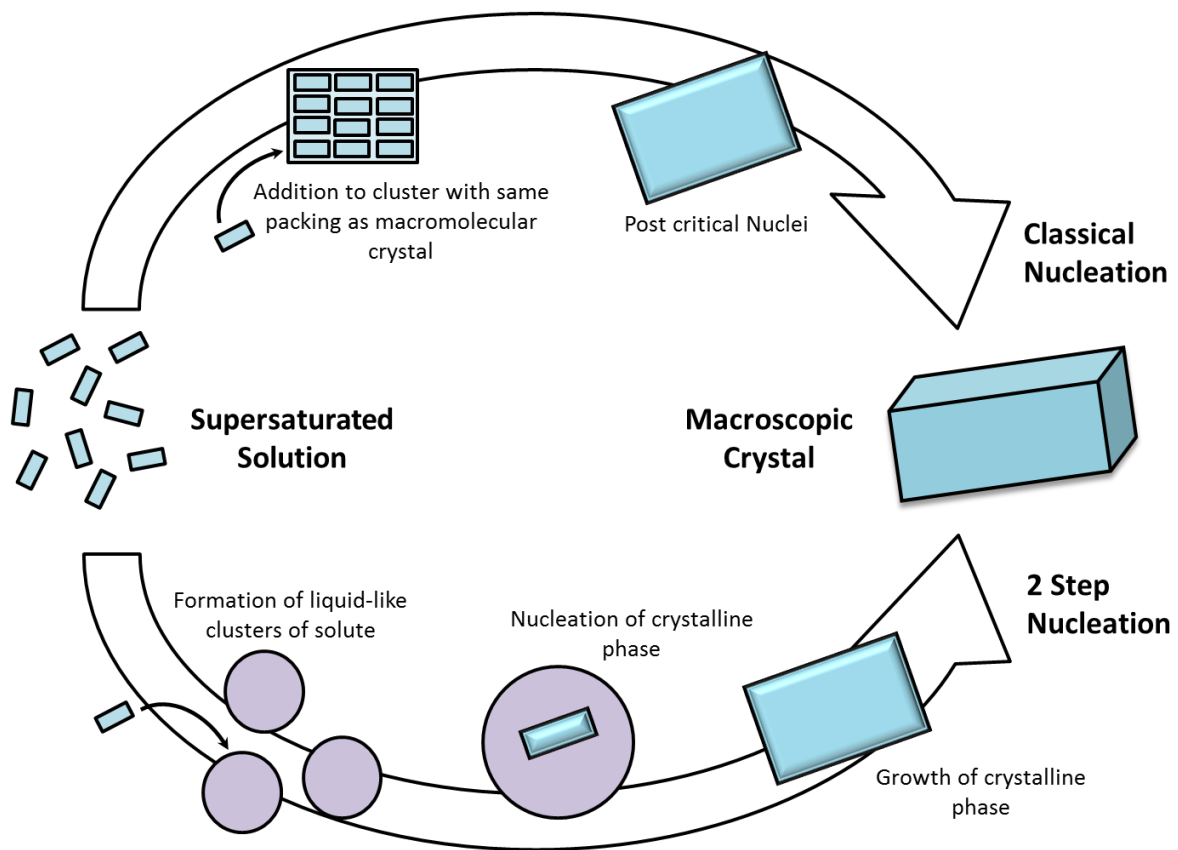
Figure 1-1 Schematic comparing the two major theories of nucleation; classical theory and the 2 step model

Recent advances in *in-situ* dynamic synchrotron scattering techniques have allowed studies to reveal similar liquid-liquid phase separations and large pre-nucleation clusters for a number of small organic molecules including glycine, 2,6-dibromo-4-nitroaniline and D,L-alanine[13,14,15,16,17,18,19]. The existence of a solute rich phase prior to crystallisation is contradictory of CNT which states that crystallisation should proceed through an addition process to a lattice structure. Findings such as these have led to the development of a more recent theory; the two step model of

3

nucleation. The two step approach suggests that a solute rich liquid phase precedes the formation of the nucleus and subsequent rearrangement of the solute molecules leads to increases in order parameters and the formation of crystal nuclei[2].

Although a number of particularly interesting studies have been carried out in this field a number of key challenges still remain. The critical challenge in nucleation currently is attempting to determine the structure of these nano-sized pre-nucleation clusters and what the structural progression is for their formation from a molecular standpoint. This structural picture combined with a molecular level understanding of the solution chemistry would be a step change towards the efficient control of the crystallisation process. This can only be achieved through the combined use of a number of state of the art *in-situ* spectroscopic, scattering, diffraction and solution analytical techniques such as Raman and UV/Vis spectroscopy.

This approach will build on the previous work of linking solution state pre-assembly to the resulting crystal structure of a polymorphic form from a crystallisation process monitored using FTIR[20] [21] [22] [23]. Advances in light scattering and synchrotron X-ray scattering methodologies will provide access to the rapid time scales required for study of such a dynamic problem as nucleation[14,15,16]. Recent advances in the determination of nucleation kinetic parameters from measurement of induction times and meta-stable zone widths of a material have provided critical methods for analysis of nucleation rates and rate limiting factors in a nucleation process[24,25,26]. The development of *in-situ* diffraction methods have also been used successfully to monitor the polymorphic selection and transformation of crystallisation processes[19,27,28.] The combination of these state of the art methodologies is required to provide the tools to build on the current models of nucleation for organic materials by revealing the structural pathway through the nucleation process and linking this to solution state assemblies.

1.2 Research Aims and Objectives

This research will use a combination of the techniques discussed above; simultaneous scattering and diffraction methods to probe nucleation from a structural perspective. A full understanding of solution chemistry will also be required so the structural information gained during diffraction and scattering studies can be related

to solution synthons and the thermodynamic and kinetic parameters prior to crystallisation. The crystallisation system of study will be p-aminobenzoic acid (PABA) which is a compound with 2 polymorphs and represents a common pharmaceutical like pre-cursor molecule commonly used in industrial synthesis.

The research question;

What is the structural progression from the self-assembly of single molecules in solution through solute clustering associated with the nucleation process to the formation of a well ordered 3-D crystal?

This question is addressed through delivery of the following core thesis objectives;

1. Characterise the solution state chemistry of saturated and under-saturated solutions of PABA
2. Investigate the role of solvent and solution concentration on the self-assembly and nucleation kinetics of PABA
3. Evaluate the structural evolution of single molecule to cluster formation during nucleation and provide a model of nucleation for PABA from its supersaturated solution
4. Elucidate the dissolution and growth kinetics of PABA from solution
5. Describe the structural development of micro-crystallite formation post nucleation

1.3 Delivery Plan

The core thesis objectives highlighted in Section 1.2, will be delivered through the application of a number of experimental and modelling techniques which aim to probe the structural aspect of nucleation;

- The solution state will be explored using infra-red spectroscopy to probe molecular level information, in an attempt to understand solute-solute and solute-solvent interactions in the saturated and under-saturated state. These spectra will then be compared to the spectra of the solid state
- The nucleation kinetics of PABA will be analysed using isothermal and poly-thermal techniques to provide an insight into the role solvent plays in directing nucleation kinetics by comparing results through a variety of solvation environments

- Development of an X-ray scattering instrument together with various liquid flow cells will be carried out to provide support for synchrotron diffraction experiments

- The solution nano-structure progression during solution crystallisation will be probed using *in-situ* time resolved synchrotron X-ray scattering experiments to resolve cluster size as a function of cooling

- The solution mediated phase transformation of the two phases will be examined using X-ray diffraction to determine the kinetic parameters which govern the growth and dissolution of both solid phases

- The structural development of nano-crystallites will be characterised using *in-situ* time resolved synchrotron X-ray diffraction to determine how crystallites grow post nucleation and the relationship to cluster formation

1.4 Project Management

This PhD has been carried out as part of the EPSRC Critical Mass Project - Molecules, Clusters and Crystals: A Multi-Scale Approach to Understanding Kinetic Pathways in Crystal Nucleation from Solution. This was a collaborative project with the University of Manchester, under the guidance of principal investigators Prof Kevin Roberts of the University of Leeds and Prof Roger Davey of the University of Manchester. The project was comprised of six work programmes supported by four co-investigators, three post-doctoral research assistants and four PhD students.

The work reported in this thesis falls into work programmes two and four of the Critical Mass Project and was supervised by Dr Xiaojun Lai and Prof Kevin Roberts of the University of Leeds. The molecular dynamics calculations of infra-red spectroscopy in Chapter 5 together with solution free energy calculations highlighted in Chapter 6 were carried out in collaboration with Dr Dimitrios Toroz. Development of the poly-thermal technique for analysing crystallisation kinetics used extensively in Chapter 6 was carried out in collaboration with Ms Diana Camacho-Corzo. The synchrotron small angle X-ray scattering experiments at the Brookhaven National Laboratory in Chapter 7 were carried out in collaboration with Dr Maya Koga of Stony Brook University, New York. The synchrotron X-ray scattering experiments at the Brazilian National Light Laboratory highlighted in Chapter 7 were carried out in collaboration with Dr Mateus Borba Cardoso. The development of the *in-situ* X-ray

transmission cell together with the design and development of the in-house small angle X-ray scattering equipment in Chapters 6 and 8 were completed in collaboration with Mr Steve Caddick of the University of Leeds. The collection of the acetonitrile data in the poly-thermal nucleation kinetics analysis, Chapter 6, was supported by MEng student Mr Andrew Curtis and Mariana Mello Dos Santos. The collection of SAXS data on the micellar systems, Chapter 7, was supported by MEng student Mr Mike Ambler and also in collaboration with Dr Tomasz Stawski of the department of Earth and Environment, University of Leeds.

1.5 Scope of the Thesis

This thesis contains 9 chapters where each chapter has an individual reference section;

Chapter 1 presents an introduction to the research covering the background to the research topic, the research question with resulting thesis aims and objectives and the layout of the thesis.

Chapter 2 introduces a literature review covering the core theory of solution chemistry, nucleation and crystallisation.

Chapter 3 provides a more in depth review on the previous and current work from the area of small angle X-ray scattering and diffraction and *in-situ* studies of nucleation and crystallisation.

Chapter 4 covers the materials utilised with experimental and computational methodology and techniques used during this research.

Chapter 5 covers the results of solubility analysis with calculations of solution thermodynamic parameters together with outcomes of infrared spectroscopy analysis to probe solution and solid state structural synthons.

Chapter 6 presents results of iso and poly-thermal nucleation studies probing the kinetics and thermodynamics of nucleation as a function of solvation environment and concentration.

Chapter 7 highlights development and commissioning of a small angle X-ray scattering instrument in addition to results of *in-situ* synchrotron scattering studies probing solute clustering during crystallisation experiments.

Chapter 8 presents the development of *in-situ* transmission flow cell for diffraction studies together with results of polymorphic phase transformations of PABA using *in-situ* X-ray diffraction.

Chapter 9 highlights the conclusions and future work which can be drawn from this research.

This is shown schematically in Figure 1-2.

Chapter 1 Introduction

➢ **Background to Research**
➢ **Aims and Objectives**
➢ **Delivery Plan**
➢ **Scope of Thesis**

Chapter 2 Crystallography Solution Chemistry and Nucleation Theory

➢ **Fundamental crystallography**
➢ **Phase transitions and solubility**
➢ **Nucleation theory**
➢ **Crystal growth mechanisms**

Chapter 3 *In-situ* Crystallisation Characterisation

➢ **X-ray diffraction theory**
➢ **Small angle X-ray theory and analysis**
➢ **Review of *In-situ* characterisation techniques**
➢ **Review of PABA**

Chapter 4 Materials and Methods

➢ **Materials used for the study**
➢ **Review of experimental methodology**
➢ **Review of computational methodology**

Chapter 5 Solubility and Solution Chemistry

➢ **Solubility determination**
➢ **Solid state FTIR molecular synthon analysis**
➢ **Solution state FTIR molecular synthon analysis**

Chapter 6 Nucleation Kinetics as a Function of Solvation Environment

➢ **Isothermal analysis of cluster sizes**
➢ **Polythermal analysis of nucleation kinetics**
➢ **Solution effect on nucleation parameters**

Chapter 7 SAXS Studies of Nucleation

➢ **Development of in-house SAXS instrument with commissioning study**
➢ **Time resolved in-situ SAXS studies of PABA nucleation**
➢ **A structural model of nucleation**

Chapter 8 In-situ Polymorphic Transformation Studies

➢ **Development and testing of in-situ flow cell**
➢ **Calibration of online XRD instrument**
➢ **Determination of transformation kinetics of $\beta - \alpha$ polymorphic phase conversion**

Chapter 9 Conclusions and Future Work

Figure 1-2 Schematic illustrating the route map of the main chapters in this thesis

9

References

[1] A. S. Myerson, *Handbook of Industrial Crystallization*, 2nd edition, 2002, Butterworth-Heinemann

[2] D. Erdemir, A. Y. Lee, A. S. Myerson, *Accounts of Chemical Research*, 2009, 42, 5, 621

[3] J. T. Carstensen, Pharmaceutical Principles of Solid Dosage Forms, 1993, Technomic Publishing Co.

[4] W. Ostwald, *Z. Phys. Chem.*, 1897, 22, 289

[5] M. Volmer, *Kinetik der phasenbildung*, 1939, Dresden & Leipeg, Steinkoff

[6] R. J. Davey, K. Allen, N. Blagden, W. I. Cross, H. F. Lieberman, M. J. Quayle, S. Righini, L. Seton, G. J. T. Tiddy, *CrystEngComm,* 2002, 4, 257

[7] I. Weissbuch, M. Lahav, L. Leiserowitz, *Cryst. Growth Des.*, 2003, 3, 125

[8] P. G. Vekilov, 2010, *Cryst. Growth Des.*, 10, 12, 5007

[9] W. Pan, O. Galkin, L. Filobelo, R. L. Nagel and P. G. Vekilov, *Biophys. J.*, 2007, 92, 267

[10] Y. Liu, X. Wang, C. B. Ching, *Cryst. Growth Des.,* 2010,10, 548

[11] A. Sauter, F. Roosen-Runge, F. Zhang, G. Lotze, R. M. J. Jacobs, F. Schreiber, *J. Am. Chem. Soc.,* 2015, 137, 1485

[12] N. Niimura, M. Ataka, Y. Minezaki, T. Katsura, *Physica B: Condensed Matter*, 1995, 213-214, 745

[13] A. Jawor-Baczynska, B.D. Moore, H. S. Lee, A. V. McCormick, J. Sefcik*, Faraday Discuss.*, 2013, 167, 425

[14] A. Jawor-Baczynska, J.Sefcik, B. D. Moore, *Cryst. Growth Des.* 2013, 13, 470

[15] S. Chattopadhyay, D. Erdemir, J. M. B. Evans, J. Ilavsky, H. Amenitsch, C. U. Segre and A. S. Myerson, *Cryst. Growth Des.*, 2005, 5, 523

[16] P. E. Bonnett, K. J. Carpenter, S. Dawsona, R. J. Davey, 2003, *Chem, Commun*, 6, 698

[17] D. Schwahn, Y. R. Ma, H. Colfen, *J. Phys. Chem. C,* 2007, 111, 3224

[18] Y. R. Ma, H. Colfen, M. Antonietti, *J. Phys. Chem. B,* 2006, 110,10822

[19] H. G. Alison, R. J. Davey, J. Garside, M. J. Quayle, G. J. T Tiddy, *Phys. Chem. Chem. Phys.*, 2003, 5, 4998

[20] R. A. Chiarella, A. L. Gillon, R.C. Burton, R. J. Davey, G. Sadiq, A. Auffret, M. Cioffi, C. A. Hunter, *Faraday Discuss.*, 2007, 136, 179

[21] S. Parveen, R. J. Davey, G. Dent, R. G. Pritchard, *Chem. Commun.*, 2005, 1531

[22] A. Gavezzotti and G. Filippini, *Chem. Commun.*, 1998, 3, 287

[23] R. J. Davey, K. Allen, N. Blagden, W. I. Cross, H. F. Lieberman, M. J. Quayle, S. Righini, L. Seton and G. J. T. Tiddy*, CrystEngComm*, 2002, 4, 257

[24] D. Kashchiev, A. Borissova, R. B. Hammond and K. J. Roberts, *J. Cryst. Growth.*, 2010, 312, 698

[25] D. Kashchiev, A. Borissova, R. B. Hammond and K. J. Roberts, *J. Phys. Chem. B.*, 2010, 114, 5441

[26] J. H. ter Horst and S. Jiang, *Cryst. Growth Des.*, 2011, 11, 256

[27] M. J. Quayle, R. J. Davey, A. J. McDermott, G. J. T. Tiddy, D. T. Clarke, G. R. Jones, *Phys. Chem. Chem. Phys.*, 2002, 4, 416

[28] R. B. Hammond, X. Lai, K. J. Roberts, *Crystal Growth & Design*, 2004 4, 5, 943

Chapter 2 Crystallography, Solution Chemistry and Nucleation Theory

The fundamental science of crystals and crystallisation is presented together a review of classical nucleation theory and solution thermodynamics, the chapter concludes with a summary of crystal growth

2.1 Introduction

The fundamental science which underpins crystallisation from solubility and solution thermodynamics, classical nucleation theory to polymorphism and crystal structures are reviewed in this chapter. To study nucleation a thorough understanding of the process which drives nucleation is required, as such a focus on solution chemistry, is provided. Further to this knowledge of the outcomes of nucleation are also required and hence a review of crystal structure together with crystal growth is also covered. Most critically the classical theory and research of nucleation are provided together with more modern approaches to studying nucleation and measurement of kinetic parameters.

The chapter starts with an overview of basic crystallography and then moves on to solutions and super-solubility to describe how crystallisation processes begin. The next topic will be nucleation and the important thermodynamic parameters related to this process, with a review of classical and non-classical theories. The chapter ends with a summary of crystal growth mechanisms.

2.2 Basic Crystallography

A crystalline material can be defined as a highly ordered arrangement of atoms or molecules in a three dimensional structure. Crystals can be recognised by this packing in a highly directional manner over essentially infinite distances, the full scale of the material, when compared to the interatomic distances in the structures, typically Ångstroms. Without this long range, directional order which defines crystallinity, a material is said to be amorphous, the classic example being glass, where SiO_2 can be crystalline or amorphous[1]. Amorphous forms of drug compounds are often used in the pharmaceutical industry to improve the drugs' solubility, however in doing so this reduces the thermodynamic stability of the material making it susceptible to transformation to another unwanted form of the drug.

Crystals are said to be anisotropic in terms of the properties they exhibit; the growth rates are face dependent as are dissolution rates; this relates to the repeating nature of crystals as different faces or surfaces of a crystal will contain different but face dependent chemical groups[2]. The internal structure of crystals can be described as a

lattice network of molecules or atoms resulting in defined faces and surfaces. There is also the possibility of incorporation of solvent molecules or other molecules into the crystal lattice stoichiometrically or non-stoichiometrically, these are referred to as solvates and co-crystals respectively[3]. The nature of crystals means that there are a number of forms a crystal can take, cubic, octahedron, tetrahedron for example and these structures are related to the repeating lattice and hence the individual symmetry elements. These elements can be an axis, point or plane symmetry but the key is that all are related to the individual structure of the crystal and as such can be used to characterise the crystal[4].

2.2.1 Crystal Systems and Symmetry

Crystalline solids are all constructed from a repeating lattice; this can be referred to as a point lattice (Figure 2-1) with each point representing an atom, molecule or cluster of molecules. Each point has identical surroundings in three dimensions and this is what gives the extended repeating nature of the solid. As each point is identical in constituent components and geometric space, the lattice can be broken into smaller repeating units known as the unit cell (Figure 2-1). The components of the unit cell as discussed will be identical and so will the geometry; this can be described in three dimensions as lengths a, b and c and the angles between these sides as α, β and γ; these dimensions are known as the lattice parameters[5].
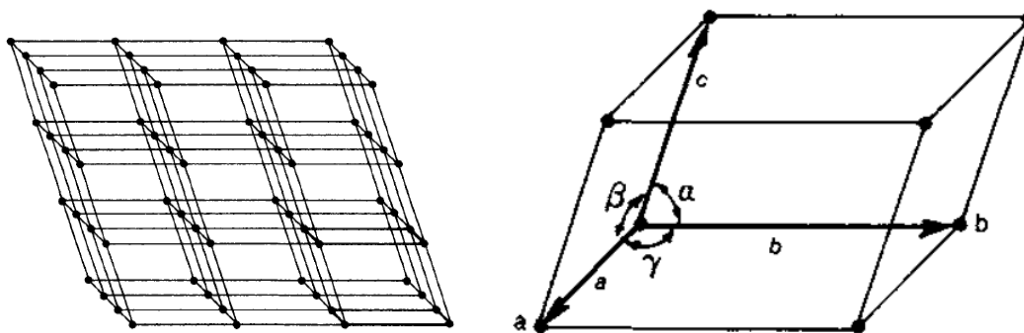
Figure 2-1 Point lattice (left) and a unit cell with lattice parameters (right)[6]

One may believe that there are an endless number of geometries for unit cells giving many point lattice structures, however the unit is required to stack to fill 3 dimensional space as efficiently as possible; minimising free energy. In 1848 Bravais[7] showed that there were in fact only 14 point lattices resulting from 7

different crystal systems and these are known as the Bravais lattices (Figure 2-2). These lattices can be described simply by how many lattice points per cell they contain for example a simple cubic cell contains 4 corner points per cell contributing ¼ point each giving a total of 1 per cell, a body centred cubic contains 2, the same 4 corner points plus 1 in the centre of mass. Another more complete way of describing the crystal lattice is by its symmetry elements.

SIMPLE
TETRAGONAL
(P)

BODY-CENTERED
TETRAGONAL
(I)

SIMPLE
ORTHORHOMBIC
(P)

BODY-CENTERED
ORTHORHOMBIC
(I)

BASE-CENTERED
ORTHORHOMBIC
(C)

FACE-CENTERED
ORTHORHOMBIC
(F)

RHOMBOHEDRAL
(R)

HEXAGONAL
(R)

SIMPLE
CUBIC *(P)*

BODY-CENTERED
CUBIC *(I)*

FACE-CENTERED
CUBIC *(F)*
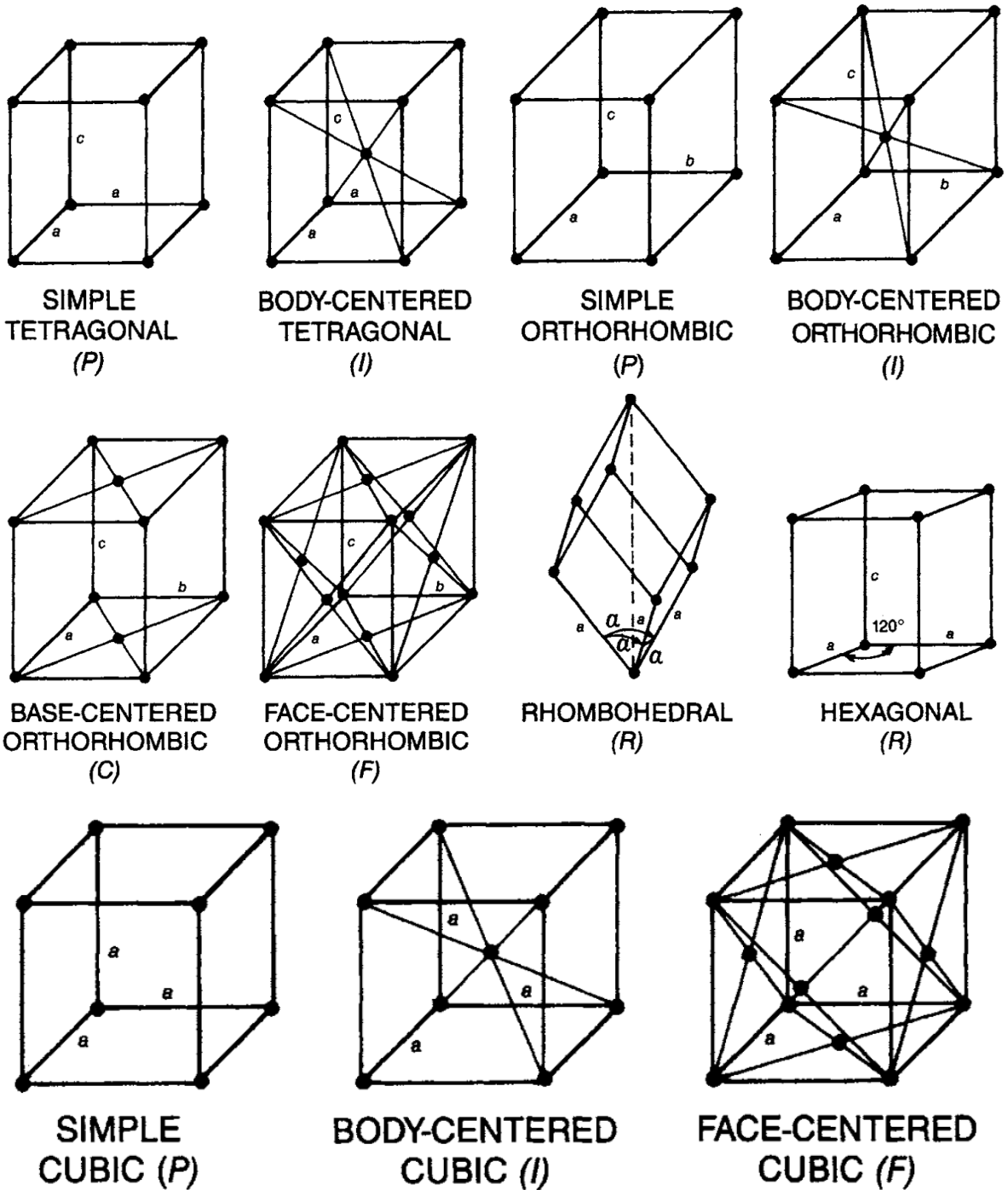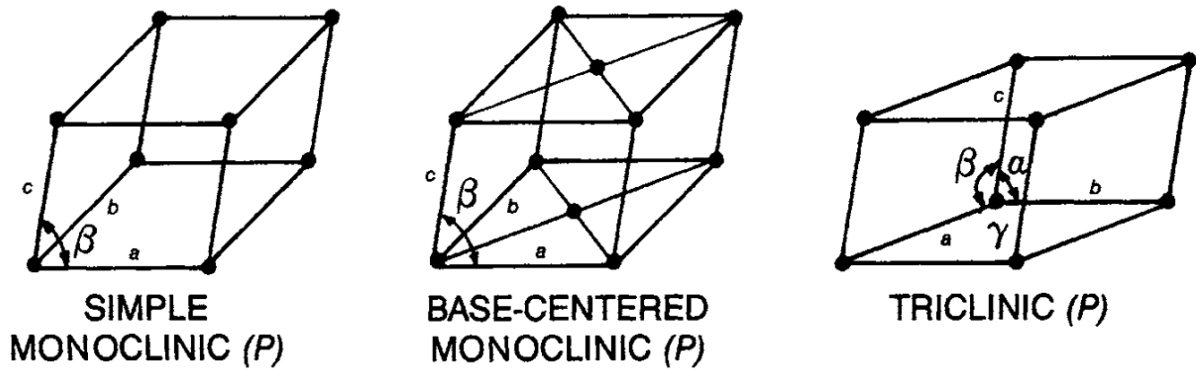
Figure 2-2 The 14 Bravais lattices[7]

Symmetry is a fundamental property of crystalline solids and defines many of their properties such as growth rate, habit, surface chemistry and optical properties. Understanding the symmetry elements of a crystal is key to studying the material and gives an insight into the atomic positions and also the individual atomic environment within the structure. The definition of symmetry is when an operation is performed on an object such as a reflection, and the object is unchanged in appearance after the operation. The major symmetry elements which are important when studying crystals are; rotation axes; notation is an integer (1, 2, 3, 4), mirror planes; notation is m, inversion centres; notation is i and rotation inversion axes; notation is $\bar{2}$, $\bar{4}$, $\bar{6}$; all are termed macroscopic as they describe the symmetry throughout the entire unit cell. So called microscopic symmetry elements require a more detailed knowledge of the individual atomic or molecular positions within the unit cell[8].

Point groups are a term used to describe the macroscopic symmetry elements of a crystal structure. The above symmetry elements must be present in all solids in at least one instance and this symmetry element(s) will pass through a single point in the structure at its centre. This combination of symmetry element(s) is a known as a point group and is given a notation which describes all of these symmetry operations. The notation used is the Hermann-Mauguin notation; an example of a point group is 2/m which contains a 2-fold rotation axis with a mirror plane at right angles to it; the combination of symmetry elements leads to a fixed number of point groups, 32 in total[8].

The space group aims to describe all symmetry elements of each lattice point i.e. the point group, in combination with the 14 Bravais lattices to give a complete picture of the symmetry elements in the crystal. This leads to microscopic crystal symmetry associated with translation symmetry and these include glide planes and screw axes. A glide plane is the combination of a translation through some distance followed by reflection through a plane; a screw axis is a combination of a rotation about an axis followed by a translation about the same axis. The notation used for space groups is again a Hermann-Mauguin notation which takes into account the lattice type; primitive, body centred, face centred etc. followed by the symmetry elements present. For example the $P2_1/m$ is a primitive lattice type with a 2_1 screw axis and a mirror plane[8].

2.2.2 Miller Indices

The faces of a crystal are important to overall properties of the material, be it physical or chemical, and being able to define these faces is important. Lattice planes in the crystal structure are also important when performing XRD experiments and give useful information on the bulk structure of the material. Both crystal faces and lattice planes can be described in terms of their axial intercepts with respect to *x*, *y* and *z* and are termed *a*, *b* and *c*. Miller (1839)[9] proposed a system of describing crystal faces by describing these intercepts as *h, k* and *l* which were described by the following;

$$h = \frac{a}{X}, \quad k = \frac{b}{Y} \text{ and } l = \frac{c}{Z} \qquad \textbf{(2-1)}$$

When h, k and l are all equal with respect to their intercepts this plane is usually referred to as the parametral plane and written as (1 1 1), all Miller indices for individual planes are written in round brackets whereas families of planes, i.e. symmetrically equivalent planes such as the (1 0 0) and (0 1 0) in a cubic system, are given braces;{ }.
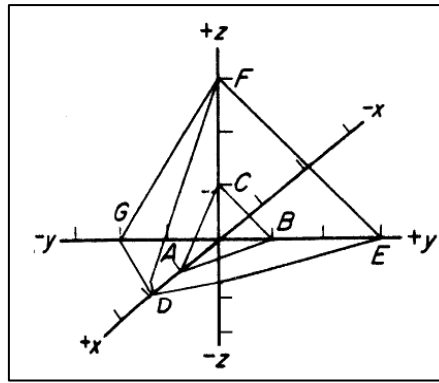
Figure 2-3 Example of planes on a crystallographic axis[4]

For the other planes of the crystal the Miller indices are calculated from their intercepts of *x*, *y* and *z*, all indices are taken as reciprocals of the intercepts and then multiplied through a common number to give whole numbers. This is done so that any intercept which is infinite, i.e. never intersects an axis is given the term 0. For example the plane DEF in Figure 2-3 gives intercepts as F=3C, E=3B and D=2A this gives reciprocals of $\frac{1}{2}, \frac{1}{3}, \frac{1}{3}$, to give whole numbers the reciprocals are multiplied by a common number of 6 t give *h k l* as (3 2 2). It should be noted that a negative intercept is represented as an integer $\bar{h}\,\bar{k}\,\bar{l}$. The planes in a crystal have equivalent planes parallel to each other separated by a distance *d*, this is known as the *d* spacing and is particularly important in XRD analysis. To calculate the *d* spacing for a cubic system for example;

$$\frac{1}{d^2} = \frac{h^2+k^2+l^2}{a^2} \quad \textbf{(2-2)}$$

2.2.3 Crystal Polymorphism

Polymorphism is the phenomena whereby a substance can exhibit more than one crystalline form; these forms are chemically identical but may have very different physicochemical properties[10]. These changes are due to the different arrangement of the molecules particularly at the surface of the crystal where varying H-bonding environments can lead to changes in solubility, thermal stability, electrical conductivity and flow behaviour of the particle[11].

Polymorphs appear when crystallisation parameters are changed and hence are very temperature and solvent dependent. Polymorphism is of particular importance and a source of frustration in the pharmaceutical industry where seemingly stable polymorphs transform to a different form in the solid state. A famous example is Ritonavir which exhibits conformational polymorphism between forms I and II, form I was the desired form however it readily transformed to form II which significantly changed the solubility and hence bioavailability of the drug[12].

According to Ostwald's rule of stages a metastable phase will be first to crystallise followed by the most stable form[13].

'An unstable system does not necessarily transform directly into the most stable state but into another transient state whose formation is accompanied by the smallest loss in free energy'

The metastable form can be a solvate or a polymorph and its stability varies widely with some metastable phases stable for seconds and some for months. The appearance of different polymorphs or metastable phases is largely due to the small energy differences between structural conformations and so accessibility of one phase to another is often easily achieved through only small changes to crystallising conditions[14,15]. Hence a thorough understanding of the intermolecular interactions in the solid state and also the conformational energies and solvent effects in solution is required in order to control polymorphism of a system.

The appearance of a polymorph in a system is a fine balance between thermodynamic and kinetic stability. A supersaturated system will aim to drive the Gibbs free energy to the lowest possible value for the lattice structure produced during crystallisation; this would be the most stable thermodynamic product. However in polymorphic systems due to the fact that they are energetically similar, this introduces the kinetic factor. If a polymorph can form more readily than another, i.e. it may require less conformational rearrangement, then this form may crystallise first even though it may be a higher energy state. This is the definition of the metastable phase which follows Ostwald's rules; the least stable polymorph forms first[12].
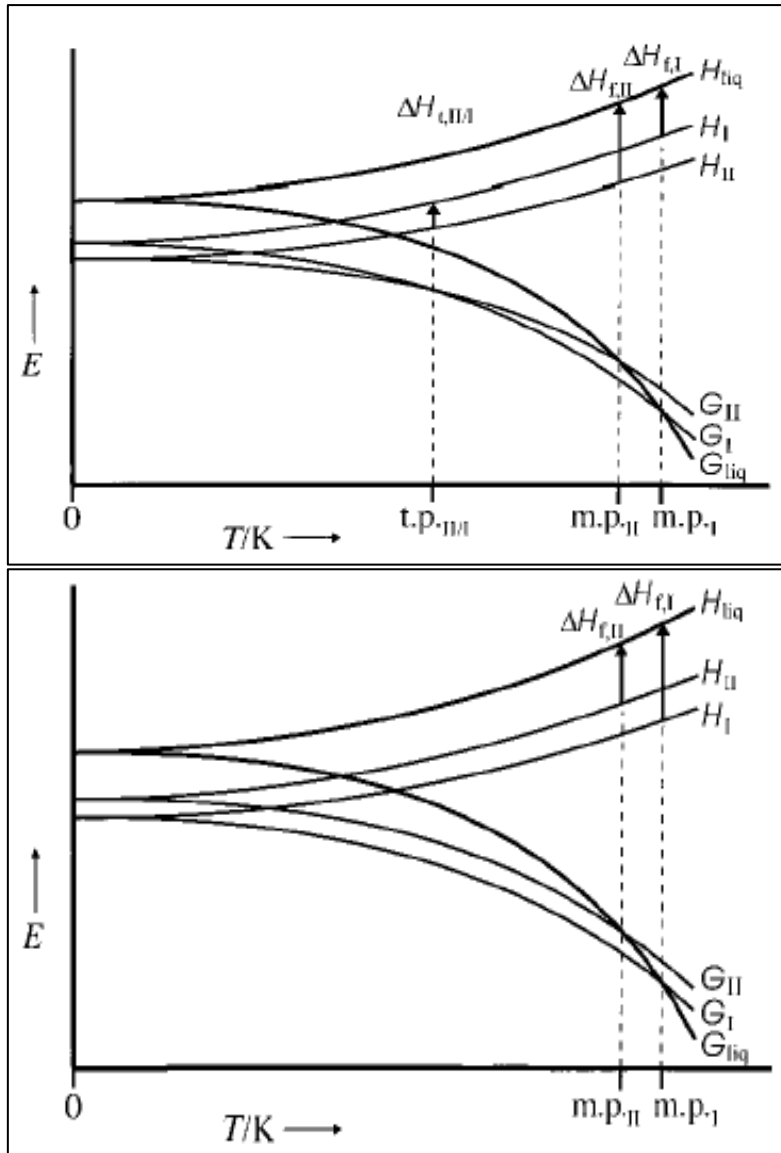
Figure 2-4 Energy vs temperature plots for an enantiotropic system (top) and a monotropic system (bottom)[16]

A simple way of explaining the stability of polymorphs is using an energy vs temperature curve to show the enthalpy, *ΔH*, and the Gibbs free energy, *ΔG* of the system. It should be noted that there are two types of polymorphism; monotropy; where the polymorphic forms are not interchangeable and enantiotropy where the forms are interchangeable with temperature for example. The diagram on the left of Figure 2-4 shows an enantiotropic two polymorphic system where *ΔG$_I$* and *ΔG$_{II}$* will cross at a transition temperature *t/P$_{I/II}$* and the enthalpy of this transition will be *ΔH$_{tI/II}$*. The monotropic system is shown on the right in Figure 2-4 and shows no crossing of

the *ΔG* curves of forms I and II; this is because the forms are not inter-convertible and inter-conversion can only happen through a gas or liquid transition[17].

2.2.3.1 Characterising Polymorphic Phase Transformations

The processes of crystallisation and solution mediated phase transformations can be classified as a heterogeneous reactions which involves reaction between two solids or a solid and a liquid[18,19]. In general the reaction in a liquid-solid mixture, the reaction is accelerated by the presence of the liquid phase due to increased mobility of reactants. As such application of solid homogeneous or solid state reaction models can be used to describe a heterogeneous process[20,21]. Generally reaction kinetics in solid-solid state reactions are expressed by plotting the fraction of transformed material (reacted material) as a function of time, these are known as α plots. An example of an interface or diffusion controlled reaction is provided in Figure 2-5.
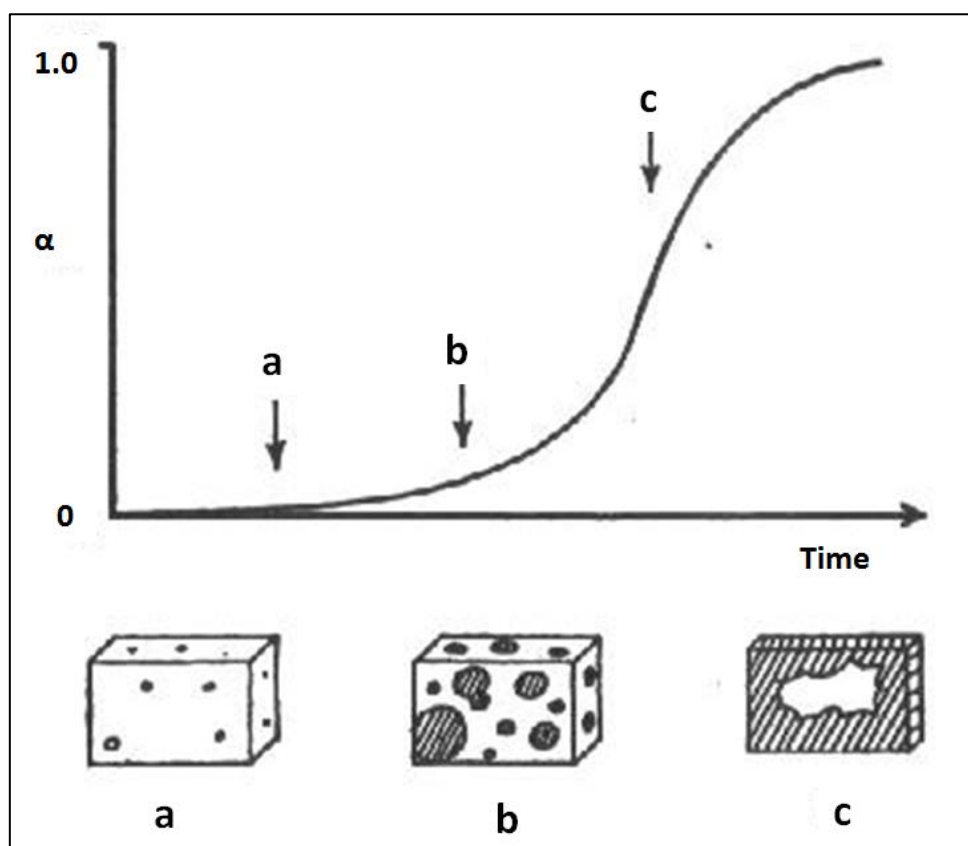
Figure 2-5 Diffusion controlled α plot[22]

The three highlighted features of the α plot are shown in Figure 2-5. Section a represents the initial induction time which corresponds to formation of stable nuclei of the newly formed product on the reactant surface. This is followed by a fast growth period, b, where nuclei grow in combination with further nuclei formation. The final stage reflects the end of the reaction profile whereby the reactive surface is at a minimum and hence the rate of reaction begins to decline[23]. Characterising the solid state kinetics of these transformations usually involves modelling of the α curves with respect to the reaction rate constant, considering also the nucleation and growth rate constants of the nucleated phase[24]. Some important solid state reaction models are provided in Table 2-1.

Table 2-1 Common solid state kinetic models for derivation of the rate constant of reaction

Reaction Mechanism	Integral form, $kt =$	Differential form, $\delta a/\delta t =$
Zero Order	X_a	k
First Order	$-ln(1-X_a)$	$k(1-X_a)$
Second Order	$(1-X_a)^{-1}$	$k(1-X_a)^2$
1D Diffusion	$1/2\,X_a^{\,2}$	$kX_a^{\,-1}$

Where k is the rate constant, t is time and X_a is the mole fraction concentration of species a. Solution mediated phase transformations (SMPT) of polymorphic forms differ from solid-solid transformations as dissolution of the meta-stable phase followed by growth of a stable phase is facilitated through the presence of solvent. Davey and Cardew[25] stated that for sufficient mechanistic insight into the rate determining step of a SMPT one must determine the solution supersaturation and crystallite size during the transformation process.

Davey and Cardew stated that the rate determining step of a solution mediated phase transformation could be the dissolution rate of the meta-stable phase or the growth of the stable phase and so the transformation time, *T*, can be represented by the following expression;

$$T = T_G + T_D \quad \text{(2-3)}$$

where T_G and T_D are the growth and dissolution times respectively. These times are related to the supersaturation, σ, the initial and final crystal sizes L_i and L_f and dissolution and growth rate constants, k_D and k_G by the following expressions;

$$T_G = \frac{L_f}{k_G \sigma} \quad \text{(2-4)}$$

$$T_D = \frac{L_i}{k_D \sigma} \quad \text{(2-5)}$$

A SMPT is said to be dissolution controlled if $T_D \gg T_G$ and growth if $T_G \gg T_D$. These two conditions can be represented by de-supersaturation profiles as highlighted in Figure 2-6. It can be seen for a growth controlled process the solution supersaturation is maintained close to the saturation concentration of the metastable phase. This is because the growth is sufficiently slow and the dissolution of the metastable phase is relatively fast. This could be due to a number of reasons such as slow nucleation of the stable phase or the slow growth which is hindered due to crystallite morphology. The opposite is true of a dissolution controlled process where the mass transfer of solute from the dissolving metastable phase to the growing stable phase is rapid and hence depletes the solution supersaturation faster than dissolution of the metastable phase. This could be caused by rapid nucleation of the stable phase or accelerated growth of the stable phase due to crystallite morphology.
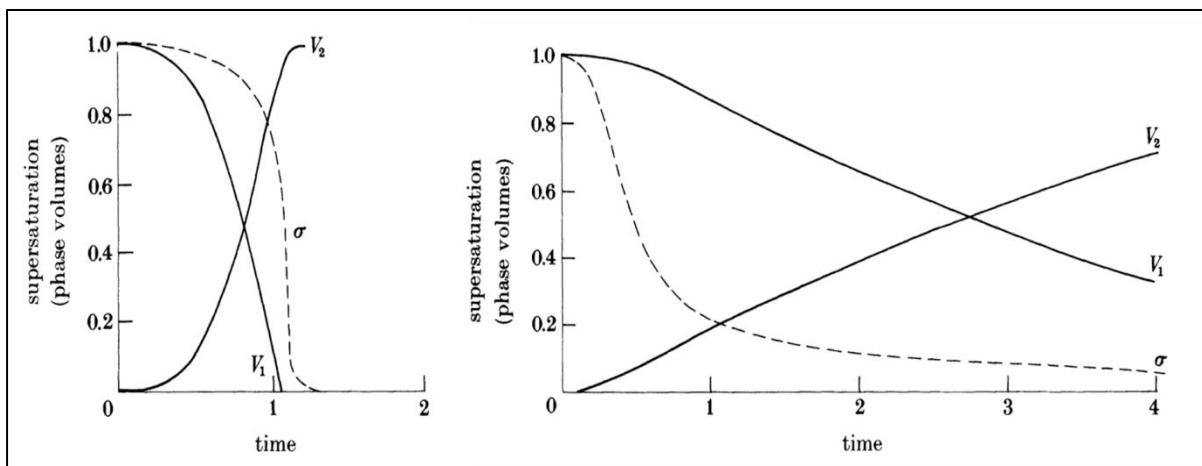
Figure 2-6 Schematic of de-supersaturation profiles for a growth controlled process (left) and dissolution controlled process (right)[25]

The overall measured rate constants of dissolution and growth from SMPT will contain a number of extra parameters, for example nucleation rates and crystal growth rates which are particularly difficult to measure on-line during a SMPT process. Most dissolution processes of pharmaceutical materials are considered zero order and act as an ideal situation for dissolution. However this is not always the case, dissolution can involve multiple steps including interfacial transport of the solute molecule away from the crystal surface followed by diffusional transport away from the solid-liquid interface[26]. Therefore the measured rate constants are likely to be much more complicated than at first glance involving multiple processes with a combination of reaction rates.

2.2.4 Crystal Morphology

Morphology and habit define the external shape of the crystal, where single polymorphs can exhibit multiple morphologies. This is because although crystal packing is the same between different morphologies of a material the external form is dependent on the growth rates of specific crystal faces. Due to this the morphology is controlled by the crystallisation environment such as supersaturation, solvent and impurity effects. Needle-like crystals for example are characterised by very fast growth along one crystallographic axis and very slow growth in the remaining directions, resulting in a long directional crystal morphology. Crystal morphology is of particular interest to the pharmaceutical industry due to impact it has on particle processing properties such as compaction, filtration, flow-ability and also solid state properties such as dissolution rate of the material.
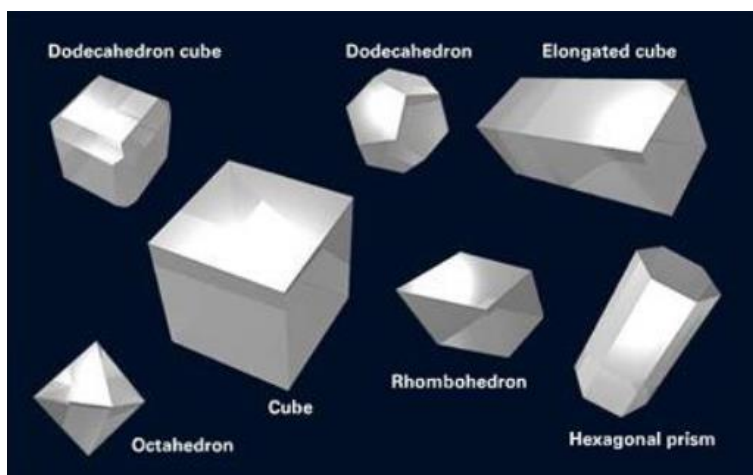
Figure 2-7 Some examples of crystal morphologies[27]

2.3 Phase Transitions, Solubility and Supersolubility

The previous section defined a crystalline material as a highly ordered arrangement of atoms or molecules in a three dimensional structure. To form this structure from a solution requires the clustering of solute molecules under supersaturation conditions to start the nucleation process, nucleation being a critical topic of this research. This section discusses the science of solubility and supersaturation and the importance of understanding the chemical, kinetic and thermodynamic properties of solutions for crystal growth. Nucleation theory will be introduced as a main concept of this research; a fundamental concept when studying the physical process of crystallisation.

2.3.1 Phase Transitions

A phase diagram is a way of representing the interchangeable regions of solid, liquid and gas phases by variation of temperature and pressure. The phase diagram can also be used to represent areas of stability of different crystal systems of a single crystalline solid for example, a phase can be defined as; 'a state of matter uniform in both physical and chemical composition' (Gibbs)[28].

Each segment of the diagram is a region of temperature and pressure where the corresponding phase is thermodynamically stable. This can change by altering the

system, for example increasing temperature and or pressure may change the phase; in this case the system has two degrees of freedom. The number of phases of a system can be calculated using the phase rule developed as follows;

$$P + F = C + 2 \qquad \text{(2-6)}$$

Where *C* is the number of components, *F* is the degrees of freedom and *P* is the number of phases. Phase diagrams are useful for describing a system to be studied by highlighting the chemical composition of the system and the effect that certain changes has on these components and the phases contained within the system.

2.3.2 Solution Thermodynamics and Composition

To understand the chemistry of a solution an understanding of some important thermodynamic parameters should be introduced other than simply the solution composition. These other parameters independent and are variables of the solution and include volume, *V*, internal energy, *U* and entropy, *S*. The volume of a system is relatively straightforward and can be calculated by taking the mass of the components and dividing through their individual densities. A more useful way of representing this is through the molar volume V_m which can be calculated through

$$V_m = \frac{M_A X_A + M_B + X_B}{\rho} \qquad \text{(2-7)}$$

Where *M* is the mass of the component, *X* is the mole fraction of the component and ρ the density. The entropy, *S*, or amount of disorder in a system, which is related to the Gibbs free energy can be calculated through the following expression;

$$dS = \frac{dq}{T} \qquad \text{(2-8)}$$

Where *q* is the flow of heat into the system and *T* is temperature. The enthalpy, *H*, of the system is also important in describing the Gibbs free energy, *G*, and can be calculated through the following;

$$H = U + PV \qquad \textbf{(2-9)}$$

$$G = U - TS + PV \qquad \textbf{(2-10)}$$

Where *U* is the internal energy of the system, *P* is the pressure and *V* is the volume.

An important parameter to describe a solution is the concentration of a solution, which may be expressed in a number of ways by various scientific communities, for example; volume/volume ratio or weight/weight ratio. A useful way to express exactly the molar composition of solution is by the mole fraction, X_A, of the various components in the solution, this is simply the moles of a component divided, n_A, by the total number of moles of components in a system through the following formula[29];

$$X_A = \frac{n_A}{n_A + n_B} \qquad \textbf{(2-11)}$$

This quantity is particularly useful when calculating the solubility of ideal and non-ideal solutions.

This short section briefly describes some of the thermodynamic properties of solutions, however a more physical description of solution chemistry can be illustrated by solute-solvent effects and why the choice of solvent on a system affects the energetics and ultimately the chemistry of that system.

A solvent brings one or more solid components into the liquid phase through dissolution, this involves interactions forming between the solvent and solute molecules. The type and strength of interaction strongly depend on the chemistry of the solvent and solute chosen. For example in ionic solutions such as salts, the electrostatic interactions dominate the solvation and usually involve electron or ion transfer. The polarisability of the solute and solvent can impact the dissolution process; a large ion maybe polarised by strongly polarising small ion which will produce an electron pair due to deformation of the electron shell. In non-ionic solutions Van der Waals forces dominate the dissolution process and also the attraction of permanent dipoles plays a large role; also known as the hydrogen bond[30].

2.3.3 Solubility

Solubility is a measure to the extent of dissolution of a solute in a solvent to form a solution; a homogeneous mixture of the two, although solubility can be used describe the mixture of gaseous, liquid and solid components[4]. The focus of this research is on organic molecules and as such the solute is usually a crystalline solid and the solvent usually a liquid organic or chlorinated solvent. Units of solubility are generally given as moles of solute per volume of solvent; usually moles per decimetre cubed in a chemistry laboratory, or mass of solute per mass of solvent; g/kg for example.

The general expression for the solid-liquid equilibrium derived in terms of activity is defined as:

$$ln\frac{\gamma_i^L x_i}{\gamma_i^S z_i} = \frac{\Delta H_{fus,i}}{R}\left[\frac{1}{T} - \frac{1}{T_{m,i}}\right] + \frac{\Delta C_{P,i}}{R}\left[\frac{T - T_{m,i}}{T}\right] - \frac{\Delta C_P}{R}ln\frac{T_{m,i}}{T} \qquad \textbf{(2-12)}$$

Where γ is the activity coefficient, ΔC_P is the specific heat capacity and x_i and z_i the molar fractions in liquid and solid phase respectively. i stands for a single component in the solution and L and S for liquid and solid phase of the components respectively. This expression relates the composition of solute in liquid and solid phases at a given temperature to thermo-physical properties of the pure solute and activity coefficients in solution for both phases.

In an ideal solution the activity coefficients will be unity, for a "single solute solution" the solid phase will contain only one compound and therefore the molar solubility, x, can be related through the enthalpy of fusion of the solid, *ΔH_fus*, and the melting temperature of the solute T_m (Equation 1-13).

$$\ln(x) = \frac{\Delta H_{fus}}{R}\left[\frac{1}{T} - \frac{1}{T_m}\right] \qquad \textbf{(2-13)}$$

This equation is known as the van't Hoff equation and is taken as the "ideal solubility model".

As $\Delta S_f = \frac{\Delta H_f}{T_m}$ Equation 1-13 can be given as;

$$\ln(x) = -\frac{\Delta H_{fus}}{RT} + \frac{\Delta S_{fus}}{R} \qquad \textbf{(2-14)}$$

In non-ideal solutions the deviation from ideality can be accounted for on the right side of the van't Hoff expression rather than by means of activity on the left hand side and therefore the solubility could be expressed as;

$$\ln(x) = -\frac{\Delta H_{diss}}{RT} + \frac{\Delta S_{diss}}{R} \qquad \textbf{(2-15)}$$

Where ΔH_{diss} and ΔS_{diss} are the enthalpy and entropy of dissolution respectively. Therefore if the experimentally determined solubility of a "single solute" solution is plotted in the form $ln\,x$ vs $1/T$, then this allows calculation of the van't Hoff enthalpy and entropy of dissolution at saturation from the slope and intercept of this line. The enthalpy reported here refers to the enthalpic change on dissolving a mole of a substance in an infinite amount of saturated solution.

For non-ideal solutions the solid-liquid equilibrium model should be expressed in terms of component activity rather than concentration. In the case of an ideal solution, solute-solvent interactions are considered to be equal to solute-solute and solvent-solvent interactions and therefore activity (a) is equal to solution concentration or $a = x_{ideal}$. In a non-ideal solution the partial molar excess Gibbs free energy, which quantifies the difference in these molecular interactions, has to be accounted for and therefore an activity coefficient has to be used so that $a = \gamma x_{real}$. At saturation (or equilibrium see Equation 1-12) these two expressions can be equated so $x_{ideal} = \gamma x_{real}$ and therefore;

$$\gamma = \frac{x_{ideal}}{x_{real}} \qquad \textbf{(2-16)}$$

Thus from the plot in the same coordinate plane of the ideal solubility and the real solubility the difference between the concentration at saturation (solubility) and that expected for ideality in the same range of temperature (T) will deliver the

dependence of activity coefficient (γ) on T, by the iterative calculation of (γ) through expression 4 [31].

If $\gamma = 1$ the solution behaves ideally, if $\gamma > 1$ the activity is higher than the concentration and therefore the "effective concentration" will be lower than that at ideality (or less than ideal), if $\gamma < 1$ the activity is lower than concentration and therefore the "effective concentration" will be higher than that at ideality (or more than ideal). This information can describe the solvation of a solute in a solvent as for $\gamma > 1$ a significant amount more association of the solute molecules would be expected. For $\gamma < 1$ solute-solvent interactions are favourable relative to solute-solute interactions.

For a specific solvent system

$$\Delta H_{solv} = \Delta H_{diss} - \Delta H_{sub} \qquad \textbf{(2-17)}$$

Where ΔH_{solv} is the heat of solvation and ΔH_{sub} is the enthalpy of sublimation ΔH_{sub} can be estimated from the calculated lattice energy E_{latt} since

$$E_{latt} = \Delta H_{sub} - 2RT \qquad \textbf{(2-18)}$$

A lower enthalpy of solvation will indicate a more favourable solvation (dissolution) process[4, 32, 33].

The non-ideal case of solubility can be roughly described by the following mechanism;

$$Solute_{solid} \rightarrow Solute_{liquid} \rightarrow Solute_{solution} \qquad \textbf{(2-19)}$$
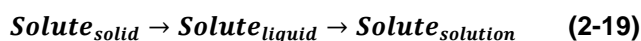
From this relationship the enthalpy and entropy of mixing ΔH_{mix} and ΔS_{mix} can be determined from the enthalpy and entropy of fusion (the solid state), ΔH_{fus} and ΔS_{fus} and ΔH_{dis} and ΔS_{dis}, this critically assumes that there is no variation of these parameters with temperature, through the following expressions[34,35,36];

$$\Delta H_{diss} = \Delta H_{fus} + \Delta H_{mix} \quad \textbf{(2-20)}$$

$$\Delta S_{diss} = \Delta S_{fus} + \Delta S_{mix} \quad \textbf{(2-21)}$$

This relationship is useful in predicting molecular aggregation however it is noted that specific solute-solute solvent-solvent and solute-solvent interactions cannot be determined in this analysis[37].

Solubility is a very sensitive measurement, as is the physical process of dissolution and many factors can influence the solubility of a solute including temperature, pH, solvent selection and critically; particle size. The relationship between particle size and solubility has been the focus of much research and to understand this correlation, Ostwald and Freundlich in the early 20th century attempted to explain this relationship with the following equation;

$$\boldsymbol{ln\frac{c_r}{c^*} = \frac{2M\sigma}{RT\rho r}} \qquad \textbf{(2-22)}$$

Where *c** is the equilibrium solubility, *c$_r$* is the solubility of particle with radius *r*, *ρ* is the density of the solid, *M* is the molecular weight, *σ* is the surface energy of the solid and *RT* is the universal gas constant and temperature respectively. The equation is also known as the Gibbs Thompson effect and goes someway to explain the solubility with respect for particle size, and this relationship holds well for dilute systems.

The major issue with this equation is that its derivation is from classical thermodynamics and as such a lot of assumptions are made regarding the solid; for example it assumes all particles are spherical and also that the surface energy is independent of particle size which is simply not possible. As such this explanation is floored by the fact that it predicts solubility continually increases with decreasing particle size, and while this true to an extent that smaller particle size increases solubility it does not hold true when particles reach the sub-micron size, simply due to the surface energy at this low size range[4].

2.3.4 Supersaturation

The previous discussion on solubility referred to measurements of solubility at equilibrium or in a saturated state. However it is possible that a solution can contain

more dissolved solid than its equilibrium concentration, either by cooling a saturated solution or by evaporation of solvent beyond the saturation point. This is referred to as supersaturation or super-solubility and is a fundamental process which must occur for crystallisation to proceed.

Supersaturation can be represented mathematically by measurements of solution concentration at equilibrium and at an absolute temperature; the ratio of the two is the supersaturation ratio *S* (Equation 2-23), which is the most common representation. Other values are the concentration driving force (Equation 2.24); *Δc* and the relative supersaturation (Equation 2-25); *σ*.

$$S = \frac{c}{c^*} \qquad \text{(2-23)}$$

$$\Delta c = c - c^* \qquad \text{(2-24)}$$

$$\sigma = \frac{\Delta c}{c^*} = S - 1 \qquad \text{(2-25)}$$

Where *c* is the solution concentration at a given temperature and c^* is the equilibrium concentration at a given temperature. All measurements of supersaturation above are dimensionless with the exception of *Δc*, and as such the measurements are very sensitive to changes in concentration so to avoid significant errors care must be taken when selecting concentration units and also when measurements of concentration are taken. When measuring supersaturation it is also useful to quote the temperature the reading was taken at; this is due to supersaturation being very temperature dependent due to the equilibrium concentration dependence on *T*. Another fundamental but useful expression is the relationship between supersaturation and the crystallising driving force of a solute from solution by the following;

$$lnS = ln\frac{a}{a^*} = \frac{\Delta\mu}{RT} \qquad \text{(2-26)}$$

$$S = \exp\frac{\Delta\mu}{RT} \qquad \text{(2-27)}$$

$$\mu = \mu_0 + RTlna \qquad \text{(2-28)}$$

Where *R* and *T* are the gas constant and temperature respectively, *S* is supersaturation ratio and *α* is activity *μ* is chemical potential μ_0 is the standard potential and α is the activity[4].

2.4 Nucleation

Nucleation is the start of the crystal growth process, it is a phenomena whereby solute molecules come together in solution to form clusters or nuclei, overcome the energy barrier for cluster stability and start the process of growth.

Nucleation in solution can be characterised into two categories (Figure 2-8); primary and secondary nucleation. Primary nucleation occurs without the presence of any crystalline matter, whereas secondary nucleation occurs in the presence of a seed crystal for example. Primary nucleation can be further split into homogeneous and heterogeneous nucleation; homogeneous is spontaneous nucleation and heterogeneous is nucleation induced by the presence of other particulate matter.

Primary (Spontaneous)	Secondary (Seeded)
↓	↓
Homogeneous	Heterogeneous

Figure 2-8 Nucleation classes, adapted from Mullin 4th edition[8]

2.4.1 Homogeneous Classical Nucleation Theory

Like all nucleation events, homogeneous nucleation must proceed via formation of a cluster of solute molecules in solution. Exactly how these solute molecules come together to form a nucleus for crystal growth is unknown and the focus of this research. The process of solute molecules coming together and ordering into a lattice geometry occurs over very short timescales depending on supersaturation, the nuclei formed in a supersaturated solution can be stable and go on to grow, or unstable and simply re-dissolve.

$$A + A \rightleftharpoons A_2 \qquad \textbf{(2-29)}$$

$$A_{n-1} + A \rightleftharpoons A_n \rightarrow critical\ cluster \qquad \textbf{(2-30)}$$
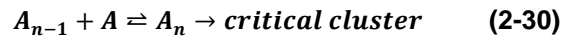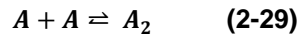
These nuclei which reach a certain size, the critical radius, are termed critical nuclei and further molecular additions from solution result in growth. A simple way to represent this formation of a critical nucleus is a bimolecular addition process as in Equation 2-29 and 2-30.

The exact structure of these critical nuclei are not known, the molecular additions to the cluster may form a perfect crystal lattice which simply expands into a macromolecular crystal, or these nuclei could be more liquid like in state with no real ordered structure to the cluster.

From classical theory of Volmer and Gibbs, the free energy, *ΔG*, of homogeneous nucleation can be used to explain the formation of a critical nucleus. The overall free energy of a solute particle in solution is equal to the sum of the surface energy, *ΔG_S*, which is the energy difference of the surface of the particle and bulk of the particle, and the volume free energy, *ΔG_V* , which is the energy difference between an infinitely large particle and a single solute molecule in solution as shown in Equation 2-31.

$$\Delta G = \Delta G_S + \Delta G_V \qquad \textbf{(2-31)}$$

$$\Delta G = 4\pi D^2 \gamma_{eff} + {}^4\!/_3\, \pi D^3 \Delta G_v \qquad \textbf{(2-32)}$$
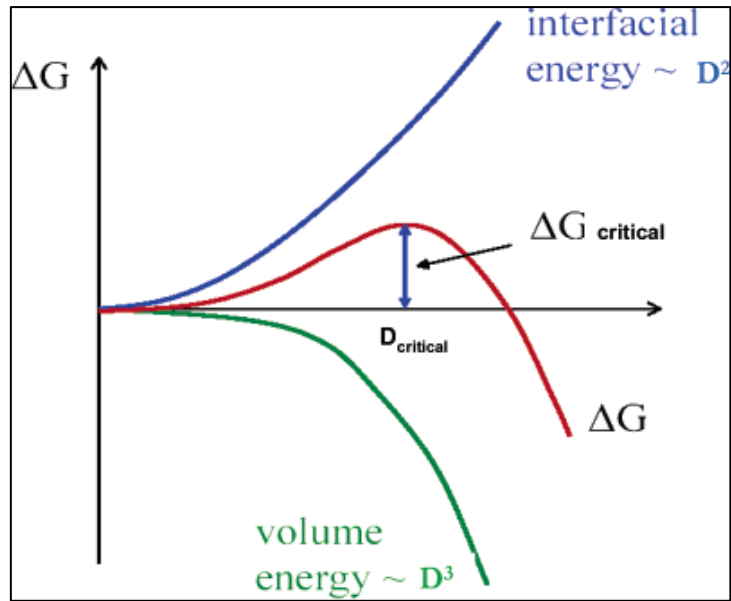
Figure 2-9 Free energy balance between the surface area and volume terms with the maximum corresponding to a critical nucleus size[38].

The derivation of these terms is based on assumptions to the system and one of the most important is that the solute particle is assumed spherical in shape. This leads to the terms ΔG_S to be proportional to D^2 (D is also represented as r in some publications) and ΔG_V proportional to D^3 as shown in Equation 2.32. In Equation 2-33 ΔG_v is the free energy change of transformation of the crystalline surface and the supersaturated solution per unit volume and γ_{eff} is the interfacial tension. It should be noted that ΔG_S and ΔG_V are opposite in sign, the graphical representation of ΔG will pass through a maximum, Figure 2-9, this is the ΔG_{crit}, i.e. the maximum free energy required to form a stable nucleus of radius D_{crit}.

$$D_c = \frac{-2\gamma_{eff}}{\Delta G_v} \qquad (2\text{-}33)$$

$$\Delta G_{crit} = \frac{16\pi\gamma_{eff}^3}{3(\Delta G_v)^2} = \frac{4\pi\gamma D_c^2}{3} \qquad (2\text{-}34)$$

The value of ΔG_{crit} can be calculated from Equations 2-34 and importantly the value of D_{crit} should be obtained from 2-35. This critical size represents an energy maxima in the nucleation process and the minimum size for a nuclei to be sufficiently stable for growth to occur. Clusters smaller than this size will tend to re-dissolve in solution

because the interfacial tension is too high and thus it is more favourable, energetically, for the particle to be in solution. Similarly clusters with radius $>D_{crit}$, will have an interfacial tension which is low enough for growth to occur.

A useful way of expressing the number of nuclei formed per unit time and volume is the nucleation rate J_t, which may be expressed in relation to temperature, supersaturation and the interfacial tension through equation 2-36.

$$D_{crit} = \frac{2\gamma_{eff}v_0}{kTlnS} \quad \textbf{(2-35)}$$

$$J_t = A\,exp\left[-\frac{16\pi\gamma_{eff}^3 v_0^2}{3k^3T^3(lnS)^2}\right] \qquad \textbf{(2-36)}$$

Where *A* is the pre exponential factor, v_0 is the molecular volume; *S* is the supersaturation, and *k* and *T* the Boltzmann constant and temperature respectively.

2.4.2 Secondary and Heterogeneous Nucleation

Secondary nucleation is a different mechanism of nucleation and generally occurs through the addition of crystalline matter to a supersaturated solution which increases the rate of nucleation. It can be shown that secondary nucleation occurs much more easily in solutions than primary nucleation and also generally at lower supersaturation. Many mechanisms of secondary nucleation have been reported in the literature to show how crystalline material could increase the number of active nuclei in a crystallisation process. Sung, Estrin and Youngquist, for example, have shown that shearing of crystalline material present in solution to create new crystal nuclei via fluid shearing in an agitated reactor vessel is possible[39].

Contact nucleation is also a well-studied area of secondary nucleation which involves collisions of crystallites with other bodies such as agitators, reactor vessel walls and other crystals. These contacts shear the crystallites to form new nuclei for crystal growth. It has been shown in research by Strictland and Constable however that these crystallites are generally badly sheared and show many dislocations, giving rise to high growth rates of the crystallites[40].

The easiest way to provoke a crystallisation event is by seeding a supersaturated solution. This is a process whereby a small seed crystal is of the desired material is

added during the super-cooling period. This method is often used to obtain particularly difficult to synthesise polymorphs, or to prevent the appearance of an unwanted hydrate, for example. The quantity and size of the seed crystals has been a topic of much research; Kubota and Fujiwara stated a critical seed size between 200 – 500 µm was sufficient to produce nuclei in saturated solutions[41]. The general consensus is that larger seeds produce more nuclei than smaller ones, simply because larger crystals generate force on collision and are also less likely to be swept around the vessel in agitator turbulence, reducing the chance of collisions. Smaller seeds also grow at a slower rate than larger seeds

Secondary nucleation can also be unintentional and crystallisation processes can be contaminated by unintended seeds making their way into crystallisers. This can occur through airborne crystallites in industrial laboratory's or through contaminated glassware or agitators for example. There are many examples of crystal products where one polymorph has been formed for several years and suddenly is seemingly not synthesisable and a new polymorph is only obtainable. These phenomena are based on a suggestion of localised seeding in industrial laboratories; for example Xylitol, prepared in 1891, has seen multiple polymorphs appear in its production as reported by Dunitz and Bernstein[42].

2.4.3 Two Step Nucleation

Where classical nucleation theory explains that nucleation must proceed through monomer addition to an ordered cluster of molecules which ultimately grow to form a separate crystalline phase, a modern approach is two step nucleation. The two step model states that the formation of an ordered crystalline phase is preceded by separation of a disordered liquid like phase where fluctuations in order have no relation to fluctuations in density i.e. density parameters can increase however this has no impact on the order parameters of clusters[43]. A comparison between the two step nucleation theory and classical theory is provided in Figure 2-10.
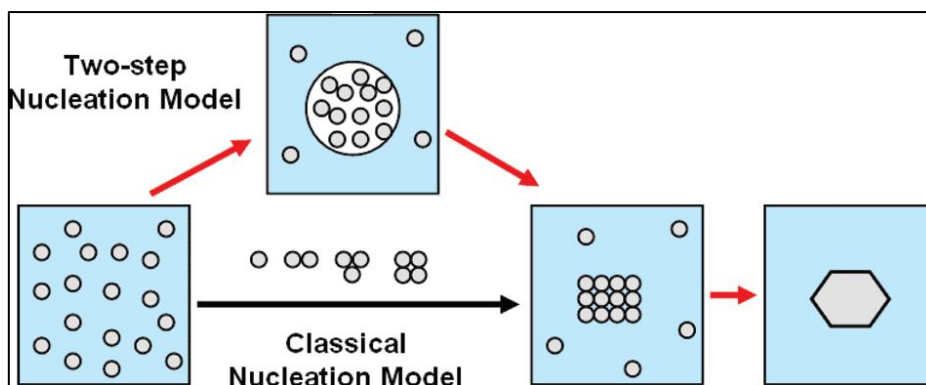
Figure 2-10 schematic of classical nucleation vs the two step model[44]

One of the earliest reports of two step nucleation was provided by computational simulations of homogeneous nucleation by ten Wolde and Frankel[45]. These Monte Carlo simulations showed that during the nucleation process large liquid like droplets formed which altered the pathway to nucleation. It was found that formation of a large disordered cluster of solute was followed by formation of an ordered nucleus; furthermore it was shown that if nucleation proceeded in this manner the nucleation rate was increased tenfold.

Further to this, molecular dynamics simulations of acetic acid in chloroform presented formation of a liquid-like micelle of acetic acid, whereby its formation was accelerated by increasing acetic acid concentration[46]. Similarly molecular dynamics results published on silver bromide, AgBr, in water indicated that the solvent seemed to induce the disorder in large aggregates of solute. Pre-nucleation clusters of AgBr were found to be highly disordered in water; however repetition of the study *in-vacuo* found the clusters to be in a highly ordered configuration[47].

A number of experimental studies have also provided support for the two step mechanism; dynamic light scattering studies have provided evidence for molecular aggregation into fractal clusters during the nucleation of lysozyme[48]. Small angle scattering studies on a number of protein and colloidal systems suggest the presence of nuclei which are fractal aggregates or droplet-like clusters which undergo rearrangement to more ordered structures[49].

Recently studies on the protein deoxy-haemoglobin S polymer by Vekilov[50] have provided perhaps the most convincing experimental evidence of two-step nucleation.

It was found that very large solute dense droplets serve as nucleation centres for deoxy-haemoglobin S polymer due to a higher concentration and hence higher driving force within the droplets. This study also concluded that there exists an optimum density fluctuation with an optimum size required to facilitate fast nucleation of an ordered nucleus[51].
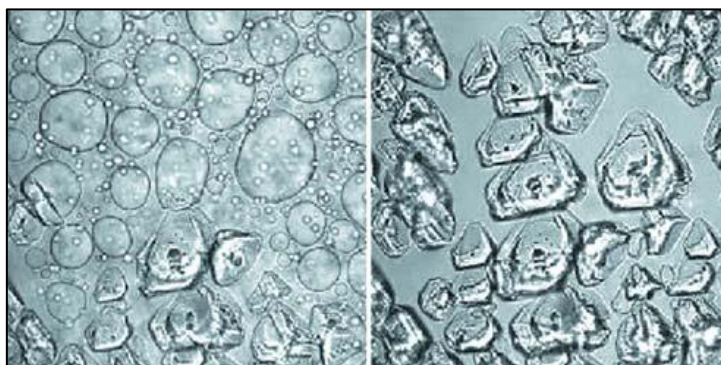
Figure 2-11 Bright field imaging of glucose isomerase crystals nucleating inside liquid dense droplets of solute[52]

When a dense liquid phase, which exists prior to nucleation of the crystalline phase, is particularly stable it can be directly imaged. This is generally the case for particularly large molecules such as proteins or polymers where rearrangement into a more stable phase or progression of the order parameters would be expected to take much longer than say for small organic or ionic systems. Figure 2-11 shows bright field imaging of dense liquid droplets of glucose isomerase which provide centres for nucleation to occur and form the crystalline phase.

Recent studies of small organic molecules have provided further evidence of a more non-classical approach to nucleation. Glycine nucleation was recently investigated using small angle x-ray scattering, it was found that dimers of glycine formed mass fractal aggregates followed growth and transformation to surface fractal clusters prior to crystallisation[53]. This positive progression of fractal dimensionality was attributed to disordered liquid-like clusters transforming to more ordered crystalline nuclei in a similar fashion to the two step model, this led to a proposed pathway of nucleation of glycine; Figure 2-12.
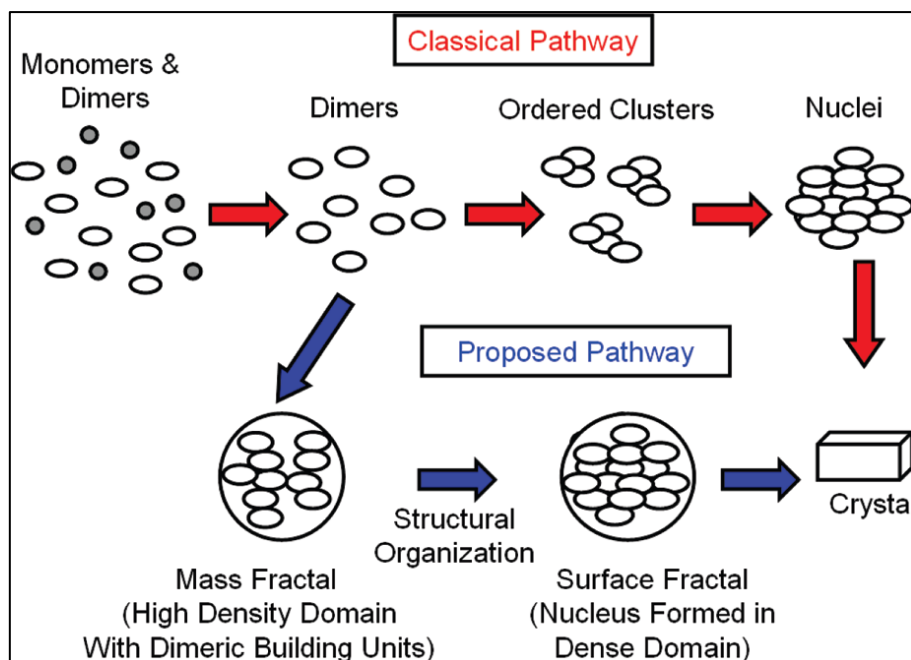
Figure 2-12 A proposed two-step pathway for the nucleation of glycine from aqueous solutions[44]

Further studies on glycine, by Sefcik and co-workers, have presented results highlighting the existence of disordered pre-nucleation clusters of glycine even in the under-saturated state upon monitoring the reverse process of nucleation, dissolution, of glycine in aqueous solutions[54]. A combination of dynamic light scattering, x-ray diffraction and Brownian motion microscopy revealed the existence of glycine nano-droplets up to 250 nm in size which are stable once the solution passes the dissolution temperature to the under-saturated state. These clusters fit better a fractal model in comparison to a smooth spherical model indicating the clusters are disordered at the interface with the surrounding solution. Interestingly during nucleation experiments in the same study it was proposed that a critical size of nano-droplet is required to nucleate micro-crystals large enough to grow outside of the large nano-droplets. This is a similar finding to those of protein crystals reported earlier.

Additionally similar large scale nano-droplets have also been observed in under-saturated aqueous solutions of D-alanine[55]. These meso-species were also found to be particularly large; in the range of 100-300 nm, whereby the size distribution from dynamic light scattering results increased upon increasing solute concentration.

The studies summarised in this section highlight the new possibility of a non-classical approach to nucleation whereby the process does not necessarily have to proceed through monomer addition to an ordered nucleus but rather by monomer, dimer, trimer etc. addition to a disordered liquid-like droplet of solute. Experimental data revealing pre-nucleation clustering in calcium carbonate[56] together with the interesting results of Colfen and co-workers[57] who suggest nucleation can proceed through aggregation pathways is particularly interesting. Further experimental data is obviously required to further understand these pre-nucleation clusters and in particular the interesting topic of the nucleus structure and its relation to these assemblies, only then can a unified model be proposed between classical and non-classical theory.

2.4.4 Induction Time

Induction time is the time elapsed between achieving supersaturation in solution and the first appearance of crystalline material. The induction period is usually measured by detecting the presence of crystalline material through measurements of the turbidity of solution. This of course is not an exact indication of the induction period as the first critical nuclei will be undetectable to these methods and so some degree of crystal growth is required for detection. The induction period is an important factor in determining nucleation kinetics and thermodynamic properties and these techniques have been used to much success in research[58].

Classical nucleation theory disagrees with the existence of an induction period as it treats the solution state in an ideal steady state condition and states nucleation should occur as soon as supersaturation is reached. This means some particular events must occur before nucleation starts and these can be stated as; t_r; a relaxation time for the solution to distribute the clusters formed in supersaturation, t_n; the time required for the formation of a stable nucleus[4]. Also time is required for the nucleus to grow to a detectable size t_g so an expression for induction time can be;

$$\tau = t_r + t_n + t_g \qquad \text{(2-37)}$$

Induction time is usually measured by heating a saturated solution past its saturation temperature and holding for a time period to allow completed dissolution of the solid.

The solution is then rapidly cooled to a point below the saturation temperature and held at the specified temperature until the crystallisation event is detected by turbidometric techniques.

As discussed in Section 2.4.1 the nucleation rate is an important parameter to characterise nucleation, this parameter can be related to the induction time through the following expression;

$$J \propto \frac{1}{\tau} \qquad \textbf{(2-38)}$$

Induction periods can be influenced by many factors, the main components being; supersaturation, impurity level, agitation speed and presence of seed crystals, and so experimental design is very important when measuring induction times.

2.4.5 Assessment of Nucleation Kinetics using Iso-thermal Analysis

Recent studies have derived nucleation kinetic parameters from the probability distribution of induction times, observed from measurements of crystallisation temperatures at a set temperature and hence supersaturation (isothermal), and these have been related to the mechanisms by which critical nuclei form in supersaturated solutions[59]. Generally the isothermal methodology relates induction time with supersaturation to calculate nucleation kinetic parameters, such as interfacial tension. There are a number of examples of this methodology successfully applied to organic materials in the literature; Rasmuson et al. have recently studied solvent effect on measured interfacial tensions of butyl paraben[60], Kulkarni et al. studied the nucleation rates of isonicotinamide in ethanol[61], and Sullivan et al. related solution chemistry to attachment frequency for para aminobenzoic acid[62].

Classical nucleation theory can provide expressions for analysing certain structural parameters relating to the crystallisation process from induction time (τ) measurements as a function of supersaturation (*S*). A relationship between τ and *S* can be applied using Equation 2-39,

$$ln\left\{\tau(S(S-1)^{md})^{\frac{1}{md}}\right\} = lnk_{md} + \frac{B}{(1+md)(kTln(S))^2} \qquad \textbf{(2-39)}$$

The value of *d* is related to the dimensionality of crystal growth and is taken as 1 for a needle-like crystallite, γ_{eff} is the interfacial tension, *m* is a crystallite growth

exponent, *B* is a term related to the molecular volume v_0 and the interfacial tension, *k* is the Boltzmann constant and *T* is the isothermal temperature. Through this relationship a plot of $ln\left\{\tau(S(S-1)^{md})^{\frac{1}{md}}\right\}$ vs $\frac{1}{T^3\ (lnS)^2}$ will yield a straight line with the slope equal to $\frac{16\pi\ v_0 2\ \gamma eff^3}{3(1+md)k^3}$ whereby the interfacial tension can be calculated. If a spherical critical nucleus is assumed the radius, *r** and number of molecules, *i**, within the critical nucleus can be calculated using Equations 2-40 and 2-41,

$$r^* = \frac{2\gamma_{eff}v_0}{kTlnS} \quad \textbf{(2-40)}$$

$$i^* = \frac{4\pi(r^*)^3}{3v_0} \quad \textbf{(2-41)}$$

2.4.6 Metastable Zone Width

The metastable zone width (MSZW) is the width of the metastable zone which lies between the solubility curve and the super-solubility curve in Figure 2-13 and has units of temperature. The process of supersaturation can be expressed using three terms, first quoted by Ostwald (1897)[13], labile, metastable and stable; these terms can be represented as a super solubility diagram (Figure 2-13).

The lower (solid line) represents the equilibrium solubility curve of a solute in a solvent, the dashed line represents the start of the labile zone (super solubility curve) and the area between the two lines is the metastable zone. The generation of the supersaturation in this case is by three methods; cooling the solution below the equilibrium solubility represented by the line A,B,C, evaporating the solvent in the solution represented by the line A,B',C', or a combination of the two by the line A,B'',C'' in Figure 2-13.

The gap in temperature between the stable and labile zones is known as the metastable zone width (MSZW), the size of which is influenced by many factors including cooling rate, evaporation of solvent, impurity level and the presence of seed crystals. The metastable phase represents the supersaturated zone where

crystallisation is said to be improbable but can be induced by seeding. The stable zone is the unsaturated region below the solubility curve where spontaneous crystallisation is impossible. The labile region is the area above the super solubility curve and crystallisation is said to be probable[63,64].
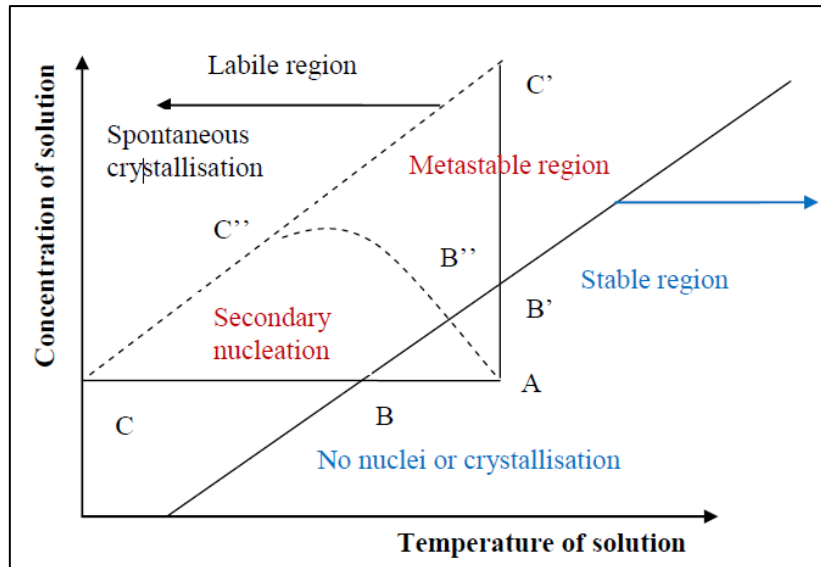
Figure 2-13 Solubility super-solubility plot highlighting the stable, metastable and labile regions[63]

The measurement of the MSZW is generally determined by a poly-thermal method to measure the critical undercooling of a solution that can be achieved before crystallisation occurs, ΔT_C. This is achieved by taking a saturated solution at T_e, the equilibrium solubility temperature, and cooling at constant cooling rate q until the first crystals are observed at the equilibrium crystallisation temperature, T_C, giving the expression[65];

$$\Delta T_C = T_e - T_C \qquad \textbf{(2-42)}$$

The MSZW is a useful parameter as it can be related to the nucleation rate, *J*, from classical nucleation theory through Equation 2-43;

$$J = k(S)^n \qquad \textbf{(2-43)}$$

Where *k* is the nucleation constant, *n* is the nucleation order. The supersaturation S can be related to the super-cooling ΔT_C through Equation 2-44;

$$S = \left(\frac{dc_0}{d_t}\right)\Delta T_{\;c} \qquad \textbf{(2-44)}$$

Where dc_0/dt is the slope of the solubility curve at the given temperature T, and combination of Equations 2-343 and 2-44gives the following relationship;

$$J = k\left(\left(\frac{dc_0}{dt}_{\;T}\right)\Delta T_C\right)^n \qquad \textbf{(2-45)}$$

The MSZW is dependent on a number of factors; solution temperature, impurities and stirring rate[66,67,68]. Recent studies by Bonnin – Paris show that the cooling rate on the MSZW of glycine solutions was the most influential factor in crystallisation temperature and thus ΔT_C[69].

2.4.7 **Assessment of Crystallisation Kinetics using a Poly-Thermal Methodology**

The poly-thermal method has also been used to study crystallisation due to the fundamental connection between the meta-stable zone width (ΔT_c) and the crystallite properties. This method relates ΔT_c to the cooling rate, q, to calculate nucleation kinetics and information about crystallite growth.

The most common interpretation of ΔT_c vs q data is using the classical Nyvlt expressions[70][71]. Nyvlts method is based on a power law expression which relates supersaturation to nucleation rates, this leads to a linear relationship between lnq vs ln ΔT_c whereby mass based nucleation kinetic parameters can be derived.

Following Nyvlts method, Kubota proposed a new interpretation of ΔT_c vs q data, this approach takes into account the number density of nuclei which reach an unknown detectable value[72]. This led to an expression relating nucleation rates to the number density of nuclei, a more useful quantity, through a linear Nyvlt-type plot. These two poly-thermal methodology's have been comprehensively reviewed and applied to paracetamol-ethanol solutions by Mitchell (2010) highlighting the kinetic parameters obtained from each approach[73]. Further work by Sangwal (2009) described a modified Nyvlt equation which led to a ΔT_c vs q formula providing an insight into nucleation kinetic parameters and their relationship to the thermodynamic properties of the crystallisation system[74][75].

More recently further development of the poly-thermal method has led to the development of a more rigorous approach by Kaschiev, Borrisova, Hammond and

Roberts[76, 77] (KBHR) which takes into account either the volume fraction or the number of crystallites nucleated. The KBHR approach allows determination of important nucleation parameters providing also an insight into the nucleation and growth mechanisms of crystallites. This poly-thermal approach was recently applied to methyl stearate crystallising from kerosene allowing values of the interfacial tension to be determined which were further validated through use of an isothermal methodology[78]. These advances in poly-thermal analysis methods have demonstrated that through their application, mechanistic insight and key kinetic parameters related to the nucleation and growth of a solute component can be derived

Using the KBHR approach the average values of T_{dis} and T_{crys} allow calculation of the critical undercooling, ΔT_c, using Equation 2-42. A related value, the relative critical undercooling, μ_c, can be calculated from Equation 2-46, where μ_c is dimensionless.

$$u_c = \frac{\Delta T_c}{T_e} \quad \textbf{(2-46)}$$

The KBHR approach has shown that measured μ_c values plotted against cooling rate (q) in ln-ln coordinates has a linear dependence, as such, information regarding the nucleation mechanism; instantaneous or progressive, can be deduced from the slope of the curve. A slope of < 3 is indicative of instantaneous nucleation, where nuclei all form at the same temperature, whereas a slope of >3 is indicative of progressive nucleation whereby nuclei are formed at various temperatures leading to varying crystallite sizes[79]. To further scrutinise the dependence of μ_c on q, the following inequalities must be met.

$$u_c < 0.1, a u_c < 1 \quad \textbf{(2-47)}$$

The values of a are calculated using Equation 2-48 where k is the Boltzmann constant and λ is the molecular latent heat of crystallisation, these values were averaged for each concentration over the various cooling rates.

$$a = \frac{\lambda}{k T_e} \quad \textbf{(2-48)}$$

Instantaneous Nucleation

For the case of instantaneous nucleation the value of q_0, a parameter related to the dependence of μ_c on q, can be related to the concentration of crystallites, C_0, at the point of nucleation, t_0, through Equation 2-49,

$$q_0 = \left[\frac{k_v\, C_0}{(n+1)^d\, \alpha_{det}}\right]^{\frac{1}{md}} (a)^n\, K_G\, T_e \qquad \textbf{(2-49)}$$

Where n and m are growth exponents for the growth mechanism of the crystallites; where $n = 1$ is associated with diffusion of solute across a crystal/solution interface, and $n = 2$ indicates the presence of screw dislocations within the crystallite. The parameter *m* can take a value between 0.5 and 1, where *m* = 0.5 indicates undisturbed diffusion of the solute to the crystal surface and *m* = 1 indicates growth through diffusion of solute through a stagnant layer around the crystal[80]. The value of *d* is the dimensionality of the crystal growth i.e. 1 for needle like crystallites. K_g is the overall growth rate of the crystal and K_v is the crystallite growth shape factor e.g. $2A_0$ for needle like crystals (where A_0 is the fixed needle cross-sectional area)

The value of q_0 can be obtained through a Nyvlt type relationship, Equation 2-50, by plotting the *q* vs *μc* in ln-ln coordinates.

$$\ln q = \ln q_0 + (n+1)\ln u_c \qquad \textbf{(2-50)}$$

Progressive Nucleation

For the case of progressive nucleation the μ_c (*q*) dependence can be related through the number of crystallites at the detection point, N_{det}, which is described through the parameter q_0.

$$\ln(q) = \ln(q_0) + a_1 \ln(u_c) - \frac{a_2}{(1-u_c)u_c^2} \qquad \textbf{(2-51)}$$

Plotting crystallisation parameters in ln *q* vs *μc* coordinates followed by a non-linear least squares fit of Equation 2-51 enables calculation of free parameters related to the nucleation and growth of crystallites.

a_1 is a parameter related to the crystallite growth exponent's *m*, *n* and *d*.

$$a_1 = 3 \qquad \textbf{(2-52)}$$

The free parameter a_2 is related to the nucleation parameter b and so can be used to calculate γ_{eff} where k_n is the nucleus shape factor ($16\pi/3$ for a spherical nucleus), v_0 is the molecular volume in the crystal.

$$a_2 = b = \frac{k_n \, v_0^2 \, \gamma_{eff}^3}{k \, T_e \, \lambda^2} \qquad \textbf{(2-53)}$$

The final free parameter q_0 takes into account growth and nucleation parameters, where K_J is the nucleation rate constant.

$$q_0 = \frac{V \, K_J \, T_e}{N_{det} \, 2b} \qquad \textbf{(2-54)}$$

Following analysis of γ_{eff} though Equation 2-55 the critical nucleus radius, r^*, can be calculated through the following expression;

$$r^* = \frac{2 \, \gamma_{eff} \, v_0}{\lambda \, u} \qquad \textbf{(2-55)}$$

the number of molecules within the critical nucleus, i^*, can be evaluated through Equation 2-56;

$$i^* = \frac{2b \, k \, T_e}{\lambda \, u^3} \qquad \textbf{(2-56)}$$

2.5 Crystal Growth

Following formation of stable nuclei, the next stage of the crystallisation process is growth of the crystallites. Crystal growth is determined by a number of solution environment factors such as supersaturation, solvent and solution impurity effects but also by internal factors of the crystal such as surface specific intermolecular interactions and also crystal defects[81].

The major stages involved in the crystal growth process are as follows;

- Transport of solute molecules to the boundary layer between crystal surface and solution

- Solute diffuses via concentration gradients through the boundary layer

- Crystal surface adsorption of the solute molecule

- Surface diffusion of the solute molecule across the crystal surface to an energetically favourable incorporation site followed by de-solvation of the solute and binding into the site
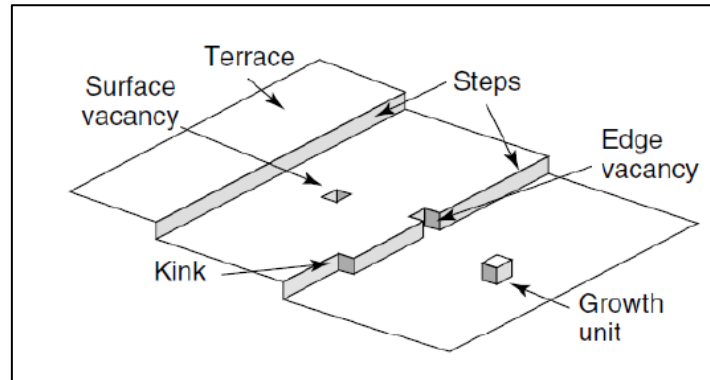
Figure 2-14 The Kosel model of crystal growth considering diffusion of the solute to the various attachment sites at the crystal face[82]

Kosel (1928)[83] describes a model of crystal growth by considering the attachment of the solute molecule to three main types of crystal faces; surface, step and kink sites as in Figure 2-14. The three types have varying bonding environments for the growth unit, whereby if considering a cube as the growth unit the bonds formed upon integration to the sites would be 1, 2 and 3 for surface, step and kink sites respectively. This also represents the favourability of the energetics of binding; where forming 1 bond is less favourable than 2 which is less favourable than 3. Generally the step and kink site faces grow faster than surface faces due to this favourability. This variation in growth rates at specific crystal faces leads to variation in crystal morphology which will be characterised by the slowest growing faces where the fast growing faces usually are not visible in the resultant morphology.

Noyes and Whitney (1897)[84] assumed the growth process was simply the reverse process of dissolution, whereby only the concentration gradient between the crystal surface and the bulk solution controlled the growth rate. The proposed equation the

rate of solute deposition, dm/dt, was related to the difference between the solubility C and the equilibrium solubility C^*;

$$\frac{dm}{dt} = k_m A (C - C^*) \quad \textbf{(2-57)}$$

where k_m is the coefficient of mass transfer and A is the crystal surface area. This equation was later modified to account for the thin stagnant layer at the boundary between the crystal and solution where the solute must diffuse.

$$\frac{dm}{dt} = \frac{D}{\delta} A (C - C^*) \quad \textbf{(2-58)}$$

where δ is the stagnant layer thickness and D is the diffusion coefficient. However this was a particularly simplistic approach as it assumed that only the film thickness controls the rate of growth, which if true would result in a situation inside stirred reactors of infinite growth of the crystallites.

To address this problem the diffusion theory was modified to take into account not only the diffusion of solute molecules to the solid surface but also the adsorption of the solute into the crystal surface[85, 86]. The growth rate of a crystal was then relative to the following diffusion and adsorption rates;

$$\frac{dm}{dt} = k_d A (C - C_i) \quad \textbf{(2-59)}$$

$$\frac{dm}{dt} = k_r A (C_i - C^*) \quad \textbf{(2-60)}$$

where k_d is the diffusion rate constant and k_r is the rate constant associated with the adsorption of solute at the surface. An analysis of the relative rates can be provided here; if $k_d \gg k_r$ the growth is regarded as a surface controlled process, where adsorption of the solute is hindered at the surface relative to diffusion. However if $k_r \gg k_d$ the growth can be considered as a diffusion controlled process where surface integration of the growth unit is fast relative to diffusion.
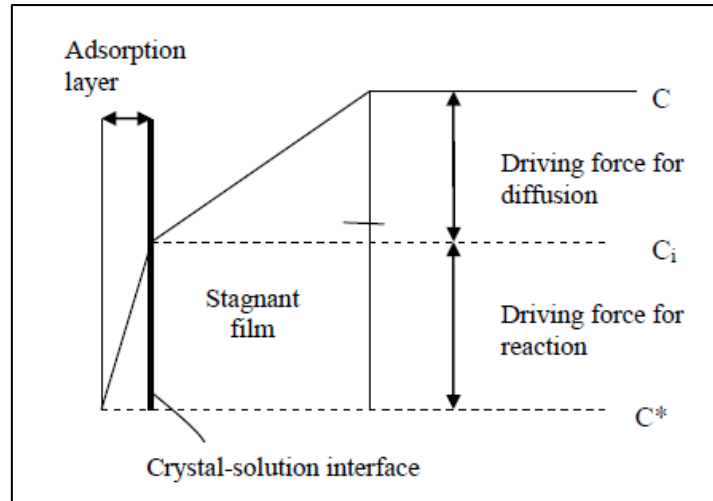
Figure 2-15 Supersaturation driving force for diffusion and adsorption during crystal growth[4]

The development of crystal growth rate measurement techniques led to a progression towards a more complete face specific model of crystal growth. Three major growth mechanisms were developed to explain molecular attachment to a crystal surface under various supersaturation conditions[87];

1. Screw dislocation mechanism (BCF model) was developed by Burton, Cabrera and Frank and is shown to occur generally where growth is less favourable at lower supersaturation conditions. As such the solute molecules diffuse over the surface and prefer adsorption into kink sites, screw dislocations on the crystal surface provide a large area of kink sites and thus incorporation of the growth unit is more accessible. This mechanism leads to the formation of growth spirals on the crystal surface as shown in Figure 2-16
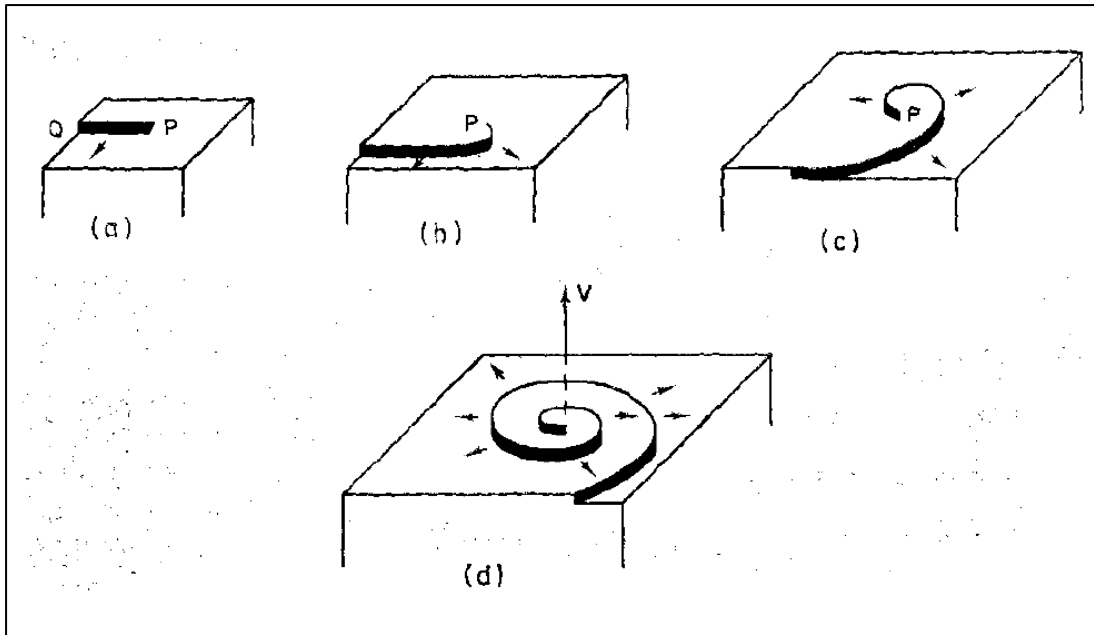
Figure 2-16 A schematic example of the BCF mechanism progressing from kink sites into a growth spiral at the crystal surface[82]

2. The two dimensional birth and spread mechanism generally occurs at higher supersaturations than the screw dislocation mechanism. This pathway results in adsorption of the growth unit in any available surface sites due to higher driving force. This mechanism starts with the creation of a smooth monolayer where further growth occurs through integration of growth units which spread across the layer, this is represented in Figure 2-17[88, 89].
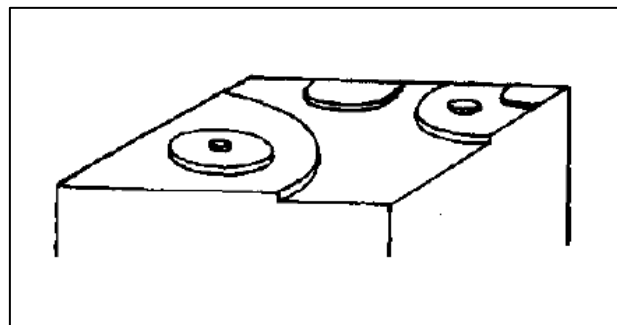
Figure 2-17 Schematic example of the birth and spread model[4]

3. The continuous growth model occurs mainly at very high supersaturations where the high driving force results in surface roughening due to very fast

growth. This produces a very large amount of kink sites across the crystal surface which leads to low attachment energy for the solute molecule in all growth directions and produces crystals with dendritic morphology such as ice crystals, Figure 2-18 highlights the effect of increasing supersaturation and the progression through the three mechanisms[90].
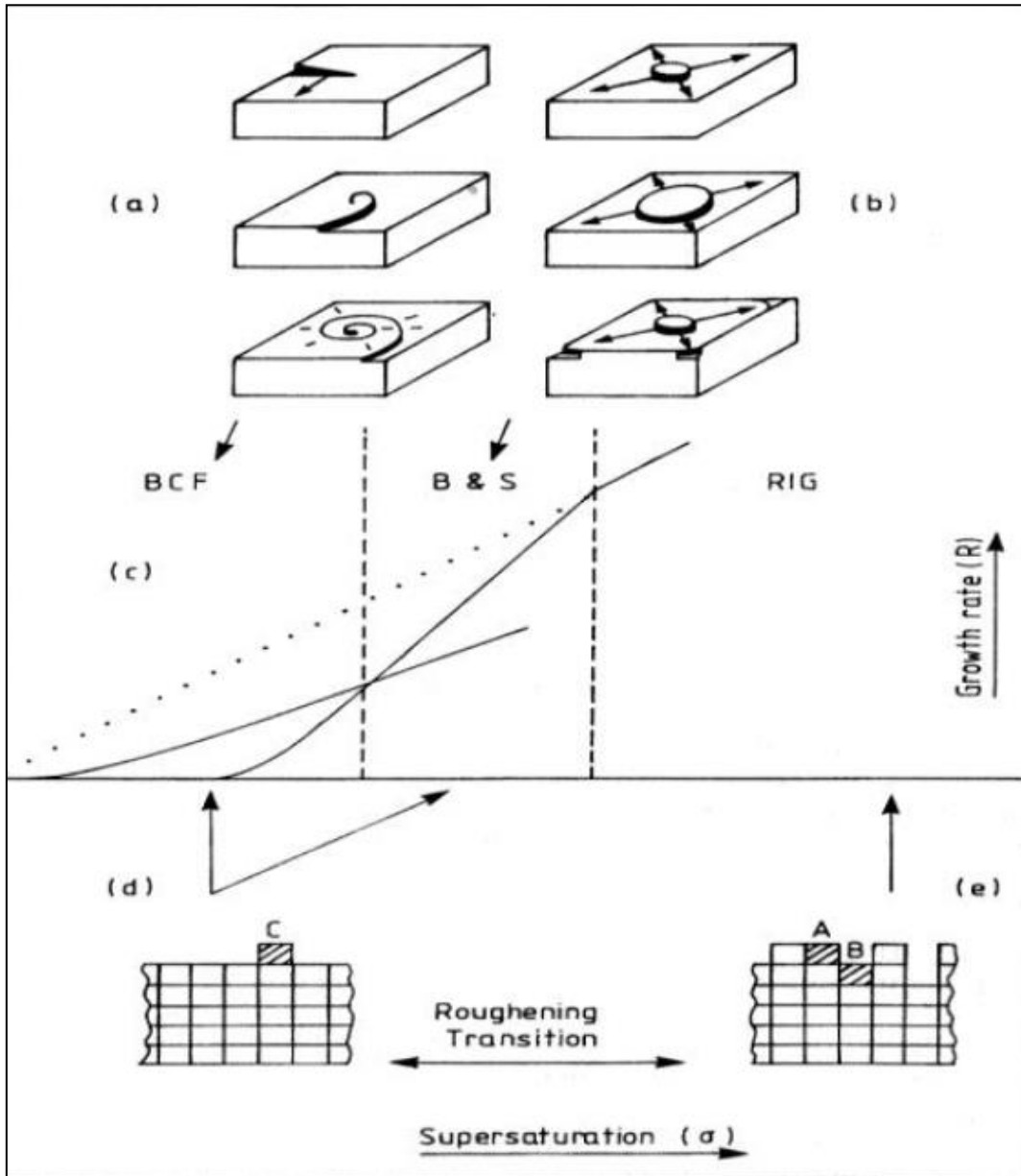
Figure 2-18 Schematic highlighting the progression of the three growth mechanisms as a function of supersaturation[90]

2.6 Closing Remarks

This chapter has introduced some of the fundamental concepts surrounding the research covered in this thesis in particular an introduction of crystallography was provided. A summary of important concepts on solution thermodynamics and ideal solubility were also covered which provide the base knowledge for studies in Chapter 5. The fundamental knowledge from the literature covering classical nucleation theory together with more modern applications deriving nucleation kinetics from measurement of the meta-stable zone width and isothermal measurements were highlighted, this provides the basis for the work presented in Chapter 6. This fundamental knowledge is significant in providing the platform for not only successful experimental planning but more importantly accurate analysis of recorded data to probe crystallisation parameters.

References

[1] Almac. Available from: http://www.almacgroup.com/api-services-chemical-development/solid-state-services/amorphous-materials/.

[2] R. Davey, J. Garside, *From Molecules to Crystallizers*, 2000, Oxford Science Publications

[3] U. Griesser, R. Hilfiker, *Polymorphism in the Pharmaceutical Industry.,* 2006*,* Wiley-VCH Verlag GmbH & Co

[4] J. W. Mullin, *Crystallisation*, 2nd edition, 1972, London: Butterworths

[5] C. Suryanarayana, M. G. Norton *X-ray Diffraction a Practical Approach,* 1998, Springer US

[6] A. S. Myerson, *Handbook of Industrial Crystallization*, 2nd edition, 2002, Butterworth-Heinemann

[7] A. Bravais, *J. l'Ec. Polytech.*, 1850, 19, 33

[8] J. W. Mullin, *Crystallisation*, 4th edition, 2001, London: Butterworths

[9] W. H. Miller, *A treatise on crystallography,* 1839, Printed at the Pitt Press for J. & JJ Deighton

[10] J. Bernstein, *Polymorphism in molecular crystals*, Vol. 14, 2002, Oxford University Press

[11] H. G. Brittain, *Polymorphism in pharmaceutical solids,* 1999, M. Dekker New York

[12] J. Bauer, S. Spanton, R. Henry, J. Quick, W. Dziki, W. Porter, J. Morris, *Pharmaceutical Research*, 2001, 18, 6, 859

[13] W. Ostwald, *Z. Phys. Chem,* 1897, 22

[14] W. Ostwald, *Grundriss der allgemeinen Chemie,* 1899, W. Engelmann

[15] W. Ostwald, *Z. Phys. Chem*, 1900, 34, 495

[16] A. Grunenberg, J. O. Henck, H. W. Siesler, *Int. J. Pharm.*, 1996, 129, 147

[17] J. Bernstein, R. J. Davey, J. O. Henck, *Angew. Chem. Int. Ed.*, 1999, 38, 3440

[18] K R. Morris, U J. Griesser, C J. Eckhardt, J. G. Stowell, *Adv. Drug Deliv. Rev.*, 2001, 48, 91

[19] J K. Haleblian, W C. McCrone, *J. Pharm. Sci.*, 1969, 58, 911

[20] A. R. Ebian, M. A. Moustafa, S. A. Khalil, M. M. Motawi, *J. Pharm. Pharmac.*, 1973, 25, 13

[21] P. J. Skrdla, V. Antonucci, L S. Crocker, R M. Wenslow, L. Wright, G. Zhou, J. Pharm. Biomed. Anal., 2001, 25, 731

[22] A. K. Galwey, *Chemistry of solids – An Introduction to the Chemistry of Solids and Solid Surfaces*, 1967, Chapman and Hall Ltd

[23] R. G. Compton, *Comprehensive chemical kinetics - Reactions at the liquid-solid interface*, Vol. 28, 1989, Elsevier, Oxford

[24] A. K. Sheridan, J. Anwar, *Chem. Mater.,* 1996, 8, 1042

[25] P. T. Cardew, R. J. Davey, *Proc. R. Soc. London,* 1985, *A398*, 415, 28

[26] A. Dokoumetzidis, V. Papadoupoulou, G. Valsami, P. Macheras, *Int. J. Pharm.*, 2008, 355, 114

[27] History, S.N.M.o.N., *The Dynamic Earth*

[28] J. N. Murnell, A. D. Jenkins, *Properties of liquids and solutions*, 2nd edition, 1994, Wiley and sons

[29] W. R. Fawcett, *Liquids, Solutions and Interfaces*, 2004, Oxford University Press

[30] D. Elwell, H. J. Scheel, *Crystal Growth from High Temperature Solutions*, 1975, Academic Press

[31] L. Williams-Seton, R. J. Davey, H. F. Lieberman**,** *J. Am. Chem. Soc.* 1999**,** 121*,* 4563

[32] J. M. Prausnitz, *Molecular Thermodynamics of Fluid Phase Equilibrium*, 1969, Prentice Hall inc

[33] F. L. Nordström, Å. C. Rasmuson, *Eur. J. Pharm. Sci.*, 36, 2009, 330

[34] J. W. Mauger, A. N. Paruta, R. J. Gerraugthty, *J. Pharm. Sci.,* 1972, 61, 94

[35] J. W. Mauger, H. Petersen, K. S. Alexander, A. N. Paruta, *Drug Dev. Ind. Pharm.* 1977, 3, 163

[36] J. W. Mauger, T. L. Breon, H. Petersen, A. N. Paruta, *Drug Dev. Ind. Pharm.* 1977, 3, 351

[37] F. Martínez, C. M. Ávilaa, A. Gómez, *J. Braz. Chem. Soc.*, 2003, 14, 5, 803

[38] R B. Hammond, K. Pencheva, K J. Roberts, *J. Phys. Chem. B*, 2005, 109, 42, 19550

[39] C. Y. Sung, J. Estrin, G. R. Youngquist, *AIChEJ*, 1973, 19, 957

[40] R. F. Strickland-Constable, *J. Chem. Soc. Faraday Trans.*, I, 1979, 75, 921

[41] N. Kubota, M. Fujiwara, *J Chem Eng Jpn*, 1990, 23, 691

[42] J. D. Dunnitz, J. Bernstein, *Acc. Chem. Res*, 1995, 28, 193

[43] P. G. Vekilov, *Cryst. Growth Des.* 2010, 10, 5007

[44] D. Erdemir, A. Y. Lee, A. S. Myerson, *Accounts of Chemical Research*, 2009, 42, 5, 621

[45] P. R. ten Wolde, D. Frenkel, *Science*, 1997, 277, 1975

[46] A. Gavezzotti, *Chem.sEur. J,.*1999, 5, 567

[47] J. D. Shore, D. Perchak, Y. Shnidman, *J. Chem. Phys.* 2000, 113, 6276

[48] Y. Georgalis, P. Umbach, J. Raptis, W. Saenger, *Acta Crystallogr. Sect. D: Biol. Crystallogr.* 1997, 53, 691

[49] D. Pontoni, T. Narayanan, A. R. Rennie, *Prog. Colloid Polym. Sci.* 2004, 123, 227

[50] P. G. Vekilov, Cryst. *Growth Des.* 2004, 4, 671

[51] O. Galkin, K. Chen, R. L. Nagel, R. E. Hirsch, P. G. Vekilov*, Proc Natl Acad Sci U S A.* 2002, 99, 13, 8479

[52] D. Vivares, E. Kaler, A. Lenhoff, *Acta Crystallogr., Sect. D: Biol. Crystallogr.*, 2005, 61, 819

[53] S. Chattopadhyay, D. Erdemir, J. M. B. Evans, J. Ilavsky, H. Amenitsch, C. U. Segre and A. S. Myerson, *Cryst. Growth Des.*, 2005, 5, 523

[54] A. Jawor-Baczynska, J. Sefcik, B. D. Moore, *Cryst. Growth Des.*, 2013, 13, 470

[55] A. Jawor-Baczynska, B. D. Moore, H. S. Lee, A. V. McCormick, J. Sefcik, *Faraday Discuss.*, 2013, 167, 425

[56] D. Gebauer, A. Völkel, H. Cölfen, *Science,* 2008, 322, 1819

[57] H. Cölfen, M. Antonietti, *Mesocrystals and Nonclassical, Crystallization*, 2008, Wiley, Chippenham, UK

[58] A. R. Gerson, K. J. Roberts, J. N. Sherwood, *Powder Technology*, 1991, 65, 243

[59] J. H. ter Horst, S. Jiang, *Cryst. Growth Des.*, 2011, 11, 256

[60] H. Yang, Å. C. Rasmuson, *Cryst. Growth Des.* 2013, 13, 4226

[61] S. A. Kulkarni, S. S. Kadam, H. Meekes, A. I. Stankiewicz, J. H. ter Horst, *Cryst. Growth Des.* 2013, 13, 2435

[62] R. A. Sullivan, R . J. Davey, G. Sadiq, G. Dent, K. R. Back, J. H. ter Horst, D. Toroz, R. B. Hammond, *Cryst. Growth & Des.*, 2014, 14, 2689

[63] H. Miers, F. Isaac, *Proc. R. Soc. A*, 1907. 79, 322

[64] H. A Miers, F. Isaac, *XLVII.— J. Chem. Soc.*, *Transactions*, 1906, 89, 413

[65] Y. Zhang, Z. Li, *Ind. Eng. Chem. Res.*, 2011, 50, 6375

[66] J. P. Klein, R. Boistelle, J. Dugua, *Techniques de l'Inge´nieur*, 1994, 2, 788

[67] Y. Zhu, P. Demilie, P. Davoine, T. Cartage, M. P. Delplancke-Ogletree, *J. Cryst. Growth,* 2005, 275, 1–2, 1333

[68] R. Shi, Y. Huang, L. Jiao, *Chem. Eng. Commun.*, 2007, 194, 9, 1176

[69] J. Bonnin-Paris, S. Bostyn, J. Havet, H. Fauduet, *Chemical Engineering Communications*, 2011, 198:8, 1004

[70] J. Nyvlt, *J. Cryst. Growth*, 1968, 4, 377

[71] J. Nyvlt, R. Rychly, J. Gottfried, J. Wurzelova, *J. Cryst. Growth*, 1970, 6, 151

[72] N. Kubota, *J. Cryst. Growth*, 2008, 310, 629

[73] N. A. Mitchell, P. J. Frawley, *J. Cryst. Growth.*, 2010, 312, 2740

[74] K. Sangwal, *Cryst. Res. Technol.*, 2009, 44, 231

[75] K. Sangwal, *Cryst. Res. Technol.*, 2010, 45, 9, 909

[76] D. Kashchiev, A. Borissova, R. B. Hammond, K. J. Roberts, *J. Cryst. Growth.*, 2010, 312, 698

[77] D. Kashchiev, A. Borissova, R. B. Hammond, K. J. Roberts, *J. Phys. Chem. B.*, 2010, 114, 5441

[78] D. M. C. Corzo, A. Borissova, R. B. Hammond, D. Kashchiev, K. J. Roberts, K. Lewtas, I. More *Cryst.Eng.Comm.*, 2014, 16, 974

[79] D. Kashchiev, *Nucleation: basic theory with applications*, 2000, Butterworth-Heinemann, Oxford,

[80] D. Kashchiev, A. Firoozabadi, *J. Cryst. Growth.*, 2003, 250, 499

[81] N. Rodríguez-hornedo, D. Murphy, *J. Pharm. Sci.*, 1999, 88, 7, 651

[82] P. Cubillas, M. W. Anderson, *Synthesis mechanism: crystal growth and nucleation. Zeolites and Catalysis: Synthesis, Reactions and Applications*, 2010, Wiley-VCH Verlag GmbH & Co

[83] W. Kossel, *Die mole kulasen vorgange beimn kristall wa unstum*, 1928, Leipziger Vortage

[84] A. A. Noyes, W. R. Whitney, *J. Am. Chem. Soc.*, 1897, 19, 12

[85] A. Berthoud, *J. Chem. Phys.,* 1912, 10, 624

[86] J. J. Valeton, *Z. Kristallogr.*, 1924, 60, 1

[87] L. Li, N. Rodriguez-Hornedo, *J. Cryst. Growth*, 1992, 121, 1

[88] M. Ohara, R.C. Reid, *Modeling crystal growth rates from solution*, 1973, Prentice Hall, New Jersey

[89] J. Van der Eerden, P. Bennema, T. Cherepanova, *Progress in Crystal Growth and Characterization*, 1978, 1, 219

[90] K., Roberts, R. Docherty, P. Bennema, L. Jetten, *J. Phys. D: Appl. Phys.*, 1993. 26, 8B, 7

Chapter 3 *In –situ* Crystallisation Characterisation

The background theory on X-ray diffraction and scattering techniques is covered together with a review on in-situ crystallisation characterisation methodologies in particular research focusing on nucleation

3.1 Introduction

This chapter aims to discuss the theory of X-ray diffraction, by covering some background relationships and instrumentation, followed by an explanation of scattering theory and data interpretation. The chapter proceeds with a review of *in-situ* characterisation techniques and the development of flow cells and puts this specific research into context. The concluding section highlights the crystallising systems to be studied in this research programme, with an explanation of the crystal chemistry of PABA.

3.2 X-rays and Diffraction

X-rays are produced when an electrically charged particle rapidly decelerates; the kinetic energy of the particle is converted to radiation, for example in a laboratory X-ray tube. The amount of X-rays produced is only ~1% of the total kinetic energy, with the remaining energy been lost as heat. This is because only some electrons are fully decelerated in one event giving the highest energy (lowest wavelength) radiation, the rest are decelerated in stages producing a band of radiation called white radiation. Kinetic energy is related to the charge across the electrodes which the electrons are accelerated towards by the following equation;

$$KE = eV = {}^1\!/_2\, mv^2 \qquad \text{(3-1)}$$

Where *m* is the mass of an electron, *V* is the voltage across the electrodes e is the charge of the electron and *v* is the velocity of the electron on impact. The electrons transmit all of their KE to the photon energy so that;

$$eV = hv_{max} \qquad \text{(3-2)}$$

Here *h* is Planck's constant and v_{max} is the largest frequency of radiation produced.

3.2.1 Laboratory X-ray Tubes

Laboratory X-ray tubes typically consist of a source of electrons, a high accelerating voltage and a metal target. The metal target is usually required to be water cooled; this is due to the amount of heat produced by the kinetic energy conversion of the electrons. The electrode which accelerates the electrons to the target is usually maintained at 30kV – 50kV as an operating condition. The most common laboratory X-ray tube is a filament source or Coolidge tube; the main components are shown in Figure 3-1.
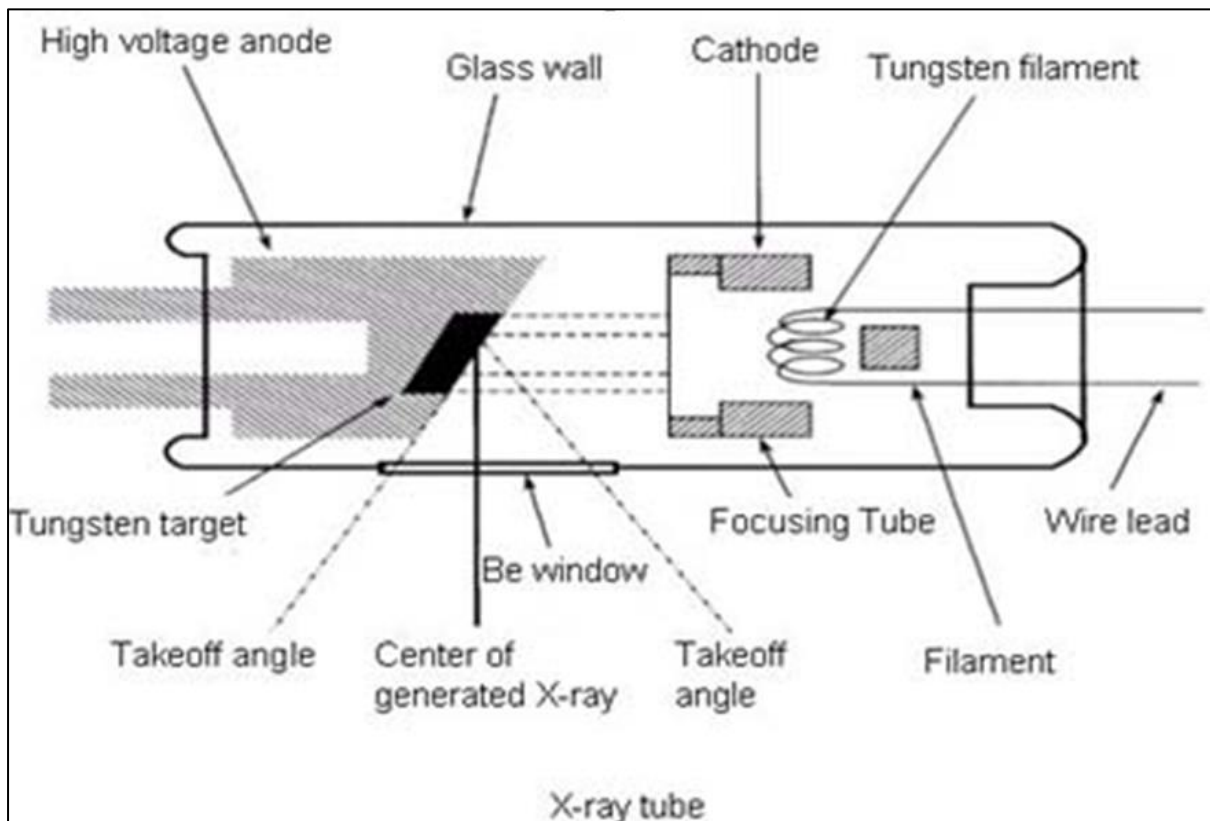
Figure 3-1 Laboratory X-ray tube[1]

The electrons hit the metal target, typically Cu or Mo, then the X-rays produced must leave the enclosed source construction. This occurs through Be windows built into the side of the tube, the material from which these windows are constructed is important to increase the intensity of the beam and so a material which transmits X-rays most effectively should be used[2].

3.2.2 Filters and Monochromators

Typical X-ray diffraction experiment require a beam which is as monochromatic as possible i.e. a single wavelength. Laboratory sources produce the desirable K_α radiation but also the undesirable K_β and white radiation, a filter is usually utilized to remove as much of these undesirable components as possible (Figure 3-2). The filter chosen should have an atomic number one less than the target material, for example Cu uses a Ni filter. This is because Ni has a K absorption edge which lies between the K_α and K_β wavelengths of Cu and so greatly increases the intensity of K_α relative to K_β.

Additionally to a filter a laboratory source should also contain a monochromator. This is used to separate further, the X-ray beam, namely the $K_{\alpha1}$ and $K_{\alpha2}$ components. This is usually done by using a single cut crystal to diffract the selected radiation, this requires a strongly reflecting crystal such as germanium, sodium chloride or graphite. The principle operates via Bragg's law; photons of differing wavelength are diffracted from the planes of a crystal at different angles. Thus by selecting a particular angle of scatter the two sources of radiation can be separated.[3]
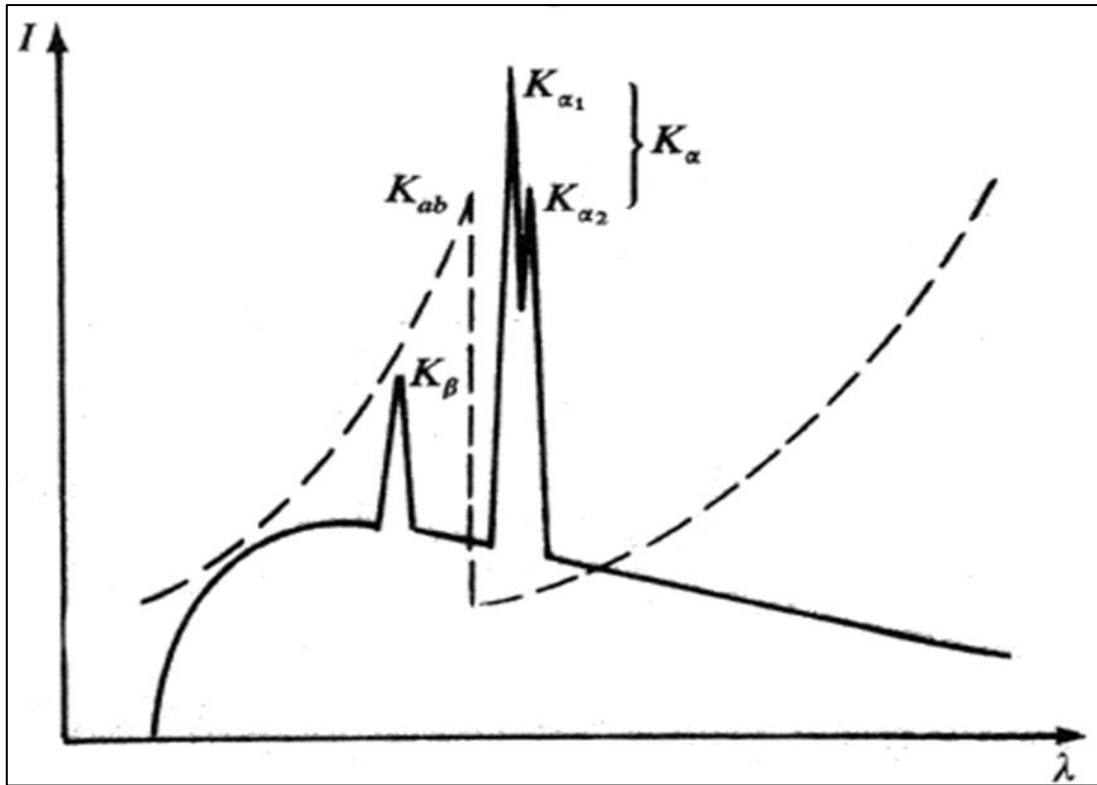
Figure 3-2 An example spectrum of K_a and K_b, the dashed line shows a filter material[4]

3.2.3 X-ray Detection

The very first method of X-ray detection was the use of photographic film, with the film developing relative to amount of X-ray intensity. This method of detection was important in the development of many of the X-ray detectors today and played a key role in the advancement of powder X-ray diffraction (PXRD). The technique paved the way for the development of digital methods of data collection using gas detectors and scintillation detectors coupled with pulse height analysers to produce diffraction data.

Proportional counters are a common lab based detection method for XRD analysis, they run primarily using an ionisable gas such as Argon, a set of electrodes and a counting circuit. The detector will generally have a metal casing comprising of X-ray transparent windows made from Kapton, for example, and an anode running the length of the window. As X-rays enter the chamber through the window the gas in the chamber is ionised producing electrons which migrate to the wire anode, this is

65

usually charged at 10kV. As the electrons hit the anode a detectable pulse of current is produced which is detected by a rate meter connected to the circuit, the pulse can then be analysed as it is proportional to the number of ionisation events.

Scintillation detectors are used via the process of X-ray induced excitation of electrons from the valence band to a conduction band of a material, generally sodium iodide. The excited electron then returns to the ground state emitting a pulse of light, the pulse is proportional to the intensity of X-rays and can be measured using a phototube.[3]

The position sensitive detector, PSD, (Figure 3-3) is used for curved area detectors in particular and is useful as it does not have to be rotated around the sample. The detector works the same as a normal proportional counter, through gas ionisation, however the electron avalanches are localised on the anode and so the position can be determined. The pulse travels the length of the anode in opposite directions, the time of arrival is measured and thus the position of origin can be calculated. This process requires a multichannel analyser to process the data and output the number of pulses (counts) as a function of channel number (*2θ*).
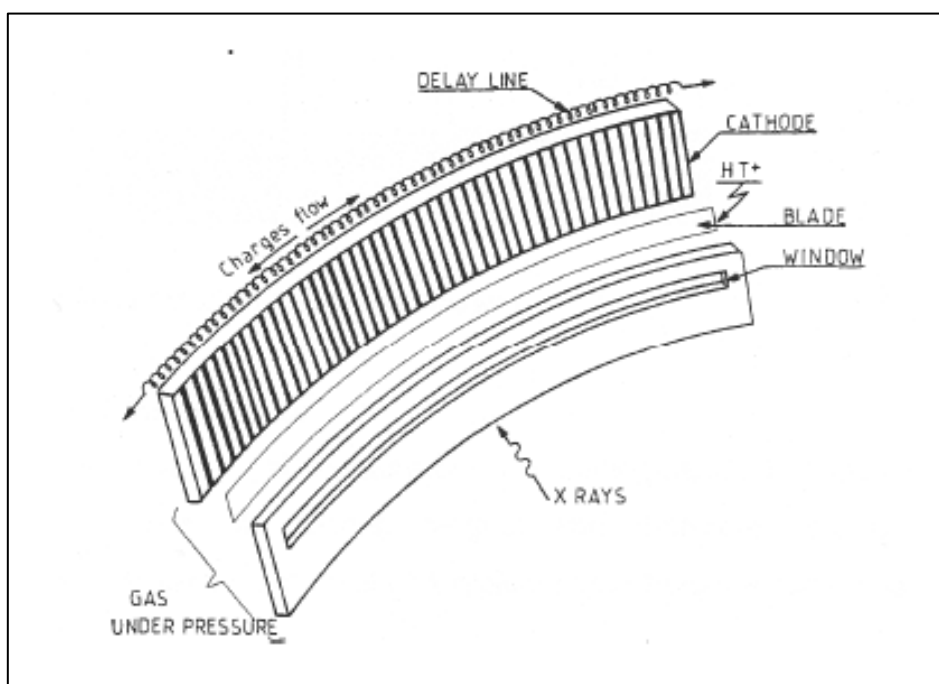
Figure 3-3 Schematic diagram of a curved PSD[5]

3.2.4 Phase Rule

Diffraction of waves occurs due to the phenomena of phase relations between waves. When two or more waves combine, any path difference in travel of the waves can result in differences in phase. These phase differences lead to changes in the amplitudes, and the greater the variance in path length the greater the difference in phase. Waves can either combine constructively, their amplitudes are added, known as in phase (left in Figure 3-4) or they can combine destructively and amplitude decreases, known as out of phase (right in Figure 3-4). The general rule is that waves are completely in phase to each other when their path lengths differ by either zero or a whole number of wavelengths[3].
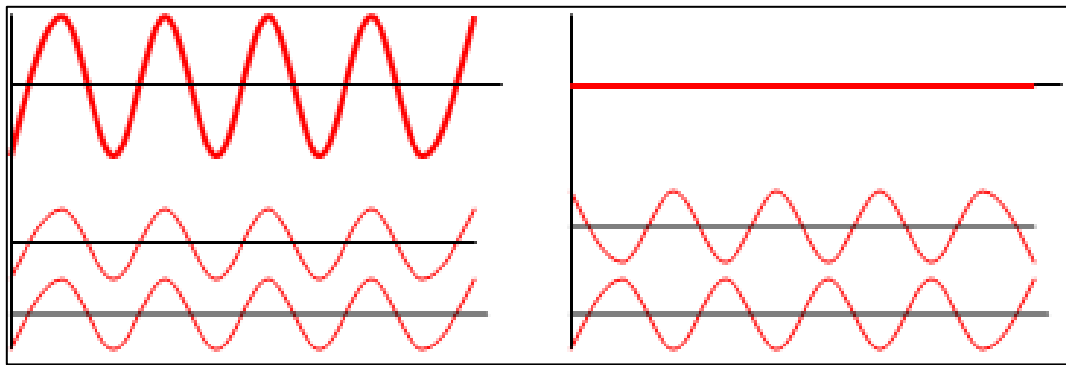
Figure 3-4 Left; waves in phase, right waves out of phase[6]

3.2.5 Braggs Law

A crystal can be thought of as repeating units arranged on sets of planes (Figure 3-5) spaced equally apart with a distance of d. If it is assumed that a beam of X-rays λ is incident to the crystal planes at an angle of θ, the Bragg angle, measured between the incident beam and the crystal planes. When diffracted, by the crystal planes, the beam will scatter in all directions but only a portion of the scattered beam will be in phase and able to reinforce each other to be a detectable diffracted beam.
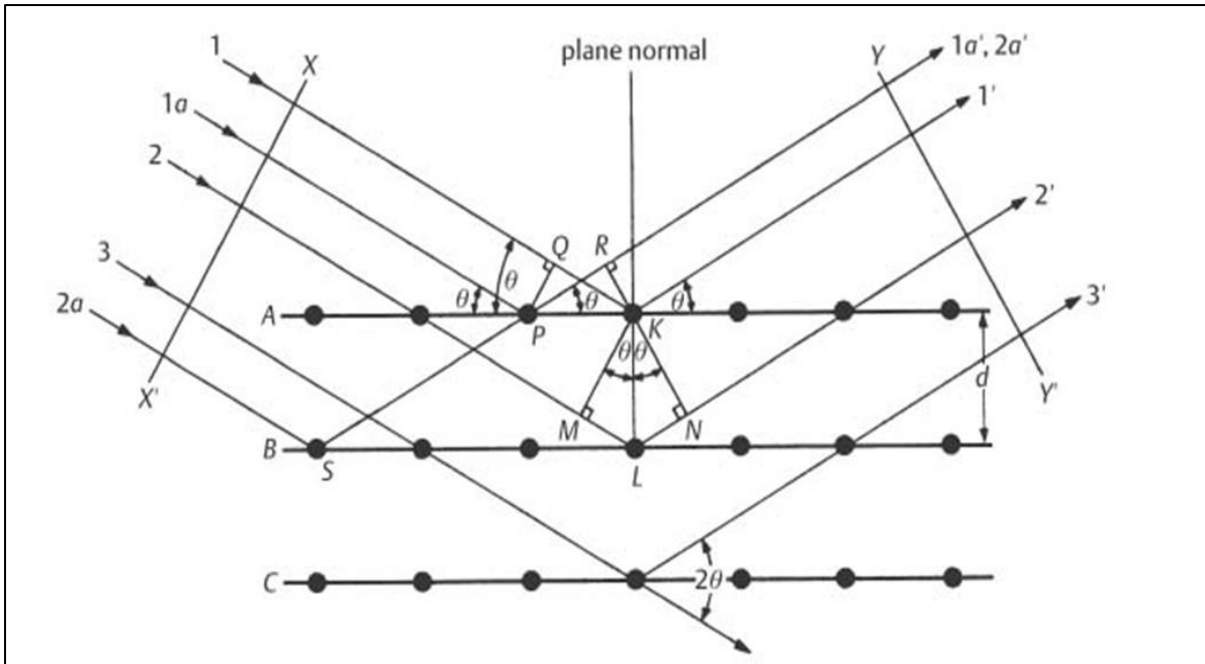
Figure 3-5 Diffraction of X-rays from crystal planes[3]

For example in Figure 3-5 incident 1 and 1a will be scattered in all directions by atoms K and P however only in directions 1' and 1a' will the diffracted beam be in phase, this is because the path difference is;

$$QK - PR = PKcos\theta - PKcos\theta = 0 \qquad \textbf{(3-3)}$$

Similarly rays 1 and 2 will have a path difference of;

$$ML + LN = d'sin\theta + d'sin\theta \qquad \textbf{(3-4)}$$

So the scattered rays 1' and 2' will be completely in phase if the path difference is equal to a whole number of wavelengths which leads to the Bragg Equation 3-5, which can be written as;

$$n\lambda = 2dsin\theta \qquad \textbf{(3-5)}$$

n here is the order of diffraction and if the values of λ and d are fixed then multiple values of *θ* can be obtained at which diffraction may occur, corresponding to *n* = 1, 2, 3[3].

3.2.6 Classical Diffraction Methods

The Laue method reproduces von Laues original diffraction experiment. In order to satisfy Braggs law and therefore θ, the position of the crystal is fixed and so the wavelength λ of the incident beam is variable. This means that the X-ray source produces white radiation only, and each set of crystal planes diffracts a different wavelength of radiation, i.e. the wavelength which satisfies Braggs law.

The rotating crystal method uses a single crystal mounted with one axis pointing at the X-ray source. A film is placed in a cylinder around the crystal while the crystal is rotated about its axis. As the crystal rotates some of the lattice planes are rotated into the correct orientation to satisfy the value of θ for Bragg reflection to occur, this results in the diffraction from each lattice plane, *hkl*, producing a horizontal line on the film[2].

3.2.7 Powder Diffraction

The powder method is one of the most useful and routinely used methods of XRD analysis due to its simplicity in instrumentation and sample preparation. The powder method can be used for structure determination through the use of Rietveld refinement. The apparatus required for a powder XRD experiment is a sample holder, X-ray source and detector, and how these components are arranged gives the different modes of operation such as reflection and transmission. These methods of PXRD were developed in the early 20th century and the two main contributors to this were the Hull/Debye-Scherer diffractometer and the Bragg-Brentano diffractometer.

As the name suggests PXRD is carried out on a powdered sample, however it is useful to visualise a powder as a collection of microscopic crystals of the substance to be studied. In this way every microscopic crystal is randomly orientated and due to the sheer number of crystals, all orientations of the reflection planes are aligned to the beam. For example the (100) planes will be orientated to the X-ray source so the Bragg law is satisfied and diffraction can occur, but similarly some crystals will also have the (110) planes orientated correctly.

Not only is every plane orientated to make the correct Bragg angle but also every plane is essentially rotated, as every possible rotation of that plane is present in the powder. This gives the diffracted radiation in a cone shape as in Figure 3-6, with each cone representing reflection from some *hkl* plane[7].
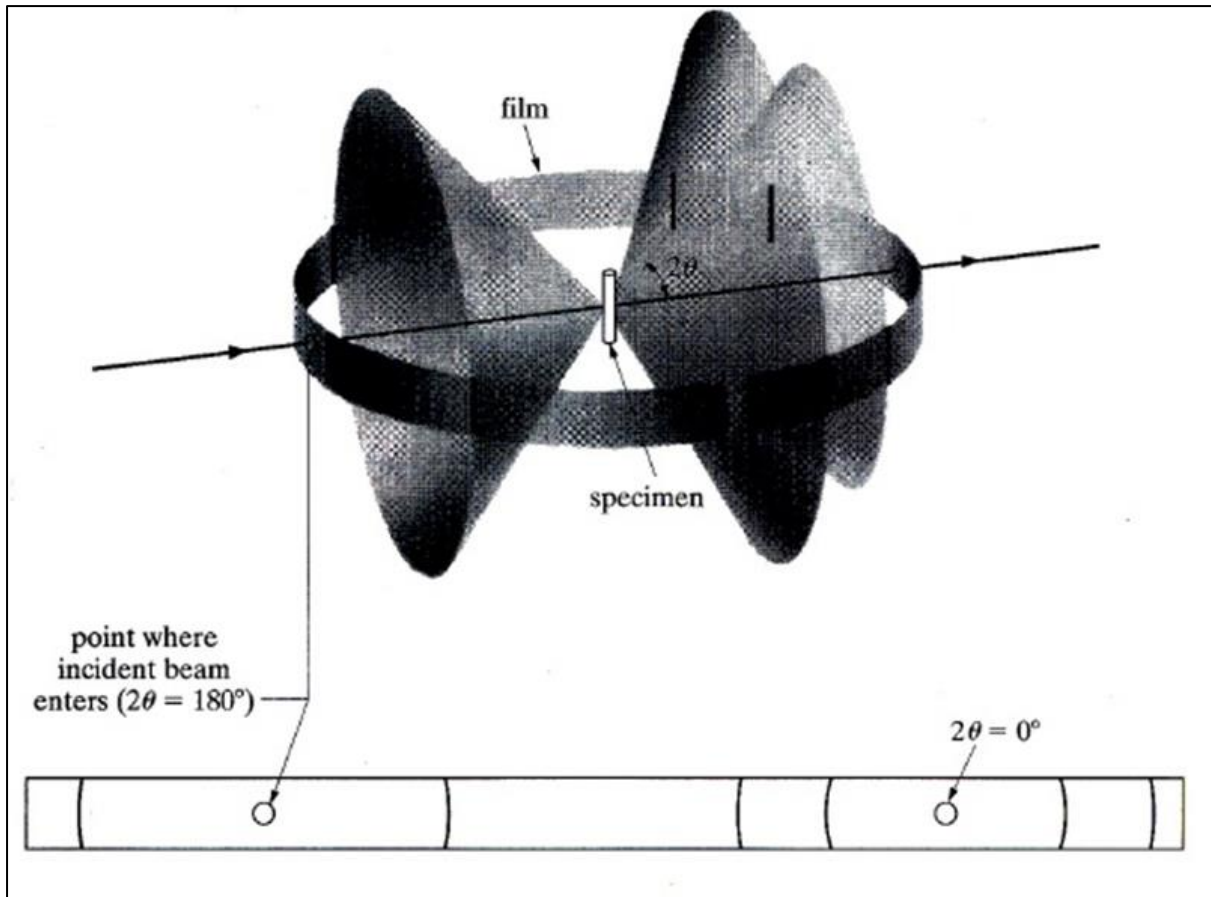
Figure 3-6 The Hull/Debye-Scherer method of PXRD[7]

The Hull/Debye Scherer diffractometer was developed by Debye and Scherer 1916 and Hull 1917 and was the first example of a powder diffractometer. The layout of this diffractometer consists of a sample holder centrally located in a diffraction circle surrounded by a ring of film with the X-ray source perpendicular to the axis of the sample. As shown in Figure 3-6 the diffracted X-rays are cones of radiation which hit the film producing a series of lines, Each line corresponds to diffraction from a single crystallographic plane, hkl, from this line θ can be determined and with λ known the *d* spacing can be calculated.

The Bragg-Brentano diffractometer uses a different geometry for the source, sample and detector to the Hull/Debye-Scherer geometry. The detector rotates about the sample axis synchronously through twice the angular rotation of sample through *θ/2θ* scans. Another type of rotation for the Bragg Brentano diffractometer is the θ/θ scan shown in Figure 3-7 where the sample is fixed and the source and detector move simultaneously in opposite directions through the goniometer circle[7].
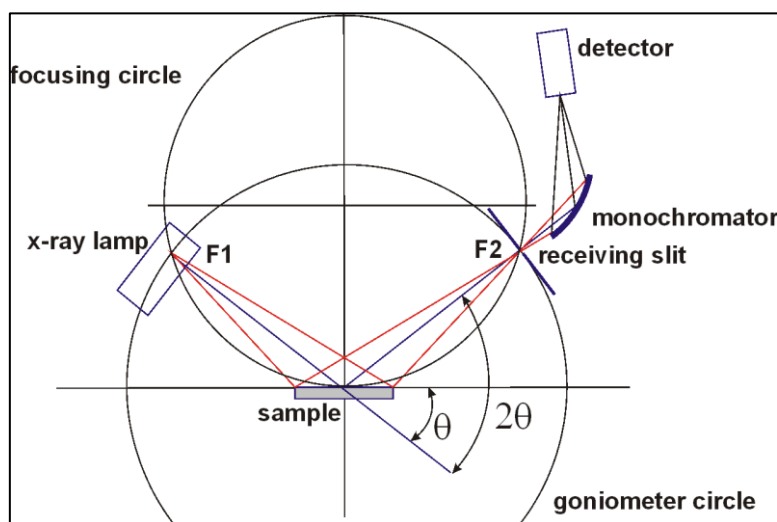
Figure 3-7 Bragg – Brentano geometry[8]

3.2.8 Powder Diffraction vs. Single Crystal XRD

Some of the very first crystal structures were solved by Bragg namely organic salts such as NaCl, KBr, KCl, CaF2 etc and were all done by single crystal diffraction experiments. Single crystal experiments are still very important and widely used today for solving structures of organic materials and proteins. With the development of precise diffractometers and automated processes for data analysis such as Patterson analysis, has meant structure determination is a process which takes hours or days rather than months.

PXRD has also developed at a significant pace and is a fundamental and routine technique used throughout science and, materials laboratories, due to its fast nature and versatility as an analytical technique. PXRD is also useful because it does not require single crystals; due to the nature of a crystallographic process a large single crystal may not be able to be grown. The ability to use PXRD under extreme

conditions is also useful and experiments that probe reaction kinetics and polymorphic transformation kinetics or crystallisation processes *in situ* then PXRD is a reliable technique.

The last example is the main reason why PXRD will be used throughout this research due to its flexibility, reliability and fast recording of diffraction patterns. There are some drawbacks to PXRD however, such as preferred orientation of the sample and so sample preparation is important when running a PRD experiment. Accidental overlapping of diffraction peaks may occur due to experimental resolution and also background noise can be a problem difficult to define[9].

3.2.9 Synchrotron Radiation

Recent improvement to laboratory X-ray sources and detector technologies have seen vast improvements reducing beam sizes and count rates which is particularly helpful to carrying out time resolved scattering or diffraction measurements. The significant problem for laboratory sources is beam divergence which prevents, in particular, high resolution scattering experiments using standard X-ray tubes. This results in many challenging *in-situ* nucleation and crystallisation experiments being carried out at synchrotron sources which provide high intensity, tuneable radiation at sub millimetre beam sizes, making it ideal for high resolution, time resolved studies of dynamic processes.

Synchrotron sources contain a main storage ring which is loaded with charged particles, electrons or positrons from a smaller accelerator ring. The electrons are accelerated to almost the speed of light, at which point insertion devices in the storage ring force electrons to radiate. The more modern types of insertion device are called undulators which produce waves of radiation which are in phase and hence provide a more intense higher brilliance electron beam[10].
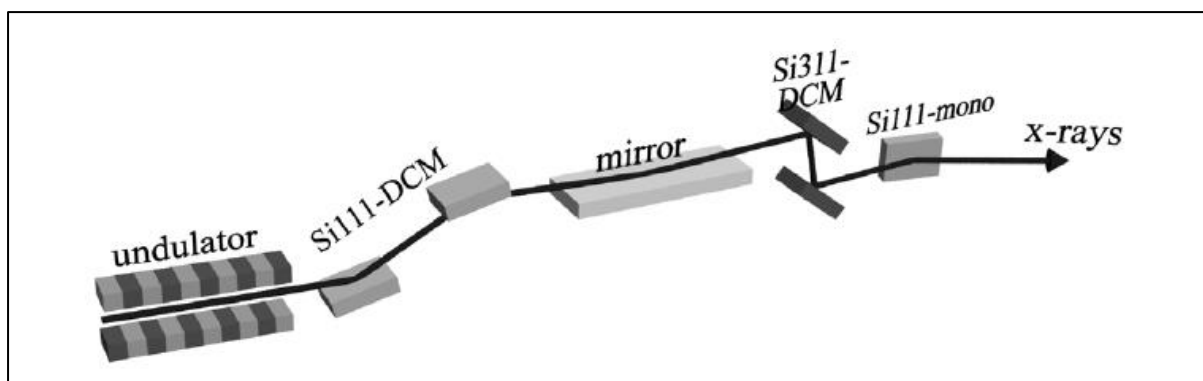
Figure 3-8 Schematic of a synchrotron beamline[11]

The beam-line optics usually consists of double crystal mono-chromators which can utilise certain Bragg reflections to pick certain photon energies with small bandwidths[11]. These can be fine-tuned depending on the experiment to provide the correct photon energy, beam size, beam divergence etc. An example of a beam-line highlighting the undulator and optics is shown in Figure 3-8.

3.3 Small Angle X-ray Scattering

The previous sections of this chapter have focussed on XRD analysis of crystals in order to determine the crystallographic structure of a solid material by analysis of how crystallographic planes of atoms or molecules diffract X-rays. This section focuses on small angle X-ray scattering (SAXS) a technique used throughout biological and materials sciences more focused on structure at Nano length scales.

3.3.1 Fundamental Concepts

The experimental hardware required for an XRD study and a SAXS study is the same; a sample, X-ray source detector and monochromator, all have been previously discussed. The major difference between XRD analysis and SAXS is the organisation of molecules which are under analysis. In SAXS the molecules are particulates or proteins usually in solution and are essentially randomly orientated and then signal from all of these orientations and the apparatus are averaged together. The scattering pattern is also symmetric (isotropic) and arises from this random orientation, although SAXS is also useful for studying long range directional

order such as in liquid crystals or polymer systems. In XRD the molecules are highly ordered and so this leads to very discrete diffraction maxima giving precise information on crystal structure. SAXS gives comparatively less information than XRD but still provides a tool for understanding the size shape and distribution of particulates in a solution or powder[12].
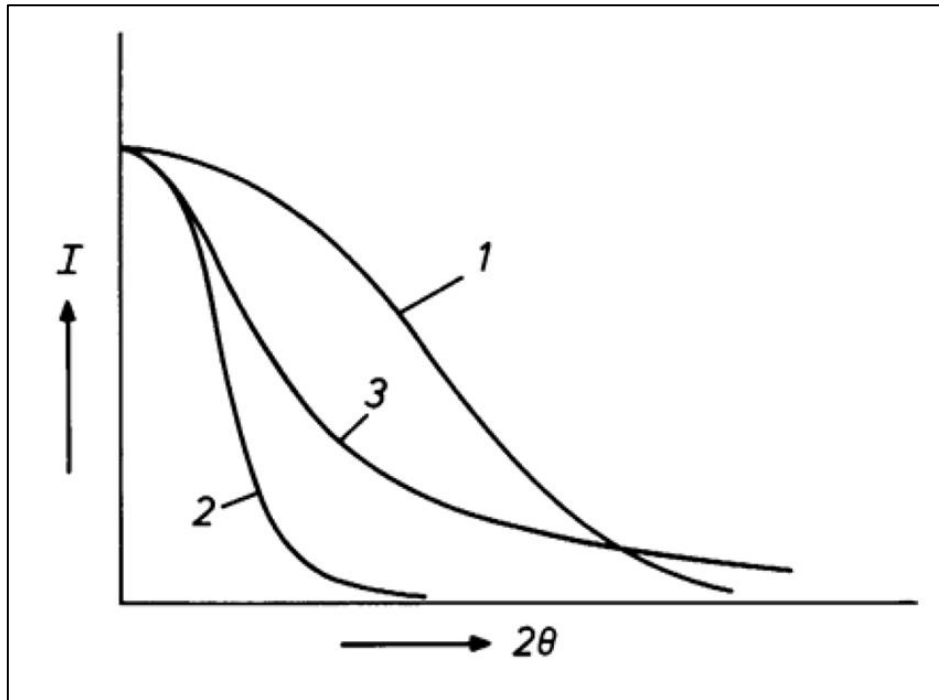
Figure 3-9 Scattering intensity for different size particulates[13]

SAXS studies are used for studying structures which are very large in comparison to the wavelength of the radiation, typically 1.54 Å for Cu radiation, whereas the dimensions studied will be 10-10^3 Å. Small angle scattering occurs due to scatter of the X-rays by electron density of the scatterer, the same principle applies as in diffraction; that the scattered radiation must be in phase. It can be said of all scattering phenomena that the small angle scattering of particulates observes a reciprocity law where large scatterers (2 in Figure 3-9) will scatter X-rays at a smaller angle than smaller scatterers (1 in Figure 3-9) [13].

3.3.2 Scattering Patterns in SAXS

Generally SAXS patterns are collected as a 2 dimensional scattering patterns, with scatterers producing rings of scattered radiation on the detector. This pattern is then radially integrated to give a 1 dimensional scattering function *I(q)* where *q* is a measure of the momentum change that the photons undergo upon scattering by electron density; *q* is related to the scattering angle by the equation;

$$q = 4\pi \, sin \, (\theta)/\lambda \qquad \textbf{(3-6)}$$

Where *λ* is wavelength of incident X-ray and *2θ* is the scattering angle; *q* is given with units of reciprocal wavelength Å^{-1} or nm^{-1}.

The general structure determination scheme (Figure 3-10) using SAXS is as follows; incident X-rays impinge on the sample which scatter the radiation at an angle *θ* to give a 2D scattering pattern. Radial integration of the 2D pattern provides a plot of intensity vs scattering vector *q*; where the peaks give information on structure as does the slope of the curve[14].
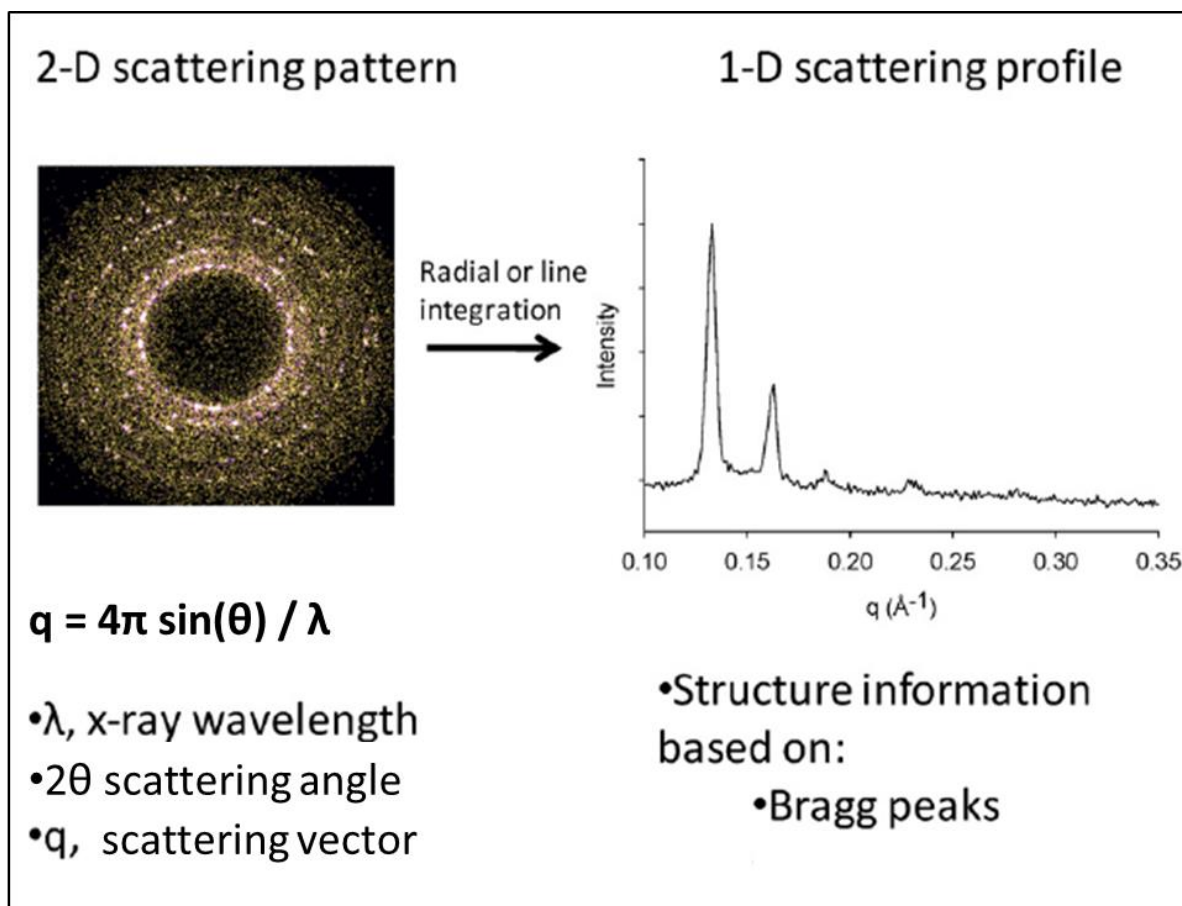
Figure 3-10 Schematic showing the SAXS scattering pattern and integration to a 1D profile[14]

3.3.3 Mono-disperse Scattering

Small angle X-ray scattering can be used to probe nano-structural information of mono and poly-disperse systems including nano-particulate samples, protein samples organic materials[15]. The ideal SAXS system is a mono-disperse system which by definition is free from inter-particle interactions and hence multiple scattering which adds discrepancy's to the scattering function[16]. The mono-disperse system is ideal for size shape and surface analysis by SAXS due to this feature as all of the scattering function arises from a single particle geometry[17].

All data analysis in SAXS is based on model fitting, usually of geometrical shapes, to the measured scattering pattern. The simple case of scattering from a homogeneous sphere of radius *R* (Figure 3-11) is described; the scattering from a

certain position on the sphere defined by the position vector, *r*, can be described by the wavefunction[12];

$$\psi(q) = \exp(-iq.r) \qquad \text{3-7}$$
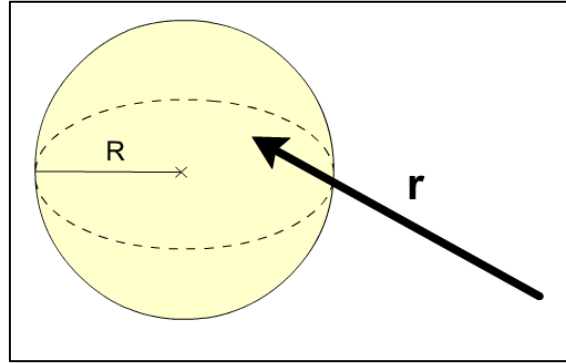
Figure 3-11 Example of a sphere of radius R and a surface position vector r[18]

The scattering pattern produced is actually a summation of all the possible points of the sphere where *p(r)* is the distribution of scattering length density averaged over the particle volume, *V*, about *r*[18],

$$\rho(r) = \Sigma \frac{b_j}{v} \qquad \textbf{(3-8)}$$

Where *bj* is the scattering length of point *j*, from this the scattering amplitude can be shown to be;

$$A(q) = \int \rho(r) \exp(-iq.r) \qquad \textbf{(3-9)}$$

However due to a sphere being free from orientation and is essentially centrosymmetric Equation 3-9 becomes

$$A(q) = 4\pi \int \rho(r) \frac{\sin(qr)}{qr} r^2 dr \qquad \textbf{(3-10)}$$

Integrating this equation between zero and the radius of the sphere, *R*, this equation becomes[19];

$$4\pi \int_0^R \rho(r) \frac{\sin(qr)}{qr} r^2 dr \Rightarrow \frac{4\pi}{q} \int_0^R \rho(r) \frac{\sin(qr)}{qr} r dr \Rightarrow \frac{4}{3}\pi R^3 \frac{3[\sin(qR) - qR\cos(qR)]}{(qR)^3} \qquad (3\text{-}11)$$

However because SAXS patterns are measured in intensity not amplitude the following relation is required to convert between the two;

$$I(q) = n\Delta\rho^2 V^2 |A(q)|^2 \quad (3\text{-}12)$$

Combination of Equations 3-12 and 3-9 for a mono-disperse sphere, the scattering function *I(q)* is derived from[15];

$$I(q) = I_0 \left[3 \frac{\sin(qr) - (qr)\cos(qr)}{(qr)^3} \right]^2 \qquad (3\text{-}13)$$

This equation can provide a model scattering curve for a homogeneous sphere of any dimension of *R*. This is the basis of model fitting for SAXS data whereby the measured scattering pattern can be fit to any geometrical shape i.e. examples of geometrical shapes and their respective scattering patterns are shown in Figure 3-12.
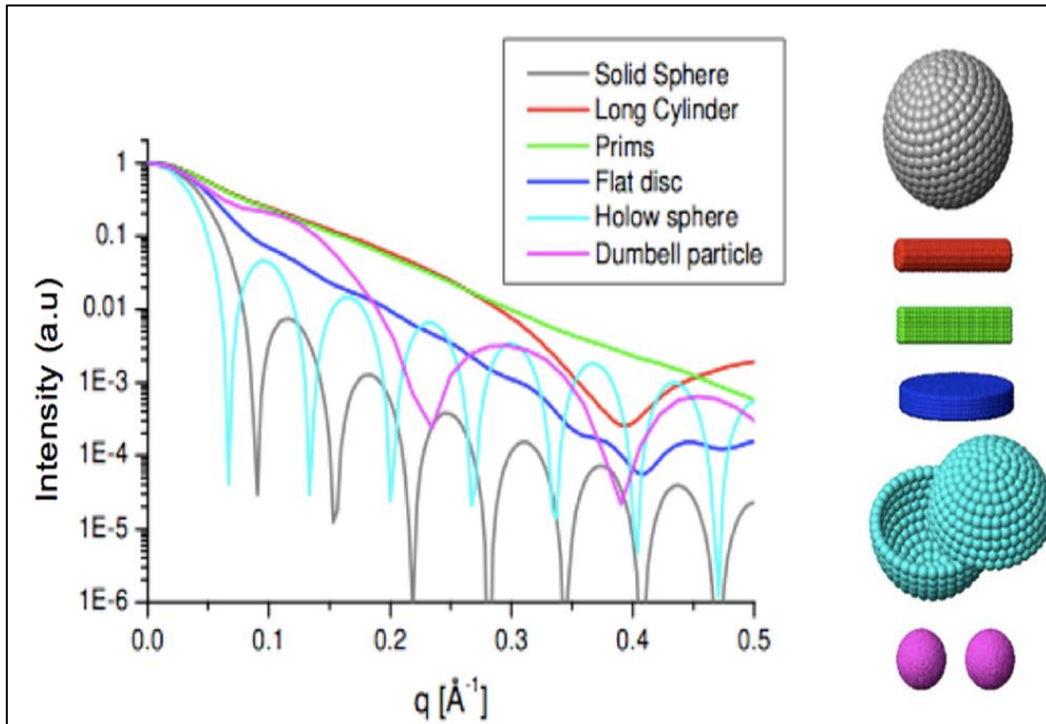
Figure 3-12 Theoretical scattering functions of some geometrical shapes[19]

It should be noted that a general practice for analysing SAXS data require some a priori knowledge of the system or corresponding complementary technique which can infer some knowledge of particle morphology, aggregation etc.

3.3.4 The Guinier Approximation

The Guinier analysis method is arguably the most simple and least time consuming analysis techniques in SAXS to gain information on the size of the scattering sample by calculation of the radius of gyration, R_g. The R_g of a scattering system can be extracted to give an estimate of geometrical sizes provided a model geometry. The Guinier analysis approximates the scattering function, $I(q)$, to a Gaussian distribution for mono-disperse systems at small values of q to[15, 17];

$$I(q) \approx I_0 e^{-\frac{R_g^2}{3}q^2} \qquad \textbf{(3-14)}$$

Where I_0 is the scattering intensity at zero scattering angle, q is the scattering variable. The R_g is equal to the root mean square of all possible distances between the electrons in the particle and its centre of mass, and hence is shape independent.

The R_g of a simple homogeneous system of spherical particles can provide information of the radius of the particles through the following expression;

$$R = \sqrt{\frac{5}{3}} R_g \qquad \textbf{(3-15)}$$

There are also other expressions which describe the relationship between Rg and geometrical parameters for a number of other particle morphologys such as rods and discs. The treatment of scattering data to extract R_g uses the following relationship[17];

$$\ln(I(q)) = \ln(I(0)) - \frac{R_g^2}{3}q^2 \qquad \textbf{(3-16)}$$

Where a linear plot of *ln(I(q))* vs *q^2* will provide a straight line with a slope equal to – *Rg^2/3*, this is known as a Guinier plot.

The Guinier approximation is only applicable to samples which exhibit low particle-particle interactions, and only in regions of the scattering curve bound by 0< *qRg*<1.3[15].

An example of Guinier analysis is provided in Figure 3-13 which presents scattering patterns of Ludox HS colloidal silica samples at various concentrations measured by Xu and co-workers[20]. The Guinier plots of the scattering data highlight two linear regions one at high q and one at lower q, this indicates a distribution of sizes within the samples whereby the higher q curve (lower calculated R_g) is likely from the presence of a population of Ludox monomers and the lower q region (higher calculated R_g) is scattering from aggregates of Ludox particles. Although one should note that Guinier analysis should only be carried out on mono-disperse systems, high concentrations in this study would likely cause agglomeration and any structural information is lost due to domination of the scattering pattern by the structure factor, $S_{(q)}$.
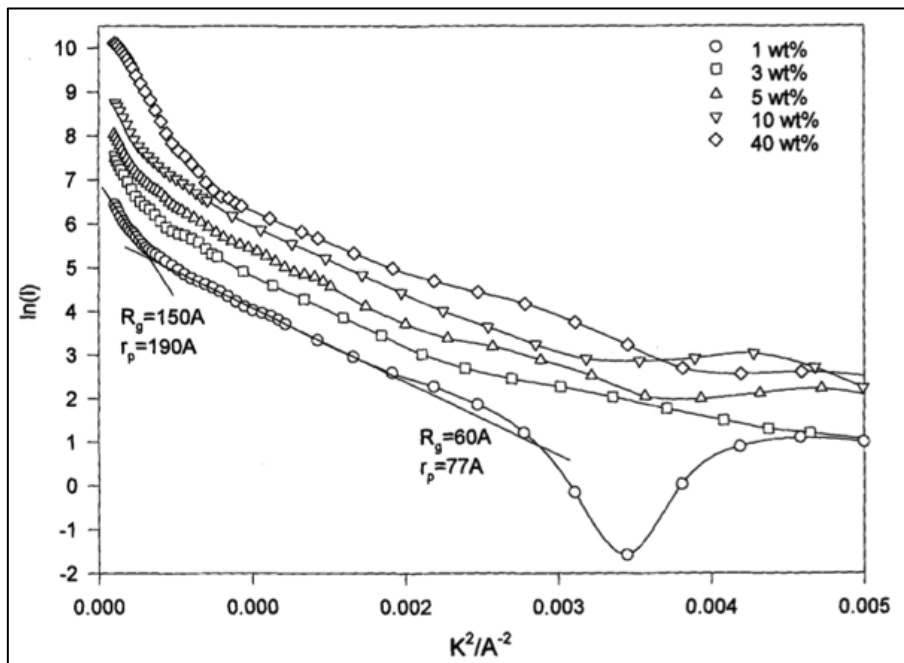
Figure 3-13 Guinier plot of measured scattering patterns of Ludox HS colloidal silica nano-particles indicating two linear regions in the scattering curve; scattering from monomer units and from aggregations of particles[20]

3.3.5 Porods Law

Porods law states that for mass fractals at sufficiently high values of q the scattering function is dominated by the structure factor, $S(q)$. This relates to a dominance of the scattering pattern by the surface properties of the particle as[21];

$$I(q) \sim S(q) \rightarrow I(q) \approx 2\pi\Delta\rho^2 q^{-(6-D_s)} \qquad \textbf{(3-17)}$$

Where D_s is equal to the surface fractal dimension and gives information on surface roughness and inter-particle aggregation. An explanation of how D_s relates to surface properties is provided in Figure 3-14.
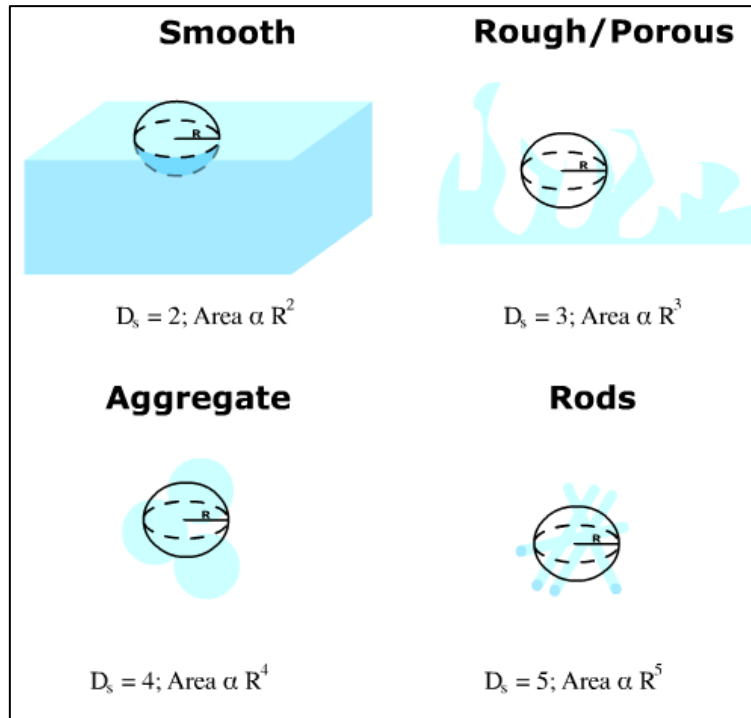
Figure 3-14 The relationship between the fractal dimension and the power law significance of surface area to the radius of a sphere[21]

Placing a perfectly smooth sphere of radius R so that mass centre point of the sphere intersects the surface will produce a circle on the surface of radius R. The area of this circle is equal to $A=\pi R^2$ and so the area of the surface contained within the particle is equal to the second power of R. Imagine that the surface deviates from ideal smoothness this would allow more of the surface to be contained within the spheres volume and hence the power of R to which the surface area is related increases[22].

A Porod plot involves rearrangement of Equation 3-17 to provide the following expression;

$$\log I(q) = A - (6 - D_s) \log q \qquad \textbf{(3-18)}$$

Where *A* is the logarithm of *Δρ* and *π* and hence plotting the scattering function in log-log coordinates will yield a linear region where the gradient is equal to $-(6-D_s)$ from which the fractal dimension can be extrapolated . Generally a $D_s = 2$ represents a smooth interface of the particle, a $D_s = 2\text{-}3$ indicates surface roughening or a porous surface, $D_s = 3\text{-}5$ is indicative of particle aggregation or very rough interfaces[22].

An example of a Porod plot of real scattering data is provided in Figure 3-15 which presents scattering data in Porod coordinates for Ludox HS colloidal silica samples[20]. The data indicates that *q* decays to the power -2 which from Figure 3-14 is indicative of particle aggregation. This provides nano-scale information on the particle-particle interactions in these samples and it is well known for the cases of colloidal silica that high solution concentration causes aggregation of the particles.
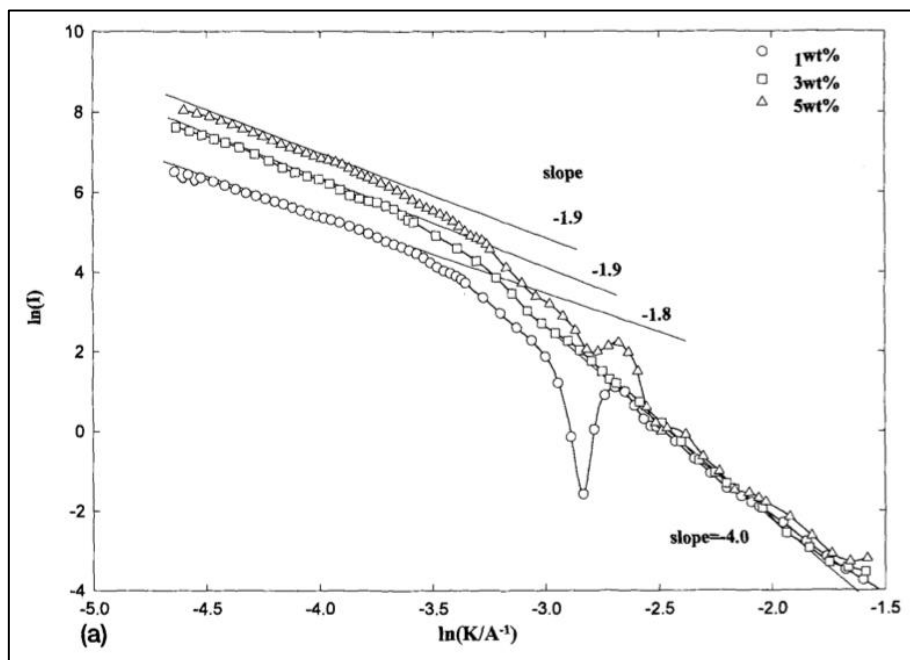
Figure 3-15 Porod plots of scattering data for Ludox HS samples indicating the slope and hence fractal dimensionality of the sample[20].

3.3.6 Pair-Distance Distribution Function

Another useful parameter calculated from the SAXS curve is the pair-distance distribution function (PDDF) *ρ(r)* and can be used to deduce structural properties of the scattering solution. *P(r)* is related to the periodic inter-electron distances within the sample which act as a grating for scattering of the incident beam relative to its wavelength. In this case the scattering pattern relates to the Fourier transform of electron distribution distances and hence a plot of *P(r)* yields information on morphology and dimensions of the particle. The inverse Fourier transform of the scattering pattern is performed through use the following equation[23];

$$p(r) = \frac{1}{2\pi} \int_0^\infty I(q)qr \sin qr \, dq \quad \text{(3-19)}$$

 Figure 3-16 highlights examples of some geometrical shapes with respective PDDF and their scattering intensities, note that *S* on the x axis here is the same as *q* mentioned in this section and has units of reciprocal wavelength[24].
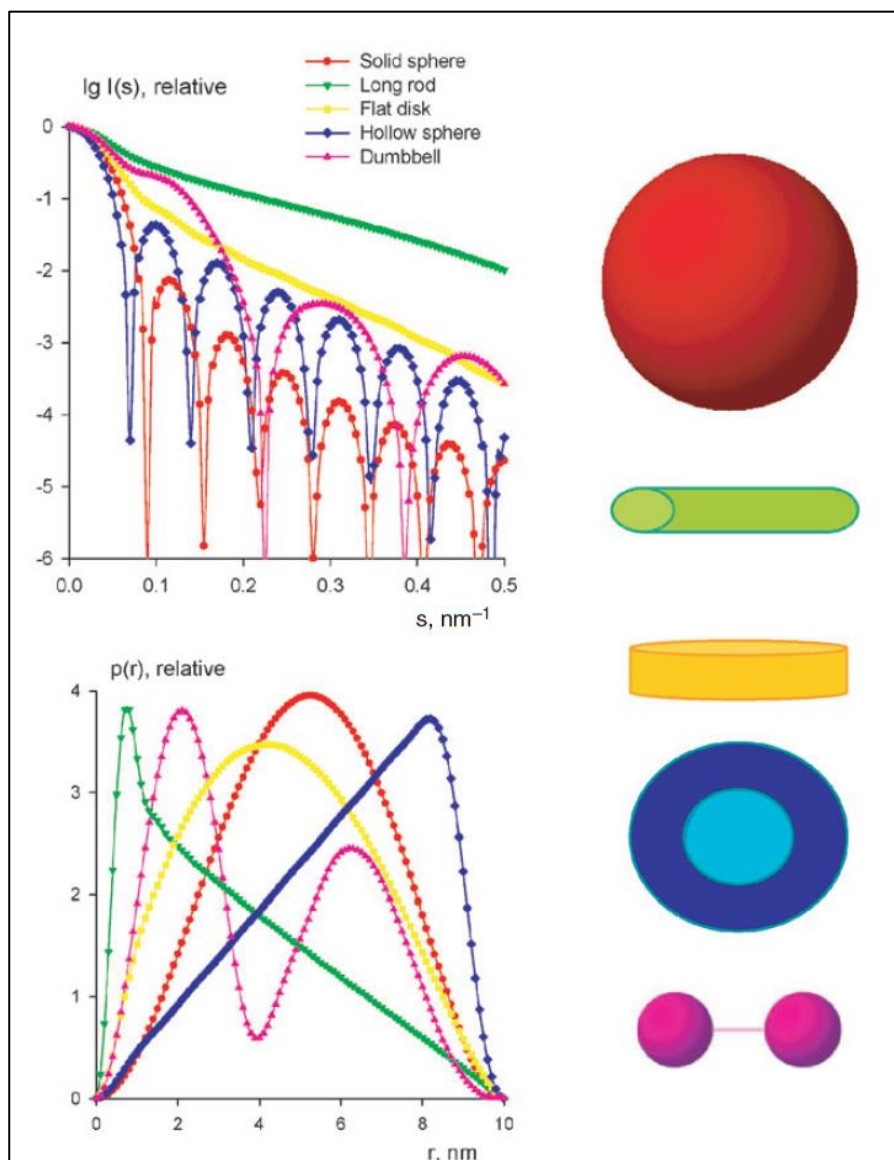
Figure 3-16 Scattering curves (top) and ρ(r) functions (bottom) of various geometrical shapes[24]

3.3.7 Unified Fit Analysis

The Unified fit method developed by Beaucage is particularly useful for deriving structural information from scattering data using Guinier and Porods Law, where the sample contains multiple levels of structure which are interrelated; such as crystallisation from solution where the primary building unit is related to the final macroscopic crystal. The Unified model derives a function that models the R_g and the power law region (Porod region) of the scattering curve for each individual

structural level without introducing any new parameters other than those used in the fitting process.

The Unified model for a structural level is as follows;

$$I_{(q)} \approx G \exp\left(-q^2 R_g^2/3\right) + B\left\{\left[erf\left(\frac{qR_g}{6^{\frac{1}{2}}}\right)\right]^3 /q\right\}^P \qquad (3\text{-}20)$$

Where q is the scattering vector in inverse length scale, $q=4\pi/\lambda sin\theta$, G is the Guinier prefactor, $G = n_e^2\ N_P\ I_e$ relating to the total number of particles in the scattering volume, N_p and the number of electrons, n, with a scattering factor for a single electron, I_e, R_g is the radius of gyration and B is the pre-factor which is specific to the power law scattering behaviour. Hence the size (Guinier, R_g) and fractal dimensionality (Porod, P) can be extracted for various structurally related scattering levels[25,26].

A particles fractal dimension can be explained from its scattering pattern as *I(q) ~ S(q)* for fractal systems and hence analysis of the power law regime from Porods law will give information on its fractal quantity. In general *S(q)* is in a power law form as Equation 3-21 [27, 28];

$$S_{(q)} \sim q^{-\alpha} \qquad (3\text{-}21)$$

Where α is the exponent which describes the fractal dimension of the system whereby for mass fractals which can be described by a crosslinking or branching chain to form a 3D network;

$$\alpha = D_{m},\ 1 < \alpha < 3 \qquad (3\text{-}22)$$

Where D_m is a non-integer number, *1 < D_m < 3* and is related to the mass and radius of the scattering particles. For surface fractals which could be described as particles with rough interfaces;

$$\alpha = 6 - D_s \qquad (3\text{-}23)$$

Where D_s is a non-integer number $2 < D_s < 3$, if $D_s = 2$ then the scattering intensity decays as $S(q) \sim q^{-4}$ taking Porods law for smooth interfaces[29, 30].

3.4 *In-Situ* Crystallisation Characterisation Techniques

This chapter has so far discussed the basic theory of XRD and scattering including instrumentation and what information is obtained by using these methods. The methods discussed so far generally involve solid crystalline samples which have been crystallised and dried as powders or single crystals. With recent advances in process analytical technology including attenuated total reflectance spectroscopy's such as infrared and ultraviolet/visible spectroscopy, the ability to probe structural and chemical parameters on-line during a crystallisation process has also made great progress. Further to this development of laboratory X-ray sources and detector technologies have resulted in methods of monitoring crystallisation processes *in-situ* which are slowly being progressed. This section summarises some of the recent advances in on-line characterisation of crystallisation processes from the literature.

3.4.1 *In-Situ* Diffraction Applications

The use of PXRD as a polymorph screening method in pharmaceutical synthesis has been used for many years and is the primary tool for the determination of polymorphic form. This method is usually carried out in the solid state by extraction of solid samples post production and screening them. However, the attraction of monitoring polymorphic form during crystallisation processes in the pharmaceuticals and materials industry has led to the development of *in-situ* characterisation. Examples include monitoring cement components during processing as analytical quality control[31] and monitoring the XRD patterns of polymorphic form transitions of an organic molecule during crystallisation[32].

Online XRD characterisation techniques generally involve four major components which are an X-ray source, an X-ray detector (typically WAXS), a flow cell with X-ray transparent window and a reactor vessel containing the crystallising system. This set up usually involves pumping a crystal slurry from the vessel through the flow cell where the X-ray source can impinge on the sample leading to diffraction and

collection of the scattered radiation by the detector. The diffraction of radiation works on the same principle as PXRD in that a slurry contains randomly orientated crystallites in large numbers so every possible (h k l) plane of the lattice structure is satisfying Braggs law.

As discussed the development of on-line XRD techniques is a relatively new field of X-ray characterisation when compared to >100 years of solid state crystallography. One of the earliest known examples of online XRD methods is the on stream phase characterisation of phosphate rock during processing at Mintek cooperation as part of process control[33]. The set up (Figure 3-17) comprised of a slurry line which was fed from one of the main processing slurry liens on site which was pumped at constant hydrostatic pressure into two windowless sample presenters upon where a Mo kα X-ray source impinged on the sample. The scintillation detectors in the system measured the diffracted X-ray intensities and the whole system was mounted on a vertical-geometry goniometer.
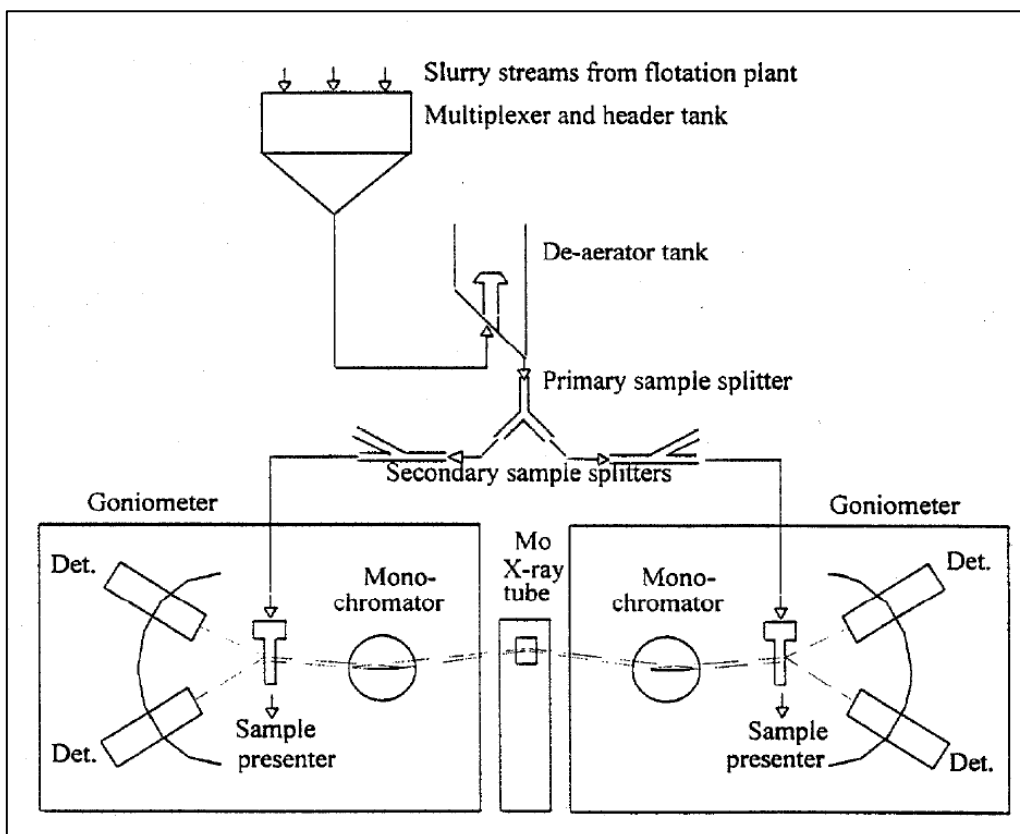
Figure 3-17 The online XRD analysis set up for monitoring mineral phases in phosphate rock[33]

The concentration of apatite and quartz could be directly analysed from the XRD profiles by determination of peak areas of the most intense; (101) peak of quart and (211) peak of apatite, and combining with calibration curves. This is the first example of phase analysis of mineral rock by XRD *in-situ* methods.

This system led to increased interest in online XRD techniques; one of the first systems to monitor pharmaceutical organic molecules during crystallisation was developed by MacCalman and Roberts[34]. The system was used to monitor the polymorphic form of an antibiotic drug during crystallisation *in-situ*. The set up consisted of a reactor vessel which was temperature controlled by water bath and PT100 probe, the vessel was connected to a windowed flow cell which allowed the crystallisation slurry to be monitored by XRD methods. The flow cell contained a mica window of 150μm which allowed X-rays to pass through preventing scatter of the incident beam. The whole system was controlled by PC and allowed recording of temperature and pH accurately to monitor the precise crystallisation of the two solvates in the crystallisation system.
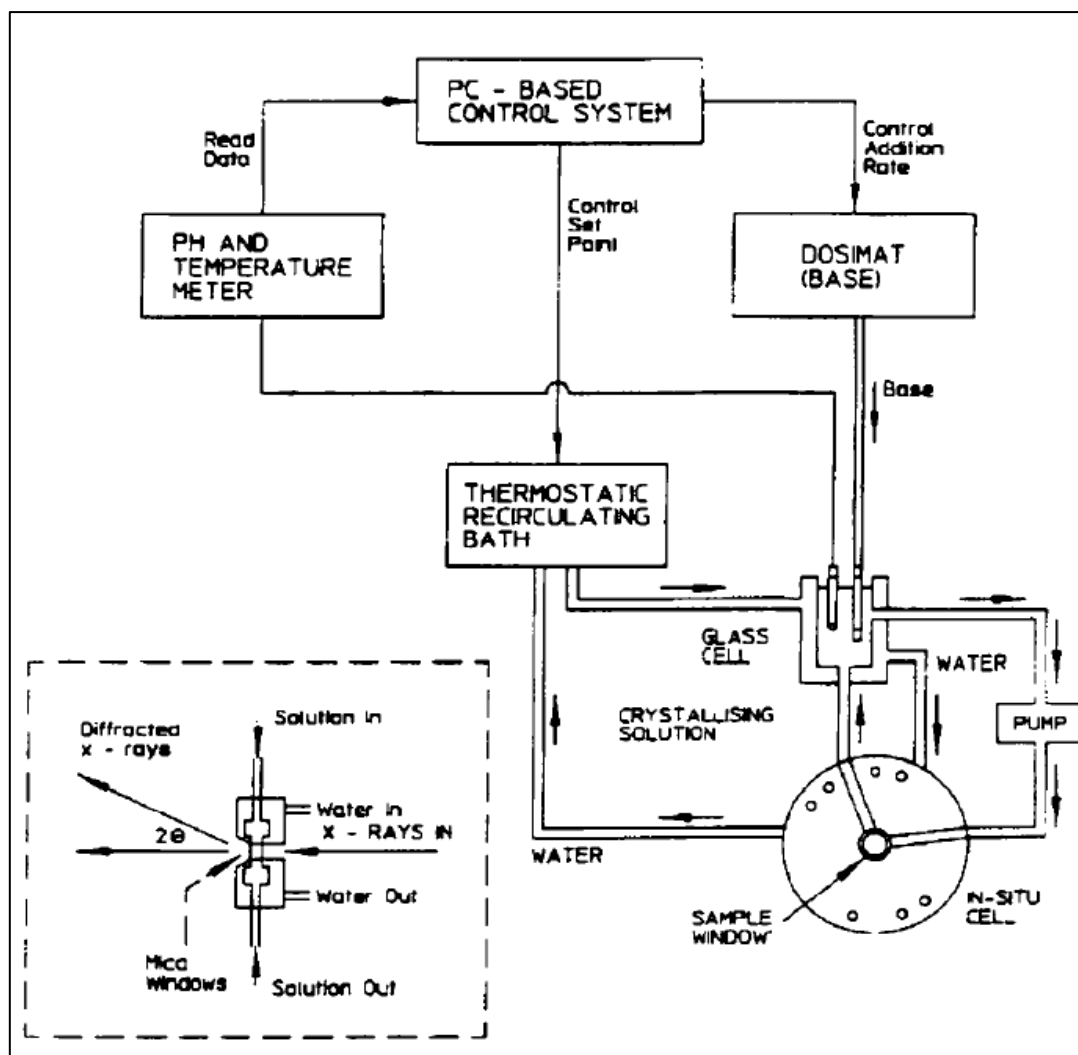
Figure 3-18 *in-situ* XRD set up with use of a windowed flow cell to monitor the crystallisation of solvates a drug molecule[34]

The development of this technique to monitor pharmaceutical compounds *in-situ* was beneficial to many pharmaceutical companies as many specialised chemicals and pharma products were undergoing cost intensive processes to monitor polymorphic changes of these types of molecules during synthesis and processing.

The flow cell set up described by MacCalman and Roberts led the way for a number of different flow cell designs to be presented for use with laboratory and synchrotron sources for monitoring crystallisation *in-situ*. A novel stopped flow cell[35], Figure 3-19 was developed to allow multiple crystallisations to be probed *in-situ* using synchrotron radiation. The system involved 'drowning out' crystallisation where a

saturated solution is supersaturated by addition of anti-solvent. With the use of this stopped flow cell and synchrotron radiation the structural evolution of β and α forms upon nucleation of glutamic acid were probed for the first time *in-situ*. This result illustrates the applications of *in-situ* XRD methods for observing phenomena of nucleation in crystal systems.
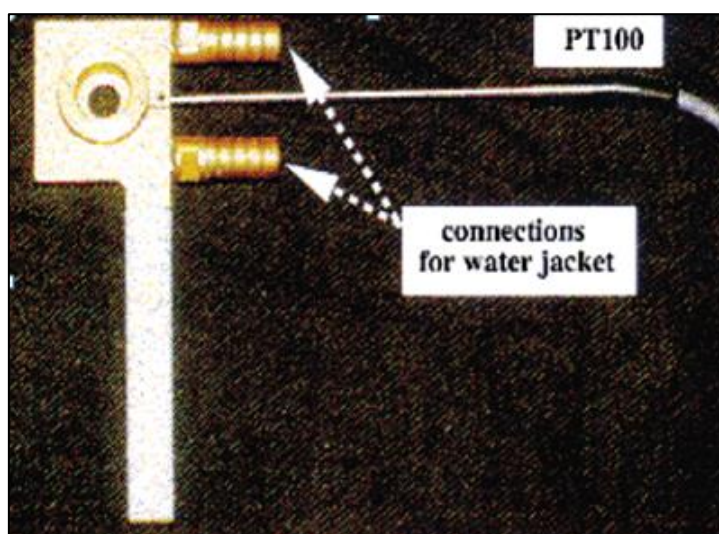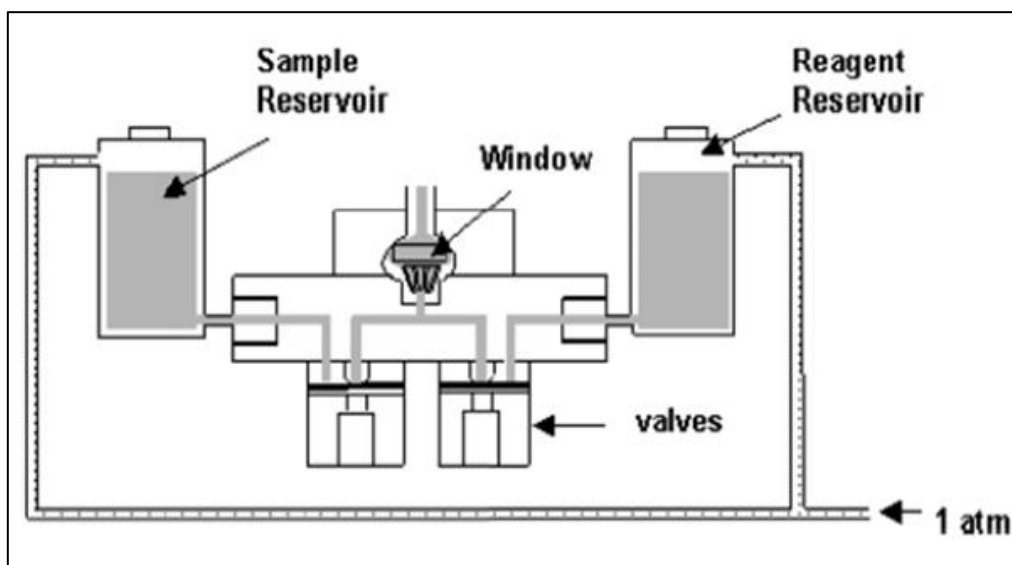
Figure 3-19 Top: Stopped flow cell by Quayle and Davey (2002)[35] Bottom: the variable temperature cell by MacMillan and Roberts (2003) [36]

The ability to probe the nucleation of crystallisation systems by identifying polymorphic phases in the crystallisation behaviour using *in-situ* methods is further highlighted by MacMillan and Roberts[36] in identifying the first crystallising polymorph

of cocoa butter. The cell used (Figure 3-19) in this study was a stagnant cell, i.e. no slurry flow was used, and was temperature controlled using a PT100 probe and water bath. The cell allowed *in-situ* WAXS patterns to be gathered using synchrotron sources to probe the crystallisation of cocoa butter fat in the early stages of crystallisation; ~ms timescale. The results revealed that form III is the initial nucleating phase; not form II as was previously believed, this is another example of online studies probing the early nucleation events of crystallisation.

The success of the flow cells experiments by MacMillan and Roberts and Quayle and Davey allowed the development of in house systems using a lab based X-ray source[37]. This specific system (Figure 3-20) consists of a CPS 120 Inel detector and electronics a Cu K_α radiation source at 35kV running capacity, collimator and a temperature controlled transmission flow cell; which was an improvement on the design by MacCalman and Roberts. The whole system was contained in a transportable X-ray cabinet for ease of use and was initially designed for polymorphic identification during batch crystallisation processes through the use of a slurry line and flow cell (Figure 3-20).
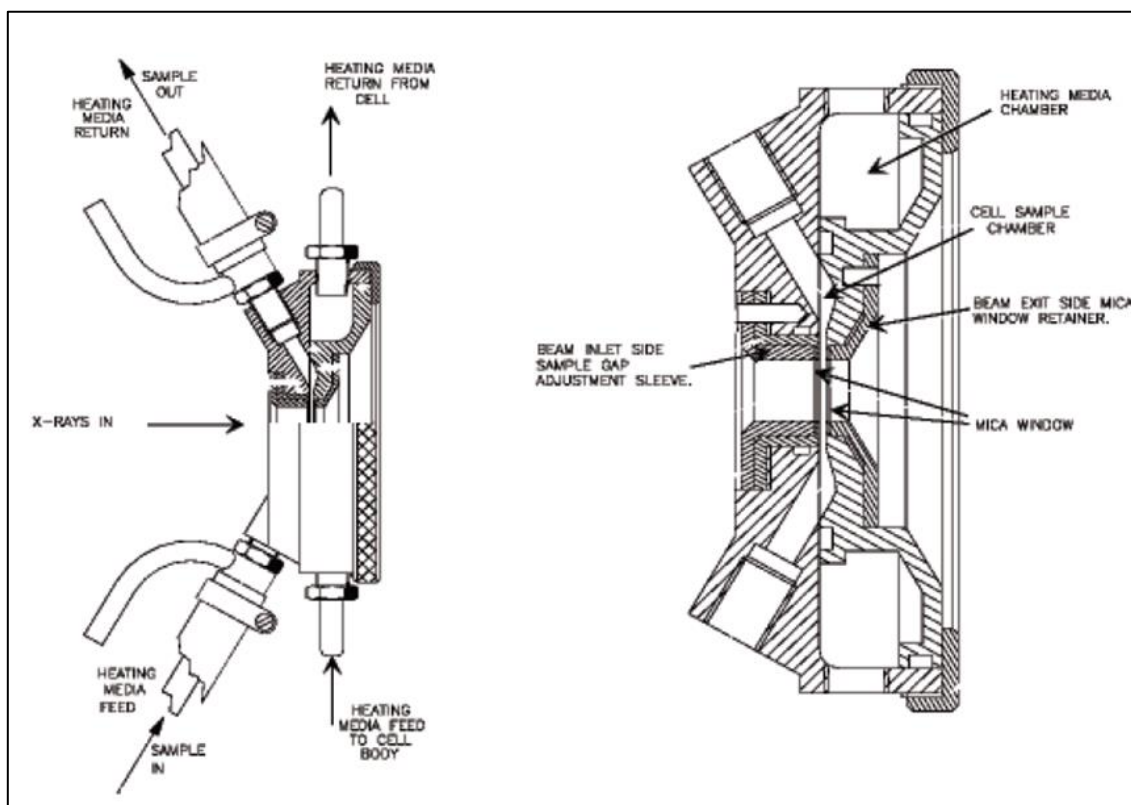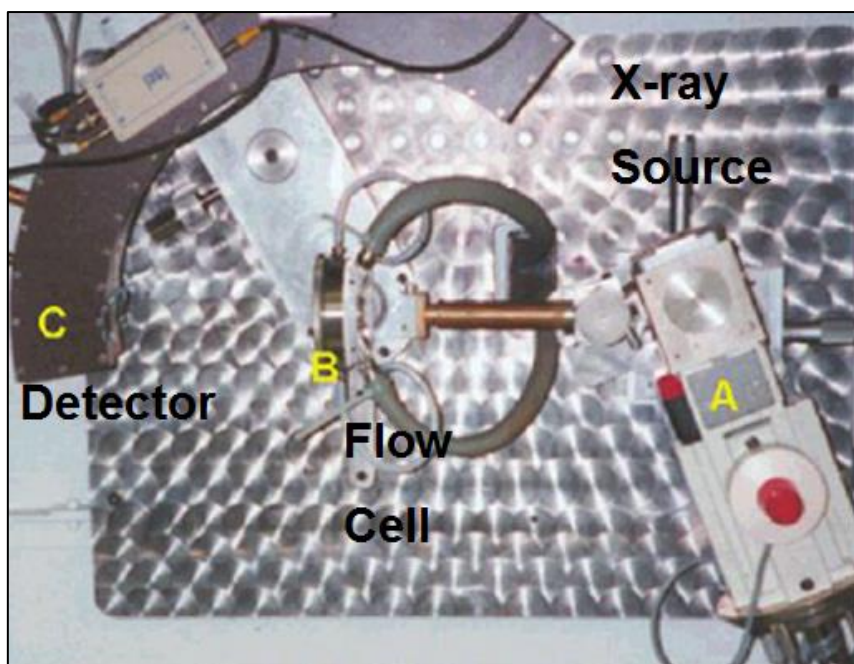
Figure 3-20 Top: the online XRD system developed by Hammond et al. highlighting the main components of the X-ray source A) the flow cell B) and the PSD C), and Bottom: a detailed drawing of the transmission flow cell used in the setup, taken from Hammond et al. 2004[37]

The system was validated using crystallisation systems of urea, monosodium glutamate and l-glutamic acid, the system was shown to have lower detection limit of 1% w/w solids concentration in transmission mode. Further studies using this experimental set up have shown the ability to monitor in-situ the phase transformation of the α and β polymorphs of l-glutamic acid by Dharmayat et al.[38]. Quantitative analysis of this transformation was successfully carried out by creating calibration curves of the relative intensities of the (102) peak of the β form and the (111) peak of the α form. This allowed the kinetics of this phase transformation to be calculated including rate constants, k, and activation energy's, E_A.

The work by Dharmayat et al. highlights the development and progress of *in-situ* characterisation using XRD methods from a polymorphic identification tool to a utility of probing phase transformation kinetics and initial nucleation forms of crystal systems.

3.4.2 *In-Situ* Scattering Applications

A novel tool of *in-situ* characterisation techniques, and one which this research is based, is the application of SAXS analysis *in-situ*. This technique can probe the Nano-scale structures within the nucleating phase through SAXS analysis; which gives information on crystallite shape and size. An application of *in-situ* SAXS was presented by Allison and Davey et al.[39], which combined a flow cell and synchrotron radiation techniques to monitor crystallisation of 2-6 dibrom – 4 nitroanaline, (DBA). Through the use of SAXS techniques and millisecond data collection times, the initial nucleating phase of DBA was seen upon crystallisation. WAXS profiles were seen to grow 0.45 s after mixing of the anti-solvent in the drowning out crystallisation method however the SAXS intensity (Figure 3-21) was seen to increase after just 0.15 s after mixing. This result suggested that a new phase is formed before the crystalline phase; the researchers interpreted this as an amorphous solid or liquid-like phase separation upon which follows transformation to the crystalline phase, possible evidence of a non-classical nucleation mechanism.
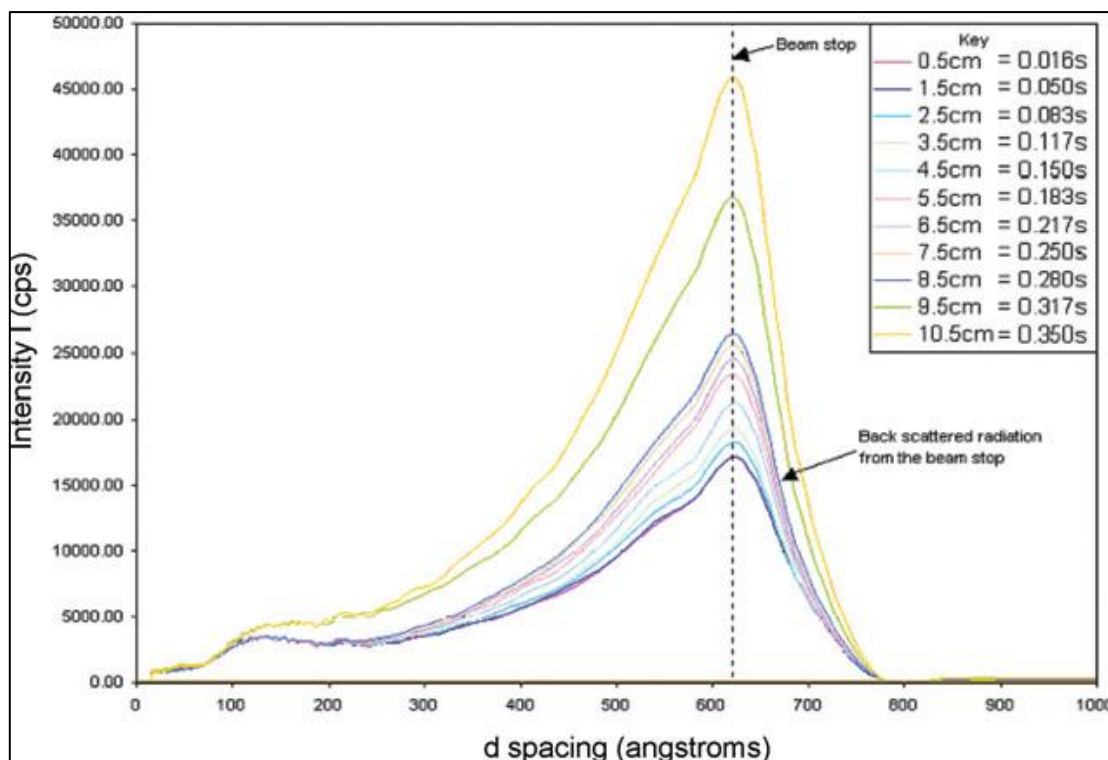
Figure 3-21 In-situ SAXS data illustrating an amorphous phase prior to crystallisation, taken from Allison and Davey 2003[39]

A more recent study by Jawor-Baczynska et al.[40] has applied synchrotron SAXS techniques to monitor the dissolution process for a glycine in water system. The SAXS analysis revealed the presence of large Meso-structures of disordered glycine which were 250nm in size at the saturation temperature of the solution. The scattering patterns were fit to a fractal model which seemed to fit much better than a hard sphere model; this indicated that the large clusters of glycine were not structurally well ordered, shown in Figure 3-22.
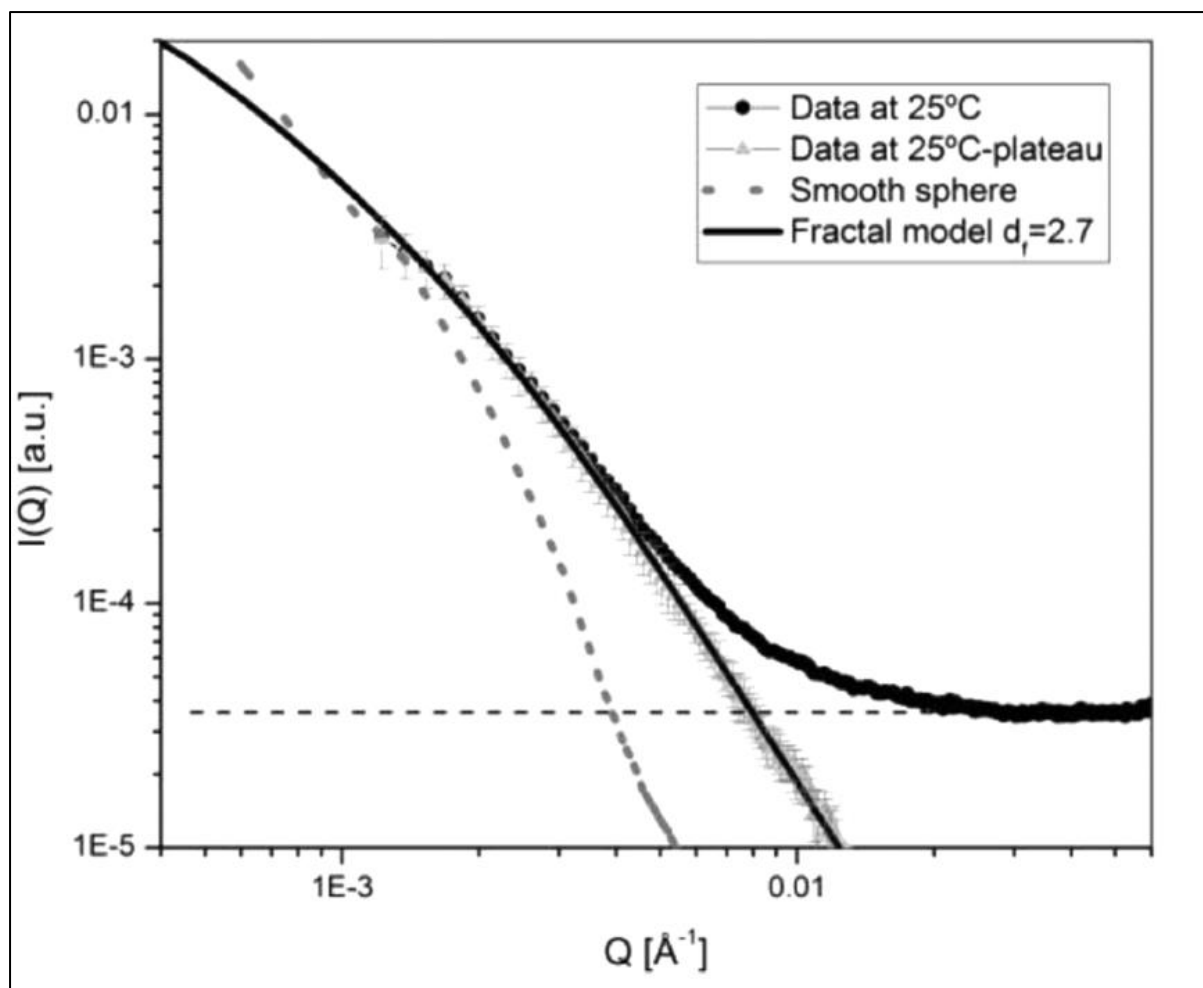
Figure 3-22 Scattering pattern from glycine dissolution experiment highlighting fits of a hard sphere model and a fractal model[40]

These findings were supported by dynamic light scattering which also confirmed the presence of large droplets of glycine under the same conditions. The study builds on work by Chattopadhyay et al. who probed the nucleation of glycine, the reverse process, by *in-situ* synchrotron SAXS and found fractal aggregates of glycine in solution which suggested a liquid-like aggregation of glycine molecules within the supersaturated state[41].

A recent study by Sauter et al.[42] have provided additional data on the nucleation and subsequent crystallisation of bovine β-lactoglobulin followed using *in-situ* synchrotron SAXS. The results reveal that the crystallisation of bovine β-lactoglobulin proceeds through the formation of aggregates of solute whereby the formation of critical nuclei appears to occur inside these large aggregates as shown through results of

microscopy experiments. The recorded scattering curves reveal formation of solute clusters ~10nm followed by the appearance of characteristic Bragg peaks relating to the crystalline phase shown in Figure 3-23.
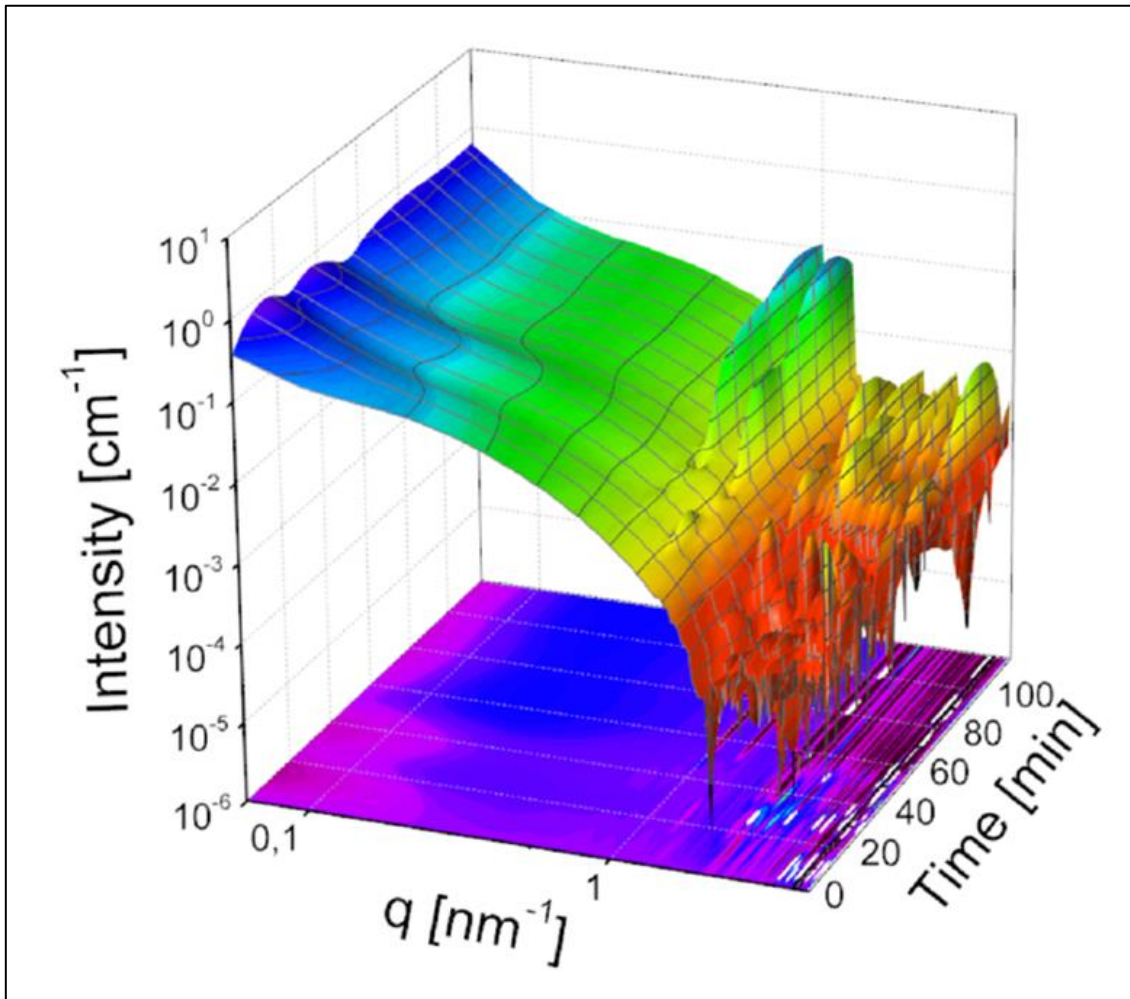
Figure 3-23 Scattering patterns as a function of time during the crystallisation of β-lactoglobulin[42]

These studies have highlighted the application of *in-situ* synchrotron SAXS techniques for revealing structural information at the Nano-scale during the dynamic process of crystallisation.

3.4.3 In-Situ Fourier Transform Infrared Spectroscopy

Infrared spectroscopy, IR, concerns the interaction of infrared electromagnetic radiation with molecular vibrations whereby the energy of a photon is absorbed by a molecule and alters its vibrational state. The fundamental parameter of infrared radiation in spectroscopy is wavenumber, $\bar{v}$, which are the units used to describe peak position in an IR spectrum. $\bar{v}$ is related to the frequency of the radiation, *v*, through the following expression;

$$\bar{v} = \frac{v}{(c/n)} = \frac{1}{\lambda} \quad \text{(3-24)}$$

Where *c* is the speed of light and *n* is the refractive index of the material the radiation is passing through. The transfer of energy in causing molecular vibrations is through the absorbance of photons which raise the energetic state of the molecule. The energy of a photon, ε_p, is related to its frequency, *v*, by the following expression;

$$\varepsilon_p = hv \quad \text{(3-25)}$$

Where *h* is Planks constant. The energy of the absorbed photon can cause a transition to higher energy levels from the ground state, this is shown schematically in Figure 3-24 where the difference between the two energy states of the molecule E_1 and E_2 is *ΔE* which is the energy required by the photon for the transition to occur;

$$\Delta E = \varepsilon_p = hv = hc\bar{v} \quad \text{(3-26)}$$

Due to this absorption of radiation certain molecular transitions in vibrational energy levels are measured to provide an infrared spectrum of a certain molecule[43]. The infrared spectrum is unique to each molecule whereby the frequency of the vibration is related to energy, the intensity is related to the polarizability of the certain bond type and band shapes is related to bonding environment[44]. This essentially provides a fingerprint for individual molecules where atomic masses, geometric arrangement of atoms and bond strengths between atoms can change the recorded spectra[45].
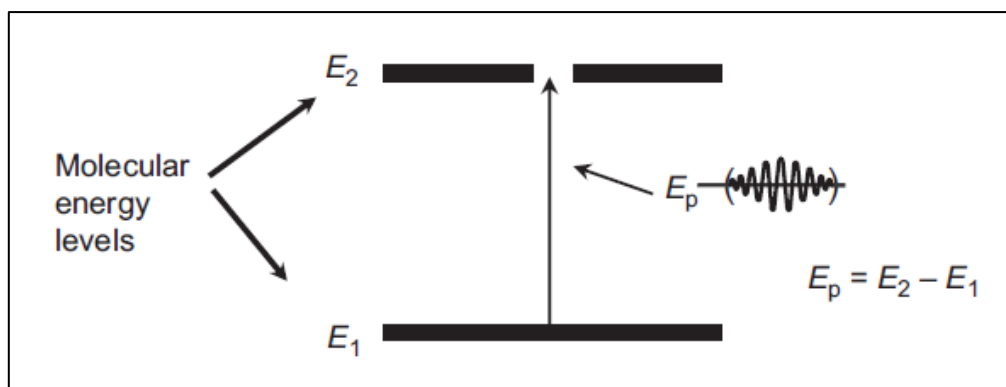
Figure 3-24 Schematic representation of electromagnetic radiation[45]

In a complex organic molecule the vibrational spectrum will include a number of coupled vibrations. However most functional groups of a molecule will produce specific vibrations associated only with that chemical group regardless to the rest of the molecule. This helps to identify the molecular structure by identifying specific functional groups; some characteristic functional group vibrational frequencies are provided in Figure 3-25.
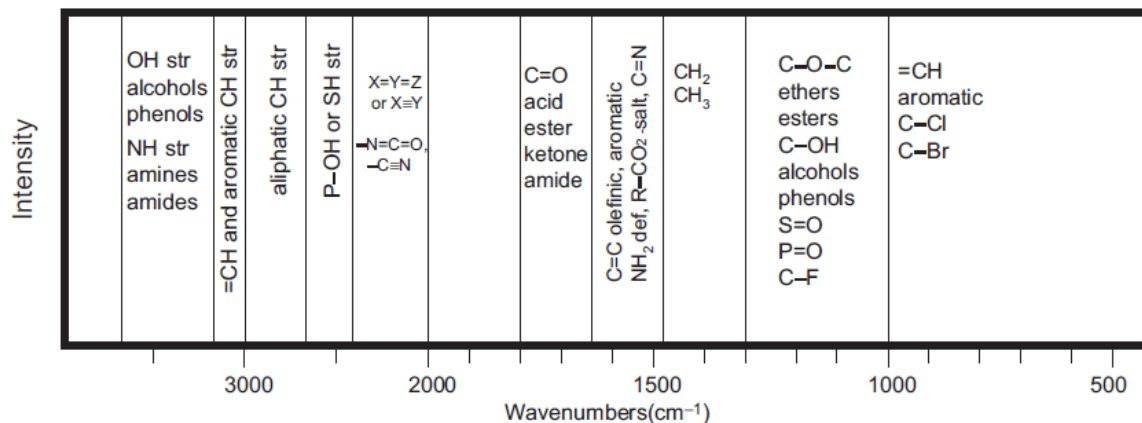
Figure 3-25 Characteristic IR vibrational frequencies of functional groups[45]

These characteristic localised vibrations are summarised in Figure 3-25, these include stretching, bending, rocking, twisting and wagging of an example methylene group. The general rule is that the stronger the intermolecular bond the higher the vibrational frequency.
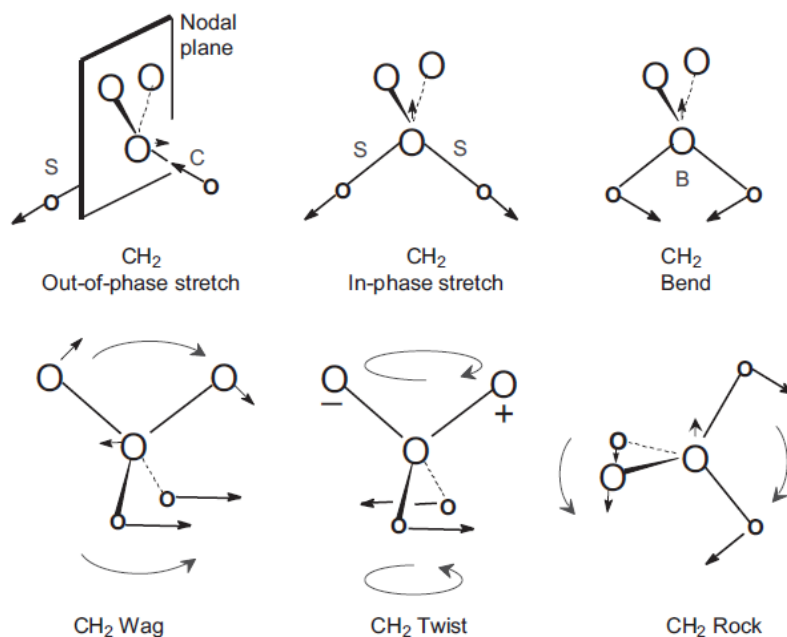
Figure 3-26 Vibrations of a CH$_2$ group S = stretch, C = contract, B = bend, O = open[45]

The nature of FTIR spectroscopy means it is a versatile tool for quantifying concentrations of materials during a crystallisation process and also for probing molecular interactions on solutions.

The link between solution chemistry and the resulting crystalline phase has led to much research in an attempt to understand how the growth units found in the solution state can be linked to the structural synthons in the crystal lattice[46][47][48][49]. FTIR has provided a probe to solution state structure. Many of these studies show a link between the appearance of self-assembled solution phase dimers and the dimeric synthons found in the crystalline phase, the cases of benzoic acid and inosine are good examples[46,50].

Conversely other systems, such as mandelic acid, which contain dimeric structural synthons in the solid state, show no evidence of solution state dimer formation due to effective solvation of the solute[50]. Some solute systems show no apparent link between the solution chemistry and final crystalline structure, thus providing no information regarding the structural pathway to nucleation and consequently to a specific polymorphic form[51][52].

Thus in-situ FTIR is a prominent tool to probe the solution structure of an organic material in solution in an attempt to understand molecular aggregation such as dimerism of solute molecules or sufficient solvation of the solute molecule.

3.4.4 *In-Situ* Attenuated Total Reflectance Beam Ultraviolet / Visible Spectroscopy

Ultraviolet visible light spectroscopy (UV/Vis) uses light in these wavelength ranges to excite electronic energy levels in a molecule which causes ground state electronic transitions to higher energy excited states. The absorbance of this radiation by the molecules can be measured by analysing the incident radiation and the absorbed radiation giving the following relationship;

$$A_b = log\frac{I_0}{I} \qquad \textbf{(3-27)}$$

Where A_b is the absorbance of the sample, I_0 is the incident intensity and I is the intensity of radiation after absorbance. Through measurement of this absorbance the solution concentration can be calculated through the Beer-Lambert law;

$$A_b = log\frac{I_0}{I} = \varepsilon c b \qquad \textbf{(3-28)}$$

Where ϵ is the molar extinction coefficient, c is the solution concentration (mol/L) and b is the path length of the sample.

The UV/Vis spectrometer consists of a detector, a source of radiation, a monochromator and a sample stage. Older ex-situ instruments use a single beam set-up whereby I_0 and I must be measured separately as a clean solvent sample for I_0 and sample solution for I. Modern spectrometers use a dual beam set-up whereby I_0 and I can measured simultaneously by splitting the incident beam in two; where one is the reference beam (100% transmission) and the other passes through the sample.

Attenuated total reflection (ATR) is utilised in in-situ UV/Vis spectroscopy by providing a flexible probe for use in solution reactors and crystallisers as a means of monitoring solution concentration. ATR technology is based on the incident light passing through a material of high refractive index (usually a sapphire or ZnSe crystal) to a material with a lower refractive index i.e. the solution. This causes

attenuation of the beam by the sample and hence providing a measure of absorbance of the incident beam by the sample.

ATR-UV/Vis spectroscopy in combination with fibre optic dipper probes is particularly useful for measuring medium to strongly absorbing species at high concentrations. The technology is usually employed to measure solution concentration on-line during crystallisation processes to control supersaturation and hence the crystallisation pathway. This generally requires an external calibration model which relates absorbance to solution concentration through measurement of standard samples.

An example of this technology used in research is provided by Howard and co-workers who used ATR-UV/Vis together with *in-situ* measurement of particle size distributions to monitor the polymorphic transformation of sodium benzoate from isopropyl alcohol / water mixes[53]. ATR-UV/Vis was used to monitor the solution concentration which indicated the time of two separate nucleation events by plotting the de-supersaturation profile of the solution.

3.5 Choice of Crystallisation System in this Research

The following section will focus the molecule that this research is focused; *p*-aminobenzoic acid (PABA). This will provide the background knowledge on the molecules and an introduction to the solution and crystal chemistry.

3.5.1 *p*-Aminobenzoic Acid
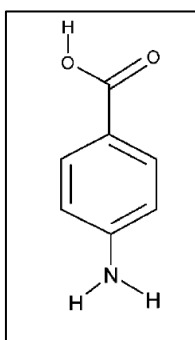
Figure 3-27 PABA molecular structure

PABA, Figure 3-27, has two polymorphs, alpha and beta; the commercially available alpha polymorph is of needle morphology and forms more readily than the beta polymorph which is of hexagonal morphology. PABA contains carboxylic acid and amino functional groups and as such exhibits the characteristics of a pharmaceutical pre-cursor molecule. The alpha crystal structure has been solved by Lai and Marsh[54] where the crystal structure is monoclinic and has the space group $P2_1/n$ with 8 molecules in the unit cell of dimensions a = 18.551, b = 3.860, c = 18.642 Å, with a β angle = 93.56°. The beta form crystal structure was presented by Gracin[55] and is a monoclinic system belonging to the space group $P2_1/n$ with unit-cell dimensions of a = 6.27 Å, b = 8.58 Å, c = 12.36 Å, and a β angle = 100.13° the number of molecules in the asymmetric unit is 4, Alleaume also solved the unit cell structure[56]. The full list of the PABA polymorphs together with unit cell parameters and reference is provided in Table 2.

Table 2PABA polymorphs with the structure reference and unit cell parameters

Ref Code	Polymorph	a (Å)	b (Å)	c (Å)	beta (°)	Space Group	Reference
AMBNAC01	alpha	18.55	3.86	18.64	93.56	$P2_1/n$	Lai, 1965[54]
AMBNAC06	alpha	18.57	3.84	18.63	93.56	$P2_1/n$	Athimoolam, 2007[57]
AMBNAC04	beta	6.27	8.58	12.36	100.13	$P2_1/n$	Gracin[55], 2005

The system is found to be enantiotropic, the transition temperature of which is currently under debate with some authors quoting a value of 25°C obtained from solubility data (Gracin, Rasmuson 2004)[58]. A more recent study involving the monitoring of the polymorphic inter-conversion of PABA using *in-situ* Raman spectroscopy quoted a value for the transition temperature as 13.8°C (Hao, Barrett et al. 2011)[59]. The alpha form is the metastable polymorph and beta the stable polymorph in both studies.

The alpha crystal structure is characterised by centro-symmetric carboxylic acid hydrogen-bonded dimers and π-π stacking interactions, Figure 3-28 (right), which lead to a needle like morphology. The molecular packing in the beta crystal structure is characterised by a 4-membered H-bonding ring structure, Figure 3-28 (left), which is more isotropic in terms of the relative strength and directions of the intermolecular interactions leading to a more prismatic morphology[60] as shown in Figure 3-29. The alpha form of PABA seems to dominate in solution crystallisations from all solvents, with the beta form only nucleating directly or concomitantly with the alpha form, from aqueous solutions[58].
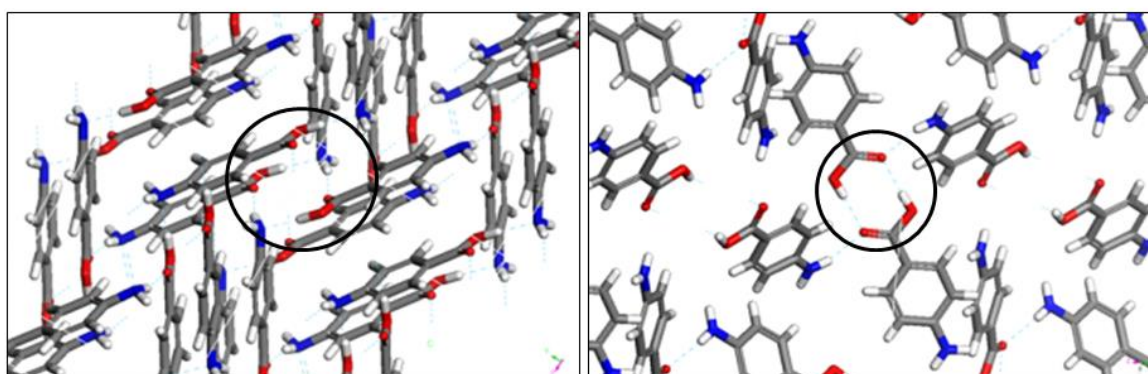
Figure 3-28 Two polymorphs of PABA, alpha right and beta left, highlighting the H bonding structures

Figure 3-29 Crystal morphologies of the prismatic beta phase and the needle like alpha phase of PABA[58]

With reference to the crystallisation behaviour of these two polymorphs it can be said that the carbonyl oxygen group is a much better hydrogen bond acceptor than the nitrogen of the amino group and so formation of the hydrogen bond through the C=O

is preferential to the same interaction through the nitrogen atom. This is due to the fact that the COOH group pulls electron density through the π system of the aromatic ring away from the nitrogen atom via a –M effect (mesomeric). There are also steric issues regarding the amino group which is more sterically hindered than the carbonyl oxygen atom hence reducing the frequency of formation of the H bond via the nitrogen atom.

This then could be one explanation for the preferential appearance of the alpha polymorph as the carboxylic acid dimers in the structure are more favourable electronically and sterically. It is also worth noting that the alpha polymorph is favoured in less polar solvents, (Gracin, Rasmuson 2004)[58].
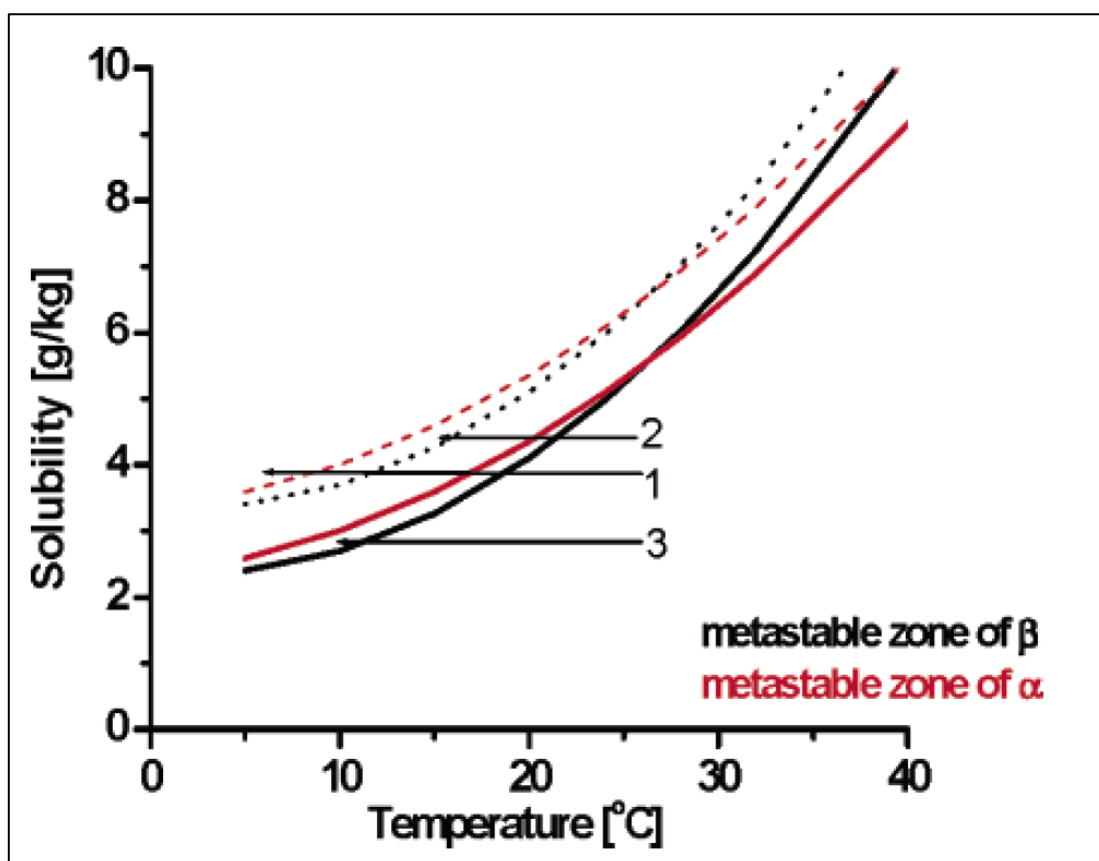
Figure 3-30 Plot of the metastable zones of the two polymorphs of PABA[58]

Another explanation for the relatively low appearance of the beta polymorph could be due to the thermodynamics of the crystallisation of both polymorphs. As can be seen from the plot in Figure 3-30 the range of supersaturation from where the beta

polymorph will form is very narrow, i.e. the MSZW for both polymorphs are very close. If line 1 is taken as an example of a cooling rate of a solution of PABA then it can be seen that this line exceeds the metastable limit for both polymorphs and both can theoretically crystallise at this point and their relative nucleation rates will likely determine which polymorph crystallises and this will be the alpha form. Line 2 represents cooling of the solution to just below the metastable limit of alpha and just over the limit of beta, in this case the beta form should crystallise but because the gap is so small to the metastable limit of alpha then this could also form as these limits are related to the probability of formation. Hence the alpha polymorph may still have time to nucleate due to the relative nucleation of beta being slow. If line 3 is followed then the solution is only supersaturated with respect to the beta polymorph and hence the alpha form should not crystallise, however the induction time of the beta polymorph is likely to be very slow. As a foot note both polymorphs do have under saturated H bond donors and acceptors so the possibility of other polymorphs and solvates is credible [58].

3.6 Closing Remarks

The nucleation and consequent crystallisation of PABA will be the subject of this thesis to provide further experimental data toward a fundamental understanding of the structural process of nucleation from solution. Using a combination *of in-situ* modern analysis techniques described in this chapter together with classical nucleation kinetics and thermodynamic analysis covered in Chapter 2, a link between the solution state chemistry through to molecular clustering will be provided. This will be supported by measured nucleation kinetic and thermodynamic parameters to give a broad structural picture of the nucleation process.

References

[1] Web reference taken from; http://www.siint.com/en/products/xrf/tec_descriptions/descriptions_e.html

[2] H P. Klug, L E. Alexander, *X-ray Diffraction Procedure for Polycrystalline and Amorphous Materials*, 2ndEdition, 1974, John Wiley & Sons Inc., New York

[3] B. D. Cullity, S. R. Stock, *Elements of X-ray Diffraction,*3rd edition, 2001, Prentice-Hall International

[4] Web reference from http://www.siint.com/en/products/xrf/tec_descriptions/descriptions_e.html

[5] INEL (2015) www.inel.fr/en/accueil/

[6] Web reference taken from http://www.wikipremed.com/image.php?img=010503_68zzzz160250_Interference_of_two_waves_68.jpg&image_id=160250

[7] M. Ladd, R. Palmer, *Structure Determination by X-ray Crystallography*, 4th edition, 2003, Kluwer Academic

[8] Web reference taken from http://www.dep.fmph.uniba.sk/mambo/index.php?option=com _content&task=view&id=259&Itemid=28

[9] G. Will, *Powder Diffraction the Rietveld Method and The Two Step Process*, 2006, Springer

[10] H. Wiedemann, Synchrotron Radiation, 2003, Springer, Berlin, Heidelberg

[11] O. H Seeck, B. M. Murphy, *X-ray diffraction modern experimental techniques*, 2015, Pan Stanford Publishing

[12] C. D. Putnam, *Quarterly Reviews of Biophysics,* 2007, 40, 3, 191

[13] O. Glatter, O. Kratky *Small Angle X-ray Scattering,* 1982, Academic Press

[14] Y. D. Dong, B.J. Boyd 2011, *International Journal of Pharmaceutics*, 417, 101

[15] E. Lifshin, *X-ray Characterization of Materials*, 2008, John Wiley & Sons, Weinheim

[16] A. K. Singh, *Advanced X-ray Techniques in Research and Industry*, 2005, IOS Press, Amsterdam

[17] A. Guinier, G. Fournet, *Small-angle scattering of X-rays*, 1955, Wiley, New York.

[18] N. Stribeck, *X-ray Scattering of Soft Matter*, 2007, Springer, Berlin

[19] C. L. P. Oliviera, J. S. Pedersen, *Small-angle X-ray scattering (SAXS): Structure of proteins and particles in solution*, 2012, Online resource Available from: noschool.au.dk/fileadmin/inano/iNANOSchool/PhD_courses/N9_Bionanotools_2012/ SAXS_intro_2012notes.pdf

[20] Y. Xu, P. L. Hiew, M. A. Klippenstein, Y. Koga, *Clays and Clay Materials*, 1996, 44, 197

[21] T. Cosgrove, *Colloid Science: Principles, Methods and Applications*, 2nd Edition, 2010, John Wiley & Sons, Chichester

[22] P. Wong, A. J. Bray, *J. Appl. Crystallogr.*, 1988, 21, 786

[23] L. A. Feigin, D. I. Svergun, *Structure Analysis by Small Angle X-ray and Neutron Scattering*, 1987, Plenum Press, New York

[24] M. H. J. Koch, P. Vachette, D. I. Svergun, *Q. Rev. BioPhys.,* 2003, 36,147

[25] G. J. Beaucage, *J. Appl. Crystallogr.*, 1995, 28, 717

[26] G. J. Beaucage, *J. Appl. Crystallogr.*, 1996, 29, 134

[27] J. E. Martin, A. J. Hurd, *J. Appl. Crystallogr.*, 1987, 20, 61

[28] J. Teixeira, *On Growth and Form: Fractal and Nonfractal Patterns in Physics*, NATO-ASI Series E, Vol. 100, 1986, Springer, Netherlands

[29] P. W. Schmidt, *J. Appl. Crystallogr.*, 1991, 24, 414

[30] H. Boukari, J. S. Lin, M. T. Harris, *J. Colloid Interface Sci.*, 1997, 194, 311

[31] N. Scarlett, I. Madsen, C. Manias, D. Retallack, *Powder Diffraction,* 2001, 16, 71

[32] T. D. Davis K. R. Morris H. Huang, G. E. Peck, J. G, Stowell B. J. Eisenhauer J. L. Hilden D. Gibson, S. R. Byrn, *Pharm.Res.,* 2003 , 20, 11, 1851

[33] A. E. Cole, J. P. R. de Villiers, *Applied Mineralogy, Proc. Int. Congress Appl. Miner, Metallurgical Soc. Of AIME*, 1985, 89

[34] M. L. MacCalman, K. J. Roberts, *J. Applied Crystallography*, 1995, 28, 5, 620

[35] M. J. Quayle, R. J. Davey, A. J. McDermott, G. J. T. Tiddy, D.T. Clarke, G. R. Jones, *Phys. Chem. Chem. Phys.*, 2002, 4, 416

[36] S. D. Macmillan, K. J. Roberts, M. A. Wells, M. C. Polgreen, I. H. Smith, *Crystal Growth & Design*, 2003, 3, 2

[37] R. B. Hammond, X. Lai, K.J. Roberts, *Crystal Growth & Design*, 2004 4, 5, 943

[38] S. Dharmayat, R. B. Hammond, X. Lai, C. Ma, E. Purba, K. J. Roberts, Z. Chen, E. Martin, J. Morris, R. Bytheway *Crystal Growth & Design,* 2008, 8, 7

[39] H. G. Alison, R. J. Davey, J. Garside, M. J. Quayle, G. J. T Tiddy, *Phys. Chem. Chem. Phys.*, 2003, 5, 4998

[40] A. Jawor-Baczynska, J. Sefcik, B. D. Moore, *Cryst. Growth Des.* 2013, 13, 470

[41] S. Chattopadhyay, D. Erdemir, J. M. B. Evans, J. Ilavsky, H. Amenitsch, C. U. Segre, A. S. Myerson, *Cryst. Growth Des.*, 2005, 5, 523

[42] A. Sauter, F. Roosen-Runge, F. Zhang, G. Lotze, R. M. J. Jacobs, F. Schreiber, *J. Am. Chem. Soc.,* 2015, 137, 1485

[43] D. A. Skoog, D. M. West, F. J. Holler, *Fundamentals of Analytical Chemistry*, 7th ed., 1992, Saunders College Publishing

[44] P. Ball, *Designing the molecular world; Chemistry at the frontier*, 10th ed, 1994,m Princeton University Press, Princeton/NJ

[45] P. Larkin, *Infrared and Raman Spectroscopy; Principles and Spectral Interpretation*, 1st Ed., 2011, Elsevier

[46] R. A. Chiarella, A. L. Gillon, R.C. Burton, R. J. Davey, G. Sadiq, A. Auffret, M. Cioffi, C. A. Hunter, *Faraday Discuss.*, 2007, 136, 179

[47] S. Parveen, R. J. Davey, G. Dent, R. G. Pritchard, *Chem. Commun.*, 2005, 1531

[48] A. Gavezzotti, G. Filippini, *Chem. Commun.*, 1998, 3, 287– 294

[49] R. J. Davey, K. Allen, N. Blagden, W. I. Cross, H. F. Lieberman, M. J. Quayle, S. Righini, L. Seton and G. J. T. Tiddy*, CrystEngComm*, 2002, 4, 257

[50] R. J. Davey, G. Dent, R. K. Mughal, S. Parveen, *Cryst. Growth Des.*, 2006, 6, 1788

[51] K. R. Back, R. J. Davey, T. Grecu, C. A. Hunter, L. S. Taylor, *Cryst. Growth Des.*, 2012, 12, 6110

[52] W. Du, A. J. Cruz-Cabeza, S. Woutersen, R. J. Davey, Q. Yin, *Chem. Sci.*, 2015, 6, 3515

[53] K. S. Howard, Z. K. Nagy, B. Saha, A. Robertson, G. Steele, D. Martin, *Cryst. Growth Des.*, 2009, 9, 9

[54] T. F. Lai, R. E. Marsh, *Act Cryst*, 1967, 22, 885

[55] S. Gracin, A. Fisher, *Act Cryst E*, 2005, 61, O1242

[56] M. Alleaume., G. Salascim. J. Decap, *Comptes Rendus Hebdomadaires Des Seances De L Academie Des Sciences Serie C*, 1966, 262, 416

[57] S. Athimoolan, S. Natarajan, *Act Cryst C,* 2007, 63, O514

[58] S. Gracin, A. C. Rasmuson, 2004, *Crystal Growth & Design*, 4, 5, 1013

[59] H. Hao, M. Barrett, Y. Hu, W. Su, S. Ferguson, B. Wood, B. Glennon, *Org. Process Res. Dev.*, 2012, 16, 35

[60] R. A. Sullivan, R. J. Davey, *CrystEngComm*, 2015, 17, 1015

Chapter 4 Materials and Methods

Materials used in this research together with a description of the instrumentation and methodology employed to carry out the experimentation and modelling work

4.1 Introduction

This chapter describes the materials used for this work together with the experimental and modelling methodologies employed in order to address the aims and objectives set by this study. The chapter begins with an overview of the chemicals used in the subsequent experiments, followed by details of the experimental methodologies. These include solubility and solution state infrared spectroscopy studies, poly-thermal and iso-thermal nucleation kinetics studies followed by small angle scattering and X-ray diffraction instrumentation and methodologies. Finally the computational methodology utilised in this work are provided.

4.2 Materials

4.2.1 Supplied Chemicals

Experimental work in this thesis was carried out using p-aminobenzoic acid 99.9% purchased from Sigma Aldrich and used as supplied; the polymorphic alpha form was confirmed using a Bruker D8 advance powder X-ray diffraction instrument.

Silicon powder – 325 mesh 99% purchased from Sigma Aldrich UK used as supplied

Silver (I) Behenate powder >99% from Alfa Aesar

Ludox TM 50 colloidal silica 50 wt% suspension in water Sigma Aldrich UK

Ludox SM colloidal silica 30 wt% suspension in water Sigma Aldrich UK

Ludox HS 40 colloidal silica 40 wt% suspension in water Sigma Aldrich UK

The samples of AOT, Triton X100 and CTAB were provided by Dr Tomasz Stawski, University of Leeds, the details of sample preparation is provided in section 4.3.7.3.

4.2.2 Supplied Solvents

The solvents used in this study were ethyl acetate >99% (GC) supplied by Sigma Aldrich UK, acetonitrile 99% supplied by Alfa Aesar, methanol anhydrous 99.8% supplied by Sigma Aldrich UK, ethanol 99.9% supplied by VWR and deionised water (DI) was supplied by the departmental laboratory. The mixed solvent system used was prepared by mixing the mass fractions of the appropriate solvents together.

4.2.3 Preparation of Beta Form Crystals

The beta form crystals were prepared by slurry inter-conversion from the alpha form at 5°C, a 10 wt% alpha form slurry in 200g of deionised water was prepared in a temperature controlled jacketed crystallisation vessel using a Julabo[1] oil bath with external Pt100 temperature probe. The slurry was held at 5°C at constant agitation using a magnetic stirrer bar set at 300rpm, the inter-conversion process was analysed offline using PXRD to determine the concentration of the alpha and beta phases by the decrease in intensity of the alpha form peaks and subsequent increase of the beta form peaks.

4.3 Experimental Methodology

4.3.1 Solubility Measurements

The solubility of PABA was measured using two methods; the first was a gravimetric analysis study and the second was UV-Vis spectroscopy method. The solvents chosen for use in both methods were; ethanol, methanol, ethyl acetate and DI water and the temperatures of study were 10C, 20°C, 30°C, 40°C and 50°C.

4.3.1.1 Gravimetric Analysis Method

An amount of solvent was placed in a sealable liquid sample vial and placed in a temperature controlled shaker for 12 hours at the set temperature to equilibrate. The sample vial of solvent was then saturated with the alpha polymorph of PABA and returned to the temperature controlled shaker; the saturated samples were shaken at the designated temperature for 12 hours to equilibrate. After this equilibration time a sample of the saturated solution was removed using a pre-heated syringe and filtered through a 20μm filter into a pre weighed liquid sample vial. The sample was placed into a vacuum oven at -0.9bar and 50°C to evaporate the solvent. The solid mass was then weighed on a four figure analytical balance to quantify the solid content in solution and hence the solubility in g/kg. It should be noted that at each temperature for each solvent 3 repeat readings were taken.

4.3.1.2 UV-Vis Spectroscopy Method

The equipment used in this analysis technique was a Zeiss MCS621 UV-Vis spectrometer[2] with a wavelength range of 190 – 720 nm (Figure 4-1). A calibration curve consisting of a number of concentrations of alpha PABA for each solvent was first analysed to provide a linear trend of absorbance against concentration, these standards are shown in Table 4-1 Solute concentrations used for the calibration curve for UV-Vis analysis.

Table 4-1 Solute concentrations used for the calibration curve for UV-Vis analysis

Ethanol g/kg	Methanol g/kg	Ethyl Acetate g/kg	DI Water g/kg
100	150	60	1
130	200	80	4
160	250	100	8
190	300	120	12
220	350		

Each concentration was prepared by dissolving the required amount of PABA in the desired solvent in a liquid sample vial and then measuring the absorbance of the sample, each sample was analysed three times and the average absorbance value taken. The saturated solutions at each temperature in the range 10°C - 50°C were prepared as stated above in the gravimetric analysis method; using the temperature controlled shaker and allowing each sample to equilibrate for 12 hours. The absorbance value of each sample was then measured and again each sample was repeated 3 times. Concentration could be calculated by taking the slope of the linear calibration curve to give the relationship of absorbance to concentration.
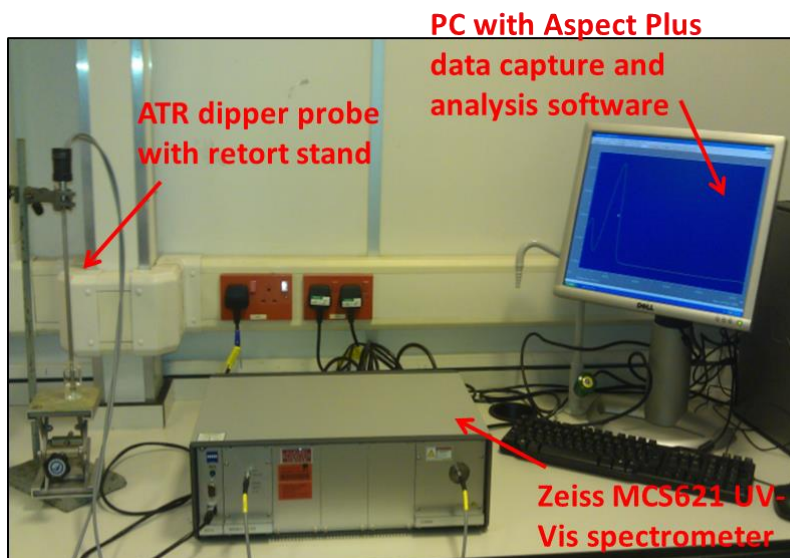
Figure 4-1 Zeiss MCS621 UV/Vis spectrometer with attached ATR probe

4.3.2 Fourier Transform Infrared Spectroscopy

4.3.3 Solid State and Solution State FTIR Experiments

A Nicolet Nexus FTIR[3] with a zinc selandide, ZnSe, ATR probe was used in absorption mode to collect IR spectra of PABA solutions. Data collection included an average of 32 scans with a spectral resolution of 0.482 cm^{-1} and a spectral range of 4000 – 500 cm^{-1}. Data collection and analysis was carried out using a PC with Thermo-Galactic[3] software.

4.3.3.1 *In-Situ* FTIR Experiments

In-situ FTIR experiments were carried out using a dipper 210 ATR FTIR immersion probe with a ZnSe internal reflection crystal together with a Bommen Work IR FTIR spectrometer in absorption mode (Figure 4-2). Data collection was achieved using a PC equipped with Grams software. The spectral range covered was 4000 – 500 cm^{-1} with an average of 64 scans / min to produce a spectrum every 60s, the spectral resolution was 8 cm^{-1} with a background spectrum of clean solvent subtracted. The crystallisations were carried out in a 500ml jacketed crystalliser which was temperature controlled using a PT100 probe connected to a Julabo F32 water bath with external control using the Julabo EasyTemp software[1]. The stirring was

provided by a three blade pitched impeller set at 400rpm. The turbidity of the solution was analysed using an in-house built laser light detection system with data collected every three seconds.
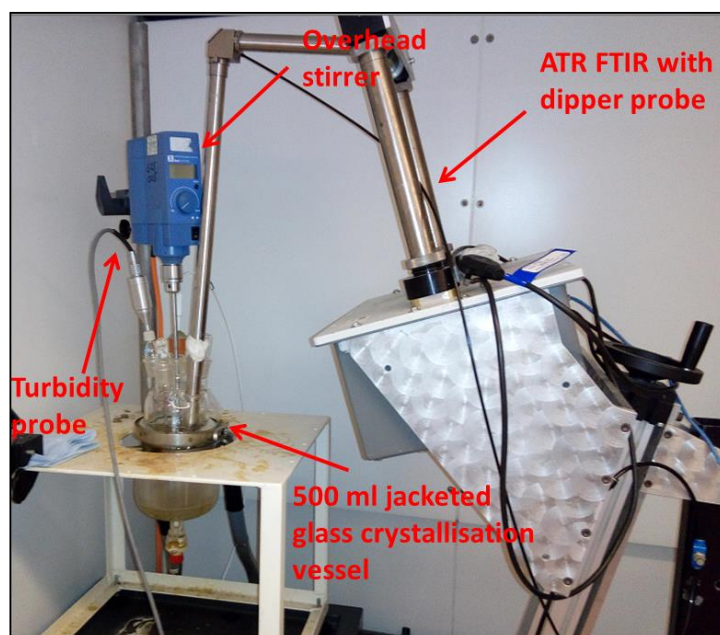
Figure 4-2 *In-situ* crystallisation rig with ATR FTIR spectrometer, turbidity and temperature monitoring

4.3.3.2 Sample Preparation

Solid state samples were measured using alpha PABA (Sigma Aldrich >99%) and beta PABA obtained from slurry inter-conversion at 5°C and purity was confirmed using a Bruker Advance D8 powder X-ray diffractometer.

The solution state samples in ethanol and acetonitrile were saturated with alpha PABA (Sigma Aldrich >99%) at room temperature (25°C) in 10ml screw top vials with magnetic stirring at 300rpm to equilibrate for 24hours.

The dilution experiment samples were prepared by weighing determined amounts of alpha PABA into screw top 10 ml vials using a four figure balance, the appropriate solvent was then weighed into the vials to prepare the desired concentrations. The concentrations studied in ethanol were; 147.7, 135.9 and 125.1 g/kg and in acetonitrile; 64.4, 55.0 and 47.1 g/kg which corresponds to saturation at 20, 15 and 10°C respectively.

4.3.4 Poly-thermal Data Collection

4.3.4.1 Instrumentation

Cooling crystallisation experiments were carried out in a Avantium Crystal 16[4] unit, this multiple reactor equipment allows sixteen 1.5ml vials, separated into 4 blocks, to be heated and cooled at specific rates by utilizing a Peltier heater and water bath system. The vials are magnetically stirred using micro stirrer bars and the crystallisation process is monitored using a turbidometric system to detect the crystallisation and dissolution temperatures.

4.3.4.2 Sample Preparation

Solutions of alpha PABA in ethanol were prepared at 170, 180, and 190, 200 g/kg, in acetonitrile at 54, 64.8, 75.6 and 86.4g/kg and in water at 6, 8, 10 and 12 g/kg at a 10 ml scale. Alpha PABA was weighed into vials using a balance accurate to four significant figures, followed by addition of the solvent. The solutions were then stirred and heated on a stirrer hotplate at 300rpm until dissolution of the material to give a clear solution; these were then transferred to the 1.5ml crystal 16 vials using pre-heated pipettes to prevent unwanted crystallisation.

4.3.4.3 Poly-thermal Methodology

The solutions were heated and cooled in a pre-programmed cycle from 5°C to 50°C where the solutions were held at the higher temperature to allow complete dissolution of the solute, the rates of heating and cooling were 0.1, 0.3, 0.5, 0.7 and 1.0 °C / min with constant stirring by a micro magnetic stirrer at 300rpm.
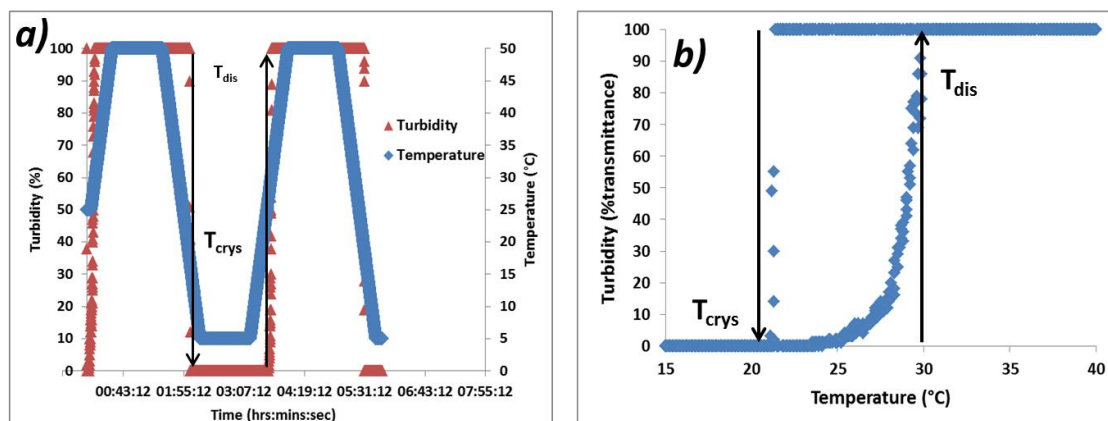
Figure 4-3 a) Typical poly-thermal cooling crystallisation profile, highlighting turbidity measurements of T_{dis} and T_{crys} .b) Turbidity transmittance % vs temperature indicating extrapolation of T_{dis} and T_{crys}

Each cooling rate was repeated five times at each concentration to give good statistics for the measured dissolution and crystallisation temperatures, T_{dis} and T_C respectively. T_{dis} and T_C were obtained using a poly-thermal cooling profile where T_{dis} is determined when the transmission value is 100% and T_{crys} is determined when the transmission percentage decreases below 90%, highlighted in Figure 4-3a) and b).

4.3.5 Optical Crystallite Size Distribution Analysis

Crystallite size analysis was carried out using optical imaging with a Malvern Morphologi G3 (Malvern Instruments, Malvern UK)[5]. Crystal samples were obtained from the Crystal 16 vials after the poly-thermal crystallisation experiments at a super-saturation of 1.2, by isolating the solids from solution using vacuum filtration, these crystals were then dried in an oven at 50°C. The samples of crystals were dispersed onto the automated glass sample stage manually with a spatula to prevent crystallite breakage. The imaging program scanned a pre-determined circular area of sample using a 20x magnification lens providing a resolution of 3.5-210 µm. Prior to each sample run the light intensity and lens focus were automatically calibrated using the instrument software. The distributions provided for analysis were d0.1, d0.5 and d0.9 representing maximum values of a particular measured parameter below 10%, 50% and 90% of the population of particles in the sample respectively.

4.3.6 Iso-thermal Data Collection

4.3.6.1 Sample Preparation

For the isothermal measurements of alpha PABA in ethanolic solutions, supersaturations (*S*) of 1.10 – 1.03 using a solution concentration of 180 g/kg and 1.15 – 1.07 for a 200g/kg solution concentration were prepared. The values of *S* were calculated using the recorded MSZW data from section 4.3.4 which gave a MSZW of 5-9 °C in the concentration range studied. Sample preparation was carried out in the same manner as highlighted in the poly-thermal methodology previously.

4.3.6.2 Iso-thermal Methodology

These solutions were then subjected to an isothermal cooling cycle whereby the Crystal 16 unit is heated 10°C above the dissolution temperature and held for one hour to ensure complete dissolution of the solute. The solution was then subjected to rapid cooling at 5°C/min to the desired holding temperature within the MSZW. The measured induction time, *τ*, was taken as the difference from the start time of cooling to the time of the measured transmittance decrease indicating crystallisation. Each supersaturation was repeated 8 times at the relevant concentration to provide an average induction time measurement.

4.3.7 In House Small Angle X-ray Scattering Commissioning

4.3.7.1 Size Sensitivity Measurements

Samples of the colloidal silica product Ludox HS, SM and TM were prepared from stock solutions as received from the supplier. The stock solutions were diluted using de-ionised water and a four figure balance to the required concentrations of 2, 4, 6, 8 and 10 wt% of each type of Ludox system. The samples were then transferred by syringe into 1 mm diameter borosilicate glass capillary tubes with a wall thickness of 10μm and sealed using heated wax.

The samples were loaded onto the capillary tube sample stage and irradiated with Cu kα radiation at 1.54 Å at 40 kV and 1.8 mA for 60 mins. The sample to detector distance was 1.7 m providing a *q* range of 0.25 – 7 nm^{-1}, the beam path contained a 1m beam tube purged with helium and evacuated to 900 mbar The q space on the detector was calibrated using silver behnate powder in the same 1mm borosilicate

capillary tubes as the samples, the *q* space was calibrated against the d001 = 5.838 nm, d002 = 11.676 nm, d003 = 17.514 nm reflections in the scattering pattern. The resulting scattering patterns of the Ludox samples were corrected in the program Fit2D[6] with background subtraction of a clean sample of de-ionised water.

4.3.7.2 Time Resolution Sensitivity Measurements

Samples of colloidal silica Ludox HS, SM and TM were prepared as discussed in 4.3.7.1. The samples were irradiated using the same X-ray and SAXS instrument as in 4.3.7.1, however data collection times were in 5min increments from 0 to 60 mins.

4.3.7.3 Electron Density Sensitivity Measurements

Micro-emulsion samples of AOT (dioctyl sodium sulphosuccinate) and Triton X100 were prepared by weighing the appropriate mass of surfactant using a four figure balance to produce a 0.1M solution in isooctane. The corresponding wt% of de-ionised water was then added to the AOT solutions to prepare W5, W10 and W20 micro-emulsion systems. The corresponding wt% of deionised water was then added to the Triton X100 solutions to prepare W5, W10 and W15 micro-emulsions.

The CTAB (hexadecyltrimethylammonium bromide) micro-emulsions were prepared in the same way but with the adition of 1-butanol as a co-surfactant which was added in a 73 wt% amount relative to the CTAB concentration. The three micro-emulsiom systems were sonicated for 60 minutes at room temperature and equilibrated for 24 hours, these samples were provided by Dr Tomasz Stawski, University of the University of Leeds. The micro-emulsion samples were irradiated using the same X-ray and SAXS instrument as in 4.3.7.1 with data collection times of 60mins and a clean sample of iso-octane was subtracted as a background.

4.3.8 Dynamic Light Scattering Measurements

Dynamic light scattering was carried out on the samples of Ludox colloidal silica described in Section 4.3.7.1 where sample preparation was the same. The liquid samples were loaded into a 1cm path length liquid sample cell and then into a Malvern Zetasizer Nano[5] with a size range of 3.8nm – 100 microns as a spherical diameter. The measurement times were 20 mins with a solvent standard of clean DI water used for calibration of the instrument.

4.3.9 Small Angle Scattering Measurements; NSLS

4.3.9.1 Instrumentation

SAXS measurements were carried out at the X27C beamline at the National Synchrotron Light Source (NSLS) in Brookhaven, Long Island, NY. The primary beam used for these measurements was set at an energy of 9.04 kev and a wavelength of 1.37 Å. The sample to detector distance was 1710 mm with a vacuum tube covering this distance to prevent unwanted air scatter. The scattered beam was recorded on a Mar charged coupled device detector with 1024 pixels at a resolution of 156 µm / pixel. Data collection times were 2 minutes with a detector binning time of 13s. The detector was calibrated using silver behenate calibration standard powder mounted in a 2mm borosilcate glass capillary tube with a wall thickness of 10µm.

4.3.9.2 Sample Preparation

Ethanolic alpha PABA solutions were prepared at a concentration of 290 g/kg which is equal to the saturation concentration at 60°C. Samples were prepared by weighing the set amount of PABA into screw top vials using a 4 figure balance followed by addition of ethanol to the desired concentration. The vials were then sealed using Parafilm to prevent unwanted evaporation of the solvent. Samples were then transferred to a stirrer hotplate and heated to 65°C and equilibrated for 1 hour stirring at 300rpm with a magnetic stirrer bar to ensure full dissolution of the solids.

The samples were then pipetted into 2mm borosilicate glass capillary tubes with a wall thickness of 10µm, using preheated glass pipettes at 65°C to prevent unwanted crystallisation. The capillary tubes were sealed using hot wax and then placed in aluminium Newport model 500B sample stage with Peltier heater and thermostatic bath temperature control, fully programmable through the provided Newport software.

4.3.9.3 Data Analysis

The analysis of the corrected scattering patterns was carried out using the program IRENA[7], where the Unified fit model was applied to the data to calculate R_g and P values at various structural levels, full details of these calculations are provided in Chapter 3.

4.3.10 Small Angle Scattering Measurements; LNLS

4.3.10.1 Instrumentation

SAXS measurements were taken at the SAXS-1 beam line[8] (Figure 4-4) at the Brazilian Synchrotron Light Laboratory, Campinas, Brazil. The on-site brass sample holder provided a 2 mm thickness static liquid sample environment with temperature control, the 8.3 keV X-ray beam size at the sample was 1.5mm in diameter. The X-ray beam flight path was fully vacuumed to 10^{-2} mbar including the sample chamber, up to the Pilatus 300K detector used to collect the scattered X-ray beam, the detector was 84 x 107 mm with a pixel size of 172 micron. Data collection times were 29s with 1s for detector binning, the set up allowed the data to be collected over a q space of $0.128 - 5.4$ nm^{-1}. The collected SAXS patterns were corrected for primary beam intensity variation, transmission and a background from a clean sample of ethanol was subtracted.
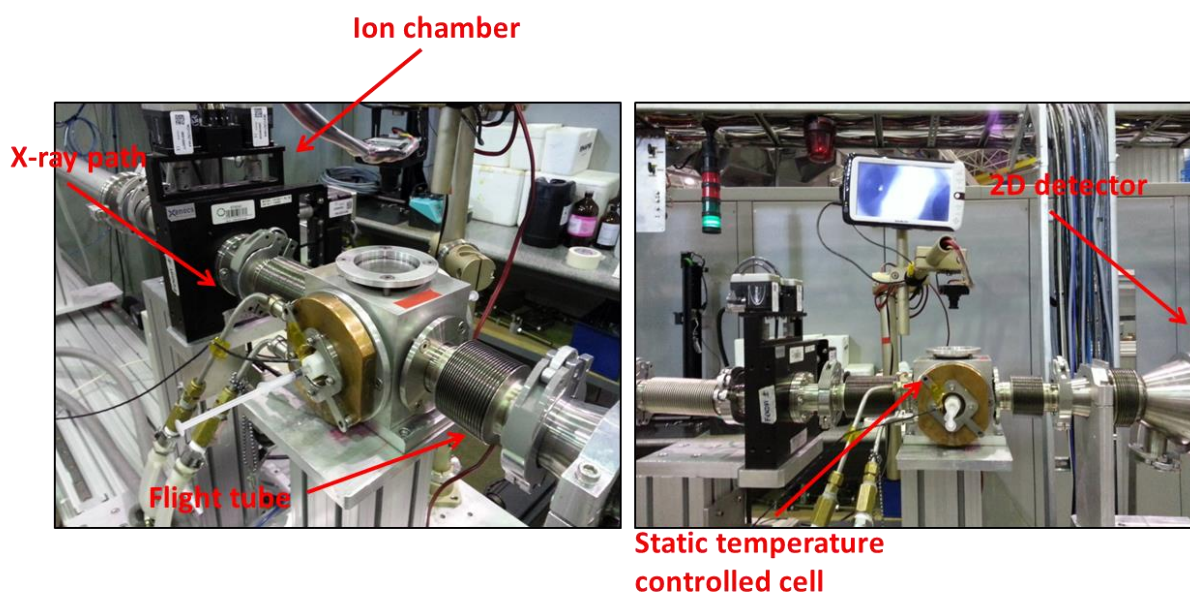
Figure 4-4 The SAXS-1 beam-line set up at the LNLS, Campinas, Brazil, highlighting the key instrumentation

4.3.10.2 Sample Preparation

Solutions of alpha PABA in ethanol at a concentration of 247 g/kg, saturation concentration at 50°C, were prepared. The solutions were heated to 55°C in a

sealed laboratory bottle with screw cap in a pre-heated water bath. Syringes, for transfer of the solutions to the sample cell, were also preheated to 55°C to prevent unwanted crystallisation of the solution before reaching the sample cell. The solutions were transferred by syringe to the 55°C preheated brass sample cell on the beam-line which used a separate water bath for temperature control, while the cell temperature was monitored using a thermocouple which could be inserted into the block next to the sample environment. The samples were injected into the brass sample cell and subjected to a poly-thermal cooling cycle from 55°C - 30°C at a rate of 0.1°C/min, data collection which was started as soon as the cooling process began.

4.3.10.3   Data Analysis

The analysis of the corrected scattering patterns was carried out using the program IRENA[7], where the Unified fit model was applied to the data to calculate R_g and P values at various structural levels, full details of these calculations are provided in Chapter 3. The form factor fitting of the scattering patterns was carried out in the program Scatter[9], further details of these calculations are also provided in Chapter 3.

4.3.11 Polymorphic Transformation Experiments

4.3.11.1   Online XRD experimental set-up

The experimental set up (Figure 4-5) regarding the *in-situ* XRD analysis in this work has been described previously[10, 11], the INEL[12] 120° curve position sensitive detector, Bede Microsource Cu kα X-ray generator with monochromator, slits and in house built collimator are unchanged and housed in the original enclosure. The flow system used in these experiments consisted of a 100ml jacketed glass crystalliser with magnetic stirrer agitation; temperature control was supplied by a Julabo F32 circulation bath with Pt100 temperature monitoring of the reactor contents.

 To carry out *in-situ* XRD a novel transmission flow cell has been designed and implemented into this system. The flow cell has a 2mm diameter borosilicate glass capillary tube to allow the 1mm diameter circular X-ray beam to impinge on the sample, the capillary tube has a wall thickness of 10µm to reduce absorption of X-ray flux at the cell and hence increase the signal to noise ratio. The cell is temperature controlled via biaxial hose connections which connect to the same Julabo F32

circulator as the reactor, this is to minimise the temperature variation at the cell and the reactor.

The flow loop, which transfers the crystal slurry from the reactor to the cell for analysis and then returned to the reactor, is powered by a Watson Marlow peristaltic pump with a four roller drive to reduce pulsation of flow. Solution concentration is monitored using a Zeiss UV-VIS spectrometer equipped with an ATR probe for integration into the reactor vessel system. Two computer stations are also connected to the rig; the first contains a multi-channel analyser for reading the CPS detector signal and also the Bede[13] software Poly-crystal for analysis of the collected XRD profiles. The second controls the UV-VIS spectrometer and is involved in data collection; this system also controls the Julabo F32 circulator and can record temperature profiles.

4.3.11.2   *In-Situ* Flow Cell Sensitivity Tests and Polymorph Calibration Experiments

The transmission flow cell used in this work was tested for online XRD performance prior to any kinetic study being carried out. This was to test the quality of the data obtained during running conditions; for example the signal to noise ratio and also the limit of detection of the cell. Saturated solutions at room temperature of alpha PABA were prepared in a 70:30 solvent mix of deionised water:ethanol, this mix was used to reduce concentration fluctuations due to any small temperature fluctuations in the system. The second reason for this solvent choice was because PABA is hydrophobic; the turbulent mixing effect of the flow loop caused the slurry to foam and phase separate, the 70:30 solvent mix resulted in a homogenous slurry negating this effect.

The limit of detection experiments were conducted by adding a specific mass of alpha PABA to the saturated solution in the crystalliser, the concentration range was 0.1-1 wt% in 0.1wt% intervals. At each slurry concentration *in-situ* XRD patterns were collected at data acquisition times of 300 seconds, each concentration was repeated 3 times and the data averaged using the Poly-crystal software package.
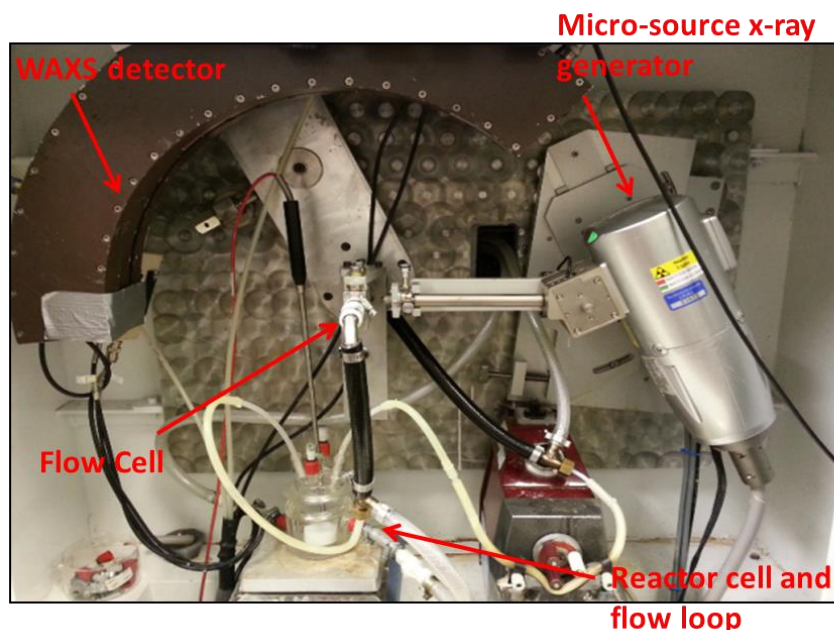
Figure 4-5 Laboratory in-situ XRD rig highlighting the main components of the system

The signal to noise ratio was also tested, this was carried out by adding 1 wt% of alpha PABA to a saturated solution at room temperature, *in-situ* XRD patterns were collected at 10 second intervals for two minutes. This was to determine at what point the diffraction signal of the solute overcomes the instrumental and solvent background effects.

Calibration studies were also carried out for later analysis in order to relate the peak area of significant peaks of the two polymorphs directly to solids concentration in the slurry. Saturated solutions of each polymorph in 70:30 DI water:ethanol were prepared at 20°C based on recorded solubility as part of this research. The solutions were held at 20°C to prevent any unwanted transformation of the beta form, at this temperature the transformation takes several hours. Several concentrations of 2, 4, 6, 8 and 10 wt% were analysed for both polymorphs with 5 minute data collection times. The collected data was smoothed using SPCA and then analysed using the software package Poly-crystal where a background function was subtracted followed by fitting of a Gaussian function to the observed peaks to obtain a fitted peak area, this value as a function of concentration was used for the calibration curve.

4.3.11.3   Polymorphic Transformation Experiments

Saturated solutions of PABA were made up in a 70:30, DI water:ethanol solution using the solubility data gathered at the specified isothermal conditions. An amount of beta PABA was then added to the reactor to produce a 7 wt% slurry with constant magnetic stirring at 300rpm. These experiments were to be seeded crystallisations as un-seeded experiments take ~ 2 days for the SMPT to occur due to the induction time of nuclei, the seeds used were alpha PABA as supplied by Sigma, these were hand milled using a mortar and pestle and characterised using a Morphologi G3, it should be noted the same seed crystals were used in each experiment.

Seed crystals, 0.2 wt% were then added to the reactor and this time was taken as time zero and the first measurement was taken. XRD scans were taken at 300 second intervals to monitor the slurry inter-conversion. Temperature control and monitoring was achieved through the use of a Pt100 probe and Julabo Easy Temp software as described previously.

The isothermal experiments ranged in temperature from 24 - 30°C in 2°C intervals, where experiments at 28°C were repeated 5 times for reproducibility testing. Monitoring of the solution composition through an in-situ UV-Vis ATR probe in the reactor vessel was also carried out and data was also recorded every 300 seconds.

4.3.12   Polymorphic Characterisation

4.3.12.1   Powder X-ray Diffraction

PXRD was used as a tool for polymorph characterisation on a regular basis for confirming the purity of the two phases of PABA. This was carried out using a Bruker D8 advanced X-ray diffractometer[14] which used Cu Kα radiation and a germanium primary monochromator in Bragg-Brentano reflection geometry. The step size used was 0.033 2θ and the step time used was 0.7 s/step over a 2θ range of 4-39.8 2θ. The detector used was a Vantec-1 position sensitive detector.

4.3.12.2   Optical Microscopy

Images of crystals recovered from various crystallisation experiments in this thesis were provided using an Olympus[15] IMT-2 inverted microscope. Images were

captured using a JVC KY F1030 digital camera with KY-Link image acquisition software. Sample crystals were placed onto glass microscope slides and the morphology analysed using magnification lenses of 4 and 20x magnification.

4.4 Computational Methodology

4.4.1 Prediction of Theoretical Scatteirng Curves of PABA Synthons

The program Crysol[16] was used to calculate the scattering profiles of the constructed monomer, NH-O dimer, the stacked dimer and the carboxylic acid dimer models; these are highlighted in Figure 4-6. These are primary structural synthons taken from the crystal structures of the polymorphs of PABA in the program Mercury[17]. The program uses multipole expansion to calculate the spherically averaged scattering pattern and also considers the solvation shell within the calculation in this case ethanol was used as the solvent. The parameters used within the calculation were default with the exception of the solvent density which was modified to ethanol, to describe more accurately the calculation process. An explanation of the step by step inputs into the program will be given.
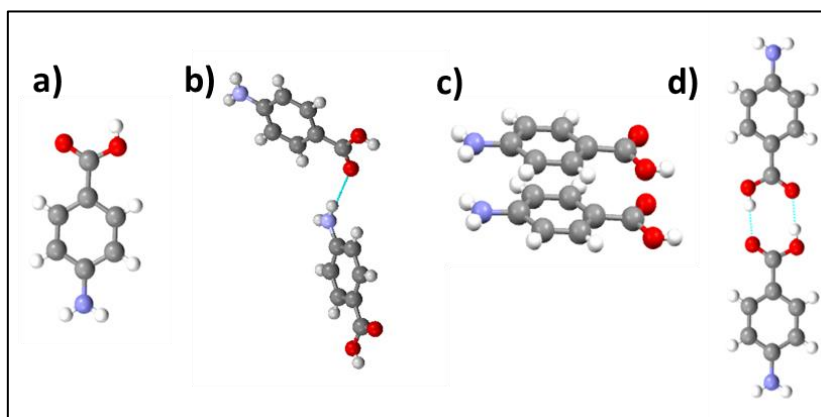
Figure 4-6 Models used in Crysol for calculation of the theoretical scattering pattern in ethanol for a) monomer of PABA, b) NH-O dimer, c) stacked dimer and d) carboxylic acid dimer

- The first command line argument is the file that Crysol reads; in this case it is the molecular cluster models in the form of the .PDB files.

- Line 1; order of harmonics (value 1-50) this defines the resolution of the scattering curve the default value is 15; for large particles larger values may be required at the expense of CPU time.

- Line 2; order of Fibonacci grid (value 10-18) defines how many grid points represent the surface of the cluster, default value is 17.

- Line 3; maximum scattering vector q; default value is 0.5Å^{-1} maximum is 1 Å^{-1}.

- Line 4; number of points on the theoretical curve; default is 51.

- Line 5; angular units in the file with experimental data; not applicable in this case.

- Line 6; electron density of the solvent; default is $0.268 \text{ e}^-/ \text{Å}^3$ for pure ethanol.

- Line 7; Contrast of the hydration shell, the difference between bulk solvent electron density and that of the solvation layer, the default is $0.03 \text{ e}^-/ \text{Å}^3$.

- Line 8 Account for explicit hydrogen's, default is N/A

- Line 9 Average atomic radius, default; 1.48 Å

- Line 10 Excluded volume; calculates this value from the model but this can be adjusted depending on the users requirements.

At the end of this procedure Crysol provides a plot of *I(q)*; the file contains the calculated scattering curve in solution, the scattering curve *in vacuo*, the solvent scattering and also the border layer scattering. The program also outputs a number of ASCII files which contain the multipoles that describe the particle envelope used in the calculation of the theoretical scattering. The values of R_g used for further analysis were taken as those provided by the particle envelope in the ethanol continuum model.

4.4.2 Solvation Free Energy Calculations Using Molecular Dynamics

The solvation free energies of PABA were predicted with molecular dynamics simulations using the thermodynamic integration technique[18]. Each of the states of PABA sampled was first minimised using the steepest descents method[19]. Then each state was equilibrated at 293 K and 1 atm for 100 ps. The initial state (λ=0) was defined by turning off the electrostatic and VDW interactions between the solute and the solvent. The final state (λ=1) was defined as having the single molecule fully solvated in a solvent box. Eight 'windows' were used for the integration pathway going from the initial to the final state $\Delta\lambda$= 0.0 0.2 0.4 0.6 0.7 0.8 0.9 1.0. For each

window, further equilibration of the system was applied for 100 ps and sampled for 500 ps. All calculations are preformed within the Gromacs programs package[20]. Topology files, bonded and non-bonded parameters were derived from the GAFF force field[21]. For the electrostatic potential, RESP charges were derived from Antechamber[22] within Ambertools based on ab-initio calculations at the MP2/aug-cc-pvTz level of theory, calculations were performed by Dr Dimitrios Toroz.

4.4.3 Molecular Dynamics Simulations of FTIR Spectroscopy

All calculations were carried out using Gaussian 09,' at the M06/6-31+G* level of theory. Each of the vibrational modes was assigned to and matched against experimental data for that vibrational mode. The calculations were performed for the single molecule and the carboxylic acid dimer of PABA. Furthermore, a minimum structure of three molecules of PABA (two of the molecule forming and carboxylic acid dimer and one non interacting single molecule) are found and the harmonic vibrational frequencies were calculated and analysed for this particular structural motif, calculations were performed by Dr Dimitrios Toroz.

4.5 Conclusions

This chapter has provided an overview of the chemicals used in this research together with all the experimental and computational methodologies employed. The methodologies for analysing solubility by UV/Vis and gravimetric analysis together with studies of solution chemistry by FTIR spectroscopy were presented. The instrumentation and experimental methodology for measuring poly-thermal and iso-thermal crystallisation parameters were also covered. The application of an in-house built SAXS instrument to measure Nano-scale structure in liquid samples was also provided. The methods of *in-situ* SAXS studies at synchrotron beam-lines together with *in-situ* X-ray diffraction methodologies were also covered. Molecular dynamics simulations of solvation free energy calculations and prediction of infrared spectra from structural models was also provided. The simulation of scattering patterns from molecular models of key PABA synthons using multipole expansion techniques was also provided.

References

[1]Julabo (2015) www.julabo.com/

[2] Zeiss (2015) www.zeiss.co.uk/corporate/en_gb/home.html

[3] Thermo (2015) www.thermoscientific.com

[4] Technobis (2015) www.crystallizationsystems.com/en/crystal16/

[5] Malvern Instruments (2015) www.malvern.com

[6] A. P. Hammersley, S. O. Svensson, M. Hanfland, A. N. Fitch, D. Häusermann, *High Pressure Research*, 1996, 14, 235

[7] J. Ilavsky, P. R. Jemian, *J. Appl. Crystallogr.*, 2009, 42, 347

[8] SAXS 1 beamline details http://lnls.cnpem.br/beamlines/saxs/saxs-2-2/saxs1/

[9] S. Forster, L. Apostol, W. Bras, *J. Appl. Crystallogr.*, 2010, 43, 639

[10] R.B. Hammond, X. Lai, K.J. Roberts, *Crystal Growth & Design*, 2004, 4, 5, 943

[11] S. Dharmayat, R. B. Hammond, X. Lai, C. Ma, E. Purba, K. J. Roberts, Z. Chen, E. Martin, J. Morris, R. Bytheway, *Cryst. Growth & Design*, 2008, 8, 7

[12] INEL (2015) www.inel.fr/en/accueil/

[13] Bede (2005) now accessible as www.jvsemi.com

[14] Bruker (2015) www.bruker.com/

[15] Olympus (2015) www.olympus.co.uk/microscopy/

[16] D. I. Svergun, C. Barberato, M. H. J. Koch, *J. Appl. Crystallogr.*, 1995, 28, 768.

[17] I. J. Bruno, J. C. Cole, *Acta Crystallographica Section B-Structural Science*, 2002 58, 389

[18] H. B. Callen, *Thermodynamics and An Introduction to Thermostatistics, 2nd ed.*, 1985, Wiley: New York

[19] M. C. Payne, M. P. Teter, D. C. Allen, T. A. Arias, J. D. Joannopoulos, *Rev. Mod. Phys.* 1992, 64, 1045−1097

[20] B. Hess, C. Kutzner, D. van der Spoel and E. Lindahl, *J. Chem. Theory Comput.* 2008 , 4, 435

[21] J. Wang, R.M. Wolf, J. W. Caldwell, P. A. Kollman and D.A. Case, *J. Comput. Chem.*, 2004, 25, 1157

[22] J. Wang, W. Wang, P. A. Kollman and D.A. Case, *Journal of Molecular Graphics and Modelling,* 2006, 25, 247

Chapter 5 Solubility and Solution Chemistry

Solubility analysis with derived thermodynamic parameters to reveal a prediction of solute interactions in various solvation environments, followed by a detailed analysis of solution structure and self-assembly using FTIR spectroscopy

5.1 Introduction

An understanding of solubility and solution chemistry of a solute system is the starting point to understanding crystallisation and thus nucleation. The link between solution chemistry and the resulting crystalline phase has led to much research in an attempt to understand how the growth units found in the solution state can be linked to the structural synthons in the crystal lattice[1, 2, 3, 4, 5].

This chapter aims to explore this interesting question on the role of solution chemistry and the structural pathway to nucleation and if there is indeed a link between the solution and solid state structures of PABA. Solubility studies aim to characterise the effect of solvent on the dissolution of PABA and how solution chemistry seems to favour the crystallisation of the alpha polymorph, even below the transition temperature of 13.8°C[6]. Thermodynamic parameters will be derived in an attempt to energetically describe solvation and the influence of solvent during this process.

Solid and solution state FTIR will be utilised with the aim of linking the solid state structural synthons found in the alpha and beta polymorph with any growth units found in the solution state spectra. This will also be validated by supporting molecular dynamics simulations of key structural synthons of the PABA polymorphs in a solution environment to provide simulated IR spectra of these states.

The following solution state studies build the foundation for the subsequent chapters by providing solubility data for the planning of crystallisation experiments but also an insight into the molecular association between the solid and solution states.

5.2 Thermodynamic Solubility Study of PABA in Protic and Aprotic Solvents

5.2.1 Experimental Solubility of PABA

Solubility analysis of alpha PABA was carried out using various solvent systems and analysis methods to obtain a broad perspective of how the solvent and hence solution environment can moderate the solubility and the solutes propensity to self-associate.

This study was focused around polar-protic and polar-aprotic solvents, as PABA is insoluble in non-polar solvents. This is due to the variation of polarity of the PABA molecule; consisting of highly polar acid and amine functional groups separated by a non-polar benzene ring. The consequence of this is not only is it important for the solvent to provide hydrogen bonds for solvation, but also the solvents ability to stabilise the non-polar aromatic moiety.

Figure 5-1 summarises the solubility study of alpha PABA in methanol, ethanol, ethyl acetate, acetonitrile, 70:30 water:ethanol mix and deionised water using three methods; gravimetric analysis, UV-Vis spectroscopy and Crystal 16 measurements of dissolution temperatures. The results show that solubility follows the trend methanol > ethanol > ethyl acetate > acetonitrile > 70:30 water:ethanol > deionised water. This indicates that for the solvent to effectively solvate the PABA molecule the presence of a polar group, i.e a hydrogen bond acceptor or donator or ideally both is required, however equally important is the presence of a non-polar group in order to stabilise the aromatic ring.
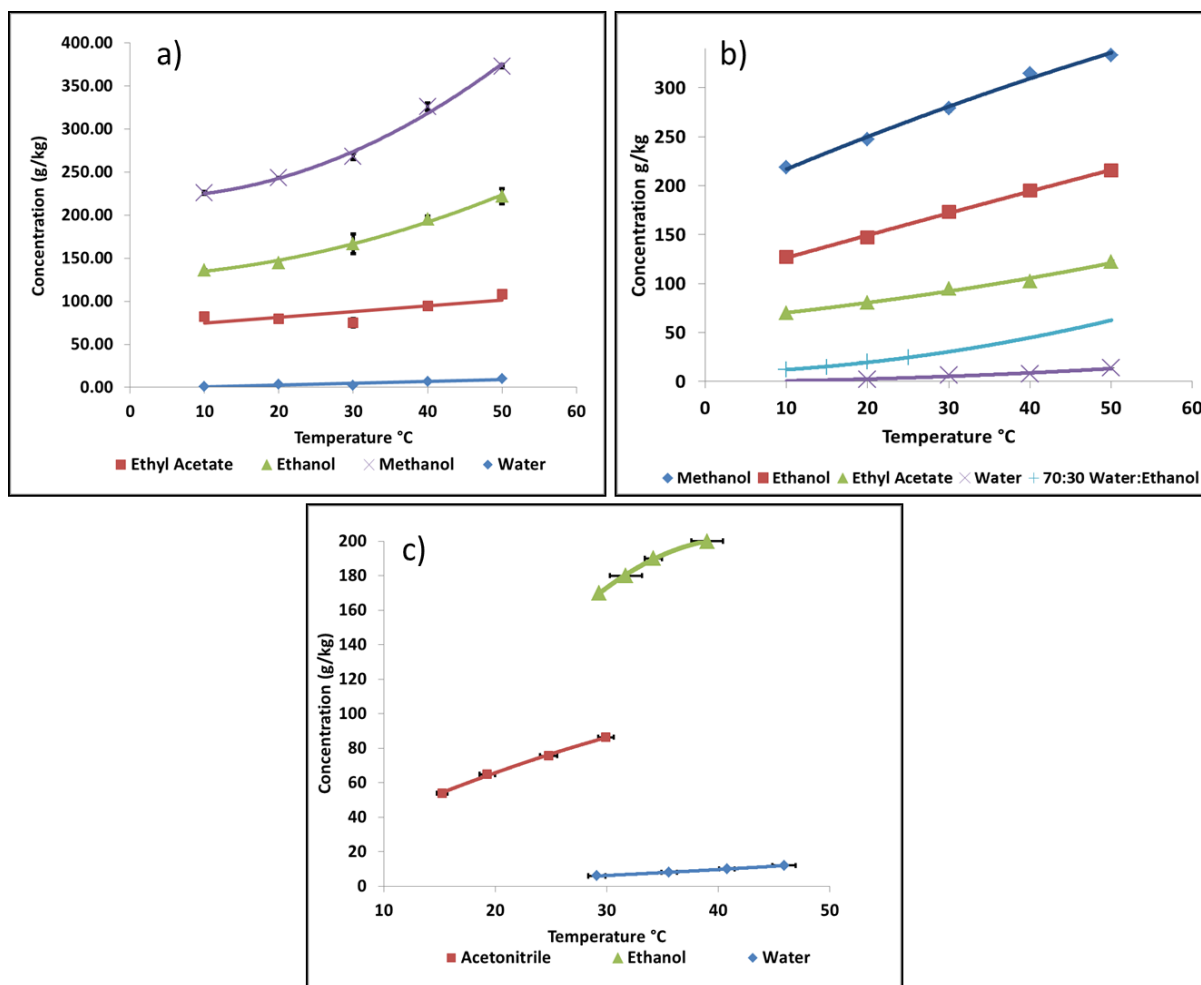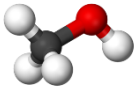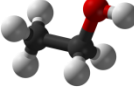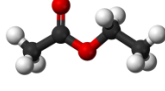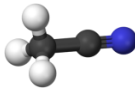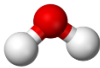
Figure 5-1 Solubility data measured using a) gravimetric analysis, b) UV-Vis analysis and c) Crystal 16 measurements

This can be explained by analysis of the physical properties of the solvents and also their chemical structure; these are listed in Table 5-1. The dielectric constant of the solvents indicates that PABA is solvated more effectively by medium polarity solvents, such as methanol, DC = 24.5 or ethanol, DC = 24.3; however as the case in ethyl acetate shows, DC = 6.02 this is not the sole factor accounting for effective solvation. Ethyl acetate, which is an aprotic solvent, has a low dielectric constant, however due to the presence of the non-polar ethyl and methyl end groups, provides a stabilisation effect for the aromatic ring and hence increases its ability to solvate. A similar case is seen in acetonitrile which is also aprotic but can provide, to a lesser extent compared to ethyl acetate, some stabilisation of the aromatic ring of PABA due to the presence of a methyl group.

Table 5-1 Molecular structures and physical properties of the solvents used in the solubility study of PABA

	Methanol	**Ethanol**	**Ethyl Acetate**	**Acetonitrile**	**Water**
Solvent Type	Polar Protic	Polar Protic	Polar Aprotic	Polar Aprotic	Polar Protic
Dielectric Constant	24.50	24.30	6.02	37.00	78.00
Dipole Moment / D	1.69	1.69	1.78	3.92	1.85

This observation is further supported by the case in water which is highly polar, DC = 78.00, and can donate and accept hydrogen bonds, however the solubility of PABA in water is the lowest of all the solvents studied due to the lack of any non-polar moiety's to stabilise the aromatic ring.

In summary PABA is solubilised most effectively by polar solvents which contain non-polar end groups to provide solvation effects for the non-polar aromatic ring, medium sized H bond donors and acceptors such as ethanol and methanol, solvate PABA most effectively by meeting both of the above criteria.

5.2.2 Ideal Solubility and Thermodynamic Parameters of Solution

Plotting solubility data in van't Hoff coordinates gives a good comparison to the ideal solubility of a molecule and an indication of its propensity to self-associate in solution based on the preferential molecular interactions of the solvent and solute. Additionally a number of thermodynamic parameters can be calculated which are useful when describing solvation and molecular aggregation.

The measured solubility from the three experimental methods highlighted in Figure 5-1 are plotted in van't Hoff coordinates in Figure 5-2 together with a comparison to the ideal solubility in each case. The data show that in all cases the solubility in the alcohols and ethyl acetate are very close to the ideal solubility line, this is due to the higher solubility in these solvents and so a more ideal behaviour is observed. The

solubility of water is very non-ideal and lies furthest from the ideal solubility, the solubility of acetonitrile and 70:30 water:ethanol mix appear in-between the two extremes.
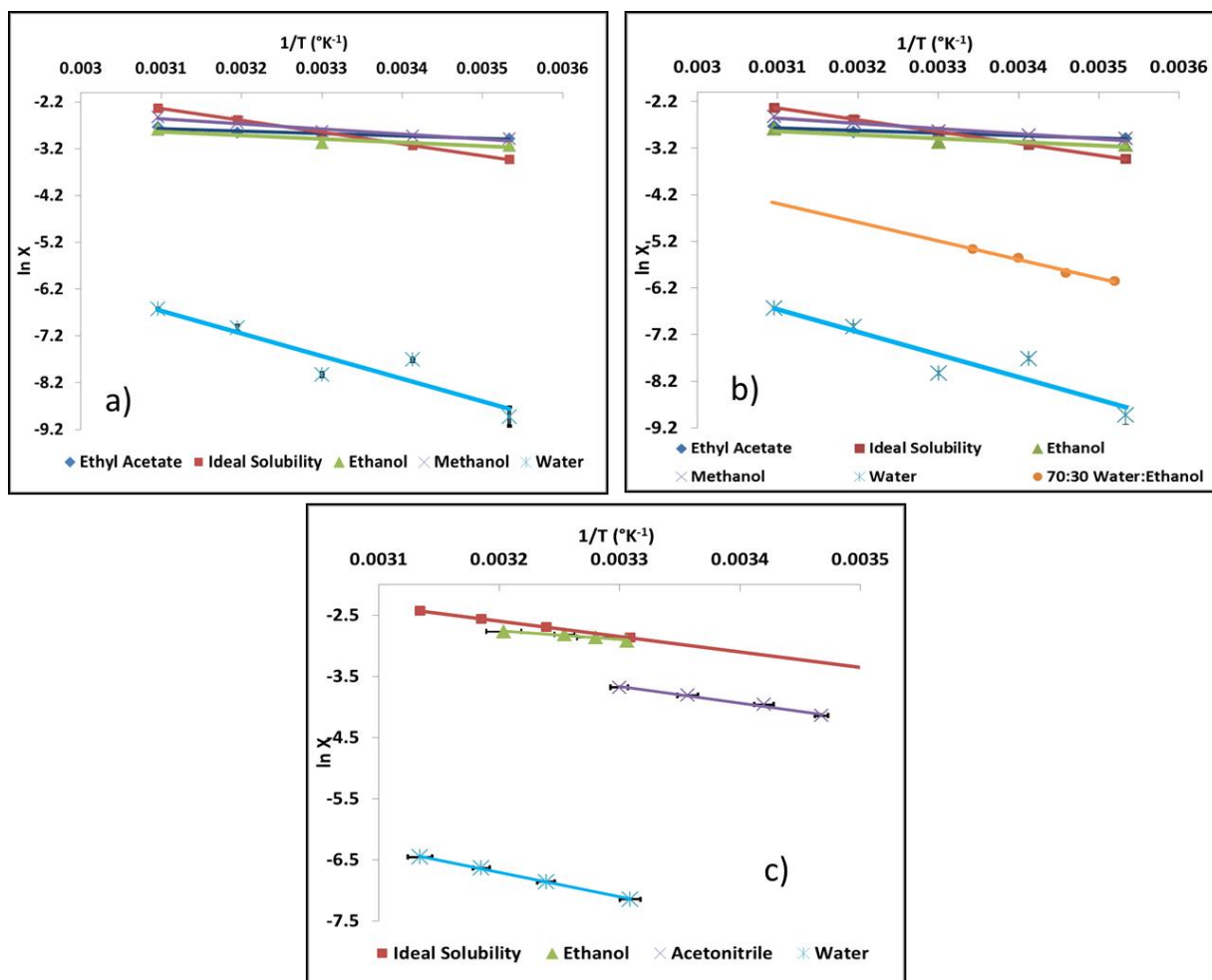
Figure 5-2 Measured solubility data using a) gravimetric analysis, b) UV-Vis analysis and c) Crystal 16 measurements, plotted in van't Hoff coordinates vs the ideal solubility

The data reveal that in all solutions the solubility is generally less than ideal and so molecular self-association could be expected in all solvents where the solute-solute interactions are preferable to the solute-solvent interactions. The order of preferential molecular aggregation of PABA in the studied solvents based on the van't Hoff plot analysis is as follows; water > 70:30 water:ethanol mix > acetonitrile > ethanol > ethyl acetate > methanol.

The observation that PABA solutions in water are likely to contain self-associated PABA molecules is interesting as water is the only solvent that the beta polymorph has been found to spontaneously nucleate from, however exactly which solute-solute interactions are likely to take place is beyond the scope of the van't Hoff analysis.

The plots of solubility in van't Hoff coordinates in Figure 5-2 allow calculation of the enthalpy, entropy and Gibbs free energy of solution using equations highlighted in 2.3.3. The thermodynamic parameters of the solubility process are highlighted in Table 5-2; analysis of the data reveals that for all solvents ΔG_{soln} is positive. The reason for this is that the values of ΔH_{soln} and ΔS_{soln} are calculated from the solubility curve and as such are at saturation point, these parameters are sometimes termed the van't Hoff enthalpy and entropy of solution. Hence the free energy required to dissolve one mole of PABA in a mole of solution at saturation temperature must be positive.

The trend is that in the alcohols and ethyl acetate the values of ΔG_{soln} are smaller than those in the water acetonitrile and 70:30 water:ethanol mix indicating that more free energy is required to dissolve a mole of PABA at saturation. The values of the activity coefficient are also listed in Table 5-2 and are calculated from the ideal and measured solubility. This gives a rough indication of the types of interactions in the certain solvent system, a high value of activity or a large deviation from ideality, is indicative of a system with a higher propensity for solute-solute interactions. The case of PABA in water is an example of very non-ideal behaviour where solute-solute interactions are favoured and the case in methanol is an example of a system tending towards solution ideality where solute-solvent interactions are more favourable in comparison.

The calculated values of solvation enthalpy are highlighted in Table 5-2 and are calculated from Equations 2-17 and 2-18, this parameter indicates the enthalpy change associated with the solvation of a mole of PABA at saturation temperature. In this case the harmonic mean temperature of the solubility studies was used and the value of the lattice energy is taken for the alpha polymorph as 102.6 KJ/mol from recent published calculated values[7]. The values of solvation enthalpy provide an estimate to the propensity of solute molecules to remain solvated. In the case of the alcohols and ethyl acetate solutions, the calculated solvation enthalpy's are lower

than in water, acetonitrile and 70:30 water:ethanol mix so are more likely to stay solvated in comparison to the later.

Table 5-2 List of the calculated van't Hoff enthalpy, entropy and free energy of solution, the enthalpy of solvation, activity coefficient and regression of the linear fits to the solubility data from the various measurement techniques

Solvent type	ΔH_{soln} (kJ/mol)	ΔS_{soln} (kJ/mol.K)	ΔG_{soln} (kJ/ mol)	ΔH_{solv} (kJ/mol)	γ	R^2
Gravimetric Analysis						
Methanol	4.49	0.0091	1.76	-103.07	0.95	0.93
Ethanol	9.10	0.0058	7.34	-98.47	1.08	0.97
Ethyl Acetate	9.17	0.0072	7.01	-98.39	1.12	0.96
Water	40.14	0.0690	19.31	-67.43	135.60	0.87
UV-Vis Analysis						
Methanol	7.78	0.0024	7.06	-99.79	0.97	0.99
Ethanol	9.62	0.0075	7.36	-97.95	1.09	0.99
Ethyl Acetate	9.74	0.0082	7.26	-97.83	1.04	0.99
Water Ethanol 70:30	33.15	0.066	13.84	-74.25	15.08	0.99
Water	40.24	0.076	17.26	-67.33	85.11	0.95
Crystal 16						
Ethanol	12.27	0.017	7.23	-95.39	1.10	0.96
Acetonitrile	22.32	0.043	9.56	-85.33	2.31	0.99
Water	33.25	0.051	17.53	-74.41	63.05	0.99

5.2.3 Thermodynamic Parameters of Mixing

The thermodynamic parameters of solution calculated from the previous section can be further utilised to describe the thermodynamic parameters of mixing of the solvation process which was highlighted in Section 2.3.3.

Equations 2-19 - 2.21 show that the dissolution process can be simplified to two steps; the melting of solid and the subsequent formation of interactions between solute and solvent, or solvation. This allows a relationship between ΔH_{mix} and ΔS_{mix} with $\Delta H_{fus,}$ ΔS_{fus}, ΔH_{soln} and ΔS_{soln} to be described[8] where ΔH_{fus} and ΔS_{fus} can be extrapolated from the ideal solubility curve.

Table 5-3 presents the values of ΔH_{mix} and ΔS_{mix} of PABA in the various solvents from the three methodologies used to measure solubility; these values are hence at saturation. The calculated values of ΔH_{mix} are negative for all cases except the in the water, acetonitrile and water ethanol 70:30 mix which have positive values of enthalpy, this suggests an energy barrier to the mixing process in these solvents whereas in the other solvents this process is spontaneous. The calculated values of ΔS_{mix} are found to be negative in all solvents except in the water and water ethanol 70:30 mix, this suggests that the entropy change on mixing is non-spontaneous in these solvents but spontaneous in the latter.

Overall it can be concluded the solution process is mainly driven by solution entropy and mixing enthalpy in all solvents with the exception of water and water ethanol 70:30 mix. The negative decrease in entropy in solvents upon mixing (with the exception of water and water ethanol 70:30 mix) indicates that there may be some solution pre-ordering in these solvents. The exact nature of the molecular interactions causing this negative entropy i.e. solvent-solvent, solute-solute, is beyond this analysis procedure, however it does suggest an interesting possibility of molecular aggregation of PABA in the alcohols, ethyl acetate and acetonitrile.

Table 5-3 Calculated values of enthalpy and entropy of mixing at saturation in the various solvents from the measured solubility data and the ideal solubility

Solvent type	ΔH_{mix} (kJ/mol^{-1})	ΔS_{mix}(kJ/mol.K^{-1})
Gravimetric Analysis		
Methanol	-16.43	-0.036
Ethanol	-11.82	-0.039
Ethyl Acetate	-11.75	-0.038
Water	19.22	0.024
UV-Vis Analysis		
Methanol	-13.14	-0.043
Ethanol	-11.3	-0.038
Ethyl Acetate	-11.18	-0.037
Water Ethanol 70:30	12.23	0.021
Water	19.32	0.031
Crystal 16		
Ethanol	-8.65	-0.028
Acetonitrile	1.4	-0.002
Water	12.33	0.006

5.3 Infrared Spectroscopy Investigation into Solution State Structure

5.3.1 Polymorph Specific Structural Synthons in the Solid State

The link between the structural motifs in a solid and in the corresponding solution phase requires an understanding of the important building blocks within the crystal structure of the specific solute system. Figure 5-3 shows the unit cells for the two polymorphs of PABA, the beta and alpha phases, it can be seen that the stable beta phase is characterised by the formation of a 4 membered H bonding ring system.

Bond	Length / Å
1	3.045
2	2.754

Bond	Length / Å
1	2.642
2	2.984
3	2.61
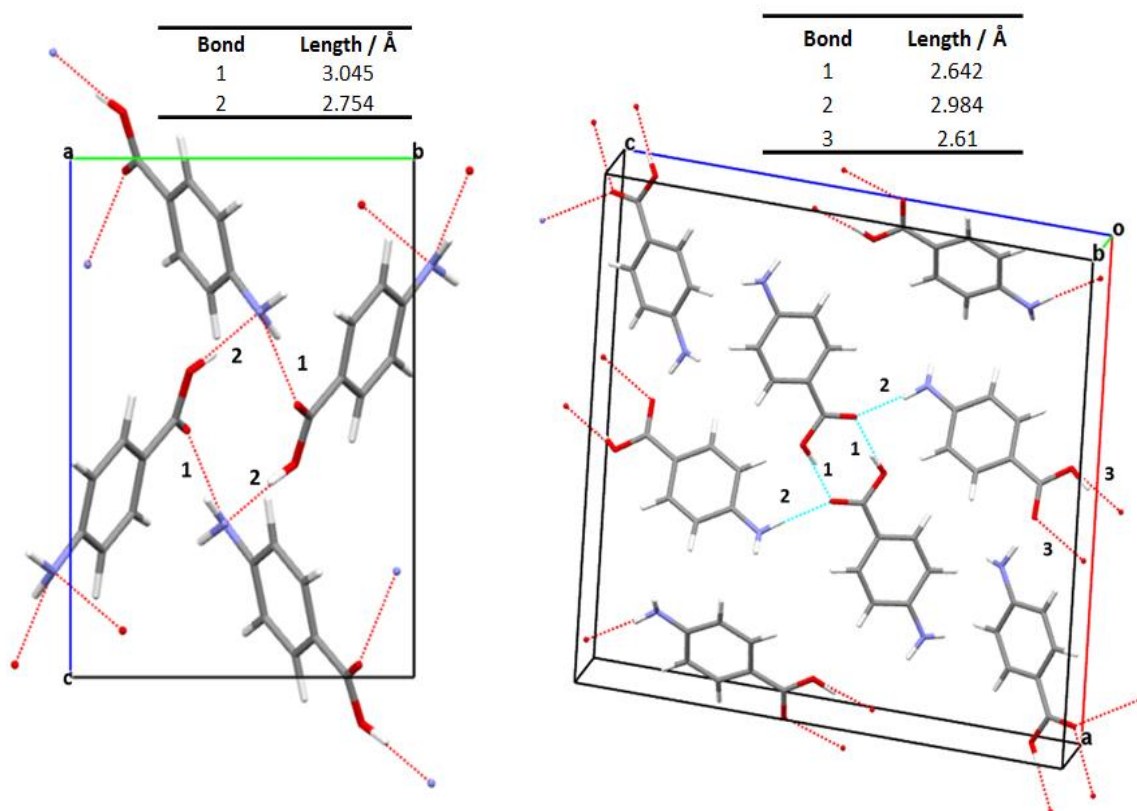
Figure 5-3 The crystal structures of the beta (left) and alpha (right) polymorphs of PABA highlighting the important intermolecular H-bonds which characterise the structure

The H-bonding ring is characterised by alternate H bonds between the amine proton and carbonyl oxygen, bond 1 in Figure 5-3 left, and between the alcohol proton and amine nitrogen, bond 2 in Figure 5-3 left, resulting in a more isotropic bonding environment. The crystal structure of the alpha polymorph is more directional in

141

nature and is characterised by two distinct R^2_2 (8) carboxylic acid dimers, formed by bonds 1 and 3. There is also a chain like motif of H bonds which runs through the alpha crystal structure formed between the amine proton and carbonyl oxygen, bond 2 in Figure 5-3 right. This initial analysis shows that the alpha structure is dominated by the formation of carboxylic acid dimers and the beta structure is not, hence a link between the structural building blocks in the solid state can be compared to observed structural motifs found in the solution state prior to crystallisation of a specific polymorph.

5.3.2 Solid State FTIR Spectroscopy
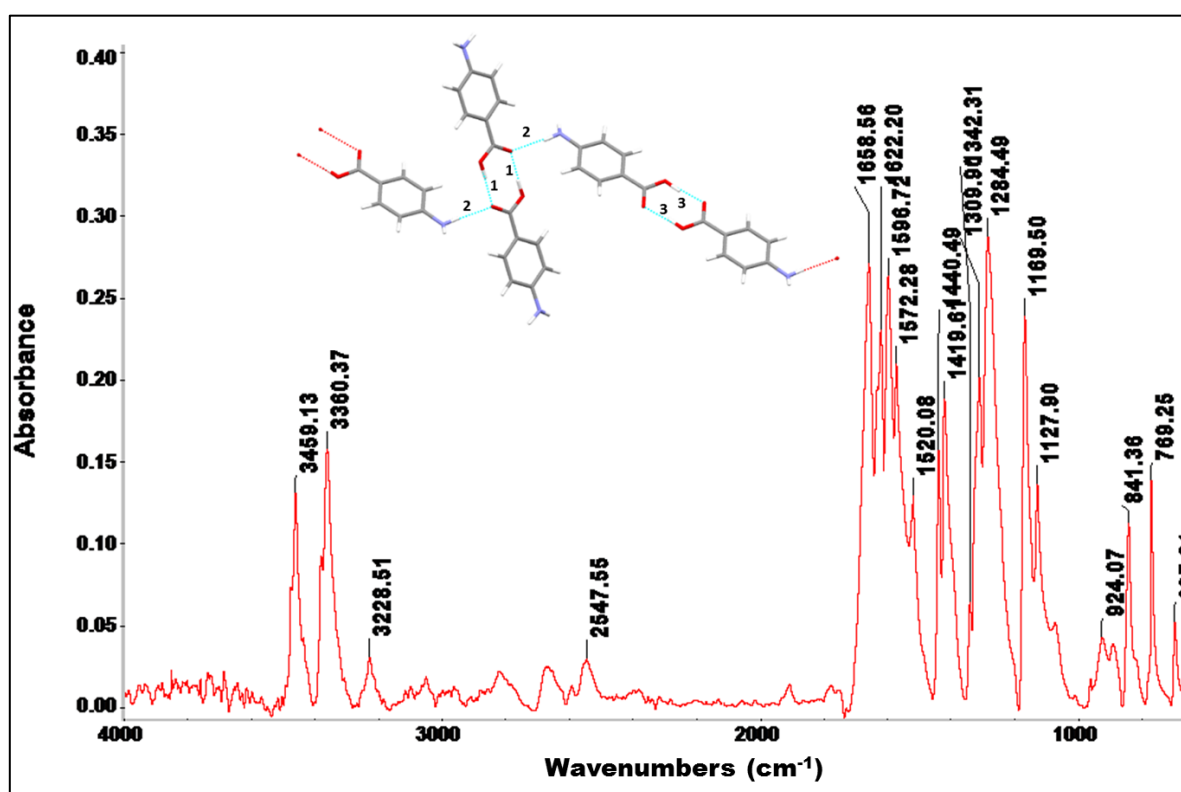
Figure 5-4 Solid state infrared spectrum of alpha PABA, inset the bonding environment within the unit cell of alpha highlighting the important H-bonding interactions

The solid state infrared (IR) spectrums of the alpha and beta polymorph of PABA were used as reference standards for comparison to the solution state spectra in ethanol and acetonitrile. The solid state spectra of alpha PABA is shown in Figure 5-4, as previously discussed the crystal structure of the alpha polymorph is characterised by the centrosymmetric H-bonding COOH dimer as well as N-H---C=O

H bonding interactions. The N-H region (3000 – 3500 cm^{-1}) of the spectrum is well characterised in the solid state, with the two peaks at 3459.13 and 3360.37 cm^{-1} corresponding to the symmetric and anti-symmetric N-H stretch of the non H-bonded amino group. The third peak at 3228.51 cm^{-1} is the H-bonded N-H stretch; this interaction is labelled as bond 2 inset in Figure 5-4, the H-bonding interaction has the effect of reducing the bond length and hence decrease the value of stretching frequency, hence a lower wavenumber.

The O-H stretching region is usually visible in the region of 2000 – 3500 cm^{-1} however in the case of alpha PABA this region is distorted with no characteristic peaks visible. This is usual for a carboxylic acid molecule such as PABA, however this is less helpful when trying to characterise the bonding environment relative to the acid group[9].

The region centred around 1700 – 1500 cm^{-1} highlights the existence of a carbonyl group, the band at 1658.56 cm^{-1} and the shoulder (easier to visualise in Figure 5-6) at ~1632 cm^{-1} indicate the symmetrical and anti-symmetrical vibrations of the carboxylic acid dimer, bond 1 in Figure 5-3 right. The band at 1622.20 cm^{-1} appears due to the carbonyl group participating in the N-H---C=O H bonding interaction, highlighted as bond 2 inset in Figure 5-3 right. The peak at 1596.72 cm^{-1}, indicates the presence of the aromatic ring in PABA.

The region which follows with the two sets of peaks 1440.49, 1419.61 cm^{-1} and 1309.9 and 1284.49 cm^{-1} are common bands indicative of either C-O in-plane stretching or O-H deformation vibrations, both of which are present in PABA[9]. The broad doublet centred around 924.07 cm^{-1} is due to the O-H wag, this region is usually used to indicate the presence of carboxylic acid dimers, with a broader band been the characteristic trend of an acid dimer. The position is also important and has been extensively studied with the usual position in the region of 960 – 875 cm^{-1}, dependant on the intermolecular interactions in the crystal structure[47,10,11,12,13,14].
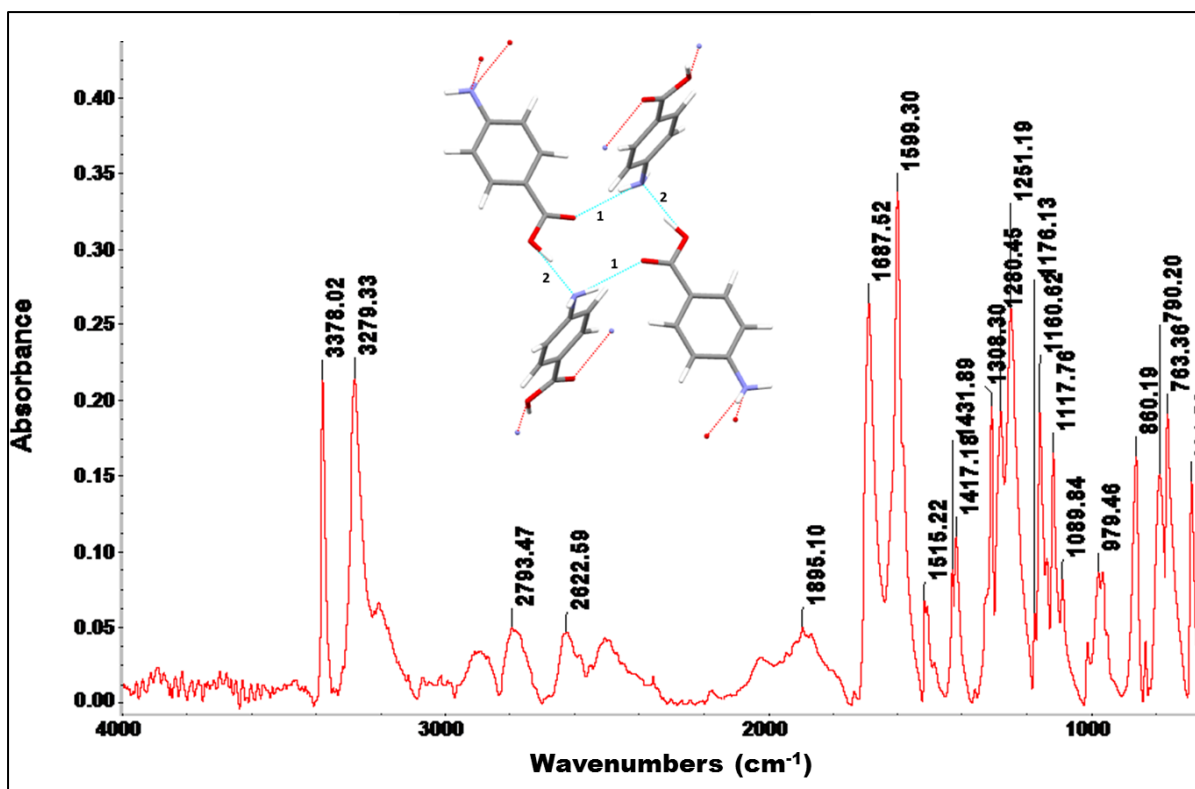
Figure 5-5 Solid state infrared spectrum of beta PABA, inset the bonding environment within the unit cell of beta highlighting the important H-bonding interactions

The solid state IR spectrum of beta PABA is shown in Figure 5-5 with the characteristic H-bonding ring structure highlighted inset with the important bonding interactions labelled. The N-H region (3000-3500 cm^{-1}) highlights the existence of two sharp bands at 3378.02 and 3279.33 cm^{-1} which are caused by the presence of the N-H symmetric and anti-symmetric stretch of the PABA molecule. It should be noted that these bands appear at lower wavenumber than in alpha PABA, due to the direct bonding between the amino and acid groups, bonds 1 in Figure 5-3 left, causing a shorter bond length hence lower wavenumber.

The O-H stretching region (2000–3500 cm^{-1}) contains a number of broad and distorted peaks which as in the alpha spectrum highlights the presence of a carboxylic acid group. The carbonyl region highlights a single C=O group 1687.52 cm^{-1}, as indicated in the crystal structure no carboxylic acid dimers are present and hence only a single carbonyl band is present. The peak at 1599.30 cm^{-1} is from the aromatic ring, the O-H region with the broad peak observed in the alpha spectrum is

not present in the beta spectrum and is indicative of a carboxylic acid dimer. This then could be one way of distinguishing between dimers and monomers in the solution state structure.
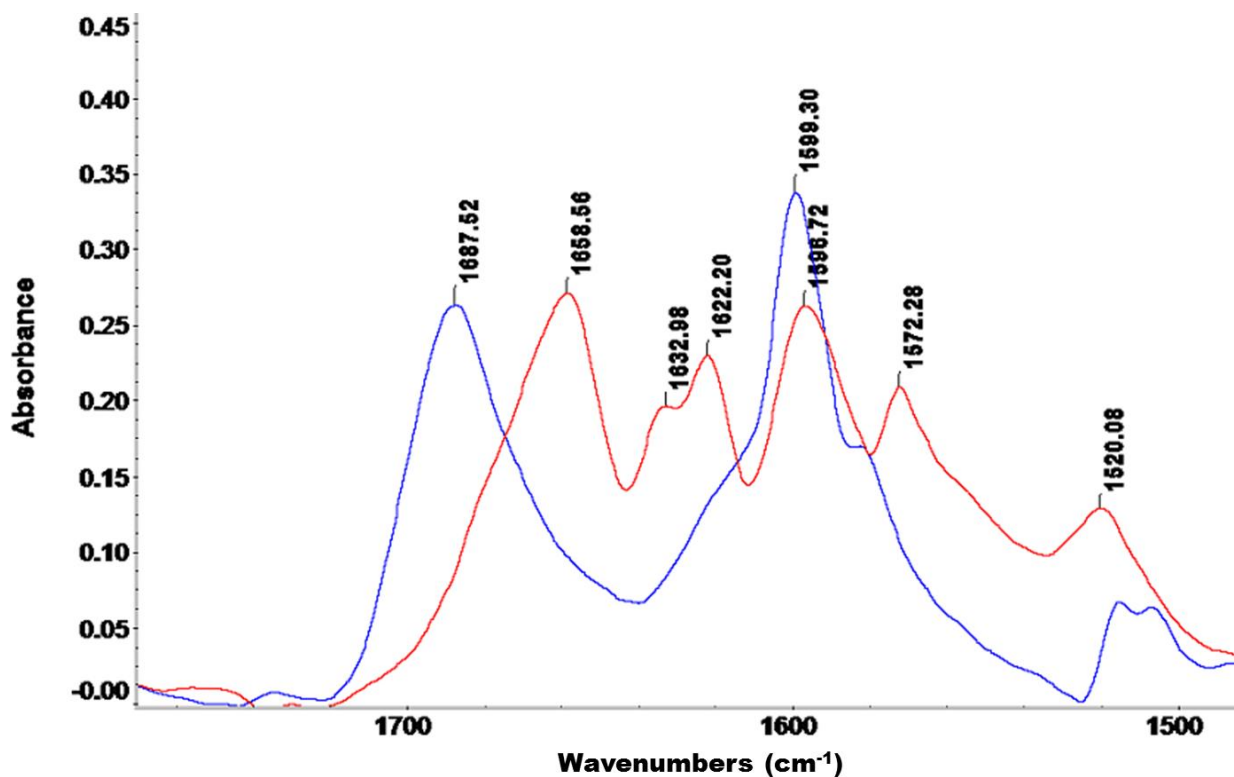
Figure 5-6 Comparison of the carbonyl region of the alpha (red) and beta (blue) IR spectra

Comparing between the two crystal structures of the alpha and beta polymorph, where the alpha form is dominated by formation of carboxylic acid dimers and beta by the H-bonding ring structure with no dimers, the two solid state IR spectrums could give an indication to possible solution state molecular self-assembly from the specific IR bands discussed. The carbonyl region, Figure 5-6, is of particular interest as it directly highlights the difference between a dimer and a monomer system, together with the O-H wag region at lower wavenumbers of ~930 cm^{-1}.

5.3.3 Solution State FTIR Spectroscopy

Solution state spectra were recorded at room temperature saturation in acetonitrile and ethanol in an attempt to determine if PABA self-associates in solution to form carboxylic acid dimers.
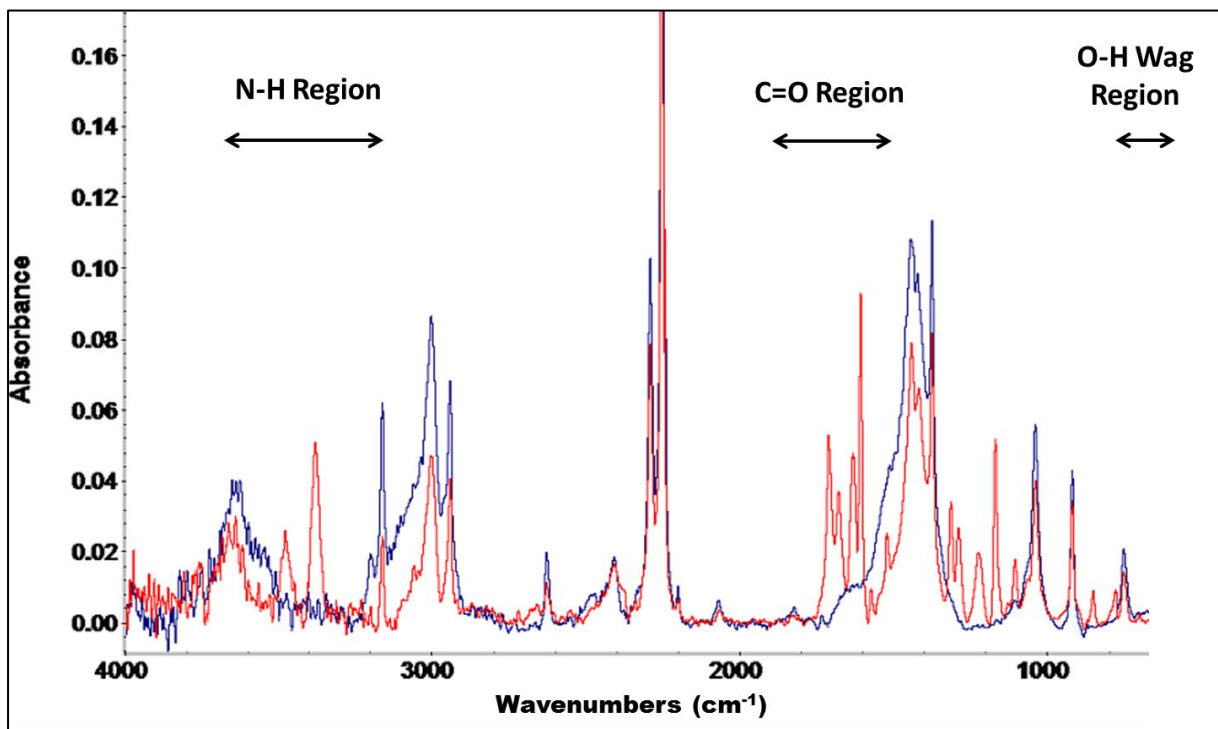
Figure 5-7 Solution state IR spectra of PABA saturated at room temperature in acetonitrile, PABA + acetonitrile (red) and acetonitrile (blue)

Figure 5-7 highlights the recorded solution state spectrum of alpha PABA saturated at room temperature in acetonitrile, the N-H symmetric and anti-symmetric stretching bands can be seen clearly and appear at 3477.24 and 3379.89 cm^{-1} respectively. In solution the molecules are solvated which causes the vibrational bands to shift to higher wavenumbers than in the solid state due to effective solvation by acetonitrile. Unfortunately the O-H wag region (860 – 960 cm^{-1}) is obscured by the solvent peaks and so a definitive characterisation of the dimer structure is difficult as usually this is a reliable 'fingerprint' peak of a carboxylic acid dimer.
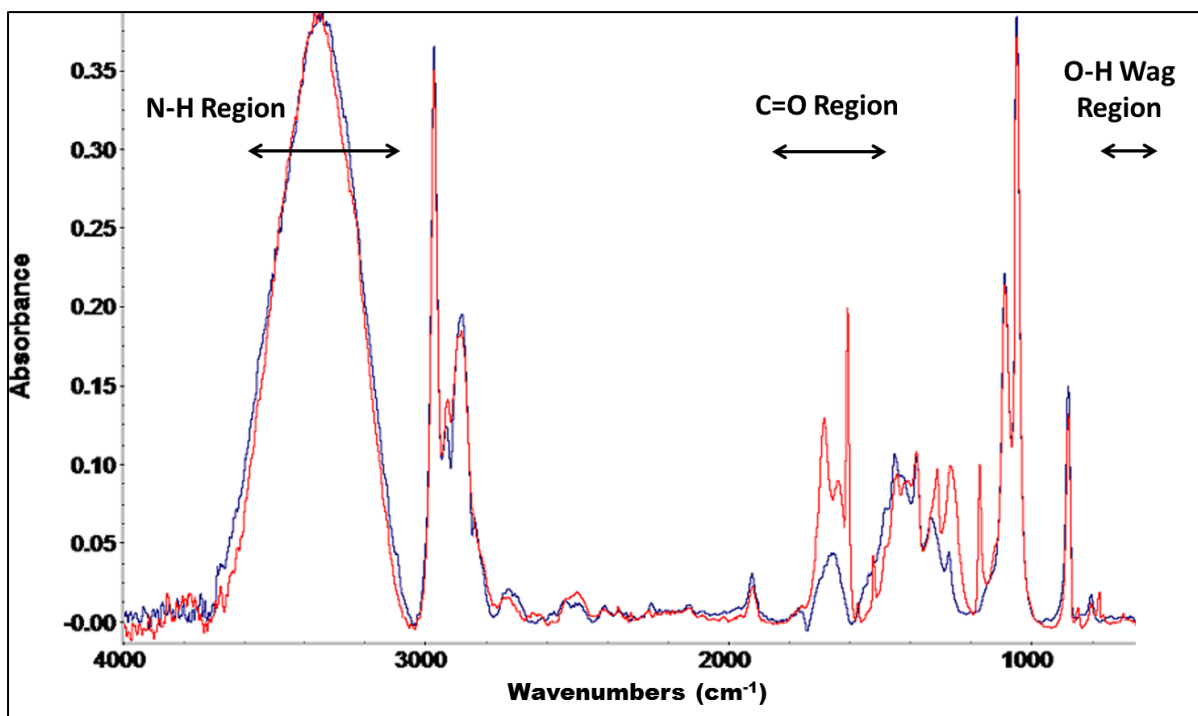
Figure 5-8 Solution state IR spectra of PABA saturated at room temperature in ethanol, PABA + ethanol (red) and ethanol at room temperature (blue)

Further to this the O-H stretching region 3000 – 2000cm^{-1} is also obscured by the solvent which further hinders the characterisation of the solution state structure of PABA in acetonitrile.

However the C=O region is well resolved with three vibrational modes at 1710.46, 1678.50 and 1633.09 cm^{-1}, the two higher wavenumber bands could represent two carbonyl environments due to their proximity to each other, within 40 cm^{-1} is the expected range for related C=O stretch, monomer and stretching, dimer frequencies.

This has been observed for a number of systems; Novak et al showed that the more effective solvation increases the C=O stretching frequency and hence the C=O stretching of a dimer structure is expected to lie at a lower wavenumber in comparison[15]. This doublet feature could indicate the presence of a solution state dimer structure as in a similar way to the doublet of carbonyl peaks in the solid state spectra of the alpha form. This has been seen in a number of carboxylic acid systems including benzoic acid[50].
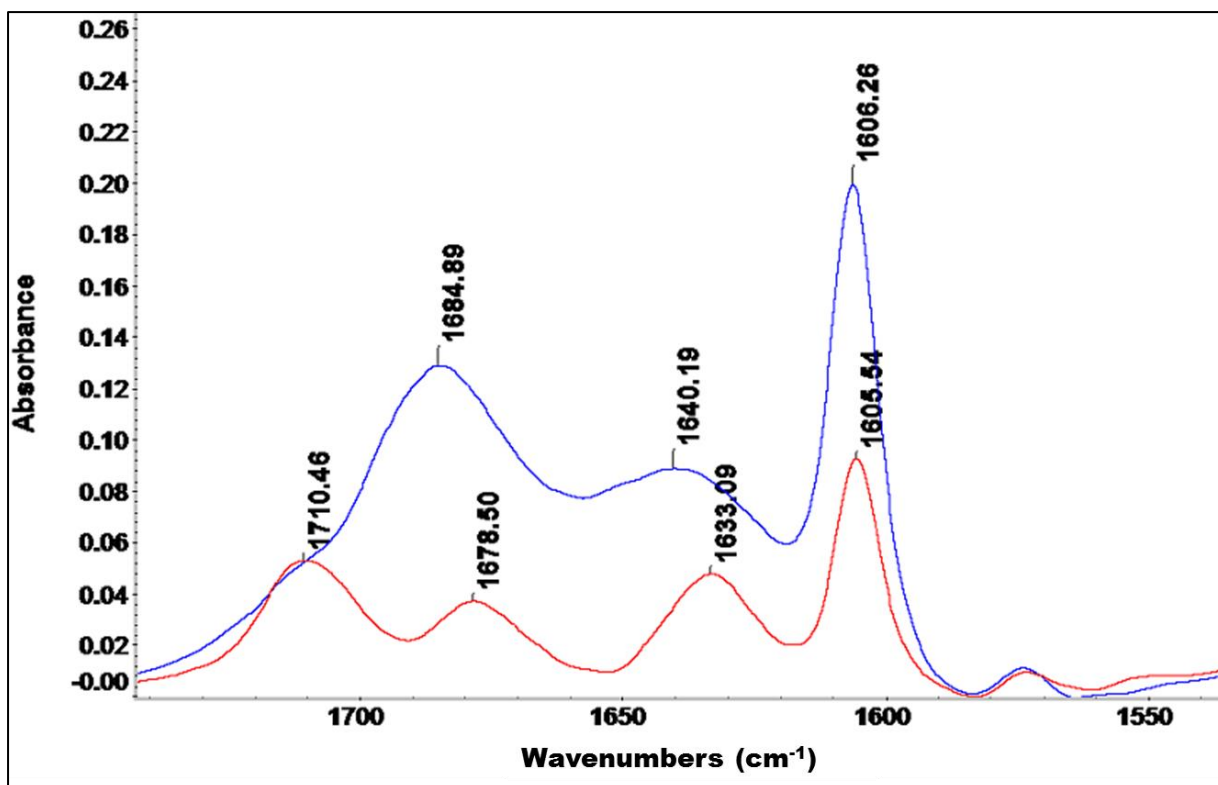
Figure 5-9 Comparison of the C=O regions in the IR spectra of alpha PABA in acetonitrile (red) and ethanol (blue) saturated at room temperature

The solution spectra of ethanol saturated at room temperature with alpha PABA together with the spectra of clean ethanol is shown in Figure 5-8. The N-H stretching region in ethanol is masked by the broad ethanol peak and so no information can be obtained regarding the solvation environment of the amino group.

Similarly to the acetonitrile data the O-H stretching and O-H wag regions are both obscured by the ethanol solvent peaks, this again makes determination of the solution structure more difficult. The C=O region is well defined in ethanol with peaks at 1684.69 and 1640.19 cm^{-1}, unlike the acetonitrile carbonyl region these two peaks are not within the expected 40cm^{-1} wavenumber range and so are likely to be not representative a distribution of monomers and dimers. The band at 1606.26 cm^{-1} is due to the aromatic ring of PABA.

Table 5-4 List of major the FTIR band shifts (cm^{-1}) in the solid state and solution state of PABA

	N-H		O-H		C=O		O-H Wag
alpha Solid	3459.13	3360.37	2800-2500	1658.56	1632	1622.2	924.07
beta Solid	3378.02	3279.33	2800-2500	1687.52	-	-	-
Ethanol	masked	masked	masked	1684.89	1640.19	-	masked
Acetonitrile	3477.24	3379.89	masked	1710.46	1678.5	1633.09	masked

In summary, the PABA spectra from saturated acetonitrile solutions seems to show two distinct bands in the C=O region which lie within 40 cm^{-1} of each other. This would suggest the existence of a population of dimers and solvated monomers present in the solution, however it should be noted that the O-H wag region is masked by the solvent peaks hence making complete assignment difficult.

The carbonyl region of the PABA spectra in ethanol seem to show two peaks also, however in this case the bands are sufficiently far apart >40cm^{-1} to suggest that this may be due to a single C=O species. Given that the first carbonyl band in ethanol is at 1684.89 cm^{-1} compared to 1710.46 cm^{-1} in acetonitrile, see Figure 5-9 for comparison, this could indicate that in ethanol the PABA molecules are solvated resulting in a longer bond length and lower wavenumber. However like the acetonitrile spectra the O-H wag region is sufficiently masked by the solvent and so any conclusions should be taken with caution, these bands for both solid forms and the solution state spectra are highlighted in Table 5-4.

5.3.4 FTIR Spectroscopy Dilution Experiments

To further investigate the solvation environment and any possible molecular self-assembly of PABA in solution, a number of dilution experiments in acetonitrile and ethanol were carried out. The focus of these experiments was the C=O band positions, as discussed in Section 5.3.3, to monitor any shifting, splitting or intensity fluctuations in the C=O stretching vibrations as a function of sample dilution.
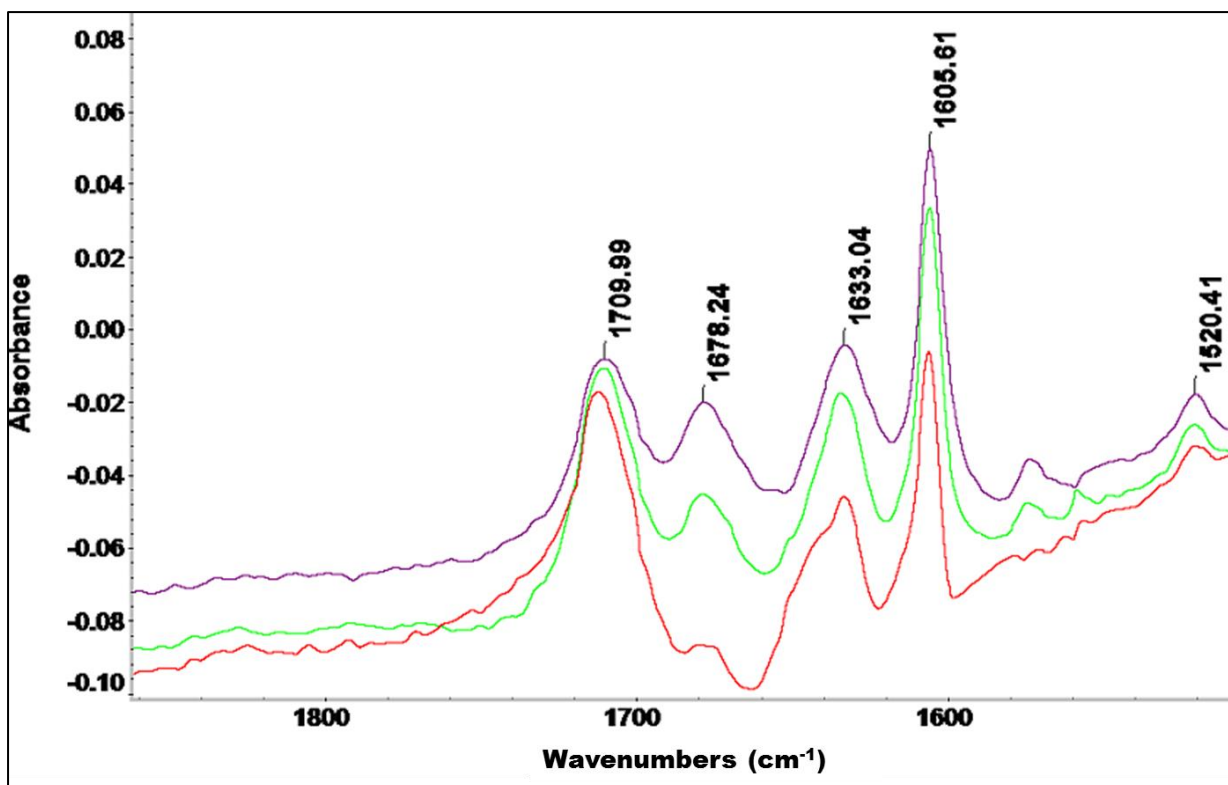
Figure 5-10 IR spectra of PABA in acetonitrile at room temperature saturation (purple), at 60 g/kg (green) and at 55 g/kg (red)

Figure 5-10 presents the IR spectra for the dissolution experiment carried out in acetonitrile, the first concentration was acetonitrile saturated at room temperature, followed by 60 and 55 g/kg, this is equivalent to saturation at 18 and 15 °C respectively. As can be seen in Figure 5-10 upon dilution of the acetonitrile solution, the C=O peak at 1678.24 cm^{-1} decreases in intensity relative to its neighbouring C=O peak at 1709.99 cm^{-1}. This seems to indicate that the peak at 1709.99 cm^{-1} is related to the solvated monomer C=O stretching vibration due to this intensity increase relative to the other C=O frequency.

This will likely be caused by H bonding between the C=O---H-Me caused by the induced dipole on the acetonitrile molecule. This dilution effect also seems to suggest that the peak at 1678.24 cm^{-1}, which decreases in intensity upon increase solvent concentration, is the carbonyl stretching of the carboxylic acid dimer C=O. Upon dilution the two peaks shift in intensity with the peak relating to the solvated monomer intensity increasing and the peak relating to the carboxylic acid dimer decreasing. This is a good indication that in relatively concentrated solutions of

PABA in acetonitrile there is a distribution of solvated monomers and carboxylic acid dimers of PABA.

Figure 5-11 presents the spectra relating to the dilution of PABA in ethanol with dilutions from saturation at room temperature to 130, 110 and 80 g/kg concentrations which are relative to saturation at 3, -3 and -17 °C respectively. There is a major C=O peak at 1684.05 cm^{-1} which lies in between the two C=O stretches of the solvated monomer and dimer peaks in the acetonitrile spectra, 1709.99 and 1678.24 cm^{-1} respectively.

This band may relate to the stretching carbonyl frequency of the solvated monomer of PABA and its position relative to the solvated carbonyl band of PABA in acetonitrile is, as expected, at a lower wavenumber due to more effective H bonding to ethanol. However the assignment of this band is hampered by the fact that upon dilution a small shoulder at the higher wavenumber side of this peak, ~1710 cm^{-1}, begins to appear.

This shoulder could represent the carbonyl stretch of the solvated monomer of PABA given that it is in a similar position to that of the same band in acetonitrile. This would indicate the lower wavenumber peak is related to the dimer structure of PABA and that a large percentage of molecules in ethanol self-assemble to form the dimer structural motif.
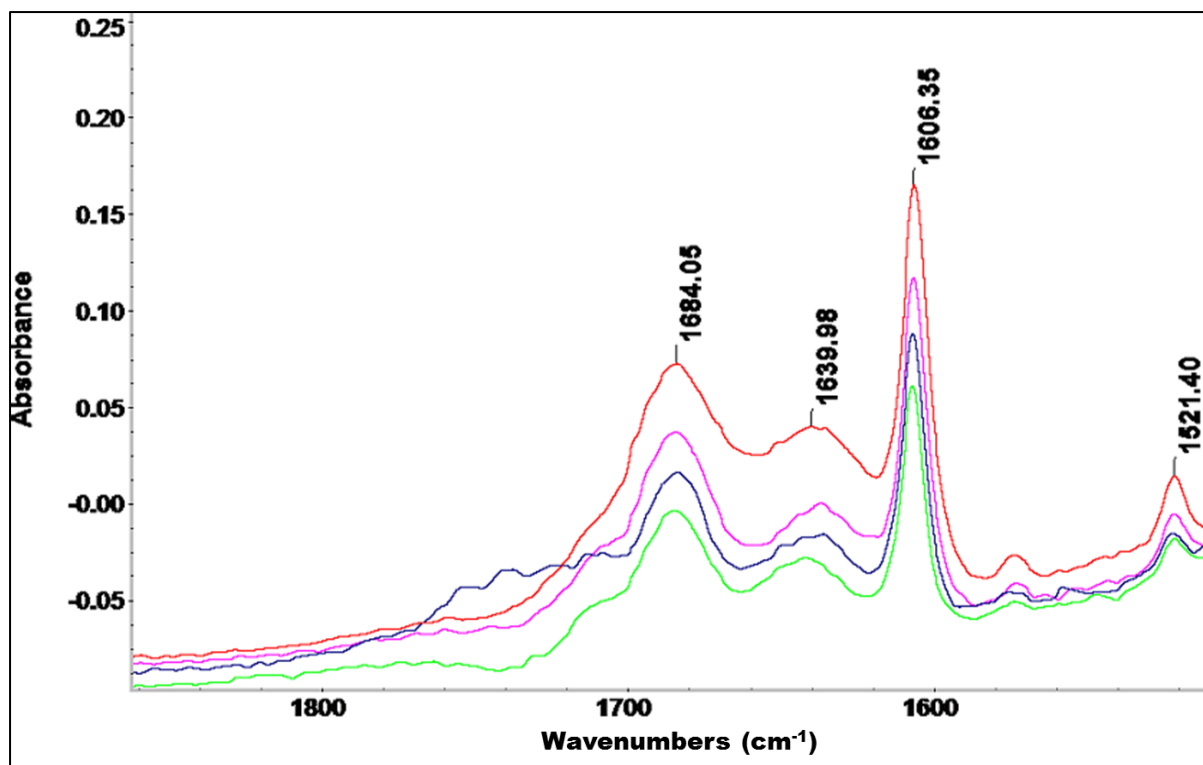
Figure 5-11 IR spectra of PABA in ethanol at room temperature saturation (red), 130 g/kg (pink), 110 g/kg (blue) and 80 g/kg (green)

5.3.5 In-Situ FTIR Spectroscopy Experiments

In-situ FTIR experiments were conducted to investigate the saturated solution state structure of PABA in acetonitrile and ethanol upon cooling of a saturated solution into the MSZW hence increasing super saturation and thus the driving force for molecular self-assembly. The degree of undercooling achievable varied between the two solvents and the recorded MSZW data using *in-situ* turbidity measurements is presented in Figure 5-12.

The data reveals that the recorded crystallisation temperature in the acetonitrile cooling experiment was 47.74°C and the saturation temperature was 51°C giving a recorded MSZW of 3.26°C. The crystallisation temperature recorded for the ethanolic cooling experiment was 44.89°C with a saturation temperature of 50°C giving a recorded MSZW of 5.11°C. At 0.1°C/min cooling this provided 51 spectra within the MSZW when using IR spectral collection times of 1 min.
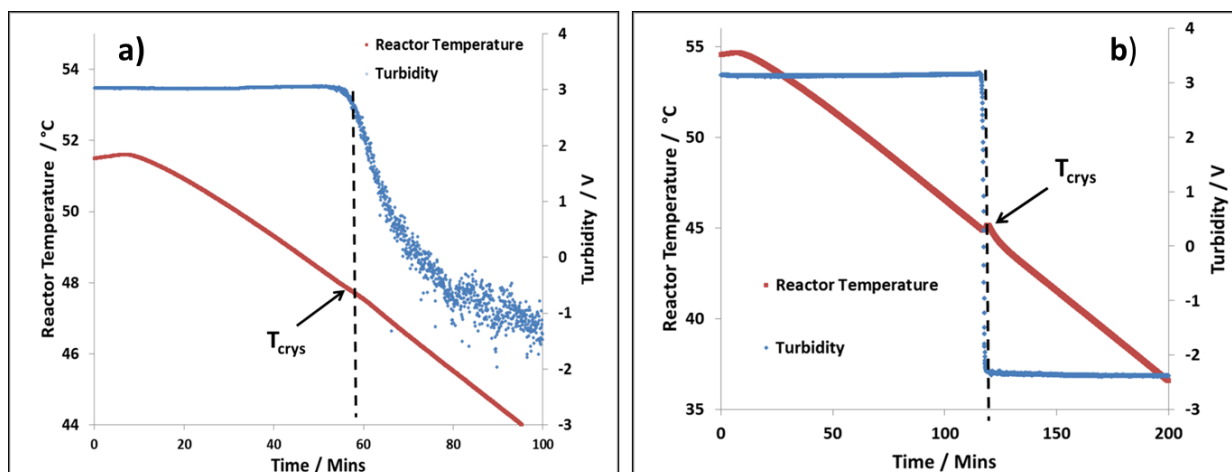
Figure 5-12 Reactor temperature and turbidity measurements during cooling crystallisations of PABA in acetonitrile a) and ethanol b). The crystallisation temperatures are highlighted

The FTIR spectra recorded during the cooling crystallisation experiment in acetonitrile are shown in Figure 5-13 as a 3D contour graph. The stretching frequencies of the carbonyl group relating to the solvated monomer and carboxylic acid dimer species respectively, 1709.99 and 1678.24 cm^{-1}, are well resolved and highlighted in the Figure. These two peaks seem to match well with the two corresponding peaks in the saturated solution state spectra, shown previously in Figure 5-9.

Upon cooling the solution there does not appear to be any significant peak shifting as highlighted by the contour map. However there is a distinct decrease in intensity around 100 minutes into the cooling process, this decrease in intensity is uniform across all of the IR bands in the spectrum. This decrease of intensity is due to the de-supersaturation of the solution post crystallisation as the crystallites formed grow in size and hence consume the solution saturation. The time of crystallisation from the turbidity measurements was found to be ~60 minutes into the cooling process and so this complements the observed decrease in intensity of the IR bands due to crystallite growth.
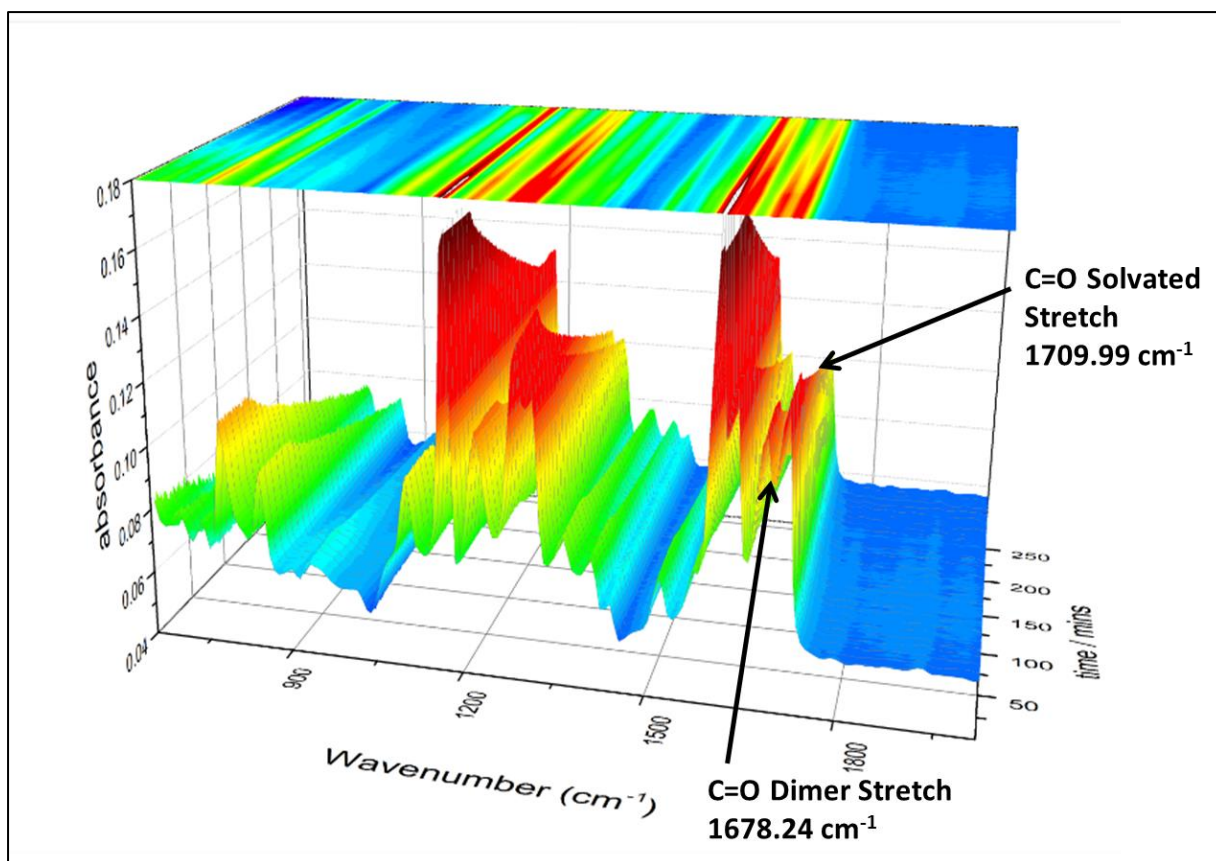
Figure 5-13 3D contour plot of FTIR spectra collected as a function of undercooling for the cooling crystallisation of PABA in acetonitrile

The stack plot in Figure 5-14a) shows the IR data recorded within the MSZW in acetonitrile, the carbonyl stretching frequencies are visible and comparable to the positions in the recorded solution state spectra at room temperature in Figure 5-9. There is an obvious change between the two carbonyl bands in the recorded MSZW data however; the ratio of the intensity seems to have increased to almost 1:1 in these experiments when compared to the room temperature data in Figure 5-12a).

The carbonyl stretching frequency relating to the solvated monomer has increased in intensity to around the same intensity as the dimer carbonyl stretching frequency, indicating the population of carboxylic acid dimers has increased when increasing from room temperature saturation to 50°C saturation. This is not unexpected as more molecules of PABA are dissolved in solution and so the effective driving force for self-assembly increases. The IR spectra also show that even at very high saturation temperatures there is still a large population of PABA molecules which are

in the monomer solvated state. This intensity ratio also does not seem to change dramatically during the cooling the process or post crystallisation and so assigning the growth unit in acetonitrile to the solvated monomer or the carboxylic acid dimer is not possible.
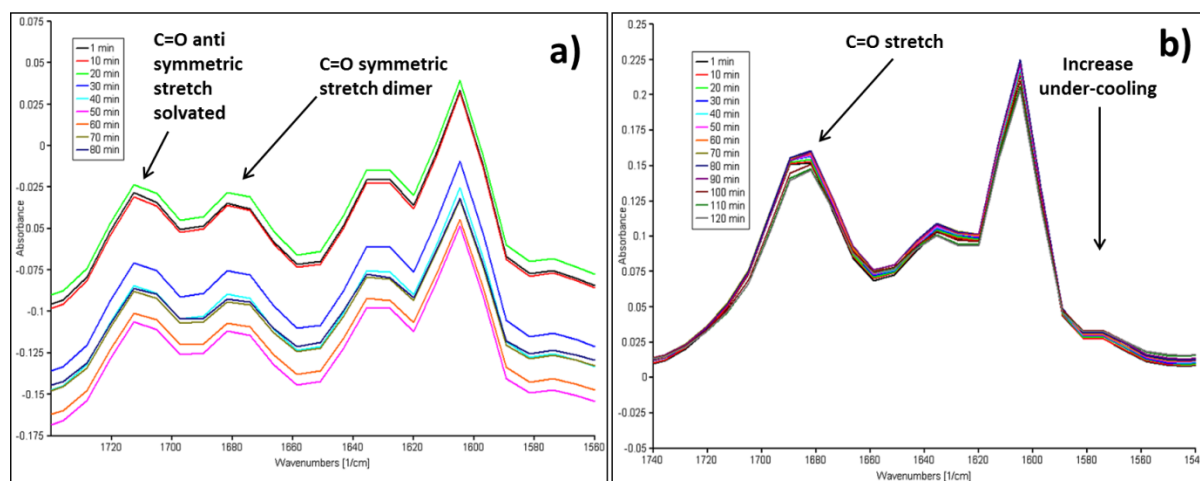
Figure 5-14 a) FTIR spectra of the carbonyl region as a function of undercooling for the cooling crystallisation of PABA in acetonitrile a) and ethanol b)

Figure 5-15 highlights the FTIR spectra recorded during the cooling crystallisation into the MSZW of ethanol, as was the case in acetonitrile the carbonyl stretching region is well defined in the spectra. Comparing to the solution state spectra recorded at room temperature in ethanol, presented in Figure 5-10, the carbonyl stretching frequency at 1684.05 cm^{-1} is visible. This IR band does not shift in position as indicated by the contour plot and the intensity begins to decrease at ~140 min, as in the acetonitrile experiment this intensity drop off is related to the de-supersaturation of the solution by growing crystallites post crystallisation at 120 minutes.
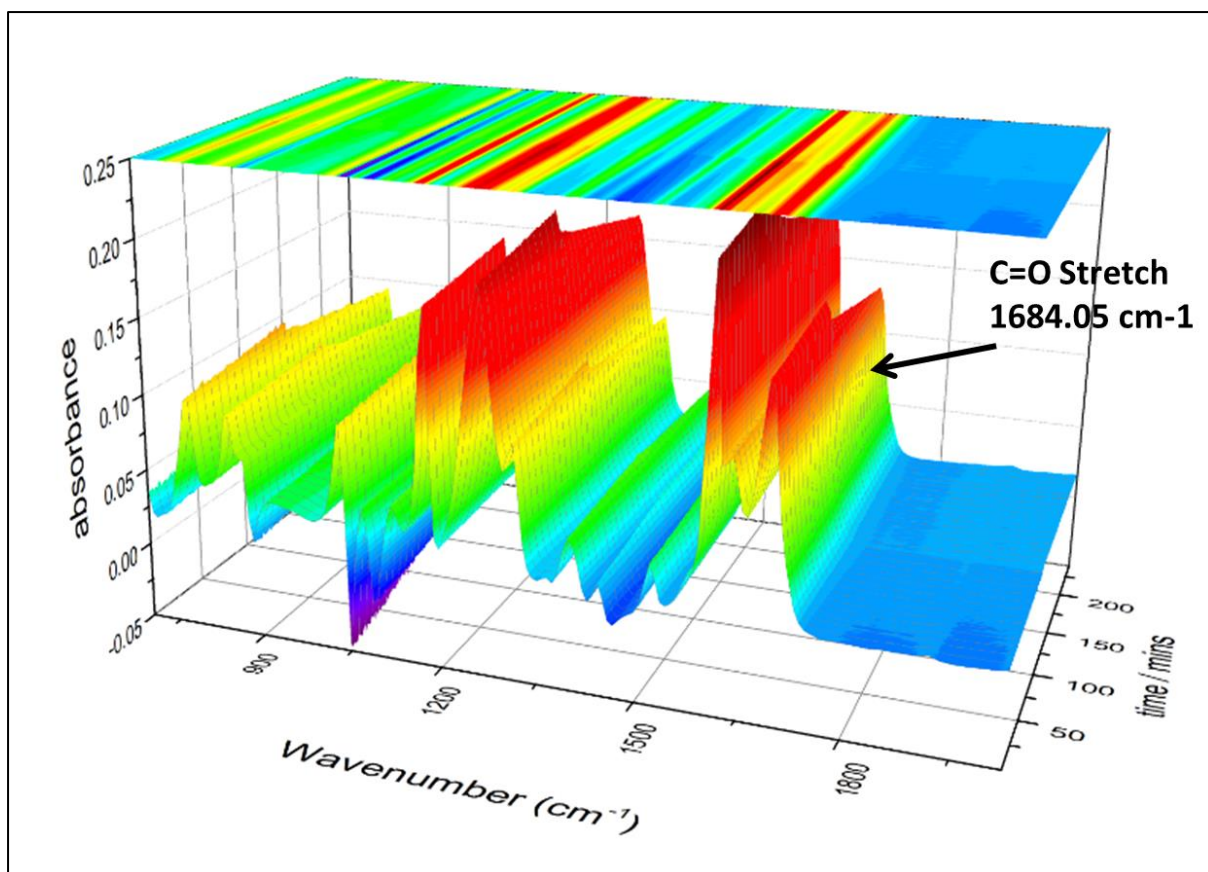
Figure 5-15 3D contour plot of FTIR spectra collected as a function of undercooling for the cooling crystallisation of PABA in ethanol

The carbonyl region is also shown in the stack plot in Figure 5-14b), the carbonyl stretching band does not shift in wavenumber but steadily decreases in intensity. The shoulder on the carbonyl peak that was visible in the solution state spectra in Figure 5-11 ~ 1710 cm^{-1}, which seemed to increase upon dilution is not visible in these spectra.

The reason for this is unknown however two possibilities are the decrease in spectral resolution for this instrument compared to the one used to collect the room temperature data. The second is that the solvated monomer population is very low in comparison to the self-assembled carboxylic acid dimers and so only the dimer stretching frequency is observed in the spectra. Overall any evidence for molecular self-assembly from these FTIR spectra in ethanol is not conclusive; this is mainly due to obstruction of the OH wag region by the solvent which prevents confident assignment of the carbonyl stretching band.

156

5.4 Molecular Dynamics Simulations of Solution State FTIR Spectroscopy

Calculated FTIR spectrums from molecular dynamics modelling of PABA in a continuum solvent model were performed to correlate differences in spectra between a monomer and a dimer of PABA. Figure 5-16 top, shows the calculated IR spectrums for PABA in a continuum of acetonitrile for both the monomer and dimer structural motifs, what can be seen is the major C=O stretching frequency for both the solvated monomer at 1753.21 cm^{-1} and the dimer at 1716.71 cm^{-1}. It can be seen from the spectra that the carbonyl stretch relating to the carboxylic acid dimer appears at a lower wavenumber when compared to the carbonyl stretch of the solvated monomer.
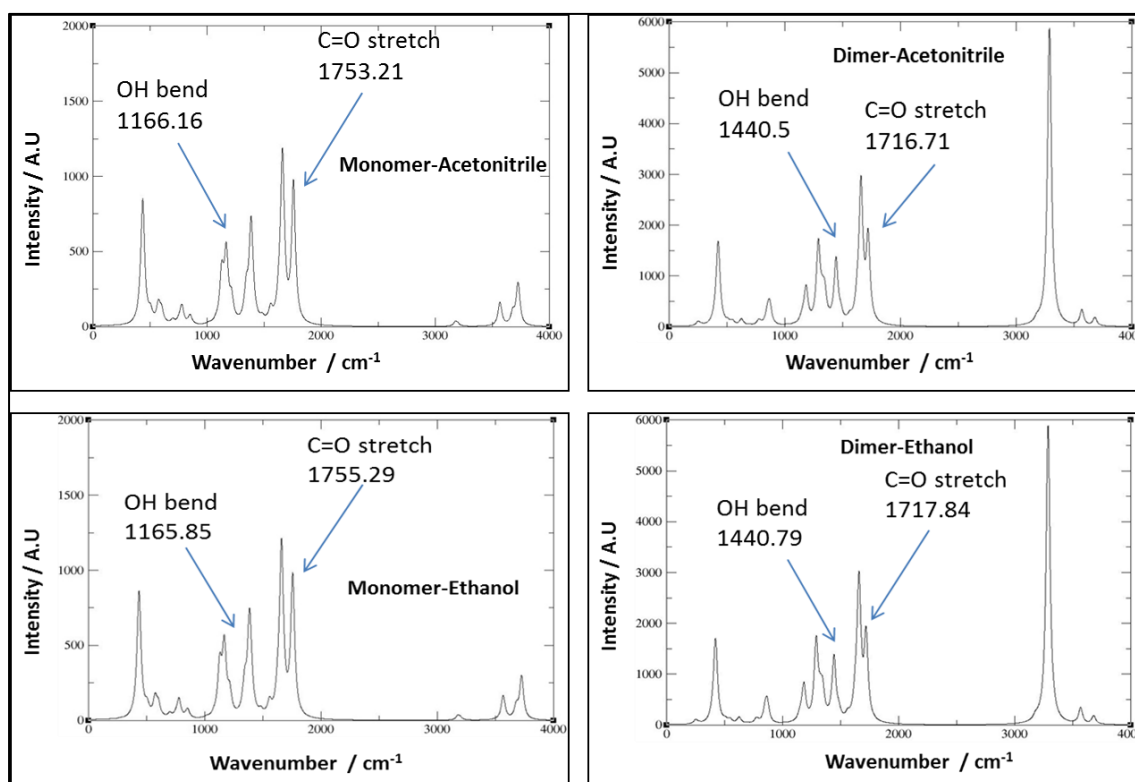
Figure 5-16 Calculated FTIR spectra of the two key structural motifs of PABA; the monomer structure and the carboxylic acid dimer structure in a continuum solvent model of acetonitrile and ethanol; calculations were performed by Dr Dimitrios Toroz University of Leeds

The case is also true for the two structural motifs in ethanol, Figure 5-16 bottom, where the carbonyl band of the carboxylic acid dimer appears at 1717.84 cm^{-1}

compared to 1755.29 cm^{-1} of the solvated monomer structure. This is expected due to the increase in delocalisation of electrons over the carbonyl group in the dimer structure creating a longer bond and hence a lower frequency when compared to the monomer structure.

This observation correlates well the experimental results described previously, where in acetonitrile solutions the band associated with the carbonyl stretching frequency of the solvated monomer was assigned at 1709.99 cm^{-1}, whereas the band related to the supposed dimer structure lies at 1678.24 cm^{-1}. Further to this the band shift related to these two peaks was 36.5 cm^{-1} in the simulation compared to 31.75 cm^{-1} in acetonitrile experiments which again correlates well and provides confidence in the band assignment for these spectra.

The case in ethanol shows the same trend in simulation however in the experimental data a clear splitting of peaks was not observed and as such a clear indication of solute-solute interactions cannot be concluded. However there is an appearance of a small shoulder on the higher wavenumber side of the peak at 1664.05 cm$_{-1}$. From the conclusions drawn above for the acetonitrile system and from the MD simulation in ethanol, this shoulder would be caused by the solvated monomer and hence the major peak at 1664.05 cm^{-1} would be related to the solute-solute dimer carbonyl stretch. This could indicate that the majority of solute molecules are dimerised in ethanolic solutions.

5.5 Conclusions

Solubility studies found that PABA has the highest solubility in the alcohols, ethanol and methanol, conversely the lowest recorded solubility was found to be in water followed by acetonitrile and ethyl acetate. The van't Hoff analysis suggested that solute-solute interactions are generally more favoured in solution than solute-solvent interactions, which led to the conclusion that molecular aggregation of PABA in solutions would be likely.

Analysis of the free energy of mixing suggested the entropy change on mixing in most solvents is a negative decrease indicating the possibility of solution pre-ordering in all solvents with the exception of water and water:ethanol mixes. This

further provided an early estimate for possible solute-solute interactions in PABA solutions.

The solid state FTIR results provided an understanding of the two key structural synthons found in the crystal structures of the alpha and beta polymorphs of PABA, the centro-symmetric carboxylic acid dimer and the four membered H-bonded ring system respectively.

Dilution experiments of acetonitrile solutions revealed the presence of a distribution of solvated monomers and dimerised PABA molecules in acetonitrile solutions. The case in ethanol upon dilution highlighted a small shoulder on the higher wavenumber side of the main C=O band in the spectra. This indicated the possibility of dimer formation where the shoulder represents the solvated monomer and the main band representing the dimer structure.

Experiments which explored the meta-stable zone of PABA in ethanol and acetonitrile at high concentrations found the same C=O bands as in other solution state spectra, however these bands did not shift in intensity ratio or position during increase in driving force induced by cooling the supersaturated solutions.

Overall these results have provided strong evidence that PABA has the ability to self-associate in saturated solutions from the calculated activity coefficients. This was confirmed using FTIR spectroscopy in acetonitrile solutions; this data provides a strong link between the solution state species present and the primary alpha structural synthon found in the crystal structure. This is a likely cause for the dominant crystallisation of the alpha crystal structure from solution and provides a basis of knowledge for further nucleation studies.

References

[1] R. A. Chiarella, A. L. Gillon, R. C. Burton, R. J. Davey, G. Sadiq, A. Auffret, M. Cioffi, C. A. Hunter, *Faraday Discuss.*, 2007, 136, 179

[2] S. Parveen, R. J. Davey, G. Dent and R. G. Pritchard, *Chem. Commun.*, 2005, 1531–1533

[3] A. Gavezzotti, G. Filippini*, Chem. Commun.*, 1998, 3, 287

[4] R. J. Davey, K. Allen, N. Blagden, W. I. Cross, H. F. Lieberman, M. J. Quayle, S. Righini, L. Seton, G. J. T. Tiddy, *CrystEngComm*, 2002, 4, 257

[5] R. J. Davey, G. Dent, R. K. Mughal, S. Parveen, *Cryst. Growth Des.*, 2006, 6, 1788

[6] H. Hao, M. Barrett, Y. Hu, W. Su, S. Ferguson, B. Wood, B. Glennon, *Org. Process Res. Dev.*, 2012, 16, 35

[7] I. Rosbottom, K. J. Roberts, R. Docherty, *CrystEngComm*, 2015, 17, 5768

[8] F. Martínez, C. M. Ávilaa, A. Gómez, J*. Braz. Chem. Soc.*, 2003, 14, 5, 803

[9] L. Bellamy, *The Infrared Spectra of Complex Molecules, Vol. 2. 3rd Ed.*, 1980, Springer

[10] M. M. Davies, G. B. B. M. Sutherland, *The Journal of Chemical Physics,* 1938, 6, 755

[11] D. Hadzi, N. Sheppard, *Proceedings of the Royal Society of London. Series A. Mathematical and Physical Sciences,* 1953, 216, 247

[12] M. S. G. Flett, *Spectrochimica Acta.,* 1962, 18, 1537

[13] R. G. Sinclair, A. F. McKay, R. N. Jones, *Journal of the American Chemical Society,* 1952, 74, 2570

[14] R. J. Davey, G. Dent, R. K. Mughal, S. Parveen, *Crystal Growth & Design,* 2006, 6, 1788

[15] P. Novak, D. Vikić-Topić, Z. Meić, S. Sekušak, A. Sabljić, *Journal of Molecular Structure*, 1995, 356, 131

Chapter 6 Nucleation Kinetics as a Function of Solvation Environment

The results of poly-thermal and iso-thermal studies are presented with the aim to derive the nucleation mechanism together with kinetic parameters from crystallisation data and relate them to solvation environment and solution chemistry.

6.1 Introduction

The solution chemistry of the solvent can strongly influence self-assembly, nucleation and growth rates and hence can impact on the morphology, habit and size distribution of particles in the resultant crystalline phase[1, 2, 3] Davey[4](1982) proposed that de-solvation rates of a solute molecule will be the rate limiting step for nucleation and crystal growth; this was recently highlighted by comparing the free energy of solvation of the carboxylic acid dimer of *p*-aminobenzoic acid (PABA) in various solvents to attachment frequency calculated from isothermal nucleation studies[5]. It is clear then that solution chemistry can change the interfacial energy at the liquid-solid interface, either of a cluster of molecules or a crystallite surface. However, further studies are required to link the solution chemistry to calculated nucleation kinetics of organic materials.

This chapter focuses on the alpha form of PABA which was investigated crystallising from binary solutions and employing three solvents; ethanol, acetonitrile and water. The aim was to identify the nucleation mechanism and characterise key nucleation and growth parameters, to compare the three different solvents in an attempt to understand how specific solvation environments direct the crystallisation of alpha-PABA.

6.2 Isothermal analysis

Induction time, *τ*, data were collected as a function of supersaturation, *S*, for the solution concentrations 200 and 180 g/kg of ethanolic alpha PABA solutions, and are presented in Table 6-1.

Table 6-1 Measured induction times (τ) and supersaturation ratios for ethanolic alpha-PABA solutions. 180g/kg and200g/kg solution concentrations were cooled to within the metastable zone at the holding temperatures stated

Holding Temperature (°C)	T(°K)	Average τ (s)	Equilibrium Conc (g/kg)	S (Supersaturation Ratio)
200g/kg				
30	303	3746	174.40	1.15
32	305	4780	180.29	1.11
33	306	5850	183.30	1.09
34	307	7700	186.37	1.07
180g/kg				
30	303	40260	174.00	1.03
28	301	8710	168.70	1.07
27	300	6083	165.90	1.08
26	299	3180	163.19	1.10
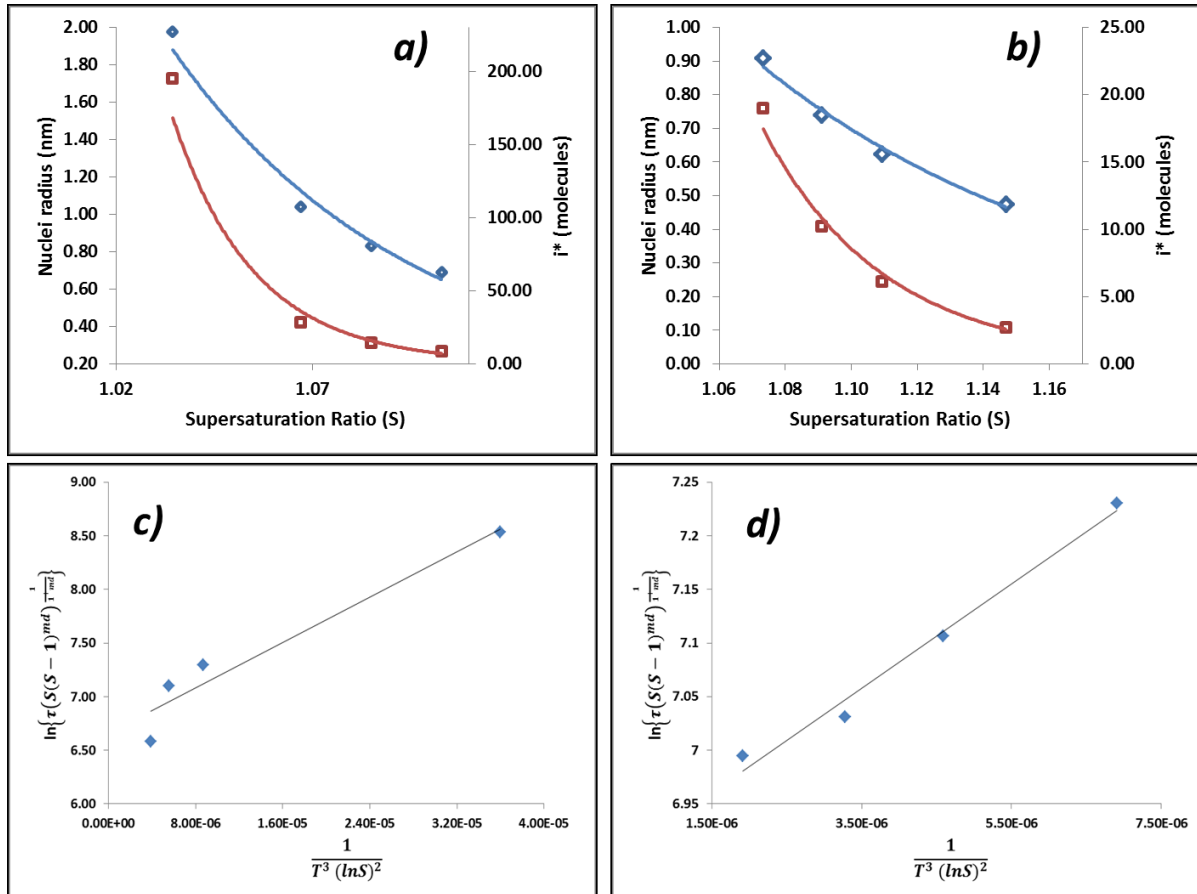
Figure 6-1 a) r* (blue) and i* (red) vs supersaturation for at 180g/kg concentration, b) r* (blue) and i* (red) vs supersaturation for at 200g/kg concentration c) Plot of the experimental induction time data to obtain SI$_{exp}$ for a solution concentration of 180g/kg and d) for the solution concentration 200g/kg

Interfacial tensions, γ_{eff}, were calculated for each concentration using Equation 2-39, and the calculated slope (SI$_{exp}$) from the linear relationship is equal to $\frac{16\pi\, v_0 2\, \gamma eff^3}{3(1+md)k^3}$. This linear relationship for the 180 g/kg concentration is shown in Figure 6-1c), where the fit to the data is represented by *y = 52935x + 6.6583*. Figure 6-1d) presents the corresponding fit to the 200 g/kg solution where the slope of the linear regression was found to be *y = 48641x + 6.8876*. The range of calculated values of *r** and *i**, from Equations 2-40 and 2-41, together with the slope of the linear fit and the resulting value of γ_{eff} for the two concentrations of ethanolic alpha-PABA solutions are presented in Table 6-2. The calculated values of *i** for the 180 g/kg solution shows increasing values from 8 – 195 molecules as a function of decreasing supersaturation, ranging from 0.10 – 0.03, and for the 200 g/kg solution the values are lower at 3-19 molecules, which is expected for a higher supersaturation. These

values are represented graphically in Figure 6-1a) and b) for a solution concentration of 180 and 200 g/kg respectively[6].

Table 6-2 Calculated values of r* and i* from the extrapolated values of yeff for ethanolic alpha-PABA solutions at the concentrations180 and 200 g/kg

Conc g/kg	SI_{exp}	R^2	y_{eff} (mJ/m^2)	r^* (*nm*)	i^* (molecules)
180	52935	0.94	0.85	0.69 - 1.98	8 - 195
200	48641	0.98	1.31	0.48 - 0.91	3 - 19

Sullivan et al[5] have recently reported calculated values of γ_{eff} for alpha-PABA in acetonitrile, 2-propanol and ethyl acetate to be in the range of 1.33 – 2.44, however the higher values in this case were calculated for a much larger range of supersaturations when compared to the range used in these experiments. The calculated interfacial tension and *r** values at 200g/kg shows good agreement to the calculated value of PABA in acetonitrile by Sullivan et al, where the supersaturation range is very similar in both studies, as such this provides some confidence to the data presented here. The low values of the calculated interfacial tension for the 180 g/kg solution are likely due to the low supersaturation range studied and hence the range of *r** values is large; 8-195.

A comparison to the interfacial tensions calculated in ethanol is provided by measurement of induction times of alpha PABA in water to give a contrasting representation of the solvation environment solution chemistry to observed nucleation kinetics. Table 6-3 provides the average measured values of τ over a range of supersaturations for 6 and 8 g/kg alpha PABA solutions.

Table 6-3 Measured induction times for 6 and 8 g/kg alpha PABA solutions in water.

Holding Temperature (°C)	T(°K)	Average τ (s)	Equilibrium Conc (g/kg)	S (Supersaturation ratio)
6g/kg				
25	298	41631	5.12	1.17
24.5	297.5	30990	5.01	1.20
24	297	24030	4.91	1.22
23	296	15405	4.71	1.27
8g/kg				
32	305	40260	6.84	1.17
31	304	8710	6.57	1.22
30	303	6083	6.30	1.27
29	302	3180	6.04	1.32

Figure 6-2a) and b) present the size of critical nuclei in nm radius and number of molecules for the two concentrations in water calculated from the derived interfacial tensions using the linear plots in Figure 6-2c) and d) to obtain SI_{exp}. The linear fit to the data were represented by $y = 848368x + 8.5945$ and $y = 1,537,652.27x + 6.96$ with R^2 values of 0.98 and 0.96 for 6 and 8 g/kg solutions respectively. The values of the calculated y_{eff} were found to be 2.36 and 2.60 mJ/m^2 and the values of r^* for a spherical nucleus were calculated as 0.71 – 1.08 nm and 0.74 – 1.31 nm for the solution concentrations 6 and 8 g/kg respectively, these calculated parameters are found in Table 6-4.
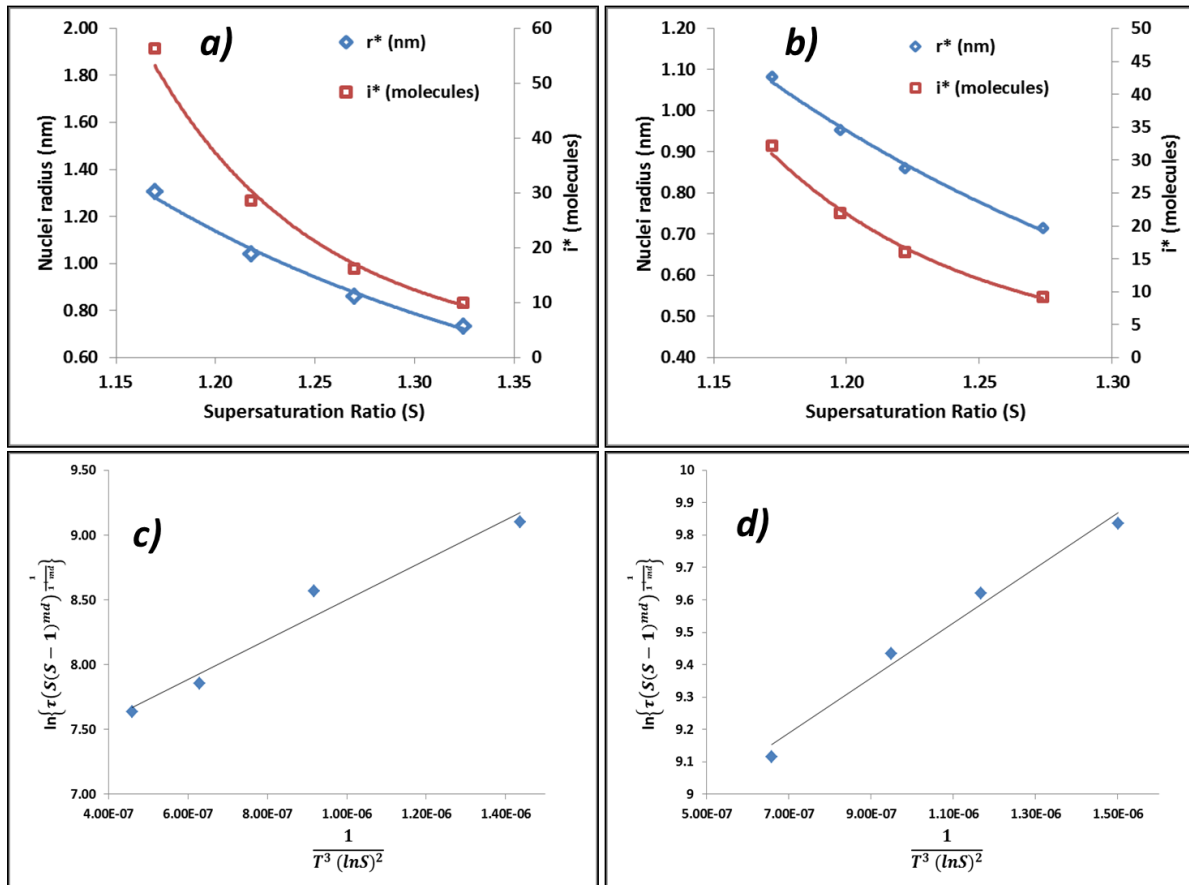
Figure 6-2 a) r* (blue) and i* (red) vs supersaturation for the 8g/kg concentration, b) r* (blue) and i* (red) vs supersaturation for the 6g/kg concentration c) Plot of the experimental induction time data to obtain SI_{exp} for a solution concentration of c) 8 g/kg and d) 6g/kg

The interfacial tension values calculated were found to be relatively similar in both concentrations of PABA - water solutions and so the calculated values of the critical nuclei are also very similar. Comparison to the y_{eff} values calculated in ethanolic solutions shows the values are higher in water however the size of the critical cluster sizes are relatively similar. The larger values of the y_{eff} in water could be caused by unfavourable solute-solvent interactions at the boundary layer between nuclei and solution, it is known from the solubility measurements in Chapter 5 that water solvates PABA very weakly whereas ethanol solvates PABA very strongly. This could cause the contrasting differences in the values of y_{eff} by contrasting more favourable interactions at the boundary layer of nuclei and solution in ethanol solutions.

Table 6-4 Calculated values of r* and i* from the extrapolated values of y_{eff} for alpha-PABA solutions at the concentrations 6 and 8 g/kg in water highlighting the regression values for the fit of Equation 2-39 to the raw data

Conc g/kg	SI_{exp}	R^2	y_{eff} (mJ/m^2)	r* (nm)	i* (molecules)
6	848368	0.98	2.36	0.71 - 1.08	9 - 32
8	1,537,652	0.96	2.60	0.74 - 1.31	10 - 56

6.3 Solution Thermodynamics and Meta-Stable Zone Width

The dissolution and crystallisation temperatures were determined from recorded turbidity vs time and temperature plots, the method for calculation of these parameters is provided in Section 2.4.7. An example of calculated ΔT_c with standard deviations for solutions in aqueous solutions at 8g/kg concentration is presented in Table 6-5. The full list of dissolution and crystallisation temperatures together with calculated ΔT_c values for all cooling rates in ethanol, acetonitrile and aqueous solutions can be found in the supplementary material.

Table 6-5 Average dissolution and crystallisation temperatures for alpha-PABA solutions in aqueous solutions at 8g/kg concentration with calculated standard deviations and critical undercooling

8g/kg Rate (°C/min^{-1})	Tdis (°C)	Tcrys (°C)	ΔTc
0.1	36.10 ± 0.61	30.22 ± 0.89	5.38
0.3	35.92 ± 1.87	28.30 ± 0.93	7.30
0.5	37.12 ± 0.58	27.10 ± 1.17	8.50
0.7	38.02 ± 1.38	29.64 ± 0.94	5.96
1	38.28 ± 0.93	25.62 ± 1.74	9.98
	$T_e = 35.58$		

Figure 6-3(a), (b) and (c) presents the dissolution and crystallisation temperatures for some selected concentrations of alpha-PABA solutions in ethanol, acetonitrile and aqueous solutions respectively, plotted as a function of cooling rate to obtain T_e and T_c.
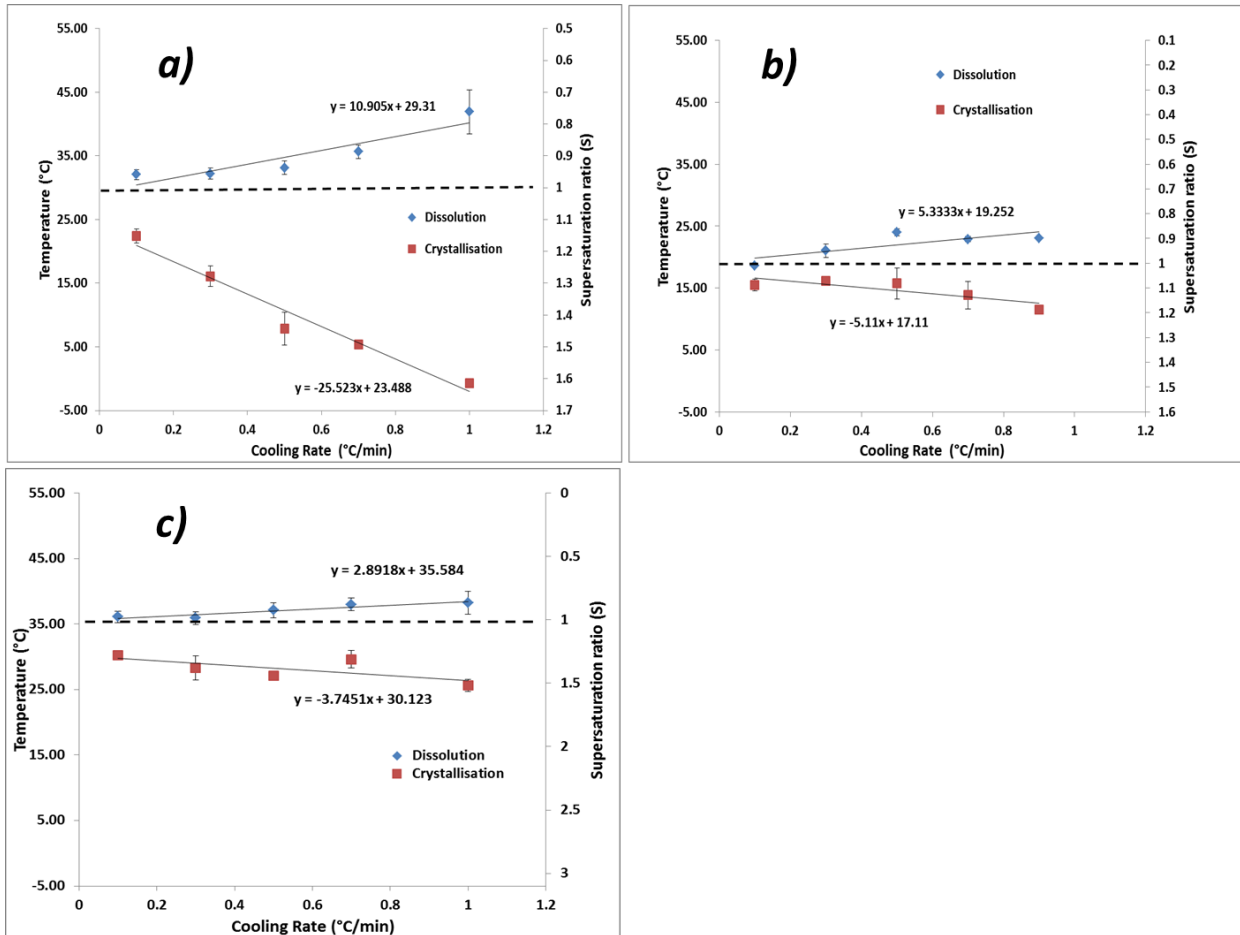
Figure 6-3 a) plot of T_{dis} and T_{crys} as a function of cooling rate and supersaturation recorded for a solution concentration of 170g/kg in ethanol b) plot of T_{dis} and T_{crys} as a function of cooling rate recorded for a solution concentration of 54g/kg in acetonitrile c) plot of T_{dis} and T_{crys} as a function of cooling rate recorded for a solution concentration of 8g/kg in aqueous solutions, dashed black lines indicate equilibrium solubility

The plots highlight the dependence of crystallisation and dissolution temperature on cooling rate. Interestingly ethanolic solutions of alpha-PABA show a high kinetic dependence on cooling rate for both crystallisation and dissolution, particularly crystallisation temperature indicated by the high value of the slope of the fitted linear trend to the data. Acetonitrile solutions were also found to exhibit some degree of kinetic dependence of crystallisation and dissolution on cooling rate, the slopes of the linear trends indicate this dependence was not as high as for ethanol but a cooling rate effect was observed. Analysis of crystallisation and dissolution

temperatures for aqueous solutions were found to vary little with cooling rate this indicating that from this solvent the process is more thermodynamically controlled with respect to the other solvents, as highlighted in the slopes of the linear trends fitted to the data.

Plots of super-solubility and solubility curves, as derived from extrapolation of T_e and T_c at 0°C/min cooling rate, indicate the effect of cooling rate on the MSZW for the three solvents. These plots can be found in the supplementary material.

The solubility of alpha-PABA in EtOH, ACN and aqueous solutions, from measured T_{dis} values, were plotted in van't Hoff coordinates and were presented in Chapter 5. The trend suggested that the ideality of the solution behaviour is in the order ethanol > acetonitrile > aqueous solutions which is consistent with an inverse relationship to the dielectric constant of the solvent[7], where aqueous solutions > acetonitrile > ethanol

Table 6-6 MD simulation results provided by Dr Dimitrios Toroz of solvation free energy calculated for a monomer of PABA in ethanol, acetonitrile and aqueous solutions respectively, for high and low concentrations given in molecular ratio, temperatures for the simulations were set at 293 °K in all solvents

Solvent	Molecular Ratio (PABA-Solvent)	ΔG_{solv} (kJ/mol)	Molecular Ratio (PABA-Solvent)	ΔG_{solv} (kJ/mol)
Ethanol	1/213	-58.5 +/-1.7	1/298	-53.5 +/-1.6
Acetonitrile	1/148	-54.5 +/-0.9	1/317	-52.9 +/-1.0
Aqueous solutions	1/1902	-42.4 +/-1.2	1/4000	-43.9 +/-1.7

The values of the enthalpy of solvation, ΔH_{solv}, provided in Table 2-2 in Chapter 2 indicate that at saturation the solvation enthalpy in ethanol is -95.4 kJ/mol and -74.4 kJ/mol in aqueous solutions; this can also be interpreted as the energy required to de-solvate a molecule of PABA at saturation and is higher in ethanol than in aqueous solutions. This trend is further supported by the calculated values of free energy of

solvation, $\Delta G_{solv,}$ from MD simulations at two concentrations presented in Table 6-6. The value of ΔG_{solv} at the lower concentration in ethanol is -53.5 kJ/mol and -41.0 kJ/mol in aqueous solutions, and so de-solvation of PABA in the three solvents follows the trend of most energetically favourable; aqueous solutions > acetonitrile > ethanol.

At the higher concentration this trend remains the same, however, the ΔG_{solv} was calculated as -58.5 kJ/mol in ethanol which indicates that an increase of solution concentration in ethanol results in a larger increase in the de-solvation energy when compared to aqueous solutions. The ΔG_{solv} in aqueous solutions at higher concentrations was calculated as -42.4 kJ/mol, and de-solvation in aqueous solutions is energetically more favourable when increasing solution concentration.

6.3.1 Cooling Rate Influence on Crystallisation Temperature

The crystallisation temperatures recorded as a function of cooling rate in each of the three solvents were plotted in vant' Hoff coordinates to highlight the kinetic effect of cooling rate upon the crystallisation temperature. These are presented in

Figure 6-4 and also indicate the equilibrium solubility and ideal solubility.

The Figures show that for the case of the aqueous and acetonitrile solutions the slopes of the crystallisation curves as a function of cooling rate are parallel and so there is no significant influence of cooling rate on crystallisation. However when compared to the case in ethanol it can be seen that the slope of the crystallisation temperature plots changes dramatically with increasing cooling rate. Although no real thermodynamic parameters can be drawn from these plots, unlike for solubility data where a value of ΔH_{diss} can be extrapolated from the slope, it is still interesting to see the effect of cooling rate on crystallisation temperatures in vant't Hoff coordinates.
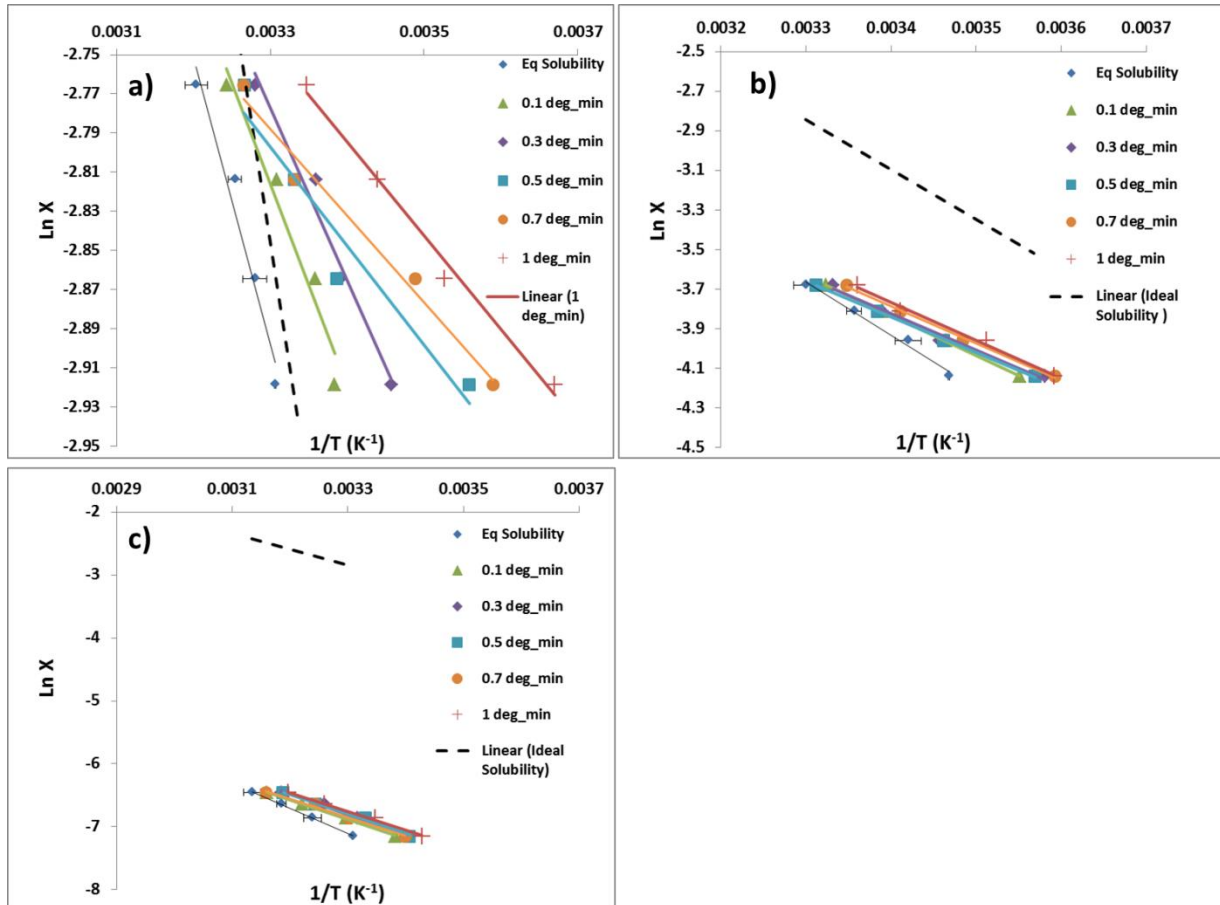
Figure 6-4 Kinetic van't Hoff plots of crystallisation temperatures as a function of cooling rates with comparison to the ideal and equilibrium solubility for PABA crystallisations in a) ethanol b) acetonitrile and c) aqueous solutions

The case of thermodynamic parameters could hypothetically be applied to these plots whereby the slope of the curves would indicate an enthalpy related to crystallisation i.e. ΔH_{crys} which could be thought of as a rough estimate of the enthalpy barrier to crystallisation. Considering this hypothetical situation, this would indicate that as the slopes of the curves decrease with increasing cooling rate in ethanol solutions, the enthalpic barrier to crystallisation decreases also. This is seen above 0.5 °C/min cooling rate and possibly indicates that when higher cooling rates are applied to more concentrated solutions and where higher supersaturations can be reached, the mechanism of crystallisation changes which alters the thermodynamic parameters associated with the process. The opposite is true for aqueous and acetonitrile solutions whereby cooling the rate has no effect on the slopes of crystallisation curves and hence the hypothetical parameter of $\Delta H_{crys.}$

Considering these observations it is also interesting to note that the ideal solubility line in ethanol is very close to the equilibrium solubility and hence the crystallisation temperatures. The opposite is true in the case of aqueous and acetonitrile solutions, combining this with the cooling rate effect on crystallisation temperatures, it seems that a solution which is further from ideality will not have as much kinetic influence on crystallisation parameters.

The closer to ideality the more of a kinetic effect is observed on crystallisation parameters as in the case of ethanol. This may be due to the stability of PABA in the solvents, for example in water solubility is low and the non-polar benzene ring is not stabilised by the very polar nature of water this results in a lower barrier to de-solvation as highlighted in the more positive simulated values of $\Delta G_{solv.}$ This case is the opposite in ethanol and so this could lead to the case where larger undercooling can be reached and higher supersaturations are achieved, the mechanism by which crystallisation proceeds can change due to the increase stability of PABA in ethanol.

This could be thought of as a concentration effect with the possibility of the system behaving not dissimilar to a colloidal one where large density fluctuations of solute exist in the supersaturated state changing the pathway to crystallisation.

6.4 Optical Analysis of Recovered Crystallites

It was observed that the size of the crystallites recovered from the poly-thermal crystallisations seemed to vary between the three solvent systems. Initial optical analysis was carried out and the results are highlighted in Figure 6-5 which indicates that crystals recovered from ethanol and acetonitrile are generally larger than those recovered from aqueous solutions.

Figure 6-6a) shows the crystallite length distributions from Morphologi G3 optical analysis (smoothed over 100 measurements) of the crystals recovered from cooling crystallisation experiments at a standard supersaturation of S = 1.2. As can be seen, the scattering of crystallite length data in aqueous solutions manifests a log normal distribution. The length distribution mean values in Table 6-7 were found to be 37.25 µm in aqueous solutions compared to 90.64 µm in acetonitrile and 113.11 µm in ethanol. This is also represented in the length distributions; d0.1, d0.5 and d0.9,

where the distribution of crystallite length has a smaller mean value in the crystallites recovered from aqueous solutions in comparison to ethanol. For example crystallite length d0.9 in ethanol is considerably larger, 262.90 µm, when compared to the same distribution in aqueous solutions at 92.60 µm. The measured d0.9 value in acetonitrile is found to be 247.63 µm indicating although there is a distribution of shorter crystallites there are also some relatively large crystallites almost comparable to those found in ethanol.
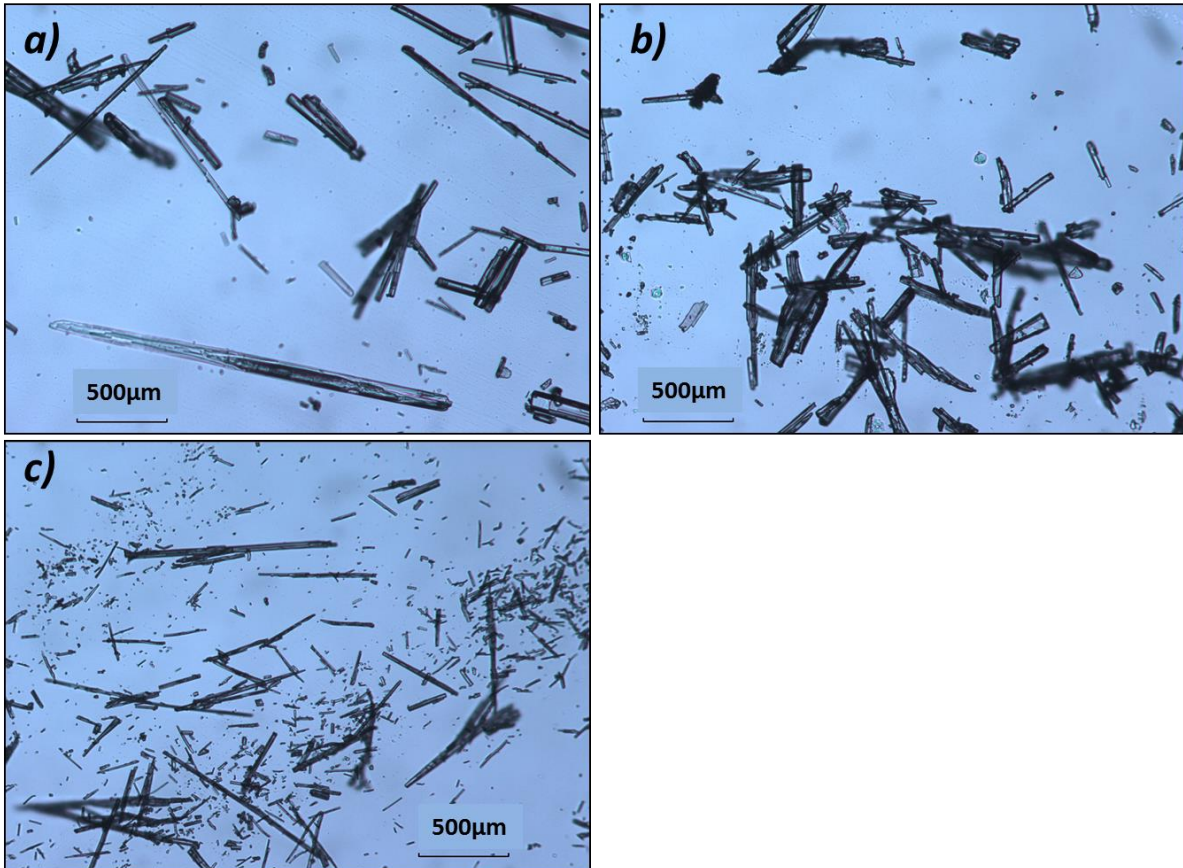
Figure 6-5 Micrographs of crystals recovered from poly-thermal cooling experiments from a) ethanol, b) acetonitrile and c) aqueous solutions
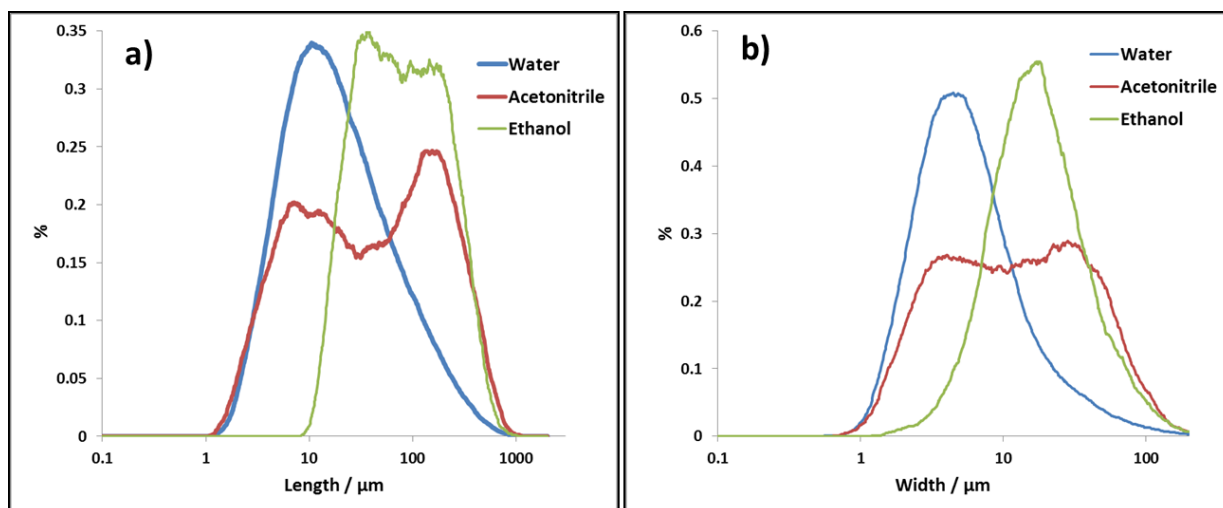
Figure 6-6 a) Length and b) crystallite width distributions of crystallites recovered from cooling crystallisations at supersaturations S=1.2 using optical analysis.

Table 6-7 Results of optical analysis of crystallites recovered from cooling crystallisations in ethanol aqueous solutions and acetonitrile, highlighting the measured crystallite length distributions and width distributions

Solvent	Mean Length µm	Length µm d0.1	Length µm d0.5	Length µm d0.9
Ethanol	113.11	23.26	72.94	262.90
Acetonitrile	90.64	4.60	40.01	247.63
Aqueous solutions	37.25	4.98	14.89	92.60

Solvent	Mean Width µm	Width µm d0.1	Width µm d0.5	Width µm d0.9
Ethanol	23.13	7.15	16.64	45.91
Acetonitrile	21.39	2.54	11.91	51.08
Aqueous solutions	9.06	2.26	5.06	17.27

Figure 6-6b) presents the analysis of the crystallite width distribution, the mean width in ethanol, 23.13 µm, is slightly higher than the mean value in acetonitrile solutions of 21.39 µm, in comparison the aspect ratio in aqueous solutions is notably smaller, 9.06 µm these values are provided in Table 6-7.

This analysis affords quantitative support of the observation that crystallites recovered from acetonitrile and ethanol are generally wider than those that grow in aqueous solutions, where larger width distributions are observed in these solvents. This can also be seen in the micrographs taken from the optical analysis in Figure 6-7 which indicates that the crystals recovered from ethanol are generally longer along the needle axis with the crystallographic surfaces more clearly defined particularly when compared to crystals grown in aqueous solutions.

The crystallites recovered from acetonitrile are generally crystallographically well defined but also wider than the crystals recovered from aqueous solutions which usually present shortened needle like crystals with less defined facets. It should be noted that caution should be exercised with over interpretation of the size data mindful of the potential of inter-particle attrition in the crystallisation vessel.
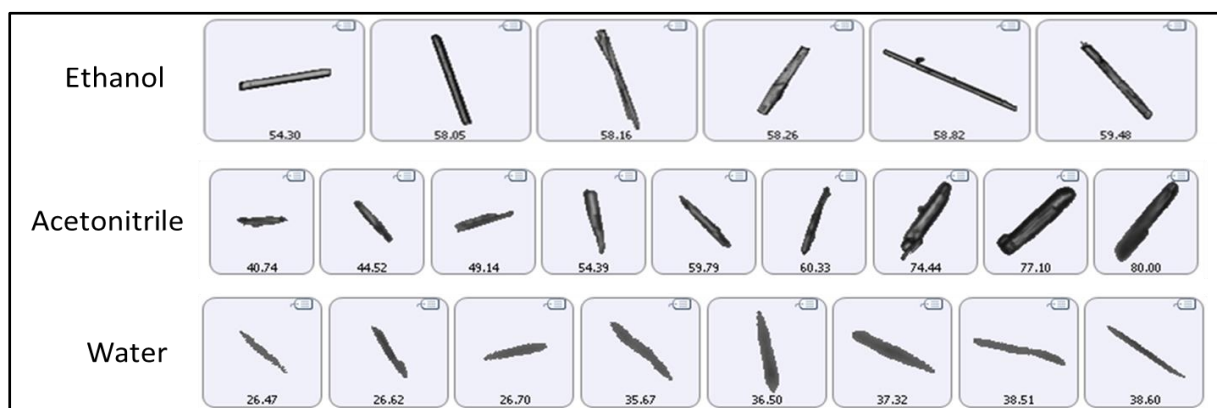
Figure 6-7 A selection of micrographs highlighting example crystallites recovered from each solvent after cooling crystallisation experiments, numbers below images indicate crystallite length in

6.5 Nucleation Kinetics using KBHR Method

The analysis procedure for the KBHR method is provided in Chapter 2, Section 2.4.7. Figure 6-8a), b) and c) show a plot of u_c vs q, in ln-ln coordinates for ethanol, acetonitrile and aqueous solutions at concentrations of 170, 54 and 6 g/kg respectively. Table 6-8 highlights the results of the KHBR analysis for all concentrations of alpha-PABA solutions in the various solvents, listing the regression values for the linear fits and the inequalities test for the data.
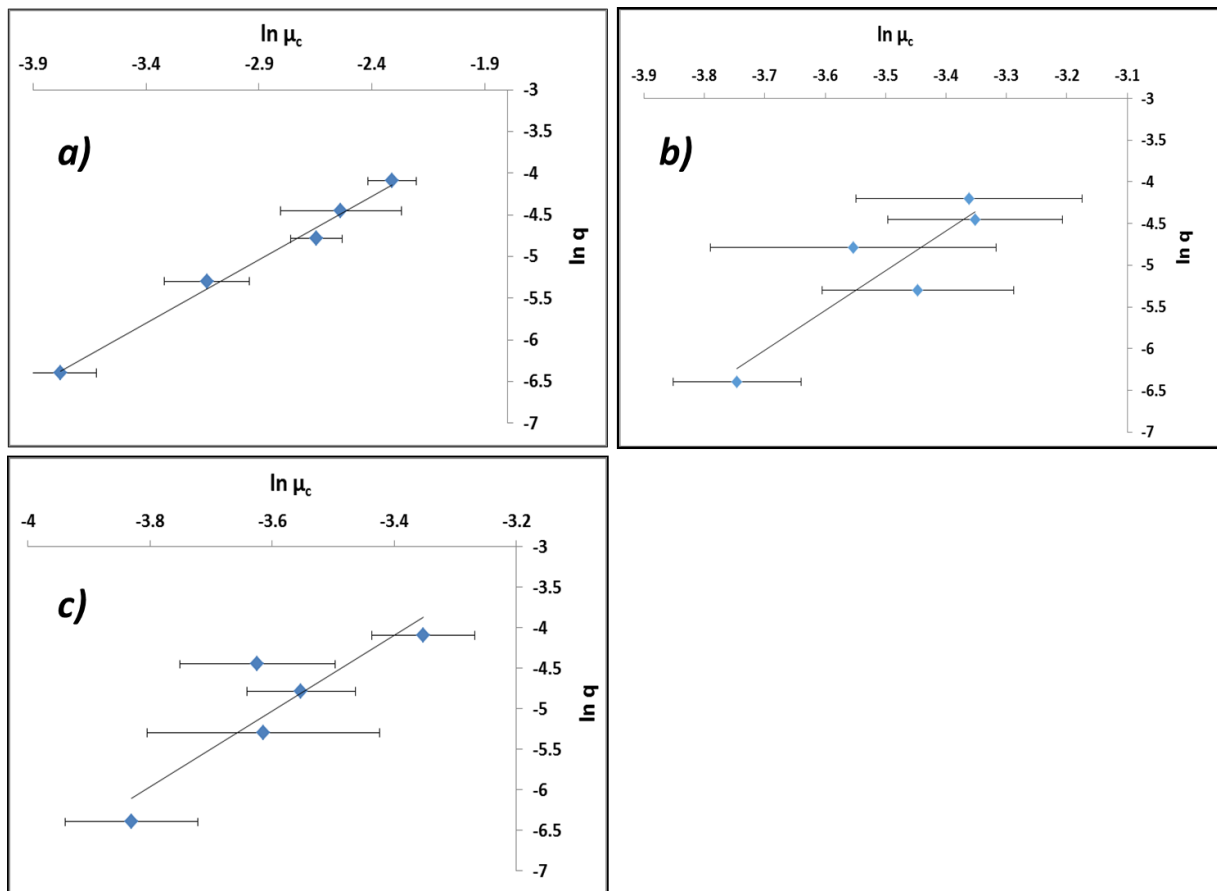
Figure 6-8 a) Plot of q vs μc in ln-ln coordinates for alpha-PABA in ethanol at a concentration of 170 g/kg, b) plot of q vs μc in ln-ln coordinates for alpha-PABA in acetonitrile at a concentration of 54 g/kg, c) plot of q vs μc in ln-ln coordinates for alpha-PABA in aqueous solutions at a concentration of 6 g/kg

The data show that for all concentrations in ethanol the slope of these plots is < 3 and as such the mechanism of nucleation for ethanolic alpha-PABA solutions in the studied concentration range was found to be instantaneous, whereby all nuclei are formed at the same time, hence the solution will contain a fixed number of crystallites following nucleation. The higher concentration acetonitrile solutions were also found

to exhibit instantaneous nucleation, however at the lower solution concentration of 54 g/kg a very large slope of 3.21 was observed and hence the nucleation mechanism here is progressive; whereby new crystal nuclei form during the nucleation process along with the older nuclei and so a varied size range of nuclei would be expected.

The results in higher concentration aqueous solutions also reveal an instantaneous nucleation mechanism but a progressive mechanism for the low concentration value of 6 g/kg. The slopes of these curves however are much closer to the value of 3 required for progressive nucleation indicating that in aqueous solutions alpha-PABA nucleates more readily. Conversely in ethanol and acetonitrile, nuclei seem to be stable for a longer time; this is also indicated by the large undercooling in these solvents.

Table 6-8 Calculated nucleation kinetic as a function of concentration for alpha PABA in ethanol, acetonitrile and aqueous solutions from the slope and intercept of the linear fit to q vs u_c in ln-ln coordinates

Conc. (g/kg) Ethanol	T_e (°K)	Slope of ln q vs. ln u_c	R^2 of linear fit to ln q vs ln u_c	Nucleation mechanism	q_{0} (K s^{-1})	n	C_o (m^{-3})	Nuclei/1 ml	ΔT_C range /°C
150	302.41	3.69	0.64	Progressive	N/A	N/A	N/A	N/A	16.10 – 25.78
160	304.85	3.25	0.97	Progressive	N/A	N/A	N/A	N/A	14.20 – 29.80
170	302.46	1.68	0.99	Instantaneous	1.36	0.68	8.60×10^8	860	8.30 – 31.37
180	304.85	1.76	0.80	Instantaneous	1.86	0.76	1.18×10^9	1180	7.32 – 21.50
190	307.32	1.56	0.53	Instantaneous	1.65	0.56	1.06×10^9	1057	5.63 – 17.10
200	312.13	1.62	0.62	Instantaneous	3.1	0.62	1.96×10^9	1957	4.22 – 13.85
Acetonitrile									
54.0	288.42	4.77	0.8	Progressive	N/A	N/A	N/A	N/A	6.81 – 10.00
64.8	292.45	1.56	0.43	Instantaneous	4.53	0.56	2.84×10^9	2838	3.78 – 7.75
75.6	297.98	1.61	0.34	Instantaneous	8.58	0.61	$5.36E\times10^9$	5364	2.96 – 4.85
86.4	303.11	1.99	0.96	Instantaneous	38.86	0.99	2.42×10^{10}	24221	2.19 – 5.51
Aqueous solutions									
6	302.25	4.53	0.79	Progressive	N/A	N/A	N/A	N/A	6.56 – 10.58
8	308.75	2.41	0.49	Instantaneous	54.60	1.41	2.18×10^{10}	21805	5.38 – 9.98
10	313.95	2.39	0.62	Instantaneous	94.63	1.39	3.78×10^{10}	37814	3.52 – 7.18
12	319.05	2.13	0.95	Instantaneous	44.70	1.13	1.78×10^{10}	17836	2.60 – 6.24

Considering that *n* can only take a value between 1 and 2, the calculated values of n presented in Table 6-8 that are all less than 1, are therefore rounded to 1. The results reveal that in ethanol and acetonitrile the growth exponent n was found to be 1, on average this value is slightly higher in acetonitrile. This is indicative of a system where the growth of the crystallites is rate limited only by the diffusion of the growth unit to the growing crystallite. The results in aqueous solutions however have revealed that the average value of n is much closer to 2 and as such this is indicative of a system whereby growth is rate limited by rearrangement of the solute at the crystal/solution interface.

The concentration of nuclei, C_o, can be calculated using Equation 2-49 and with the assumption of the following parameters; where $d = 1$, $m = 1$, $\alpha_{det} = 1\times 10^{-6}$, $K_G = 1 \times 10^{-8}$ *m/s*, $K_v = 1.28 \times 10^{-10}$. The value of *d* is assumed for a needle-like crystallite; *m* is a growth exponent for the system and is assumed to be 1 for growth mediated by diffusion of the solute through a stagnant layer around the crystal. K_g is the overall growth rate of the crystal and is estimated from a combination of *in-situ* growth studies of alpha-PABA in ethanol solutions[6]. K_v is the crystallite growth shape factor calculated from $k_v = 2A_0$, where A_0 is the fixed cross-sectional area in the direction of the long axis of the needle, which is nearly square shaped. The widths of alpha-PABA crystals were measured using optical microscopy after poly-thermal cooling crystallisation experiments. The measured values of the width were found to be in the range 10-20 µm, a median value of this range, 10 µm, was chosen as a good approximate value and used to calculate A_0.

The values calculated for C_0 at the various solution concentrations are presented in Table 6-8, the values show good agreement with calculated values for aspirin, a similar organic molecule, using this methodology.[8] The relevant values of nuclei/ml for the three solvents were found, in general, to be low for ethanol solutions and higher for acetonitrile and aqueous solutions. This observed trend follows an inverse relationship to solubility; alpha-PABA has the highest solubility in ethanol (144.0 g/kg at 20°C), but is found to nucleate the lowest number of nuclei at T_0, whereas in

aqueous solutions the solubility of alpha-PABA is very low (3.4 g/kg at 20°C), however a large number of nuclei are formed upon IN.

Recovery of the crystals after poly-thermal crystallisation reveals that the crystals formed in aqueous solutions are very small in both the needle axis and across the width of the needle axis, although from the higher concentration of nuclei calculated this is not surprising. The reverse is seen in ethanol where the needle morphology is much more defined and the dimensions in all axis directions are larger than crystals recovered from aqueous solutions. The case in acetonitrile shows that the morphology is relatively well defined however the crystals have smaller dimensions than those recovered from ethanol, micrographs in section 6.4 highlight these differences.

The data measured at lower concentrations of the acetonitrile and aqueous solutions which displayed progressive nucleation behaviour were further analysed using Equations 2.51-2.56.
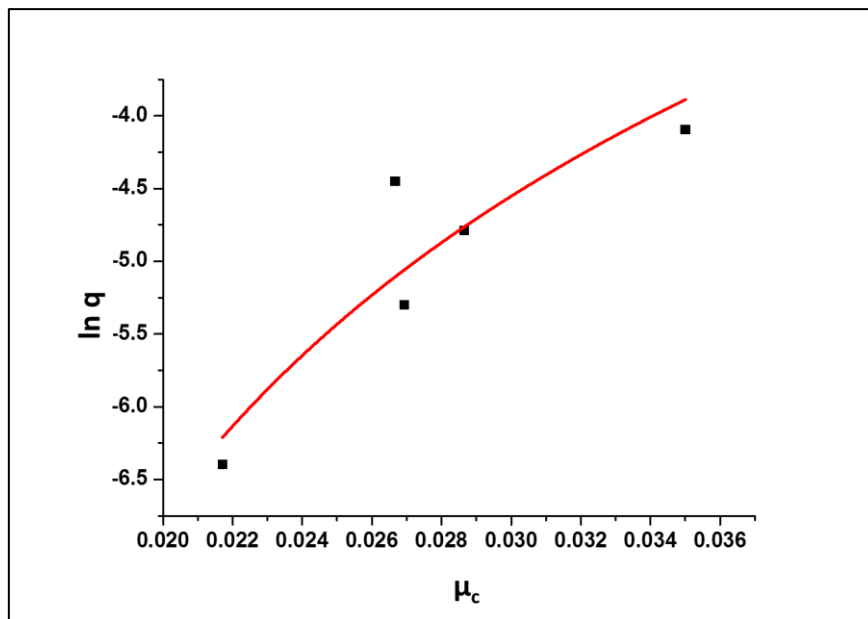
Figure 6-9 Relative critical undercooling as a function of ln cooling rate for a solution concentration of 6 g/kg in aqueous solutions, highlighted is the results of the best fit of Equation 2.51 to the data

An example of this curve fitting for the aqueous solutions at a concentration of 6g/kg is highlighted in Figure 6-9 and the results of the fit are provided in Table 6-9. The

free parameter a_1 was set as 3 in aqueous solutions and 4.5 in acetonitrile as this gave the best R^2 fit to the data. Parameter a_2 which is related to the dimensionless nucleation parameter b allows calculation of interfacial tension through Equation 2.53, where v_0 is equal 1.66×10^{-28} m^3 , the shape factor was assumed for a spherical nuclei as $k_n = \frac{16}{3}\pi$ and λ is equal to 3.47×10^{-20} J calculated from the literature values of the enthalpy of fusion. Table 6-9 presents values of r^* and i^* from Equations 2.55 and 2.56, this was calculated for the high and low values of critical undercooling; 0.022 – 0.035 in aqueous solutions and 0.024 – 0.035 in acetonitrile.

Table 6-9 Results of fitting the lnq vs μc data to Equation 2.51 for acetonitrile, aqueous and ethanol solutions at 54, 6, 150 and 160 g/kg respectively, highlighted are interfacial tension values, critical nucleus radii and number of molecules in the critical nucleus

Concentration (g/kg)	R^2 of the fit to equation 2.51	a_1	$a_2 = b$	ln q_0	γ_{eff} (mJ/ m^{-2})	r^* (nm)	i^* (molecules)
Aqueous solutions / 6	0.77	3	$6.73 \times 10^{-4} \pm$ 4.53×10^{-4}	6.74 ± 0.68	1.95	0.53 - 0.84	4 ¬ 15
Acetonitrile / 54	0.74	4.5	$1.36 \times 10^{-4} \pm$ 5.39×10^{-4}	10.85 ± 0.66	1.13	0.31 - 0.44	1 ¬ 2
Ethanol / 150	0.53	3	$1.82 \times 10^{-3} \pm$ 3.4×10^{-3}	3.38 ± 0.83	2.71	0.30 – 0.49	0.7 – 3
Ethanol / 160	0.96	3	$5.21 \times 10^{-4} \pm$ 6.6×10^{-4}	3.05 ± 0.18	1.79	0.17 - 0.37	0.1 – 1

The results from the progressive nucleation analysis seem to indicate that the interfacial tension values in the case of acetonitrile and aqueous solutions are relatively low and quite similar. The results in acetonitrile are found to be in good agreement with calculated values of γ_{eff} for alpha-PABA solutions in acetonitrile from induction time measurements by Sullivan et al[5], where a calculated value of 1.33 mJ/m^{-2} was presented.

6.6 Crystallisability in Relation to Solution Chemistry

The data reported in this work is summarised in Table 6-10 and can be applied in order to gain an improved understanding of the role played by solvent in the self-assembly, nucleation and ultimately crystal growth of alpha-PABA from the various solvents studied. From examination of the solubility and van't Hoff analysis in Chapter 2 it is clear that in all solutions solute-solute interactions are favoured over solute-solvent interactions and more so in aqueous solutions then acetonitrile and then ethanol. Importantly the values of ΔH_{solv} calculated in the van't Hoff analysis follow the same trend as those calculated from MD simulations, -74 kJ/mol in aqueous solutions and -95 kJ/mol in ethanol, where de-solvation of PABA in aqueous solutions costs less free energy in comparison to the case in ethanol.

This can perhaps be understood in terms of the structure and polarisability of the solvent molecules whereby water strongly solvates the polar acid and amino groups of PABA but provides much lower interactions with the non-polar benzene ring. In contrast ethanol can also solvate the polar groups of the molecule but additionally can also provide van-der Waals (vdW) stabilisation of the non-polar benzene ring from its constituent ethyl group; this would have the effect of increasing the free energy of de-solvation relative to the situation in aqueous solutions. The behaviour of acetonitrile lies between that of aqueous solutions and ethanol, as acetonitrile is solely a H-bond acceptor it can only solvate the O-H of the acid group, additionally the methyl group provides less vdW stabilisation of the benzene ring compared to the ethyl group in ethanol.

The free energy of de-solvation is an important factor when considering the nucleation rate of a solute and therefore is directly related to the achievable undercooling of a solution prior to crystallisation. The values of ΔH_{solv} directly correlate with the measured values of μ_c, whereby undercooling is greatest in ethanol and de-solvation is expected to be slowest, conversely in aqueous solutions the calculated values of μ_c are less than those in ethanol and de-solvation is expected to be faster.

Recent work relating attachment frequency, f^*, to the free energy of de-solvation of PABA by Sullivan et al[5] has shown that f^* increases with decreasing de-solvation

free energy of the carboxylic acid group. So it can be expected that the rate of nucleation is strongly proportional to the de-solvation free energy of the solute in a saturated solution. This leads to the postulation that the nucleation rate is likely to be slower in ethanol than in aqueous solutions, in line with the calculated values of ΔH_{solv} and ΔG_{solv} from van't Hoff analysis and MD simulation respectively.

The calculated values of γ_{eff} from the progressive nucleation analysis at the lower concentration of 6g/kg in aqueous solutions were found to be 1.95 mJ/m^3, this is significantly higher than the values of γ_{eff} calculated in ethanol which were found to be 0.85 – 1.31 mJ/m^{-2} in Section 6.2. According to classical theory the nucleation rate $J(t)$ is given by

$$J_{(t)} = K_J e^{\frac{-b}{(1-u)u^2}} \quad \textbf{(6-1)}$$

where b is the thermodynamic exponential function which is related to the interfacial tension, γ_{eff} through Equation 6-2;
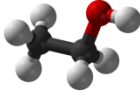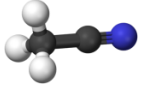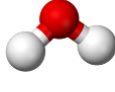
$$b = \frac{k_n v_0^2 \gamma_{eff}^3}{k T_e \lambda^2} \quad \textbf{(6-2)}$$

and where the nucleation rate constant K_J is related to the Zeldovich factor, z, C_o and the frequency of attachment of the molecular building blocks to the nucleus, f^* [9, 10].

$$K_J = z f^* C_0 \quad \textbf{(6-3)}$$

Considering this, an argument can be made that in the case of ethanolic alpha PABA solutions $J_{(t)}$ is not limited by the γ_{eff} and hence the thermodynamic parameter b, but is instead limited by f^*, which is likely a consequence of a higher free energy of de-solvation. This is also supported by the observed kinetic dependence of T_{dis} and T_{crys} on cooling rate highlighted in Figure 6-3. Comparatively the case in aqueous solutions can be expected to be the contrary, where $J_{(t)}$ is likely limited by γ_{eff} and not by f^*, this is again highlighted in the observation of the more thermodynamically controlled crystallisation parameters whereby the dependence of T_{dis} and T_{crys} on cooling rate is not significant.

Table 6-10 Solvent properties and a summary of results from van't Hoff, solution thermodynamics and KBHR analysis of the poly-thermal data collected

	Ethanol	Acetonitrile	Aqueous solutions
	CH_3CH_2OH	CH_3CN	H_2O
Dielectric Constant	24.3	37	78
# Atoms	9	6	3
Solubility at 20°C / g/kg	144.4	65	3.41
Solution Ideality	Most ideal	Mid ideal	Least ideal
Activity Coefficient γ	1.10	2.31	63.05
ΔH_{solv} / kJ/mol (from experimental solubility measurements)	-95.4	-85.3	-74.4
ΔG_{solv} / kJ/mol (from MD simulation)	-53.5	-52.0	-41.0
Cooling effect on T_{dis} and T_C	Kinetic	Kinetic	Thermodynamic
Achievable undercooling	High	Low	Low
C_0 Nuclei concentration / m^{-3}	8.60×10^8 - 1.96×10^9	2.84×10^9 – 2.42×10^{10}	1.78×10^{10} – 3.78×10^{10}
Growth exponent *n*	0.56-0.76	0.56-0.99	1.13-1.41
Growth rate limiting, from n	Diffusion of growth unit through solution	Diffusion of growth unit through solution	Surface rearrangement of growth unit at crystallite surface
Crystallite Length Mean / μm	113.11	90.64	37.25

Further to this an interesting observation was made between the calculated values of C_0 and the calculated values of ΔH_{solv} and ΔG_{solv}. The values of C_0 in ethanol were found to be 8.60×10^8- 1.96×10^9 much lower than the case in aqueous solutions with values of 1.78×10^{10}- 3.78×10^{10}. However, considering that ΔH_{solv} and ΔG_{solv} are higher in aqueous solutions, de-solvation is likely to be more favourable, and f^* is likely lower in comparison to ethanol, this further supports the notion that nucleation rates would be higher in aqueous solutions resulting in the observed lower values of μ_c. The case of acetonitrile solutions seems to lie within the middle of the aqueous and ethanol solutions in terms of the values of ΔH_{solv} and ΔG_{solv} and as such the nucleation rate will likely be a middle value between the two.

These results and observations are consistent with a model for crystallisation of alpha PABA whereby water fails to stabilise the non-polar properties of the PABA molecule in solution which leads to lower free energy of de-solvation resulting in a higher nucleation rate. Similarly nuclei are not stabilised by the polar aqueous solutions resulting in a lower barrier to nucleation and hence lower μ_c values. The opposite case can be expected for ethanol where a larger free energy of de-solvation, due to stabilisation of the non-polar benzene ring, affords a higher degree of undercooling and larger nuclei size. It should be noted that although the results of this analysis give a good indication of the nucleation behaviour of PABA, the exact structure and size of the nuclei discussed are unknown.
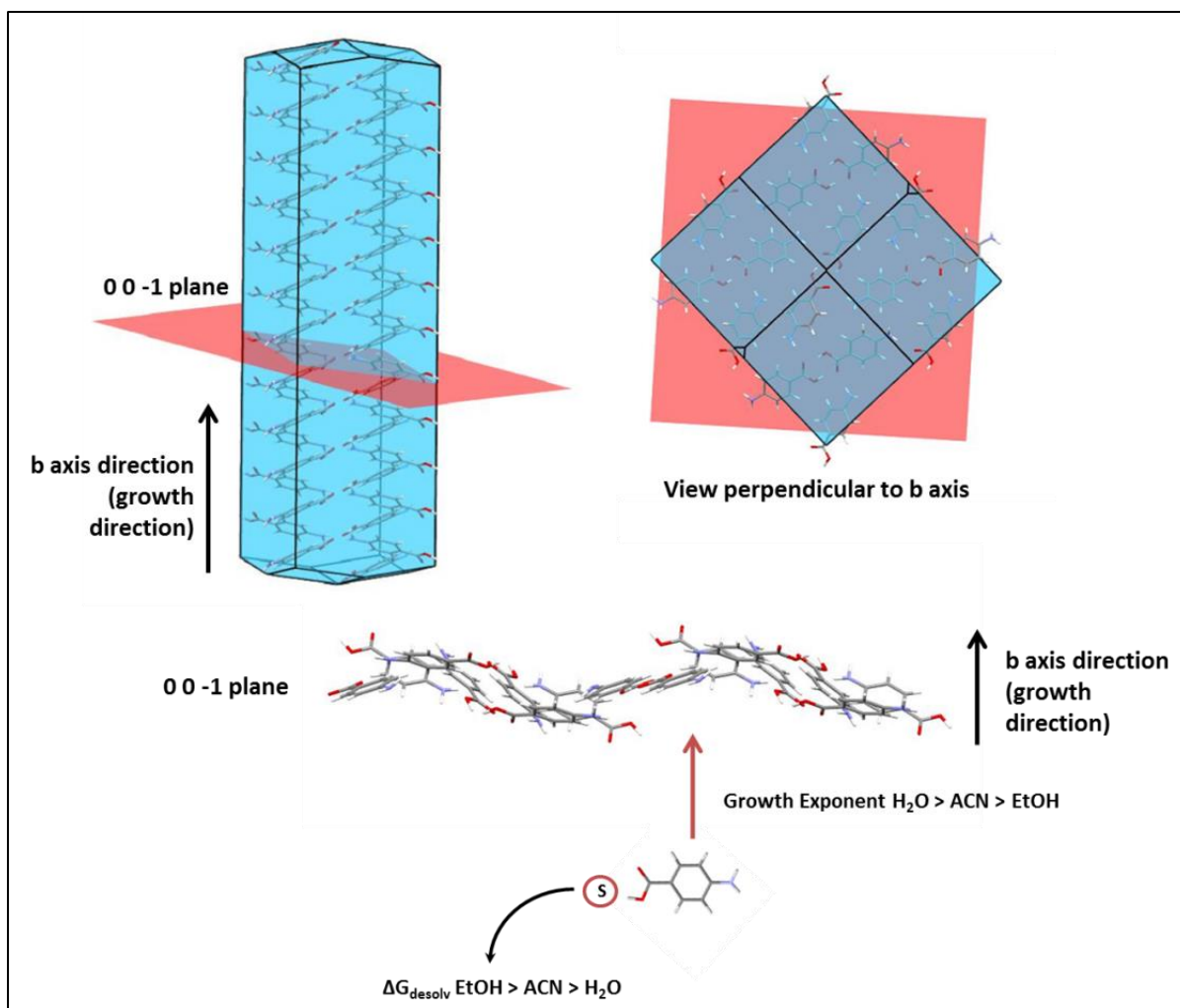
Figure 6-10 An illustrated example of the possible pathway to nucleation and growth of alpha PABA considering addition to the fastest growing 00-1 plane of the needle b axis

As the values of the growth exponent, n, are calculated from this analysis, crystallite growth of alpha PABA should be considered. Recently Toroz et al[6] have concluded that the growth direction of alpha PABA crystals is along the b axis in the (0 0 -1) plane with the fast growing, needle axis dominated by π-π stacking interactions of the aromatic rings[11].

The greater value of n=2 in aqueous solutions suggests that the rate limiting step in crystallite growth is surface rearrangement of the growth unit at the crystallite surface. Conversely in ethanol and acetonitrile, n=1 where growth is rate limited by diffusion of the growth unit to the crystallite surface. This is supported by examination of the crystals recovered after the crystallisation experiments as shown in Figure 6-5 and Figure 6-6 where crystallite sizes in ethanol and acetonitrile are

larger than those recovered from aqueous solutions, particularly in the direction of the needle axis.

If the only barrier to crystal growth was the free energy of de-solvation, it should be expected that crystals would be largest in aqueous solutions where the growth unit can de-solvate at a greater rate. However the trend is the contrary and so it is likely that the attachment frequency to the fast growing (0 0 -1) surface is relative to crystallite size. This observation suggests there is a barrier to growth at the (0 0 -1) surface in aqueous solutions which is not present or is decreased to a large extent in ethanol and acetonitrile solutions.

Sullivan et al [5] have recently indicated the importance of dimer formation as a key step in attachment to the alpha PABA crystal during crystallisation. Additionally, the FTIR results in Chapter 5 provided support for COOH dimer formation in supersaturated solutions of PABA in acetonitrile and possibly ethanol; this leads to speculation that formation of the COOH dimer could be the rate limiting step for growth allowing a favourable π-π stacking interaction to occur at the (0 0 -1) surface.

This mechanism for growth or addition to a nucleus assuming classical theory, is presented in Figure 6-10, where the de-solvation process takes place before addition to the fast growing (0 0 -1) surface which is dominated by π-π stacking of the benzene rings of PABA.

6.7 Concentration Effect on Nucleation Kinetics

The effect of concentration in the three solvents was noted to have an effect on the nucleation kinetic parameters and hence the observed nucleation mechanism, presented in Section 6.5. The general trend in the data shows that decreasing concentration forces the system to a more progressive nucleation mechanism. The case of ethanolic solutions provides the best opportunity to discuss this apparent concentration effect due to the large number of concentrations studied in this solvent system.

Table 6-11 highlights the key kinetic and thermodynamic parameters calculated from the KBHR approach and from published isothermal experiments on 200 and 280 g/kg samples of ethanolic PABA solutions. Starting with the solution

thermodynamics its can be seen that the values of ΔG_{solv} from MD simulation are higher for higher concentration solutions and lower for lower concertation solutions. This indicates, as discussed previously, the de-solvation of a molecule of PABA would be thermodynamically more favourable at lower concentrations than higher.
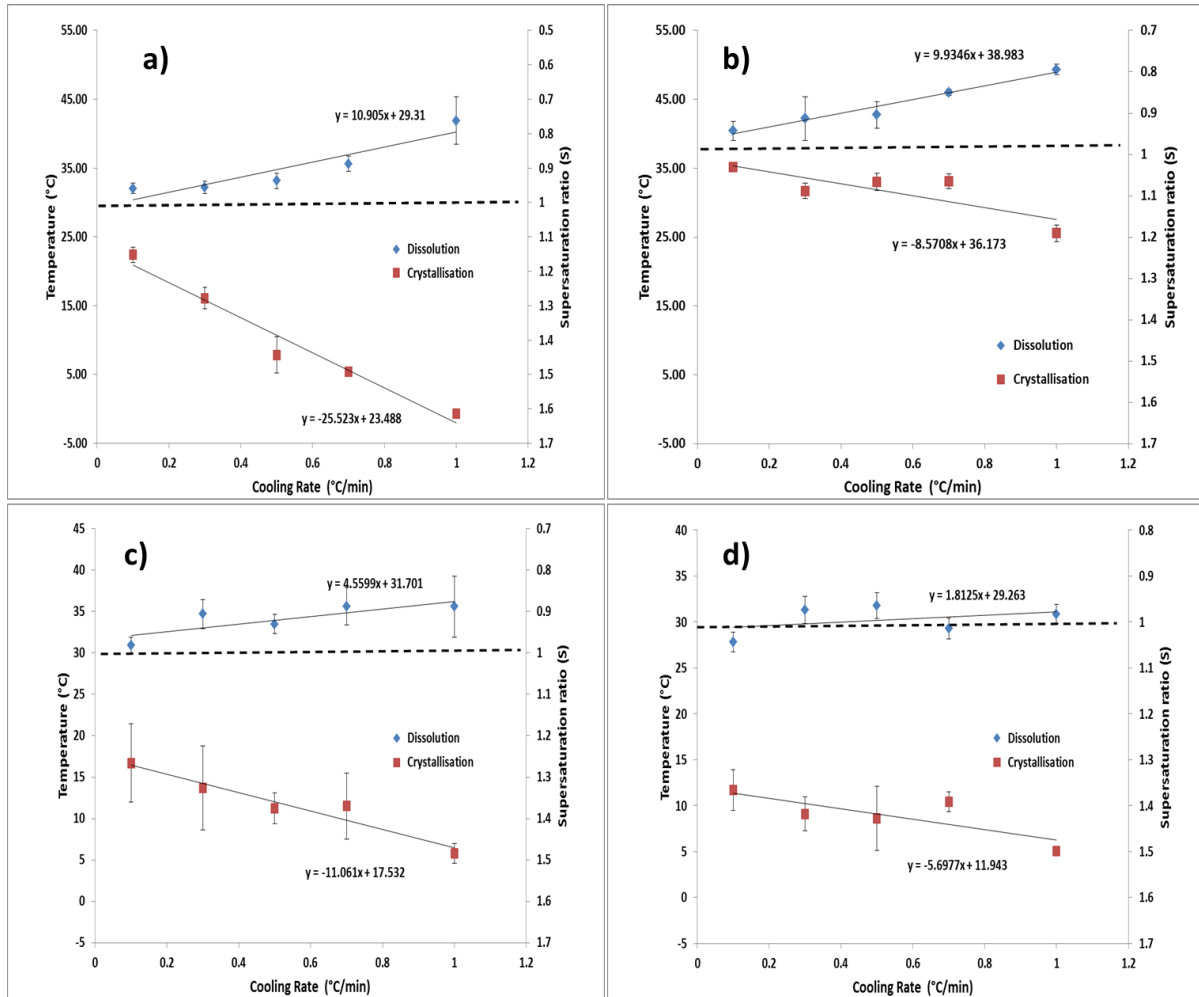
Figure 6-11 Comparison of the cooling rate effect on the dissolution and crystallisation for ethanolic PABA solutions at concentrations of a) 200g/kg, b) 170g/kg, c) 160 g/kg and d) 150g/kg

Considering the results of Sullivan et al on isothermal studies of PABA solutions, *f** is likely to increase with decreasing de-solvation free energy. Considering this and the decrease of de-solvation free energy with lower concentrations, then *f** can be considered as being lower in higher concentration ethanolic solutions and higher in lower concentration solutions. A higher value of *f** is likely to result in increased nuclei number during nucleation and this is also supported by the calculated value of

C_0. The value of C_0 in the lower concentration, 160 and 150 g/kg, is an order of magnitude higher at 1.83×10^{10} and 1.33×10^{10} m^{-3} in comparison to the concentration samples where 1.96×10^9 m^{-3} is the highest calculated value which is consistent with a higher attachment frequency in lower concentration samples.

The calculated values of γ_{eff} in higher concentration solutions in section 6.2 were found to be 0.85 and 1.31 mJ / m^{-2} for a 180 g/kg and 200 g/kg ethanolic PABA solution. Comparatively the calculated values of γ_{eff} from the KBHR analysis, 1.79 and 2.71 mJ/m^{-2}, are higher for the solution concentrations of 160 and 150 g/kg respectively.

When considering the higher value of γ_{eff} in lower concentration solutions and that f^* is likely to be much larger in these solutions, it can be postulated that the nucleation rate will be limited by γ_{eff} in low concentration solutions and in the higher concentration solutions by f^*.

These results are consistent with the measured supersaturation ranges reached for each concentration where the supersaturation ranges increase from 200 – 170 g/kg solutions and then subsequently decrease once the concentration is 160 and 150 g/kg. This is also reflected in the plots of T_{dis} and T_{crys} vs cooling rate, Figure 6-11, which show a large dependence on cooling rate at higher concentrations and a much lower dependence at lower concentrations. This demonstrates the switch between an instantaneous kinetically controlled nucleation mechanism and the more thermodynamically controlled progressive mechanism at 160 g/kg.

Table 6-11 results of the KBHR analysis for the ethanol samples as a function of concentration highlighting the nucleation mechanism change at lower concentrations

Conc. (g/kg) Ethanol	*S range*	$C_o\,(m^{-3})$	$\gamma_{eff}\,/mJ/m^{-2}$	$r^*\,(nm)$	Nucleation rate limiting factor$^\lozenge$	ΔT_C range /°C	Slope of ln q vs. ln u_c	Nucleation mechanism
150	1.34– 1.49	1.83×10^{10}	$2.71^\dagger$	0.30 – 0.49	γ_{eff}	16.10 – 25.78	3.69	Progressive
160	1.28 – 1.53	1.33×10^{10}	$1.79^\dagger$	0.17 - 0.37	γ_{eff}	14.20 – 29.80	3.25	Progressive
170	1.21 – 1.64	8.60×10^{8}	N/A		f^*	8.30 – 31.37	1.68	Instantaneous
180	1.12 – 1.42	1.18×10^{9}	$0.85^\ddagger$	0.69–1.98	f^*	7.32 – 21.50	1.76	Instantaneous
190	1.08 – 1.31	1.06×10^{9}	N/A		f^*	5.63 – 17.10	1.56	Instantaneous
200	1.06 – 1.25	1.96×10^{9}	$1.31^\ddagger$	0.48–0.91	f^*	4.22 – 13.85	1.62	Instantaneous

†calculated from poly-thermal KBHR analysis

‡calculated from iso-thermal analysis in section 6.2, also referenced in Toroz et al[6]

◊taken from published iso-thermal data relating f^* to ΔG_{solv} of PABA in a range of solvents[5]

6.8 Conclusions

Isothermal studies showed that calculated values of γ_{eff} were higher in water and lower in ethanol and that critical cluster sizes were very similar in both solvents, this analysis also yielded the critical nuclei sizes in water and ethanol.

It has been demonstrated that ethanol can stabilise the supersaturated state of PABA during nucleation, acetonitrile offers less stabilisation and water provides very little which is reflected in the calculated values of μ_c. This trend is also seen in the thermodynamics of de-solvation; where ΔG_{solv} follows the trend water > acetonitrile > ethanol.

The nucleation mechanism was found to be instantaneous at higher concentrations and progressive at lower concentrations in all solvents. The nuclei number upon instantaneous nucleation followed the trend water > acetonitrile > ethanol which suggests that f^* is greatest in water and lowest in ethanol, which was supported by previous studies of PABA nucleation[5].

The concentration effect which increased the progressive nature of nucleation with decreasing concentration was found to be caused by an increase in f^* combined with a higher γ_{eff} at lower concentrations causing the thermodynamic component of the nucleation rate to become rate limiting. This resulted in a more thermodynamically controlled process and hence a more progressive mechanism.

The growth exponent, *n,* followed the trend of water > acetonitrile > ethanol correlating well with measured crystallite lengths suggesting that there is a barrier to growth in water at the surface of the growing crystallite which is not apparent or relatively decreased in the cases of ethanol or acetonitrile. This was extended to the specific (0 0 -1) surface, which lies in the plane of the fast growing needle axis suggesting that formation of a dimer structure could result in faster attachment at the growing surface. This was supported by previous findings of possible dimer formation in ethanol solutions from FTIR experiments in Chapter 5.

The results discussed have highlighted the importance of how the properties of a solvent and concentration can influence the de-solvation process, the nucleation mechanism and hence the crystallisation kinetics of PABA and thus delivers on core objective 2 of this thesis.

References

[1] S. Parveen, R. J. Davey, G. Dent, R. G. Pritchard, *Chem. Commun.*, 2005, 1531

[2] R. A. Chiarella, A. L. Gillon, R. C. Burton, R. J. Davey, G. Sadiq, A. Auffret, M. Cioffi, C. A. Hunter, *Faraday Discuss.*, 2007, 136, 179

[3] R. A. Granberg, C. Ducreux, S. Gracin, Å. C. Rasmuson, *Chem. Eng. Sci.*, 2001, 56, 2305

[4] R. J. Davey, *Solvent effects in crystallization processes*, in E. Kaldis, *Current topics in materials science*, vol. 8., 1982, Amsterdam: North-Holland Publishing Company

[5] R. A. Sullivan, R. J. Davey, G. Sadiq, G. Dent, K. R. Back, J. H. ter Horst, D. Toroz, R. B. Hammond, *Cryst. Growth & Des.*, 2014, 14, 2689

[6] D. Toroz, I. Rosbottom, T. D. Turner, D. M. C. Corzo, R. B. Hammond, X. Lai and K. J. Roberts, *Faraday Discuss*, 2015, 179, 79

[7] I. Smallwood, *Handbook of Organic Solvent Properties*, 2012, Butterworth-Heinemann, Oxford

[8] K. Pencheva, Ph.D. Thesis, University of Leeds, England, 2006

[9] D.M.C. Corzo, A. Borissova, R. B. Hammond, D. Kashchiev, K. J. Roberts, K. Lewtas, I. More *Cryst.Eng.Comm.*, 2014, 16, 974

[10] D. Kashchiev, *Nucleation: basic theory with applications*, 2000, Butterworth-Heinemann, Oxford

[11] I. Rosbottom, K. J. Roberts, R. Docherty, *CrystEngComm*, 2015, 17, 5768

Chapter 7 *In-situ* Small Angle X-ray Scattering to Probe the Supersaturated State

In-situ small angle X-ray scattering studies, including details of the commissioning of an in-house built SAXS rig and experiments probing nano-scale structural changes during the nucleation of PABA from solution.

7.1 Introduction

The nucleation process is not fully understood from a structural perspective; however progress has been made recently using a variety of techniques including dynamic light scattering[1], small angle X-ray scattering[2], nuclear magnetic resonance spectroscopy[3] and ultracentrifugation[4]. The structural pathway to nucleation is particularly important in understanding polymorph selection; particle size distributions and crystal quality during a crystallisation process. Glycine in particular has been the subject of much study into the structure of possible pre-nucleation clusters which form during crystallisation from aqueous solutions[5]. There has been much debate as to whether such pre-nucleation assemblies represent the molecular packing of the final macroscopic crystalline phase or whether nucleation proceeds through a liquid-like cluster during concentration fluctuations in the solution, from which the crystalline phase nucleates.

These questions are the focus of this chapter with the aim to explore the structural pathway from single molecule to cluster formation during the crystallisation of PABA from supersaturated solutions. A description of the construction and commissioning of an in-house built SAXS device to be used for *in-situ* studies of nucleation will be provided. This is followed by the results of *in-situ* synchrotron radiation SAXS studies of PABA crystallisation from the supersaturated state to probe structural changes at the nano-scale, with the aim of revealing solution structure and structural information regarding pre-nucleation assemblies.

7.2 Development of the SAXS System

The planned experiments to measure key structural parameters regarding the *in-situ* nucleation of PABA from solution requires an experimental rig to provide small angle X-ray scattering (SAXS) hardware and data collection capabilities. The main features of the system design are a SAXS detector which provides a tool to monitor particulate shape, size and size distribution in solution during the nucleation process. An X-ray source fully collimated to provide a small area high intensity beam for sample diffraction and scattering, along with a one meter beam pipe to be filled with helium to reduce air scatter of the beam during analysis. The whole system, including all components, is housed in a sturdy X-ray shielded cabinet.

The enclosure, made from a mixture of steel and aluminium, was constructed in order to house the hardware components, sample environments and all the electronics associated with the equipment, see Figure 7-1 for an overview. The enclosure is a two metre construction which is fully mobile with six lockable wheels fixed to the corners and centre, the underneath section holds a stand to mount a water bath which is connected to the X-ray head.

The sides of the enclosure are manufactured from sheet steel to prevent radiation escaping the enclosure and have windows mounted along the sides for viewing access. One side of the construction, which is the access side, consists of two sliding doors which are fully interlocked to the X-ray system to prevent accidental exposure. The inside of the enclosure consists of a central rail system made of two aluminium rails to which the hardware is mounted, this provides two main advantages; the hardware components are always perfectly aligned in the horizontal direction and the positions of the components are fully adjustable; so the effective beam path is tuneable depending on the experiment.
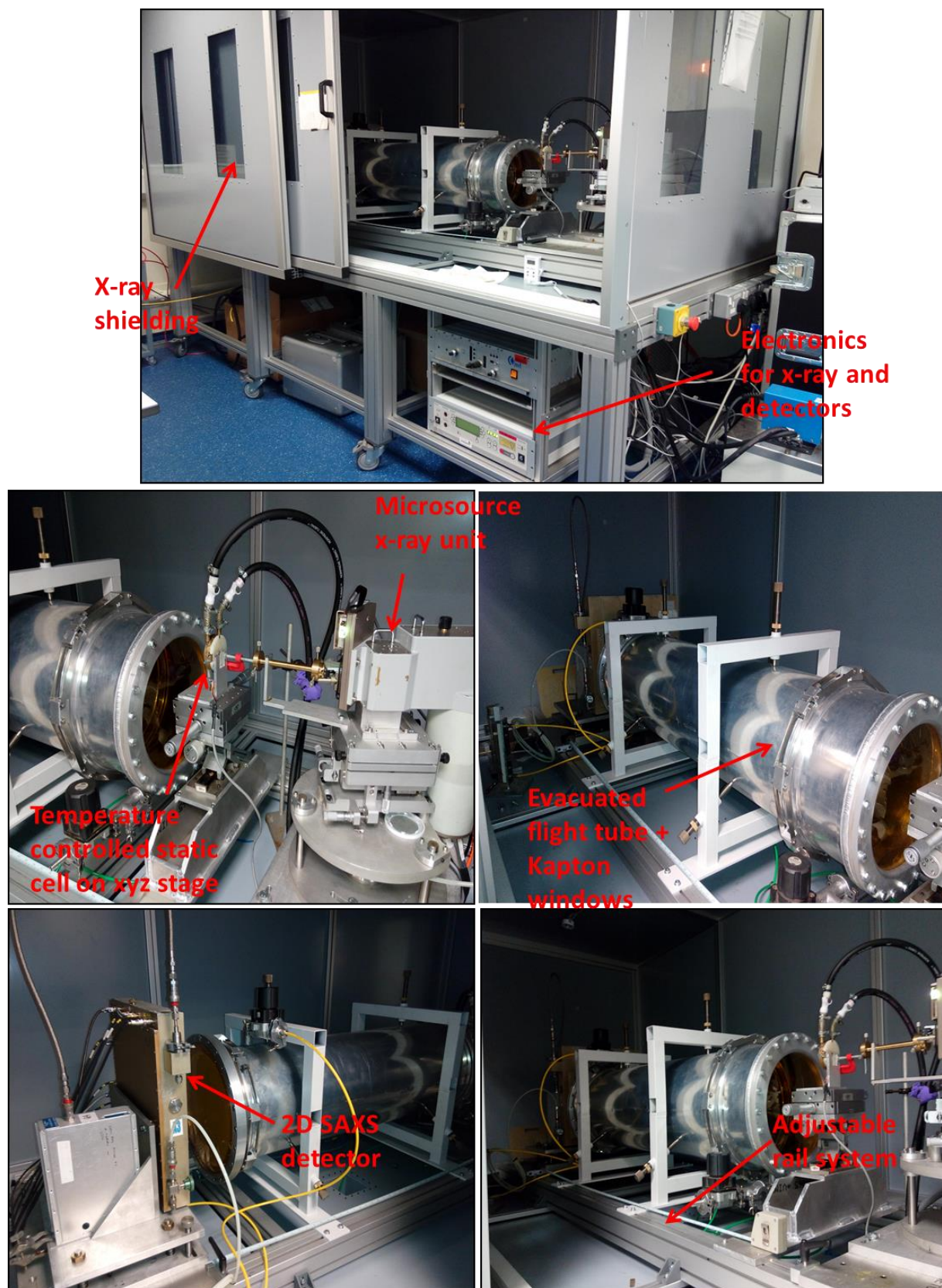
Figure 7-1 In-house built SAXS instrument highlighting the major components of the system

The diffractometer components are currently set up in a Debye-Scherer/Hull design operating in transmission mode. The hardware components consist of a Bede Microsource®[6] which is operating with a Cu source (1.5408Å) at 40 kV and 1.8 mA using a curved graphite crystal monochromator. The source head also contains the poly-capillary optics which collimates the beam prior to exiting the head, further to this an in house incident beam collimator has been constructed to further reduce air scatter and beam divergence before impinging on the sample.

The Microsource® head is fully adjustable through the use of micrometer stages which allow rotation of the head about an axis perpendicular to the beam, and can also be adjusted horizontally about the same axis. A sample stage consists of a fully adjustable micrometer in the directions *x, y, z,* the stage allows multiple sample holders to be fitted; powder samples in capillary tubes, flow and static solution cells.

The SAXS system which was provided by Daresbury Laboratory is situated at the far end of the enclosure on a stand rail system to allow movement. The detector itself is a multi-wire proportional gas delay line detector, the ionisation gas is 64% argon, 16% carbon dioxide, 20% xenon composition, the detector area is 200 mm^2 and the optimum running energy is 8.85 keV. A separate computer was also supplied by Daresbury Laboratory and this contains the data capture software which was designed in house at Daresbury laboratory, the computer is fitted into a trolley which also houses all the electronics for the SAXS detector.

Due to the large path length to the SAXS detector from the sample (~1.6 m), a beam tube, also supplied by Daresbury Laboratory was fitted to the rail system between the X-ray source and SAXS detector. Multiple beam tubes are available at 0.2, 0.5 and 1.0 m to allow path length tuning. The pipes have window sections at either end with 10 µm thick Kapton windows to reduce the absorption of the scattered beam. The pipe is filled with helium through a valve in the top of the pipe; following this the pipe is reduced in pressure to 800 mbar using a pump fitted with a vacuum controller.

7.3 Commissioning of the In-House SAXS Equipment

Sensitivity testing of the in house SAXS system was carried out to test a number of capabilities; the first of these included using size standard silica Nano-particulate samples to test the size resolution of the instrument. Secondly, the time resolution of the detector was tested to obtain a lower limit to the scan times required to obtain accurate structural data from the recorded scattering patterns. The final experiment was an electron density test to provide a lower limit of electron density of the sample required for useful scattering data to be recorded above background scattering.

7.3.1 Colloidal Silica Nanoparticle: Size Analysis and Sensitivity

The three sample types of colloidal silica Nano-particles; Ludox *SM*, *HS* and *TM* were analysed using the in-house SAXS instrument to test the size sensitivity and *q* space of the detector. The samples were provided with a manufacturer mean diameter of the spherical particles for comparison to those measured from Guinier analysis of the scattering patterns Table 7-1 highlights manufacturer mean diameters and also those calculated by Chen et al[7] using SAXS, for the three types of colloidal silica.

Table 7-1 Mean spherical particle diameters of the colloidal silica suspensions from the manufacturer and measurements using SAXS by Chen et al

Ludox Colloidol Silica Sample	Manufacturer Diameter / nm	Chen et al. Diameter / nm (SAXS data)
SM	8.4	10.7
HS	12.9	16.7
TM	23	28.6

The scattering patterns recorded for the *SM* and *HS* samples exhibited a major peak in the scattering pattern containing. The scattering patterns also exhibited oscillations at lower *q* spacing <0.3 nm^{-1}, this can be attributed to inter-particle interference due to the high concentrations used in this experiment. This particle-particle interaction is caused by elastic scattering of radiation between scatterers and due to the homogenous size distribution this oscillation is observed.

The samples of Ludox *TM* gave a scattering pattern which was cut off slightly by the lack of *q* space resulting in no structural information for these samples. This is also helpful in characterising the SAXS system as the current set-up provides an upper limit on spherical particles between 23-28.6 nm in diameter, anything below this size is visible on the detector.
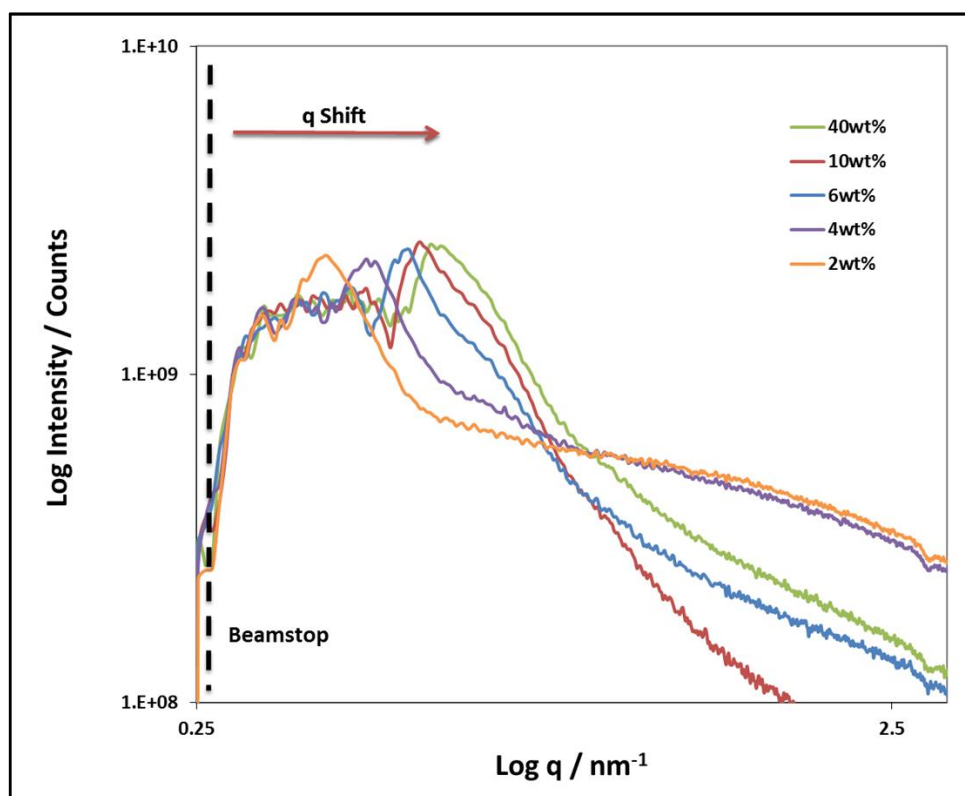
Figure 7-2 Scattering patterns following background subtraction for the Ludox HS samples as a function of concentration

Figure 7-2 highlights the scattering patterns from the Ludox *HS* samples as a function of solution concentration. It can be seen that as the concentration increases there is a general increase in the size of the low *q* oscillations which result from

particle – particle interactions. This can be expected as increasing concentration will have the effect of increasing particulate aggregation.

The interesting feature of these oscillations is that they appear in all the scattering patterns which would indicate that all samples contain some degree of aggregation. This was also confirmed by TEM experiments in a recent publication by Yang et al[8] which provided examples of particle aggregation in Ludox TM at a concentration of 40%.

Further to this there is an observable q shift of the major peak in the scattering patterns which generally shifts to higher values of q with increasing concentration. This is indicative of an aggregated system where the structure factor is dominating the scattering of the system as $I_{(q)} \approx P_{(q)}.S_{(q)}$ where S is the structure factor and P is the form factor. This results in a large structure factor peak of q_{max} in the scattering pattern caused by the multiple scattering effect of the aggregated nanoparticles of silica. Unfortunately this results in the lack of a Guinier regime in the scattering pattern due to masking by the structure factor peak and hence no radius of gyration or size parameters of the scatterers can be examined.

Table 7-2 Position of q_{max} and the calculated values of inter-particle spacing, d for Ludox HS samples

HS Sample	q_{max} / nm^{-1}	d / nm
2	0.37	16.98
4	0.43	14.61
6	0.49	12.82
10	0.52	12.09
40	0.54	11.64

The position of q_{max} as a function of solution concentration seems to increase and this allows calculation of a useful parameter relating to the average distance between scatterers, *d*. This can be calculated using $q_{max} = 2\pi / d$ and the results of these calculations are presented in Table 7-2. As can be seen the inter-particle distances decrease with increasing solution concentration which seems reasonable, considering particle aggregation should increase with increasing solution concentration.

These results suggest that the in-house SAXS equipment can successfully resolve silica Nanoparticles to provide information sample aggregation, unfortunately due to high solution concentrations particle shape and size information was not available due to masking of the Guinier region by the structure factor peak. This study has also provided an upper size limit on the particles that can be detected using this instrument which is ~ 23-28.6 nm as a spherical diameter.

7.3.2 Colloidal Silica Nanoparticle: Time Resolution Sensitivity

The time resolution of the in-house SAXS system was tested using Ludox HS silica Nanoparticles at 0.5% concentration to determine the minimum time required to record a scattering pattern which contains structural information. This was determined when the scattering patterns were consistent with those measured over a 1 hour data collection time in the size analysis, Section 4.3.1. This is important when commissioning *in-situ* experimental apparatus as it allows the user to plan the experiments based on the capabilities of the equipment, for example cooling profiles used on a temperature controlled cell can be considered when the minimum data collection time is known.

Figure 7-3 presents the background subtracted scattering patterns for the 0.5% solution of Ludox HS recorded at intervals of 5 minutes for 1 hour. The data shows that at the 20 minute time point the background subtraction is still slightly higher than the scattering from the sample. For comparison the pattern recorded at the 60 minute point is fully formed.

Considering this it can be seen that following the scattering pattern at 35 minutes the slope of the curve does not change. It can be concluded that for a colloidal silica –

water dispersion the minimum data collection times to obtain structurally consistent data is 35 minutes.
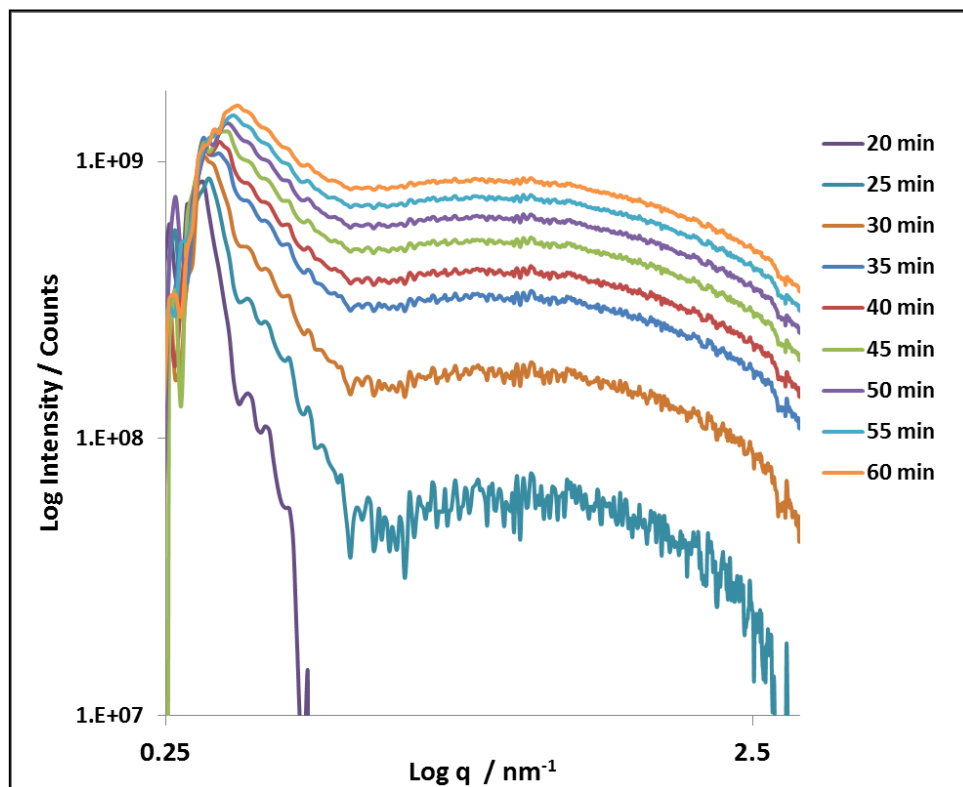
Figure 7-3 Scattering patterns recorded for a 0.5 wt% Ludox HS solution recorded at 5 minute intervals for time resolution analysis

7.3.3 Micro-Emulsions: Electron Density Sensitivity Analysis

A selection of micro-emulsion samples were analysed by SAXS for the purpose of testing the electron density, $\Delta\rho$, resolution of the 2D detector installed on the in-house SAXS instrument. This allows the lower limit of $\Delta\rho$ required between the solute and its surrounding solution to be determined, this is important when planning SAXS experiments, particularly in organic systems where $\Delta\rho$ contrast is usually low.
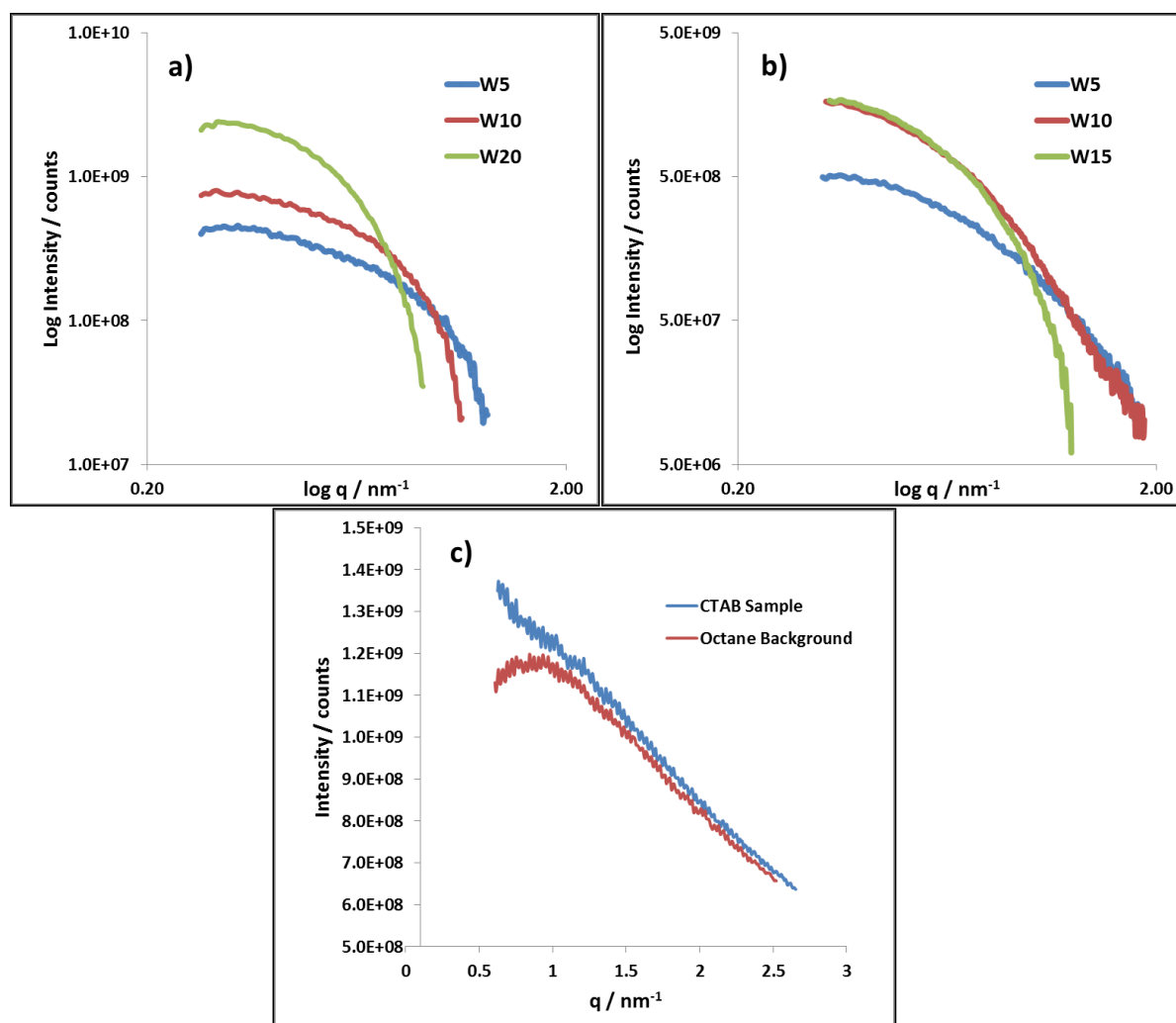
Figure 7-4 I(q) curves in log-log coordinates for samples of a) AOT and b) Triton X100 as a function of water content following background subtraction of clean octane, c) I(q) curve for the CTAB sample raw data with a comparison to the octane background scan

The water in oil micro-emulsions prepared were CTAB, Triton X100 and AOT in octane with $\Delta\rho$ values of 19.2, 179.0 and 309.2 e.u/nm^{-3} respectively, these samples were provided by Dr Tomasz Stawaski, University of Leeds. This provided a suitable range of $\Delta\rho$ to test the detector capabilities. Figure 7-4a) and Figure 7-4b) presents the background subtracted *I(q)* curves for the AOT and Triton samples as a function of water content, it should be noted that the CTAB samples, Figure 7-4c), provided no useful scattering information over the background scattering of clean octane, this is unsurprising however given the very low value of $\Delta\rho$ for this system. The general trend in the AOT and Triton X100 data seems to be that increasing the water content increases the intensity and also the Guinier slope. This observation matches well

with current literature; it is known that for these particular micro-emulsion systems there is a positive dependence of micelle size with water concentration[9].

Analysis of the Guinier and Porod regions provides further support for this observation; Table 7-3 highlights the calculated values of R_g and P, for the AOT and Triton X100 samples. The trend in R_g increases as a function of water content, from 2.19 to 3.36 nm for the AOT samples and 2.33 to 3.03 nm for the Triton X100 samples. This results in a spherical diameter of 7.36 nm increasing to 8.40 nm and 6.01 increasing to 7.83 nm for the AOT and Triton X100 samples respectively.

Table 7-3 Results of Guinier and Porod analysis for samples of AOT and Triton X100 as a function of water content, highlighting calculation of the spherical diameter of the micelles

Sample	R_g / nm	P	Spherical Diameter/nm
AOT			
W5	2.19	3.68	7.36
W10	2.49	4.00	8.00
W20	3.36	4.20	8.40
Triton X100			
W5	2.33	3.07	6.01
W10	2.94	3.65	7.58
W15	3.03	4.00	7.83

Figure 7-5 shows the calculated distance distribution functions, *ρ(r)*, from the measured scattering curves presented in Figure 7-4. The distribution functions for the AOT solutions present a Gaussian distribution for all samples indicating a spherical morphology of particles which appear to be relatively mono-dispersed. This correlates well with previous studies which have reported spherical micelles at low water concentrations < W = 50[10]. The values of *ρ(r)max* were found to be 2.64, 3.09 and 4.25 nm which represent the spherical radii of the W5, W10 and W20 samples respectively.

This trend is mirrored in the Triton X100 samples where $\rho(r)_{max}$ values were found to be 2.82, 3.28 and 3.4 nm for the W5, W10 and W15 samples respectively. This further reflects the observation of water pool enlargement with increasing water concentration in both micelle systems and also provides a simple correlation between these parameters.

The distance distribution functions of the W10 and W15 Triton X100 samples present a shoulder at higher size end of the curve; this could be due to particle agglomeration or particle poly-dispersity. These poly-dispersity effects in reverse phase micelles at higher water content have been previously reported and seem to agree well with this observation[11].
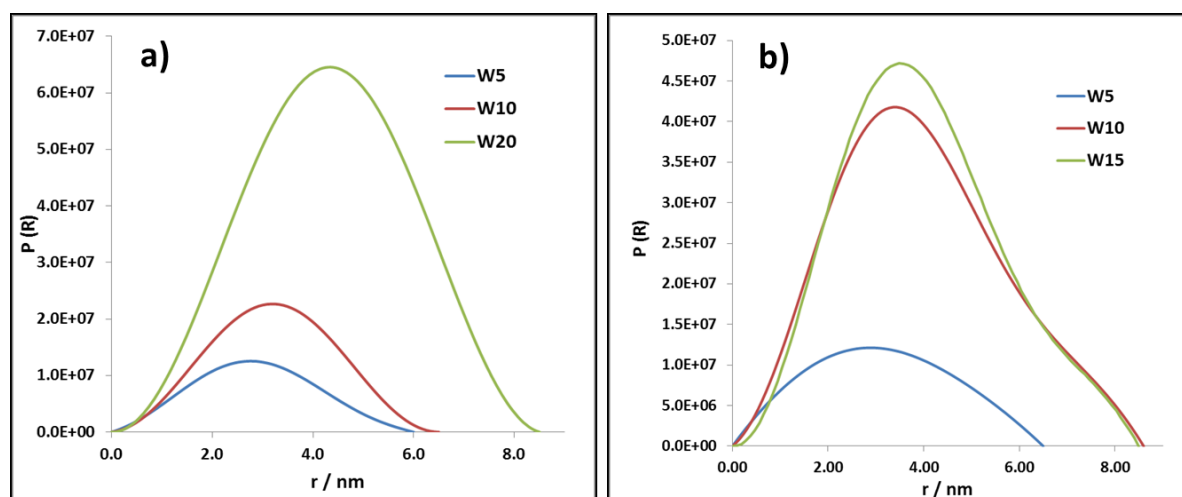
Figure 7-5 Distance distribution functions, ρ(r), for the AOT solutions a) and the Triton X100 solutions b) as a function of water content

The relationship between water pool size and water concentration for the AOT and Triton X100 samples is plotted in Figure 7-6. It can be seen from the data that a linear trend is observed between the W parameter and $\rho(R)_{max}$ providing regression values of 0.99 and 0.90 for the AOT and Triton X100 samples respectively. This linear correlation confirms previous studies on the AOT reverse micelle system where this relationship was also found[12].
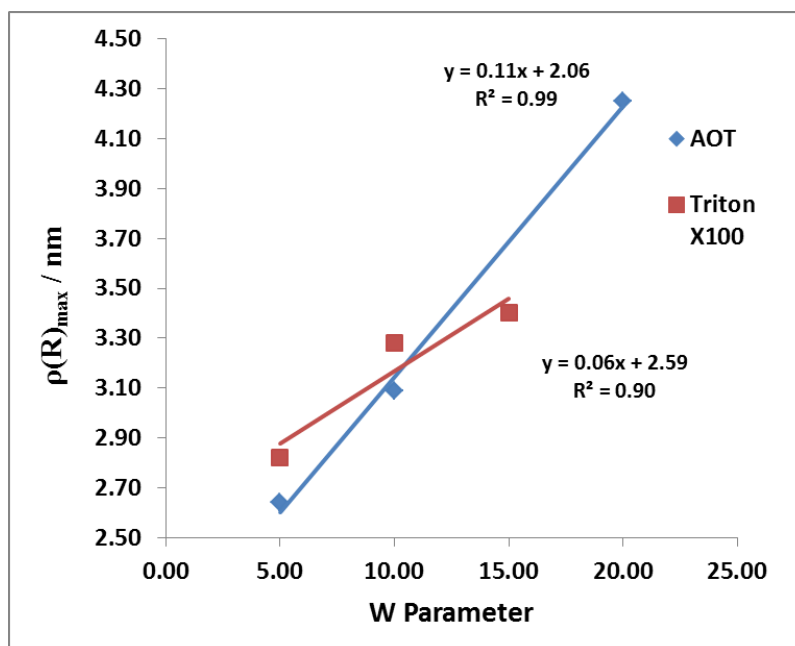
Figure 7-6 Linear correlation between water concentration and ρ(R)$_{max}$ for the AOT and Triton X100 micelle systems

To summarise these studies of micro-emulsion samples reveal that the in-house SAXS system can resolve AOT and Triton X100 samples above the background scattering of octane, however the system failed to provide any useful scattering data for the CTAB micro-emulsion. This provides a range for the lower limit of *Δρ* required for successful scattering experiments using this instrument, which falls between 19.2 and 179.0 e.u/nm^{-3}.

Further to this the results have provided useful structural information related to the AOT and Triton X100 reverse micelle phases. These results, particularly the calculated R_g values and the linear correlation of water content and *ρ(R)$_{max}$*, are in good agreement with previously published work on synchrotron radiation scattering experiments concerning these samples.

Considering the results of these commissioning experiments, the application of this instrument to the study of Nano-particulate and micellar static samples has shown the capabilities of the technique to reveal Nano-scale structural information. However the time resolution of 30 minutes seen in the study of silica Nanoparticles for this system is not sufficient when considering the study of kinetic applications such as that of nucleation. The other drawback to this system is due to the long beam path

and low intensity laboratory X-ray source; large values of $\Delta\rho$ are required for sufficient structural information to be ascertained. The $\Delta\rho$ value of PABA and ethanol is 164 e.u/nm^{-3}, this lies in the range of the minimum $\Delta\rho$ value required for successful scattering which was calculated in the reverse phase micelle study as 19.2 - 179.0 e.u/nm^{-3}.

7.4 *In-situ* Small Angle X-ray Scattering of Iso-thermal Crystallisation at The National Synchrotron Light Source

To overcome the problem of low time resolution and high background to signal count, *in-situ* synchrotron radiation SAXS experiments were utilised to study the crystallisation of PABA from ethanol, an overview of the methodology is provided in Section 4.3.9. The results presented in Figure 7-7 show the scattering curves of a 290 g/kg solution (saturation at 60°C) of alpha PABA in ethanol during an iso-thermal cooling crystallisation, as a function of holding time at 5°C. Due to data correction limitations at the beam-line, the data presented from this experiment does not account for primary beam decay or beam absorption, hence absolute intensity calculations cannot be performed and so the figures present raw data.
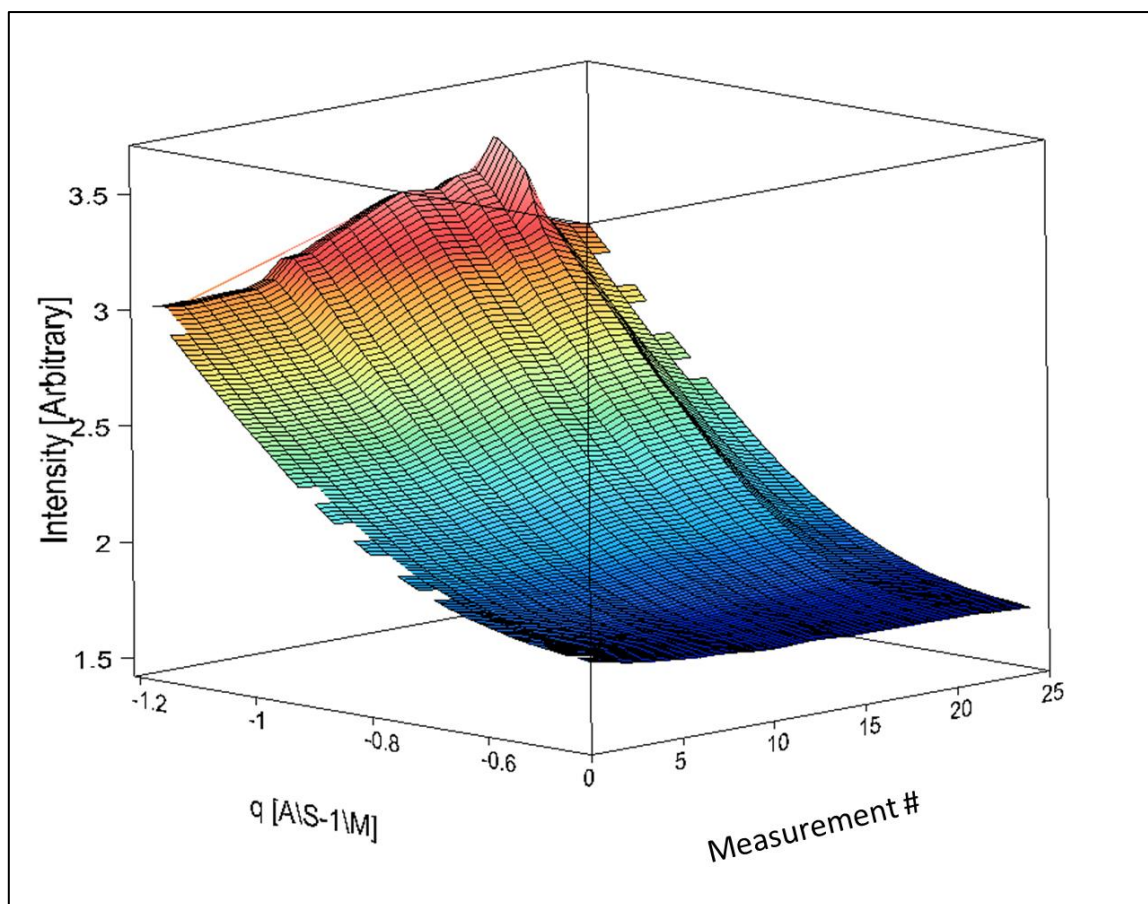
Figure 7-7 Raw I(q) scattering data in the q region 0.06 to 0.3 Å^{-1} from the 5°C isothermal experiment with a solution concentration of 290 g/kg, plotted as a function of experimental time

The interesting region of the scattering curve is the power law region from 0.06 to 0.3 Å^{-1} , highlighted in Figure 7-8, which shows a progression in intensity and also a slope increase as a function of time during the isothermal hold at 5°C. This indicates that the scattering species in solution are increasing in size and also number, it can be seen that a point is reached in the experiment, ~scattering pattern 20 (40 minutes holding time) where the intensity and slope of the scattering curve reaches a maximum (highlighted in Figure 7-8).

Following this maximum the intensity drops off rapidly, this could be due to the scatterers increasing to a d spacing size beyond the q space range of the detector. Due to the absence of a Guinier region which is cut off due to q space limitations on the detector, and the fact that this region is within the size range of 2 – 10 nm in d

spacing, it can be concluded that the scattering species here are larger than this size.
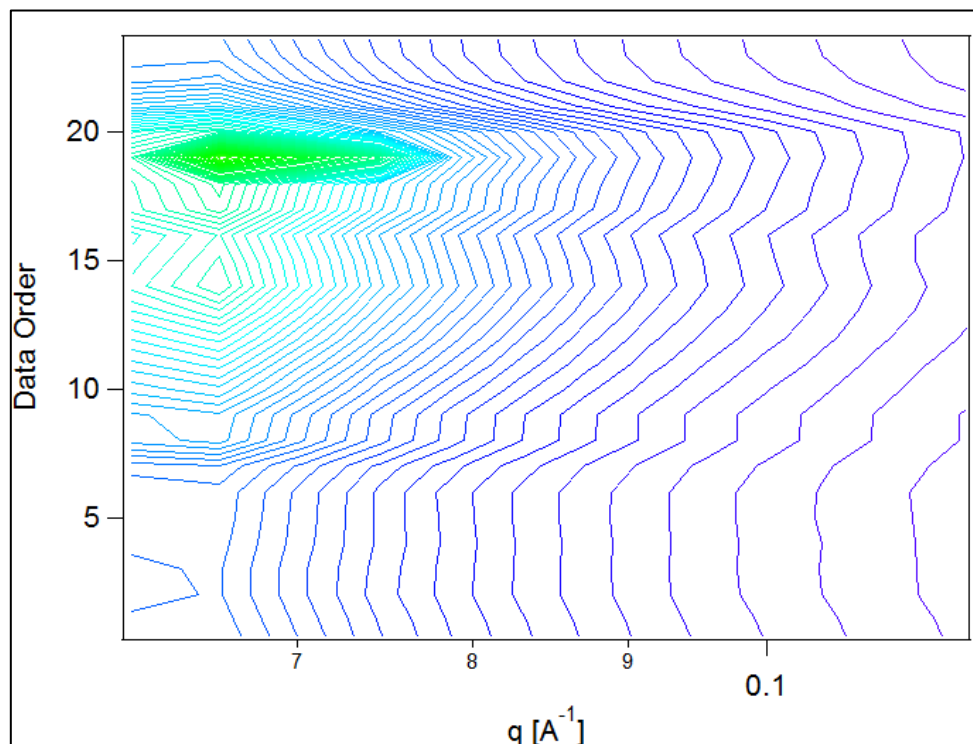
Figure 7-8 Contour plot of q space in the region of 0.06 to 0.2 Å^{-1} vs intensity, where green indicates high intensity and purple represents low intensity, as a function of time, each data point is 2 minutes in holding time at 5°C

The slope increase at the low q region can be explained by assuming a fractal approach to the scattering system, where a slope of 2-3 represents a mass or surface fractal system and a slope > 4 indicates a sharp interface. The data in the low q region were fitted to a fractal model to obtain values of *P*, the power law value, indicating the slope and hence fractal dimensionality of the structural level. Caution should be taken here due to the fact that the data analysed are not fully corrected and hence are not in absolute intensity units, however the values of *P* still give an indication as to the progression of the structure of these large scattering species.

The fitted values of *P* are shown as a function of holding time in Figure 7-9, it can be seen that at the start of the temperature hold the best fit of the *P* value is ~2.5 and stays around this value until a steady increase at 10 mins. The *P* value steadily increases to ~3.5 at 35 mins followed by a large jump to a *P* value of 4 followed by a

sharp decline until the final measurement at 50 minutes. This indicates that the larger structures, which increase in size as a function of temperature holding time, also seem to increase in fractal dimensionality steadily throughout the experiment indicating an increase in structural order.
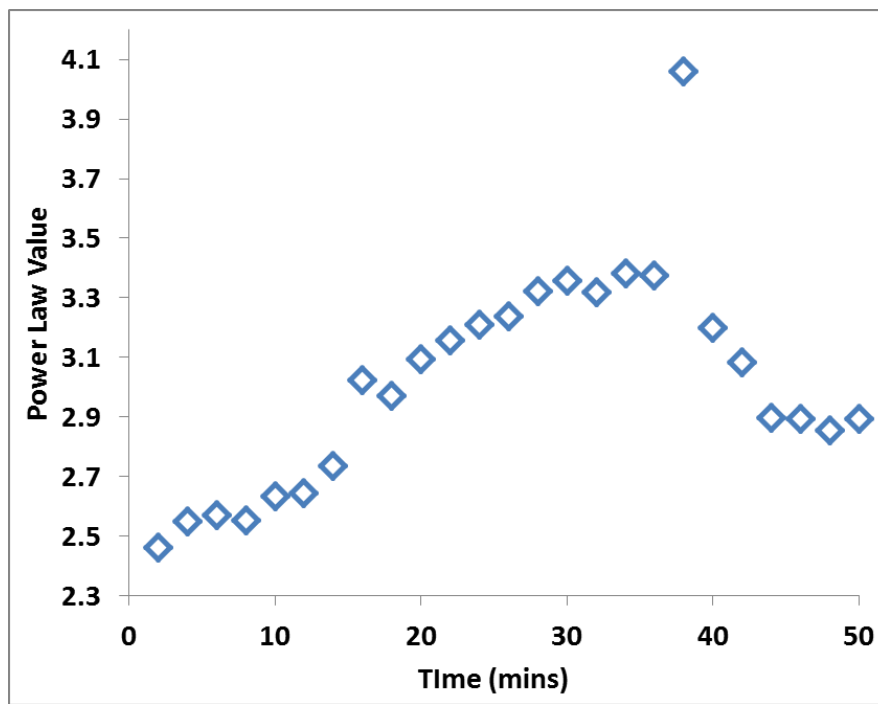
Figure 7-9 The fitted values of P for the q space region 0.06 to 0.2 Å^{-1} as a function of holding time at 5°C

Expanding these observations to the process of nucleation, a likely explanation to the identity of the large structures >10nm, is that of a distribution of meso-structures within the solution which are present not only in the supersaturated state but also at the beginning of the isothermal cooling in the under-saturated state.

This leads to the postulation about the existence of clusters of PABA molecules which are not meta-stable, that is to say these structures appear to be present in both saturated and under-saturated ethanolic PABA solutions. Further support for the postulation that these are clusters of PABA molecules rather than sample impurities, is found in the fact that the size of the clusters, indicated by the slope and intensity, seems to increase throughout the isothermal experiment. If the clusters were impurities a smooth progression of size would not be seen during the

isothermal holding time, a more likely explanation is that these clusters undergo growth due to molecular addition.

Another interesting observation is that the fractal dimensionality of these meso-structures increases from a value of 2.5 steadily to a value of 3.5 during the isothermal experiment. As discussed previously, caution must be taken when analysing the finite values of these power law slopes, however certainly the trend seems to indicate that the structural ordering of these clusters of molecules increases. This is followed by a large spike in the intensity and power law values at ~ scattering pattern 20 in Figure 7-8 and time = 40 mins in Figure 7-9. This could indicate the crystallisation time of the sample where a sharp increase in fractal dimensionality of the system is indicating the formation of a smooth interface, that between the crystallites and the saturated solution.

Further to this although the exact *P* values cannot be considered here, it is interesting to note that the scattering patterns do not fit well to a hard sphere model but instead fit very well to the fractal model. This indicates that these clusters of molecules do not contain a diffuse interface with their surrounding solution in the under-saturated or the saturated state prior to crystallisation, a good example of this behaviour would be silica Nanoparticles in a water dispersion, but instead fit a fractal model with a mass or surface fractal state.

This behaviour is not uncommon and has been highlighted in a number of studies for glycine and 2,6-dibromo-4-nitroaniline crystallisation[5, 13]. Chattopadhyay et al found that for a poly-thermal cooling crystallisation of glycine saturated at 60°C, the power law value increased from an initial value of 2.6 to a maximum of 3.2 during the cooling process[5]. Glycine solutions saturated at 55°C measured using SAXS by Jawor-Baczynska et al were found to also fit best to a fractal model where P was found to be 2.7 [2]. These previous findings for a similar small organic molecule at comparable concentrations seem to agree well with the data presented here for ethanolic PABA solutions.

The findings of this experiment supported by previous SAXS studies of glycine seem to suggest that the meso-strucutres of PABA have a rough interface with the surrounding saturated solution and thus will have a similar structure, i.e. these clusters are likely disordered in a 'liquid-like' state. This would result in a very low

interfacial tension between the saturated solution and the Nano-species, this hypothesis fits well when considering the calculated γ_{eff} values for ethanolic alpha PABA solutions of 0.85 – 1.31 mJ/m^{-2} in Chapter 6, which are particularly low for an organic system.

To conclude, this experiment has provided an initial insight into the structural progression of PABA crystallisation, indicating the presence of large Nano-species which increase in size and fractal dimensionality throughout the isothermal crystallisation experiment. The scattering patterns of the discussed mesostructured species fit best to a fractal model suggesting that the clusters are disordered and 'liquid like' rather than containing a diffuse interface to the surrounding solution.

7.5 *In-situ* Small Angle X-ray Scattering of Poly-thermal Crystallisation at The Brazilian Synchrotron Light Laboratory

The iso-thermal SAXS experiments highlighted in Section 7.4 provided an initial insight into the structural progression of alpha PABA crystallisation from ethanolic solutions. Following these findings further synchrotron SAXS experiments were required to further probe the structure of these large scattering species, and also to probe the solution structure and the molecular synthons which form these larger structures, further details of the instrumentation for this experiment can be found in Section 4.3.10.
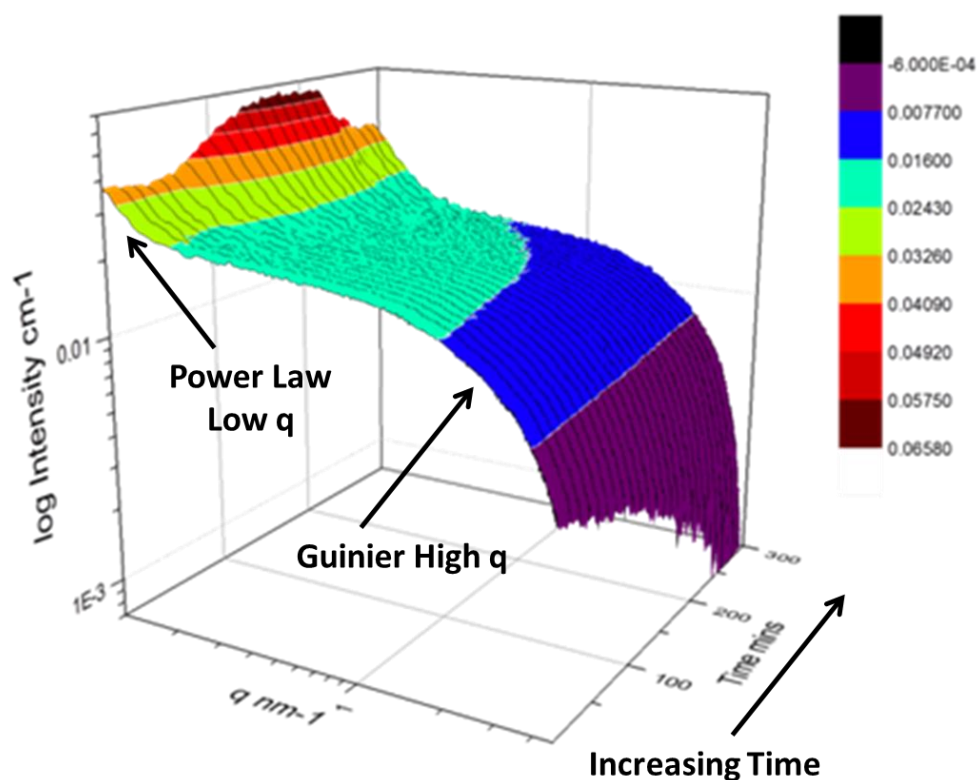
Figure 7-10 3D log log plot of absolute I(q) vs q as a function of time during a poly-thermal cooling crystallisation at 0.1 °C/min, indicating the Guinier region of the high q species and the power law slope of the low q species

Figure 7-10 shows a three dimensional plot of the fully corrected data from the 0.1°C/min cooling crystallisation experiment of alpha PABA from ethanolic solutions, plotted as intensity against momentum transfer, *q*, against time in minutes. The data

which reflects the PABA system during the cooling process as the solution enters the meta-stable zone and subsequently crystallises reveals two regions of interest. The first region is the low q region centred around 0.15 nm^{-1} which exhibits intensity and gradient increases during the cooling process, indicating increasing numbers and size of scatterers. This is particularly interesting as this trend in scattering function at low values of q, < 1.0 nm^{-1} was also seen in the isothermal experiments. The second region is the high q region around 3-4 nm^{-1} which exhibits slope increases and also intensity decreases throughout the cooling process (Figure 7-11), suggesting the scatterers are increasing in size but decreasing in number.
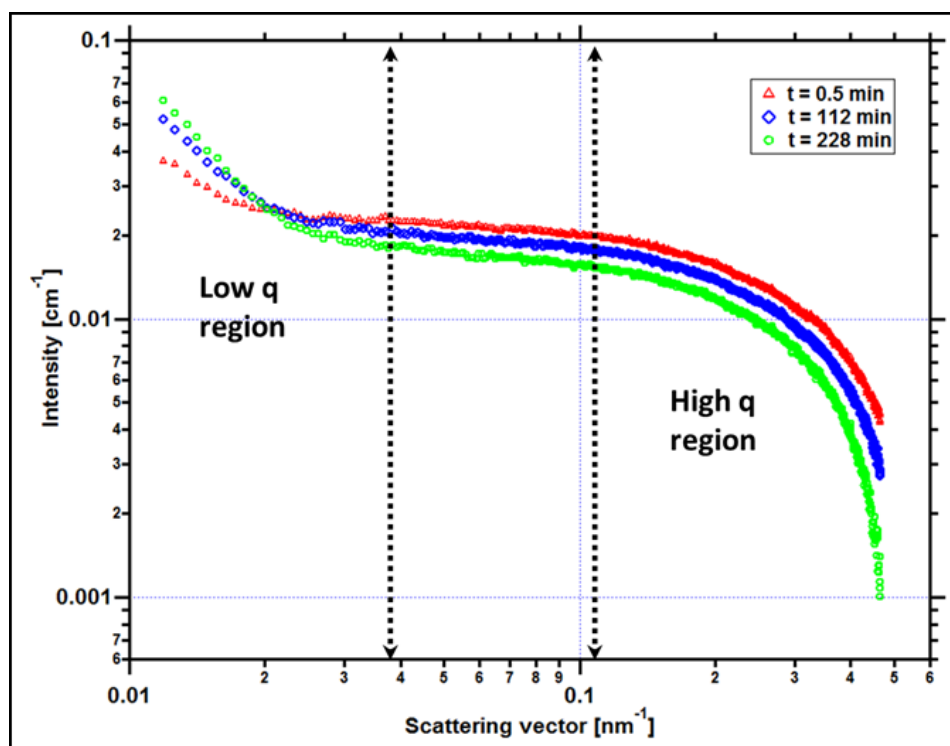
Figure 7-11 Log-log I(q) vs q at the start of the cooling profile, 0.5min, the middle of the cooling profile, 112 min and at I$_{max}$ for the low q region, 228 min

The high q region was found to be well represented in q space and exhibited a Guinier region followed by a power law regime. This latter area is consistent with scattering from the monomer of PABA or small aggregations of 1-2 nm in size, such as a dimer of PABA. The low q region was not found to be very well differentiated in the data due to the intensity cut off by the beam-stop, which limited the low q region beyond 0.1 nm^{-1}. The scattering in this region can be expected to be due to larger

aggregates in the region of 10-40 nm, however a complete analysis of this region was not found to be possible due to the low number of data points and as a result the Guinier region at low q was not found to be observable. This is unfortunate as this prevents the exact size and shape of these larger structures being calculated.
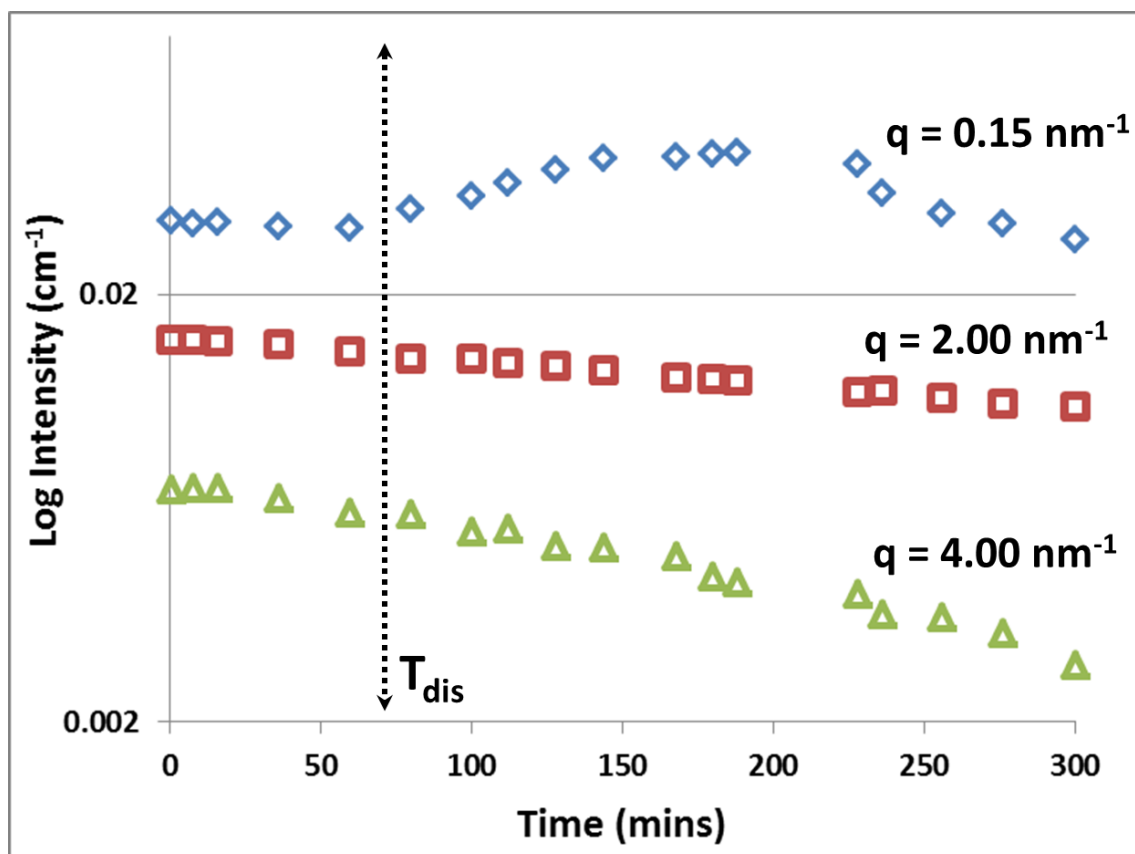
Figure 7-12 Intensity change throughput the cooling process for three regions of q space; 0.15 nm^{-1}, 2.00 nm^{-1} and 4 nm^{-1}

Figure 7-12 shows the intensity variation for three regions of the q range; low (0.15 nm^{-1}), medium (2 nm^{-1}) and high (4 nm^{-1}) values of q. The intensity from the low q region exhibits an increase in intensity at around 60 mins, this corresponds to the time the solution temperature entered the meta-stable zone. This could indicate the formation of the large molecular aggregations or clusters seen at low q. The data is consistent with the size and numbers of these clusters growing as evidenced by the intensity increase throughout the cooling process until around 230 min. The intensity at this latter stage of the cooling process was then found to decrease, which would

be consistent with these larger clusters having grown beyond the range of *q* space observable by the detector. The intensity was found to change at 2 and 4 nm^{-1} showing a general decrease throughout the cooling process which is likely due to the molecules of PABA being consumed by the nucleation process and consequently by the subsequent crystallisation process, whereby molecules of PABA would be expected to transfer to the larger clusters observed in the low *q* region.
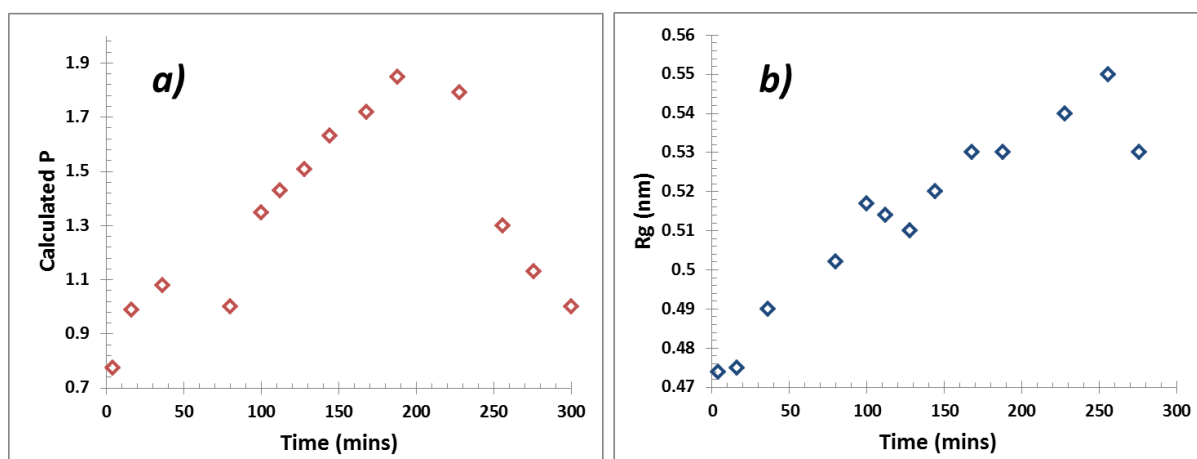
Figure 7-13 a) Progression of the power law value (P) at low q values and b) R$_g$ (nm) progression at high q during the cooling crystallisation

The data collected were analysed using the unified fit model, which allowed various related structural levels of the system to be analysed with respect to the radius of gyration (R_g) and to the power law value (*P*) to give a calculated fit to the data. The R_g values of the monomer NH…O dimer, stacked dimer and carboxylic acid H bonding dimer structure for alpha-PABA calculated in Crysol[14] were found to be 0.39 nm, 0.58 nm, 0.45 nm and 0.56 nm respectively. The structural models and the calculated R_g values are shown in Figure 7-14a), c), e) and g). The R_g progression, measured from the unified fit analysis of the experimental high *q* region, shows an increase from the initial value of 0.47 nm, to its maximum at 0.55 nm, prior to crystallisation (Figure 7-13b). This seems to be consistent with a model of molecular aggregation whereby a distribution of monomers and dimers of PABA exist in solution prior to crystallisation. This distribution seems to shift towards a dimer structure as supersaturation increases but the data obtained could not reveal the exact structure of this dimer. However, comparison of the calculated R_g values for

the stacked dimer, NH…O dimer and the carboxylic acid H bonding dimer with the measured values from the unified fit analysis shows the maximum observed R_g exceeds the calculated R_g for the stacked dimer. This suggests the molecular aggregations observed at this stage of the cooling process do not exhibit this stacking motif but may suggest formation of the NH..O or carboxylic acid H bonding dimer.

The calculated *P* values for the low *q* region are shown in Figure 7-13a) which shows a progression from 0.8 to a maximum of 1.9 as a function of time, after which the maximum P value was found to rapidly drop, consistent with the intensity drop off of the low *q* region. A decay of intensity of q^{-1} or q^{-2}, taking a fractal approach to the system, would indicate the presence of a mass fractal dimension. The increase of the *P* value from 1 – 2 indicates increased ordering of the cluster structures in the low q region. This may represent the presence of disordered aggregations of molecules in the size range of >40nm which increase in size and also become more ordered as the solution supersaturates. This is mutually consistent with the results of the isothermal SAXS studies which revealed the presence of large structures > 10nm even in the under-saturated state. This appears to be the case in this study also, where large clusters appear in the under-saturated state and increase in size and fractal dimensionality as a function of cooling time. The dimer structures identified from the high *q* region are likely transferred to the growing larger aggregates of the low *q* region during this process.
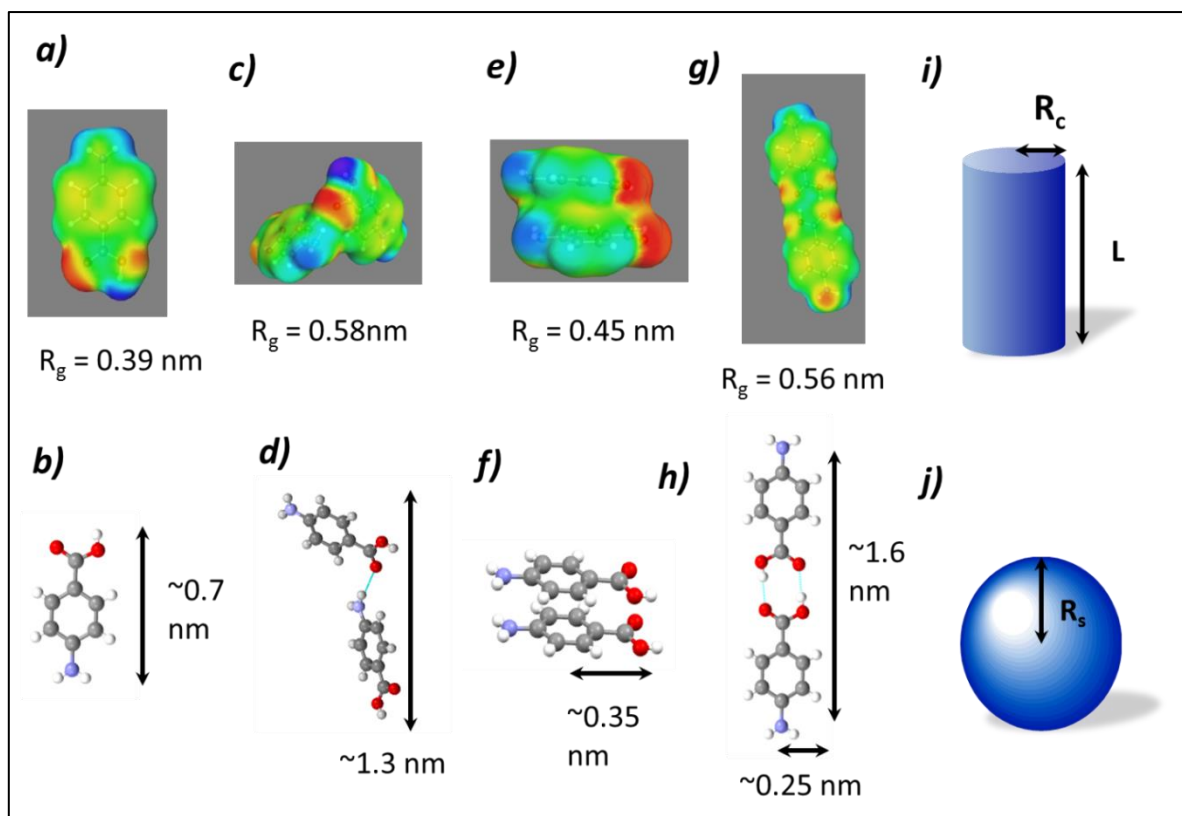
Figure 7-14 a), c), e) and g) represent surface charge density distributions of the single molecule, NH…O dimer, stacked dimer and carboxylic acid H bonding dimer of PABA respectively, indicating the calculated R_g valuesb), d), f) and h) are the ball and stick models of the single molecule, NH…O dimer, stacked dimer and carboxylic acid H bonding dimer respectively indicating the molecular dimensions, i and j are the geometric form factors for a cylinder and sphere indicating the parameters used to model the scattering intensity I(q)

To further investigate the proposed dimer cluster structure observed during the unified fit analysis, fitting of the experimental data was carried out using simple geometric form factors, $P_{(q)}$, of a cylinder and a sphere. This was rationalised by analysing the surface charge density distributions, calculated using the conducting solvent di-electric continuum approach[15], in ethanol for a NH…O dimer, stacked dimer and the carboxylic acid H bonding dimer, shown in Figure 7-14c), e) and g) respectively. A simple comparison can be made for a carboxylic acid H bonding dimer or NH…O dimer represented by a cylindrical form factor, with the stacked dimer represented by a spherical form factor indicated in Figure 7-14i and j.

Table 7-4 results from the program Scatter for fitting of cylindrical and spherical form factors, P(q), to the low q region of the experimental scattering curves as a function of time. Fitted parameters were I(0), L and R_s, Chi^2 values are also provided to highlight the goodness of fit to the data

Time (Mins)	Cylinder *I(0)*	Cylinder *L* (nm)	Cylinder chi^2	Sphere *I$_{(0)}$*	Sphere R_s (nm)	Sphere chi^2
0.5	2.11E-02	1.15	1.11	2.20E-02	0.64	0.62
36	2.09E-02	1.14	1.17	2.15E-02	0.64	0.68
80	1.96E-02	1.18	2.02	2.04E-02	0.65	0.99
128	1.90E-02	1.30	2.05	1.95E-02	0.66	1.01
168	1.79E-02	1.30	1.50	1.88E-02	0.68	1.66
228	1.71E-02	1.45	2.61	1.72E-02	0.69	1.43
256	1.65E-02	1.48	2.65	1.67E-02	0.70	2.07
300	1.56E-02	1.53	2.45	1.55E-02	0.68	2.00

Taking both of these form factors into account and fitting to the high *q* region good fits to the data were achieved, as can be seen from the chi^2 values in Table 7-4. As expected the value of *I$_{(0)}$* in both cases falls as time increases, this represents a decrease in the number of scatterers as the small monomer/dimer units are consumed by the larger growing structures, >40 nm, seen in the low q region.

The spherical radii of the fitted form factor increases from 0.64 nm to a maximum value of 0.70 nm during the cooling process and this value appears too large when compared to a maximum radii of 0.35nm for the stacked dimer. This overestimation of the calculated value of R_s maybe due to the assumption of a spherical form factor for the stacked dimer rather than a more elongated structure as seen in Figure 7-13f). The cylindrical form factor length increases from 1.15 nm to 1.53 nm as shown in Table 7-4, this is an intermediate value between the monomer length, 0.7 nm and the carboxylic acid H bonding dimer length, 1.6 nm. The maximum calculated cylinder length of 1.53 nm is larger than the NH…O dimer dimensions,

and this could indicate that the carboxylic acid H bonding dimer is the structure favoured due to better agreement to the molecular dimensions.

In conclusion the poly-thermal SAXS experiments have indicated the existence of large Nano-species which exist even in the under-saturated state, and begin to increase in size at the point the solution temperature reaches the 50° C saturation temperature (~60 mins). Due to this observation these large structures must be clusters of PABA rather than Nano-bubbles or impurities. The large Nano-species were found to fit best to a fractal model rather than a hard sphere model suggesting that the clusters are disordered at the surface and thus the interfacial tension must be low to the surrounding solution.

 Further to this the high q region revealed the existence of a population of smaller structures in the 1-2 nm range whose numbers decrease throughout the cooling process. These structures were identified as the monomer and dimer of PABA whereby the population shifts to the dimer structure throughout the cooling process, as indicated by the shift in R_g towards the dimer value of 0.56 nm. The dimer structure was confirmed as the hydrogen bonded carboxylic acid dimer from form factor fitting of the high q data to a simple sphere and cylinder model which ruled out the possibility for formation of the stacked dimer. This seems to indicate that the dimer structures are formed under high driving force upon cooling, however it is still not clear whether the growth unit is the dimer or the monomer from this analysis.

7.6 A Model for PABA Nucleation

The results of the synchrotron SAXS experiments highlighted in 7.4 and 7.5 have provided structural information regarding the progression of nano-scale assemblies during solution nucleation of PABA from ethanol and as such combining these observations a model for PABA nucleation can be hypothesised in Figure 7-15.
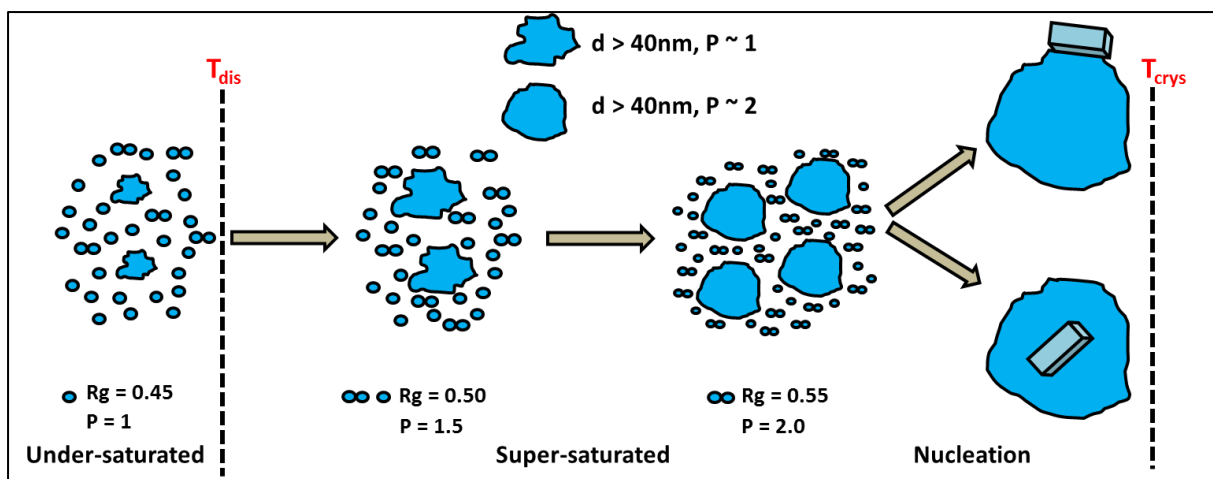
Figure 7-15 A structural model for PABA nucleation from ethanolic solutions indicating large liquid-like clusters surrounded by a population of monomer and dimerised PABA molecules

The results of both the iso-thermal and poly-thermal nucleation SAXS studies have revealed the interesting possibility that even in the under-saturated state very large Nano-clusters of PABA > 40 nm exist together with solvated PABA molecules in solution. Fitting of a fractal model to these clusters provides a *P* value of 1 which reveals that they are very disordered at the surface indicating that the clusters must have a low interfacial tension to the surrounding solution and so can be considered liquid-like.

This observation was in good agreement with the calculated low values of interfacial tensions of high concentration solutions of PABA in ethanol from isothermal studies in Chapter 6 and which suggest that the meso-scale clusters are relatively similar in structure to their surrounding solution. The iso-thermal experiments calculated the γ_{eff} to be of the order of 0.85 – 1.31 mJ / m^{-2} in solution concentrations 180 – 200 g/kg, these values are particularly low for a small organic molecule. Previous studies on similar organic materials have quoted γ_{eff} values for benzoic acid as 4.95 mJ / m^{-2} [16], for m-aminobenzoic acid as 8.7 mJ / m^{-2} [17] and L-histidine as 5.1 mJ / m^{-2} [17].

Further to this these high concentrations of PABA solutions were shown to nucleate by an instantaneous nucleation mechanism in Chapter 6, which suggests that the nucleation proceeds via large undercooling into the meta-stable zone. This further supports the results of the SAXS study where, certainly, formation of disordered

liquid-like clusters of PABA molecules would allow larger undercooling of the solution to be achieved by proceeding through these meta-stable cluster structures. Interestingly published calculated values of γ_{eff} for the protein lysozyme were found to be 0.51 mJ / m^{-2} [18], through SAXS studies this protein has also been found to nucleate through a two- step mechanism via formation of large disordered aggregations of molecules[19].

Evaluation of the high q region in the under-saturated state showed that the calculated value of the R_g was consistent with a population of monomers and dimers of PABA with the majority of molecules likely as solvated monomers. The dimer structure, as highlighted previously, was confirmed as the carboxylic acid dimer from form factor fitting.

Following the under-saturated state when the solution is cooled into the super-saturated state the size of these large Nano-clusters was found to increase as does the population of dimers in the surrounding solution. This was confirmed from temperature measurements of the sample which indicated the SAXS intensity increases at the point the solution reached the dissolution temperature, this further provided confidence that the clusters are related to PABA.

The calculated value of the power law term also increased from 1 to 1.5 indicating a progression in structural ordering of the large Nano-clusters and although still in a mass fractal state, they have more structural order than in the under-saturated state. The increase in carboxylic acid dimer formation with driving force is consistent with the results seen in the FTIR experiments in Chapter 5, where dimer formation was found to be favoured with increasing concentration for solutions of PABA in acetonitrile and possibly in ethanolic solutions.

The next step in the nucleation path way of PABA was a further increase in the P value of the large Nano-structures which increased from a value of 1.5 to 2, indicating a progression from a mass fractal state towards a surface fractal state prior to crystallisation. This was evidence for an increase again in structural ordering of the large Nano-structures. A change from a mass fractal to a surface fractal state indicates that the molecules at the interface are more ordered, this would suggest an increase in intermolecular interactions between solute molecules.

The final step in the nucleation pathway was formation of the crystalline phase followed by growth. Examination of the solution cell after these experiments showed that in both cases of iso-thermal and poly-thermal experiments the end result was, in most cases, a single needle-like crystal of alpha PABA. The specific details regarding the formation of this crystalline phase in relation to the large nano-clusters are not clear. A true two stage nucleation pathway results in formation of the stable nuclei within these large clusters of solute compared to nucleation at the interface between cluster and solution for example as shown in Figure 7-15. However SAXS experiments cannot currently probe this information which is missing in the structural pathway of nucleation.

This model of the nucleation pathway for PABA, built upon SAXS studies and previous experiments on PABA is consistent with a number of other published data on concentrated solutions of small organic materials. Glycine solutions have also shown to exhibit this supposed pathway to crystallisation,

7.7 Conclusions

The in-house SAXS experiments provided detailed commissioning information regarding sample size and electron density limitations of the current equipment. Particle size characterisation of Ludox silica nano-particles provided an upper limit of the particle size that is observable on the detector as 23-28.6 nm in diameter. The micro emulsion experiments provided a useful measure of electron density contrast required between sample and its surrounding solution. This was further extended to provide a correlation between micelle size and water pool concentration for AOT and Triton X100.

Synchrotron SAXS experiments at the LNLS and NSLS provided experimental evidence of large nano-clusters of PABA which seem meta-stable even in the under saturated state. These large meso-structures increased in size and fractal dimensionality as a function of increasing driving force. This was combined with measurement of the R_g for the low q region which highlighted an increase from the value of a monomer to the value of a dimer. This provided evidence for a population of monomers and dimers of PABA in highly saturated solutions which is consistent with FTIR and solubility results presented in Chapter 5.

Combining these results a model for PABA nucleation was also presented whereby nucleation proceeds through the large meso-structures of liquid like PABA, likely by dimer addition to the clusters. The model thus suggested a more non-classical approach to nucleation which may be related to nucleation mechanism changes due to a solution concentration dependence presented in Chapter 6.

Overall this chapter has provided a detailed structural description of the nucleation process of PABA crystallising from saturated solutions from the perspective of molecular aggregation to formation of liquid-like cluster structures, thus delivering on core objective three of this thesis.

References

[1] A. Jawor-Baczynska, B.D. Moore, H. S. Lee, A. V. McCormick, J. Sefcik, *Faraday Discuss.*, 2013, 167, 425

[2] A. Jawor-Baczynska, J.Sefcik, B. D. Moore, *Cryst. Growth Des.* 2013, 13, 470

[3] A. Spitaleri, C. A. Hunter, J. F. McCabe, M. J. Packer, S. L. Cockroft, *CrystEngComm*, 2004, 6, 489

[4] D. Gebauer, A. Volkel, H. Colfen, *Science*, 2008, 322, 1819

[5] S. Chattopadhyay, D. Erdemir, J. M. B. Evans, J. Ilavsky, H. Amenitsch, C. U. Segre, A. S. Myerson, *Cryst. Growth Des.*, 2005, 5, 523

[6] Bede (2005) now accessible as www.jvsemi.com

[7] G. Chen, Y. Wenchua, D. Singh, D. Cookson, J. Routbort, *J. Nanopart. Res.*, 2008, 10, 1109

[8] X. Yang, Z. Liu., *Nanoscale Research Letters*, 2010, 5, 1324

[9] R. Hilfiker, H. Eicke, W. Sager, C, Steeb, U. Hofmeier, *Berichte der Bunsengesellschaft für physikalische Chemie*, 1990, 94, 677

[10] H. Gochman-Hecht, H. Bianco-Peled, *J Colloid Interface Sci.*, 2005, 288, 230

[11] T. K. Jain, G. Cassin, J. P. Badiali, M. P. Pileni, *Langmuir*, 1996, 12, 2408

[12] M. Hirai, R. Kawai-Hirai, M. Sanada, H. Iwase, S. Mitsuya, *J. Phys. Chem. B*, 1999, 103, 9658

[13] H.G. Alison, R.J. Davey, J. Garside, M.J. Quayle, G.J.T Tiddy, D.T Clarke, G.R Jones, *Phys Chem Chem Phys,* 2003, 5, 4998

[14] D.I. Svergun, C. Barberato, M.H.J. Koch, *J. Appl. Cryst.*, 1995, 28, 768

[15] F.A. Momany, L.M. Carruthers, R. F. McGuire, H. A. Scheraga, *J. Phys. Chem*, 1974, 78, 1595

[16] R. J. Davey, S. L. M. Schroeder, J. H. ter Horst, *Angew. Chem. Int. Ed.*, 2013, 52, 2

[17] S. Jiang, J. H. ter Horst, *Cryst. Growth Des.* 2011, 11, 256

[18] O. Galkin, P. G. Vekilov, *J. Cryst. Growth* 2001, 232, 63

[19] N. Niimura, M. Ataka, Y. Minezaki, T. Katsura, *Physica B: Condensed Matter*, 1995, 213-214, 745

Chapter 8 *In-situ* Polymorphic Phase Transformation Studies

Development of a novel in-situ flow through transmission cell and its application together with XRD techniques to study the solution mediated polymorphic transformation of the beta to alpha forms of p-Aminobenzoic Acid.

8.1 Introduction

The advent of state of the art *in-situ* process analytical technologies led to a leap forward in the ability of monitoring solution and solid state properties in real time during crystallisation processes[1,2]. In particular the ability to probe the chemical kinetics of a crystallisation process has led to an increase understanding of polymorph selection and the kinetics which drive the transition from one polymorphic form to another[3,4]. Recent studies have highlighted the application of *in-situ* FTIR[5,6,7,8], Raman spectroscopies[9,10,11,12] and *in-situ* XRD[13] experiments to monitor the solution mediated phase transformation (SMPT) of polymorphic systems. This allows derivation of transformation kinetic parameters to understand the rate limiting steps of the transformation process in terms of dissolution and growth of the respective phases.

The following chapter highlights the development and commissioning of a novel *in-situ* transmission cell with sensitivity testing and calibration experiments conducted to relate specific diffraction peaks to solids concentration of a particular polymorphic form of PABA. The *in-situ* XRD studies of the solution mediated phase transformation (SMPT) of PABA are then discussed providing a detailed analysis on the rate determining steps involved by comparison of the solids and solution supersaturation transformation profiles. This analysis is then linked to the two polymorphs of PABA to provide a molecular level understanding of the observed results and how these relate to nucleation.

8.2 Construction of a Novel *in-situ* X-Ray Transmission Cell

In-situ studies of the polymorphic phase transformation of PABA require a method of transferring the crystallising medium from the reactor to the X-ray source for analysis; this led to the construction of a novel flow cell for *in-situ* X-ray diffraction (XRD) work.
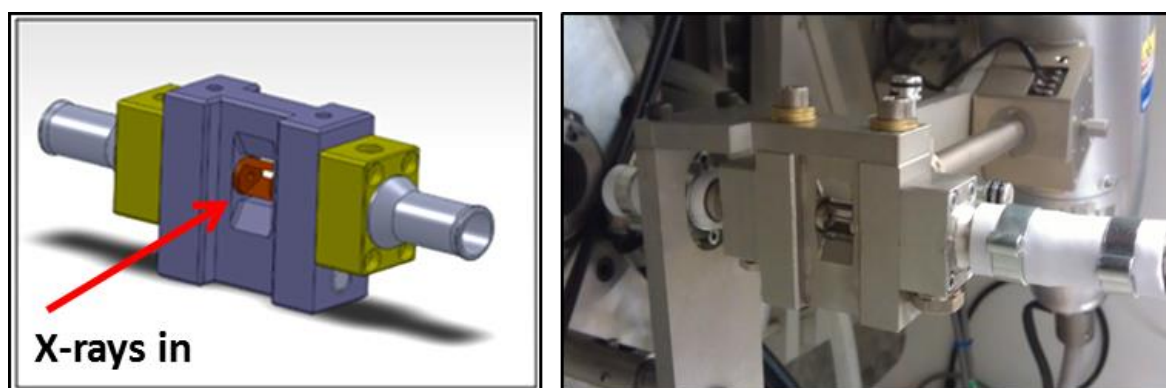
Figure 8-1 Mechanical drawing of the transmission cell indicating X-ray impingement upon the sample (left), transmission cell in position on the in-situ XRD rig

The capillary transmission cell (Figure 8-1) used for *in-situ* XRD data collection, consists of a steel biaxial hose connection on both the inlet and outlet of the cell for connection of the reactor vessel for the crystal slurry, located on the inner pipe, and a hose connection on the outer pipe which allows temperature control of the slurry line using a water/oil bath. This allows complete temperature control of the slurry throughout the system for cooling or heating; the cell is unjacketed only at the capillary tube itself for ~ 1cm to allow X-rays to impinge on the sample.

In order to achieve this window for X-ray analysis, the jacketing water flow must be re-directed around the window; this was done using the bypass tube which sends the water flow around the capillary cell and re-joins prior to exiting the cell. The capillary tube is constructed from borosilicate glass with a wall thickness of 10μm; this is to reduce the amount of unwanted x-ray diffraction by the tube itself. A significant feature of this design is the removable casing which holds the capillary tube, whereby the capillary tube is glued into the housing using solvent resistant glue. This design provides a method for disposal of any blocked or broken tubes during experiments; this will save time by preventing the need for disassembling or reconstruction of the cell in such scenarios.

8.2.1 Commissioning of the *in-situ* Transmission Flow Cell

When using any laboratory X-ray source for *in-situ* methods, there is a significant contribution to the observed signal by the solution phase diffraction, which reduces the ratio of peak intensity to background; this has the effect of increasing the limit of detection (LOD). The LOD is important as identification of certain polymorphs or phases in as little time as possible in both quantitative and qualitative analysis.

In order to improve the LOD when using this transmission cell, a method developed within the group during a previous project − smoothed principal component analysis (SPCA) [14]− was employed to overcome this problem. In this next section, an overview of the experiments carried out to determine the unprocessed data quality of the transmission cell followed by application of SPCA methods to improve data quality is presented.

8.2.2 XRD Count Rate Experiments

To compare the count rate, i.e. counts per second at the detector, obtained on a typical laboratory X-ray source, experiments were carried out using a 10% wt/wt% slurry of alpha−PABA in a 70:30 water:ethanol solvent mix. This would give an indication of the time resolution for future *in-situ* studies. The count rate was determined by recording a diffraction pattern every 10s for 2 minutes to determine the signal-to-noise performance; the patterns shown in Figure 8-2 are the collected raw diffraction data.

Each pattern in Figure 8-2 is a 10 second data collection and offset along the ordinate for clarity. As can be seen the count rate for the crystalline phase is higher than the solution and background scattering even at short data collection times (<30s); the appearance of the unique (103) reflection at ~15.5° 2θ is seen at 10s. The (202) reflection (~14° 2θ), is also visible after ~10s however a fully resolved diffraction pattern including these two peaks is not observable until ~60s.
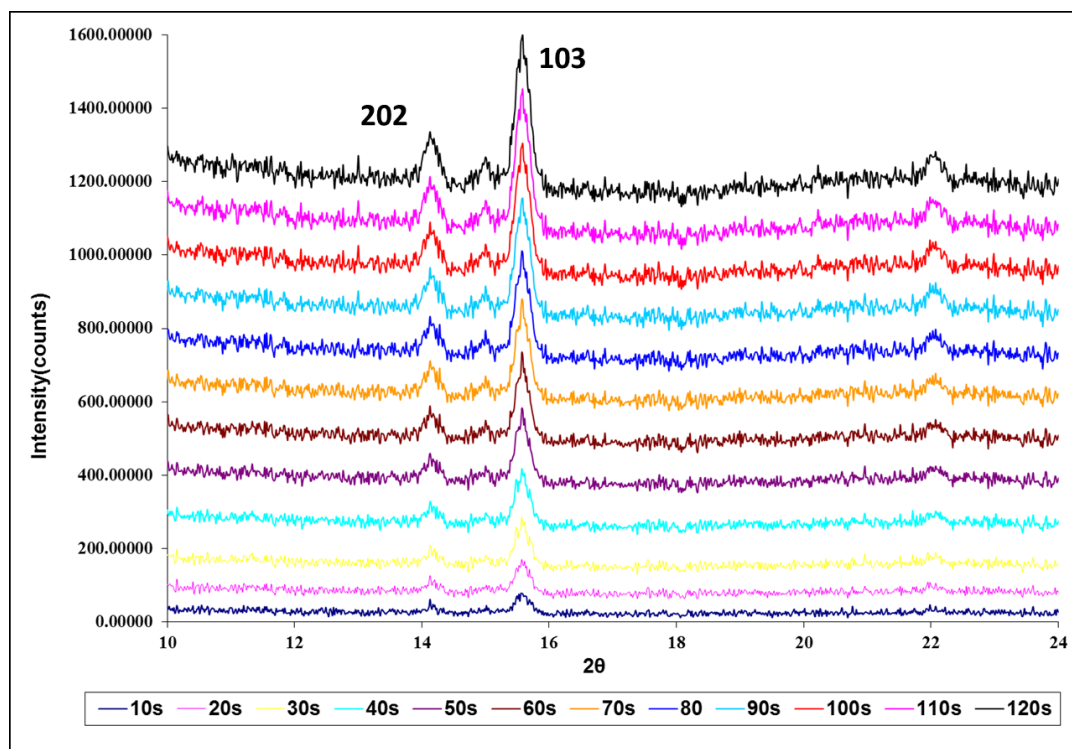
Figure 8-2 Results of count rate test for the transmission cell indicating the (202) and (103) reflections of the alpha polymorph of PABA

8.2.3 Application of Smoothed Principal Component Analysis for Limit of Detection

To characterise the data collection capabilities of the cell, further the LOD was established. This was done by examining varying slurry concentrations of alpha−PABA in 70:30 water:ethanol solvent; concentrations from 0.1–0.9 wt/wt% in 0.1 wt/wt% increments were chosen. Data was collected for 300 seconds for each concentration; identification of the alpha polymorph would be by using the unique (103) reflection at ~15° 2θ as this gave the highest diffracted intensity. Figure 8-3 shows the overlay of the unprocessed XRD patterns of alpha−PABA with increasing concentration (offset along the ordinate for clarity). It can be seen that the data has a low signal-to-noise ratio with the instrument and solution background contributing heavily to the observed signal. The LOD for alpha−PABA with unsmoothed data was found to be 0.9 wt/wt%.alpha
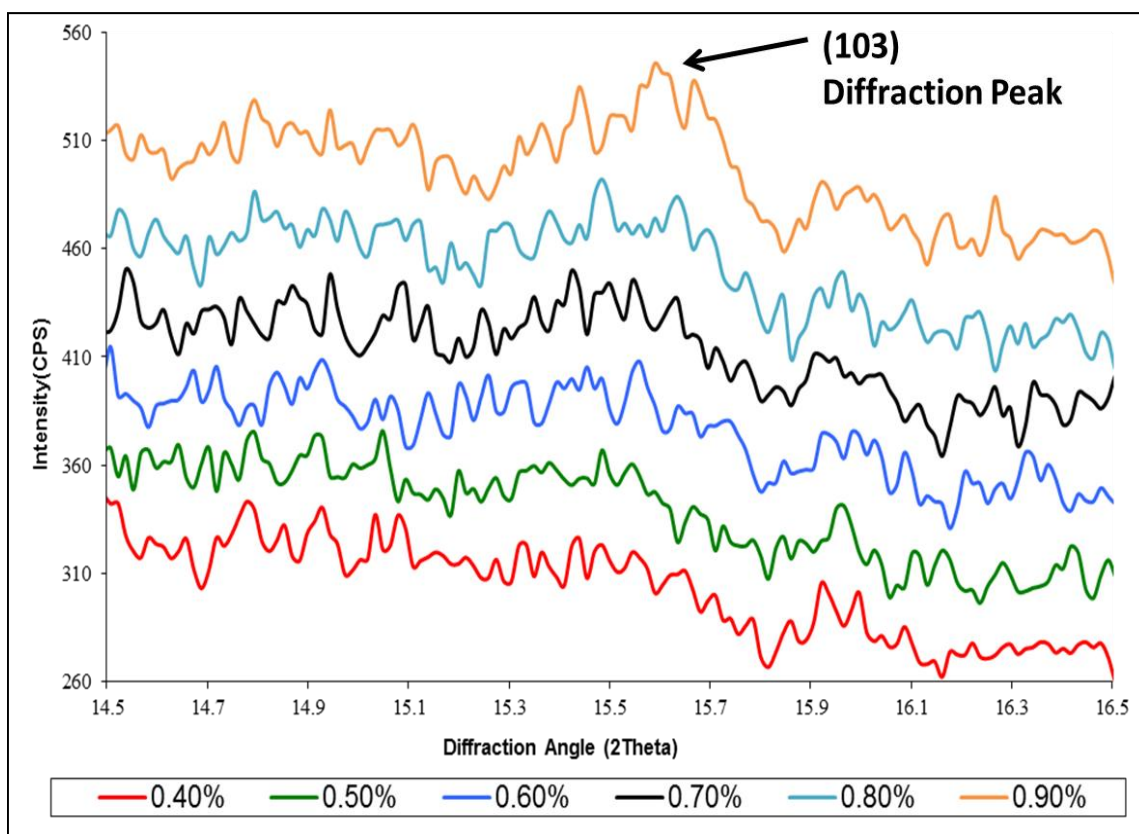
Figure 8-3 Unsmoothed alpha PABA XRD pattern for increasing slurry concentration

To further improve the LOD when using the transmission cell for *in-situ* work, a mathematical procedure developed by Chen et al[14] called smoothed principle component analysis (SPCA) was employed during the processing stage of data analysis. SPCA allows smoothing of the observed signal to reduce the effects of solvent background and instrument effects, to improve signal-to-noise ratio. SPCA can be employed on any XRD pattern collected using a MATLAB function − further information on this method can be found elsewhere[14].

The main benefits of SPCA is that the peak shape and area are unchanged when using this method and allows the LOD to be reduced, which allows identification of phases more quickly to improve quantitative measurements, and also qualitative identification of polymorphs. SPCA was applied to the raw data previously collected which showed the LOD to be 0.8 wt/wt%. The smoothed data after processing is shown in Figure 8-4. It can be seen that application of SPCA greatly reduces the background noise and improves the signal-to-noise ratio. The LOD for the alpha

polymorph after smoothing was found to be 0.5 wt/wt% which is a large improvement over the unsmoothed data.
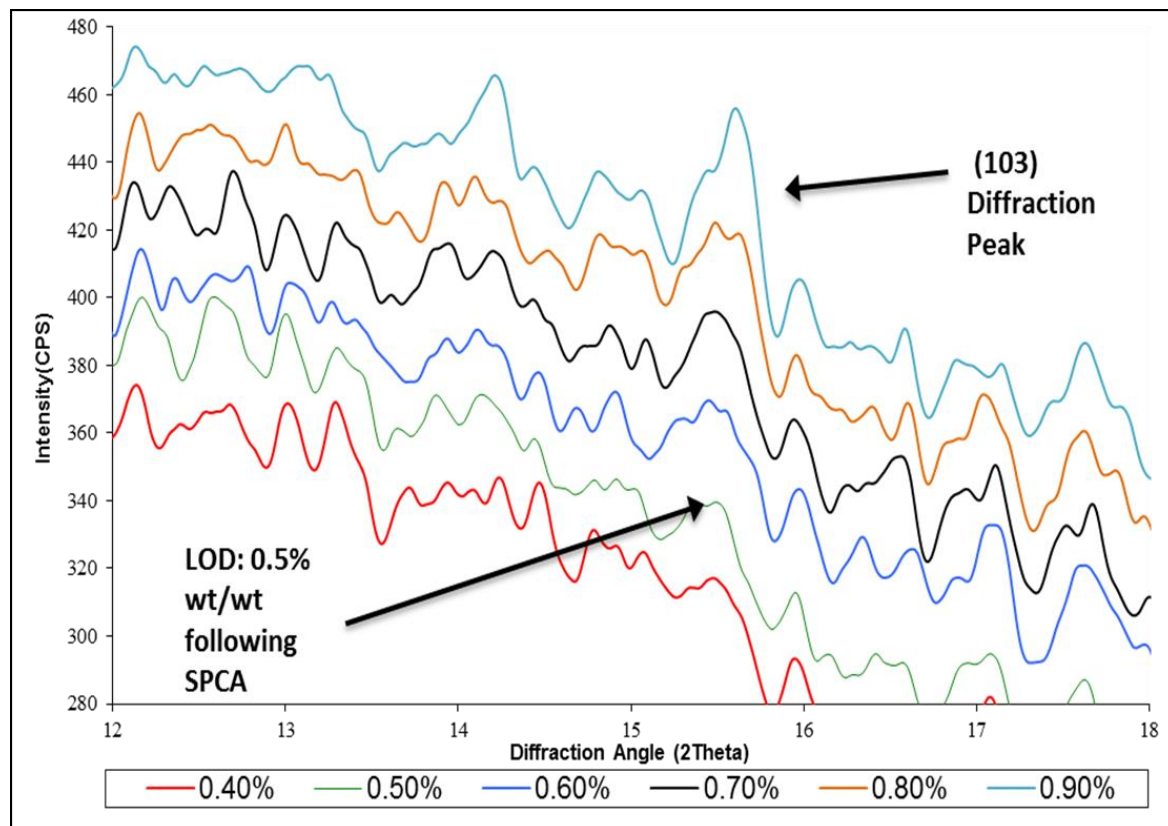
Figure 8-4 Smoothed PABA alpha XRD pattern for increasing slurry concentration (SPCA applied).

8.3 Beta – alpha Polymorphic Phase Transformation

8.3.1 Qualitative Phase Analysis and Concentration Calibration

Calibration studies were carried out in order to relate the peak area of fingerprint peaks of the two polymorphs directly to solids concentration in the slurry. Saturated solutions of each polymorph in 70:30 DI:EtOH were prepared at 20°C based on recorded solubility. The solutions were held at 20°C to prevent any unwanted transformation of the beta form, at this temperature the transformation takes several hours. Several concentrations of 2, 4, 6, 8 and 10 wt/wt% were analysed for both polymorphs with 3 repeat measurements; 5 minute data collection times were chosen.
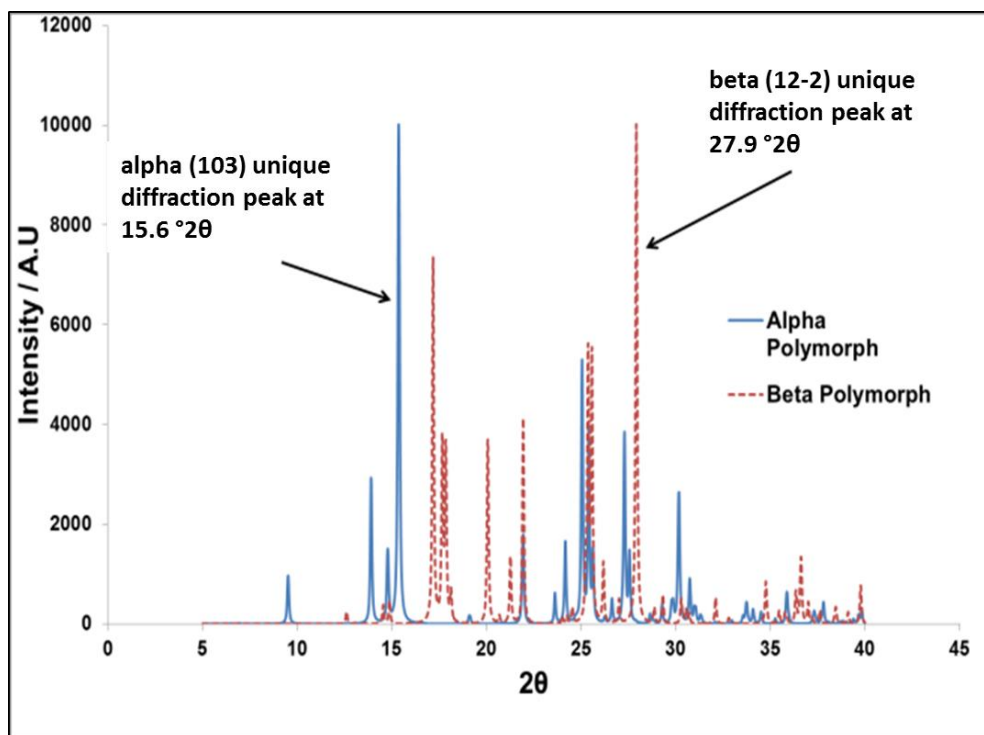
Figure 8-5 Simulated PXRD data for both polymorphs of PABA showing the unique single peaks of (103) for the alpha polymorph and (12-2) for the beta polymorph

The collected data was smoothed using SPCA (highlighted in Section 8.2.3) and then analysed using the software package Polycrystal, a Gaussian function was fitted to the observed peaks to obtain a fitted peak area, this value as a function of concentration was used for the calibration curve.
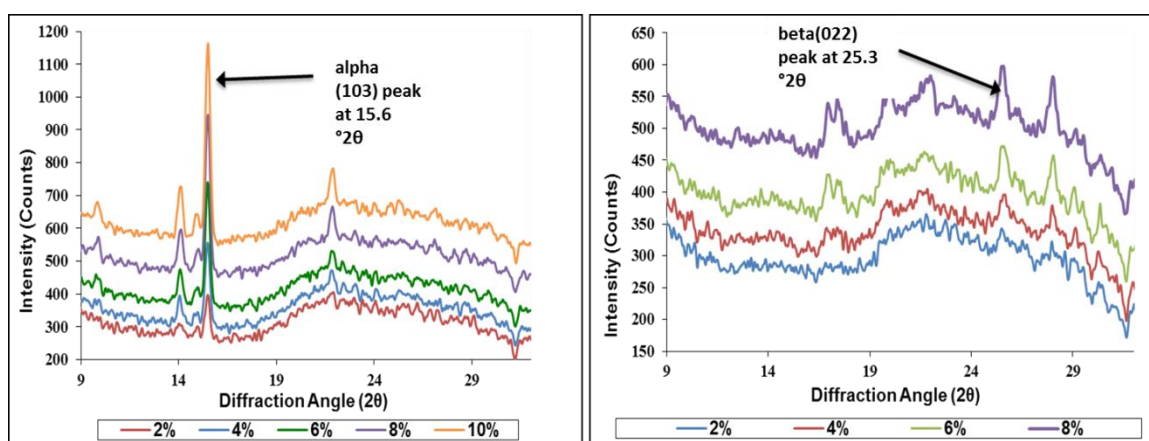
Figure 8-6 Recorded X-ray diffraction patterns of the alpha (left) and beta (right) polymorphs as a function of solids concentration for peak area calibration purposes

The modelled XRD patterns of the two polymorphs of PABA are shown in Figure 8-5, which presents the unique (103) peak of the alpha phase which was chosen for the calibration experiment. The unique beta phase reflection of the (12-2) plane at 27.9 2θ is also highlighted however when it came to performing the calibration experiments this reflection did not yield the highest intensity. As such the (022) reflection of the beta phase at 25.3 2θ was used instead as this provided the highest intensity relative to the background. No overlap between this reflection and the alpha phase was observed during the phase transformations due to the preferential orientation of the alpha phase. The calibration curves for both polymorphs are shown in Figure 8-7, it can be seen that the regression values of both are greater than 0.99 and a linear relationship fits well.
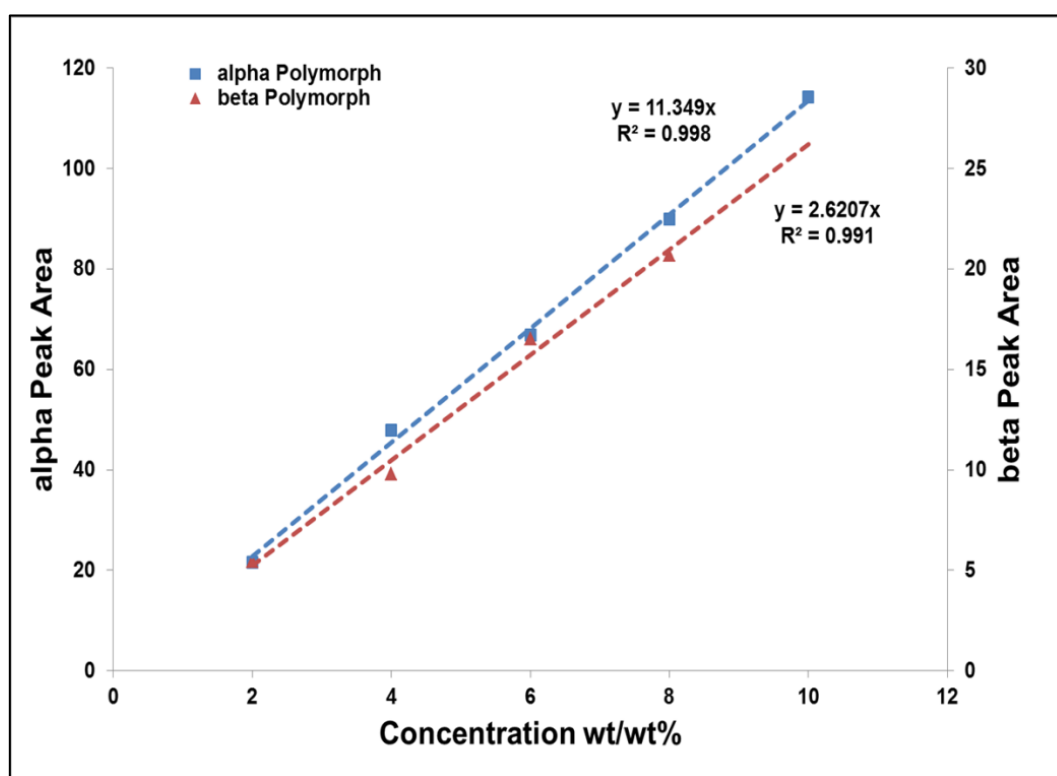
Figure 8-7 Calibration curves for the alpha and beta polymorph relating fitted peak area of the (103) and (022) peaks to solids concentration in wt%/wt%

8.3.2 Transformation Experiments

The seeded solution mediated polymorphic transformation (SMPT) experiments were carried out as highlighted previously, the raw data collected every 300s were

first smoothed using the SPCA method and then background subtraction was carried out followed by peak searching and fitting using a Gaussian function in the program Polycrystal. Figure 8-8 shows overlaid data for the phase transformation of the beta-alpha polymorph at 30°C, the data is offset along the ordinate for clarity with increasing time, the unique (103) alpha peak and (022) beta peak can be seen as dissolution of the beta phase occurs rapidly followed by growth of the alpha phase. Figure 8-9 highlights the same SMPT at 24°C and can be seen the major beta peaks are still visible but dissolution is much slower, and as such the growth of the alpha phase occurs less rapidly. Using the fitted areas of these peaks corresponding to a particular polymorph, and the linear equations in Figure 8-7 of the calibration curves, the wt/wt% solids concentration in the slurry can be calculated.
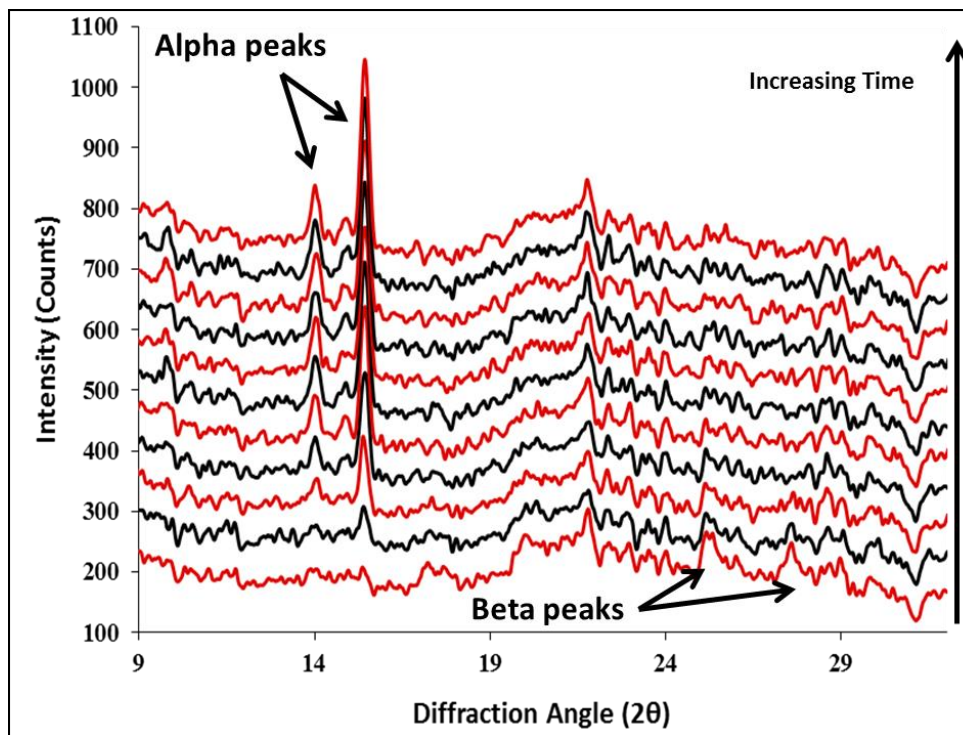
Figure 8-8 Phase transformation of the beta to alpha polymorph as a function of time at 30°C, diffraction patterns are offset along the ordinate for clarity
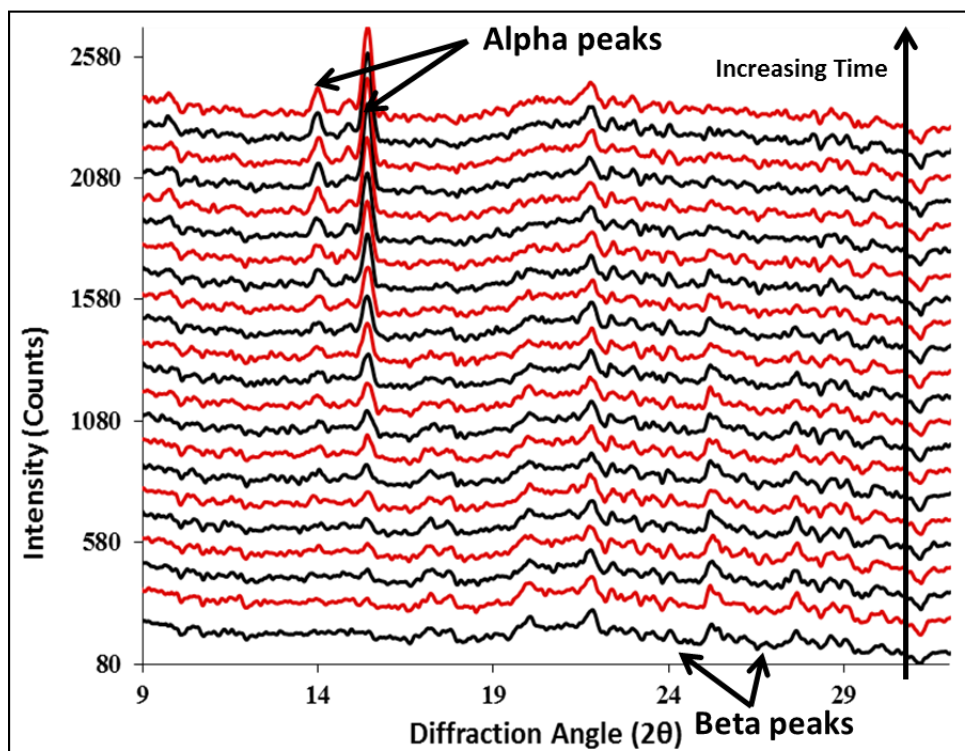
Figure 8-9 Phase transformation of the beta to alpha polymorph as a function of time at 24°C, diffraction patterns are offset along the ordinate for clarity

The solids concentration of both phases can be plotted as a function of time for the SMPT, Figure 8-10 shows how the concentration of solids of both phases changes with time during the 30°C SMPT. It can be seen that there is a very fast decrease of solids concentration of the beta phase due to rapid growth of the alpha phase and de-supersaturation of the solution at higher temperatures.

8.3.3 Determination of Kinetic Parameters

Application of solid state reaction models was performed to further characterize the dissolution and growth processes of each isothermal temperature condition. To do this the solids concentration measured must be altered to the mass fraction of solids converted. The mass of each phase was calculated from the wt/wt %, this could then be converted to mass fractions using Equations 8-1 and 8-2.

$$X\beta = 1 - \left(\frac{C\beta(t)}{C\beta(i)} \right) \quad \textbf{8-1}$$

$$X\alpha = \frac{C\alpha(t)}{C\alpha(f)} \quad \textbf{8-2}$$

Where Calpha(t) and Cbeta(t) are the concentrations of the respective phases at a given point in the reaction, Calpha(f) and Cbeta(i) are the concentration of alpha phase formed at the end of the reaction and the initial starting concentration of the beta phase respectively.
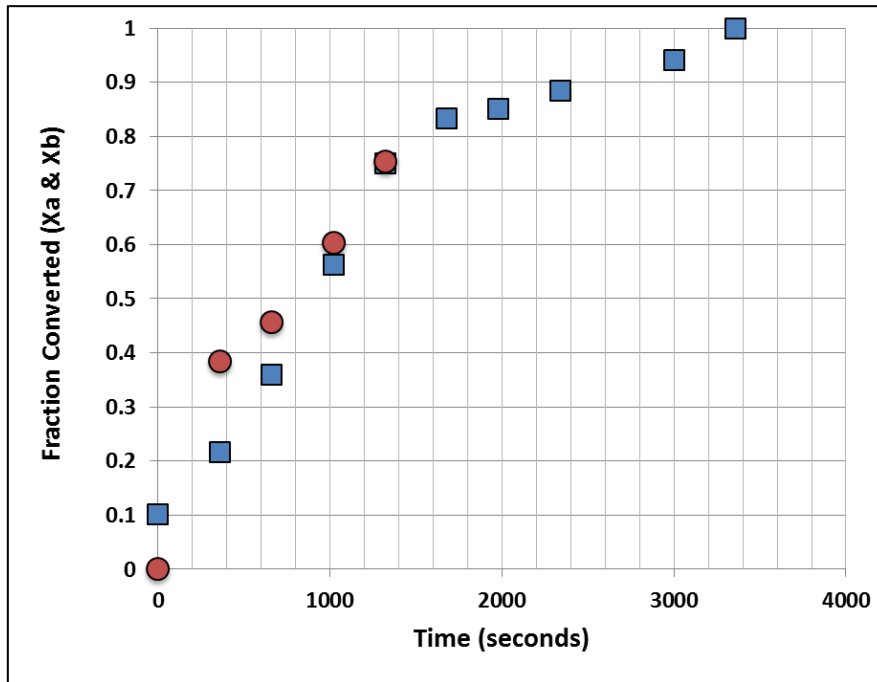
Figure 8-10 Mass fraction of solids converted as a function of time for the SMPT at 30°C, red circles; mass fraction of beta phase converted, blue squares; mass fraction of alpha phase converted.

Figure 8-10 shows the fraction of solids converted of each phase for the 30°C SMPT, this analysis was carried out for each isothermal experiment. This data was then used to apply a number of common solid state reaction mechanisms, listed in Table 2-1 to further analyse the kinetics of the growth and dissolution processes. The integral form of the rate equations listed, were used to apply these models to the data using Origin Pro (Figure 8-11). This allowed derivation of the rate constants from the various fits to the data. The regression values of the fits for the growth and

dissolution processes can be seen in Table 8-1 and Table 8-2 respectively, the best fits to the models are highlighted for clarity. The growth profiles of the alpha phase seem to fit a first order mechanism for the higher temperature reactions (30 and 28°C), however at the lower temperature (26 and 24 °C) the zero order mechanism seems to have a better regression value. This seems to indicate a change in mechanism between the two temperatures; however a more likely explanation is that the growth of the alpha phase is initially much lower at the lower temperatures and hence providing a much more linear like profile which fits to a zero order mechanism.

Table 8-1 Various solid state kinetic models for the growth of the alpha phase showing regression values.

Reaction Mechanism	30 °C	28 °C	26 °C	24 °C
Zero Order	0.73	0.89	0.95	0.94
First Order	0.96	0.92	0.84	0.81
Second Order	0.91	0.81	0.37	-0.23
1-D Diffusion	0.93	0.89	0.79	0.71

Table 8-2 Various solid state kinetic models for the dissolution of the beta phase showing regression values.

Reaction Mechanism	30 °C	28 °C	26 °C	24 °C
Zero Order	0.90	0.86	0.85	0.78
First Order	0.97	0.80	0.79	0.76
Second Order	0.83	0.57	-1.35	-14.75
1-D Diffusion	0.99	0.67	0.71	0.62

The dissolution of the beta phase follows a zero order mechanism and this is often seen for most organic materials. This highlights that the beta phase dissolves very quickly at the beginning of the SMPT to provide the necessary supersaturation for the fast growing alpha phase.
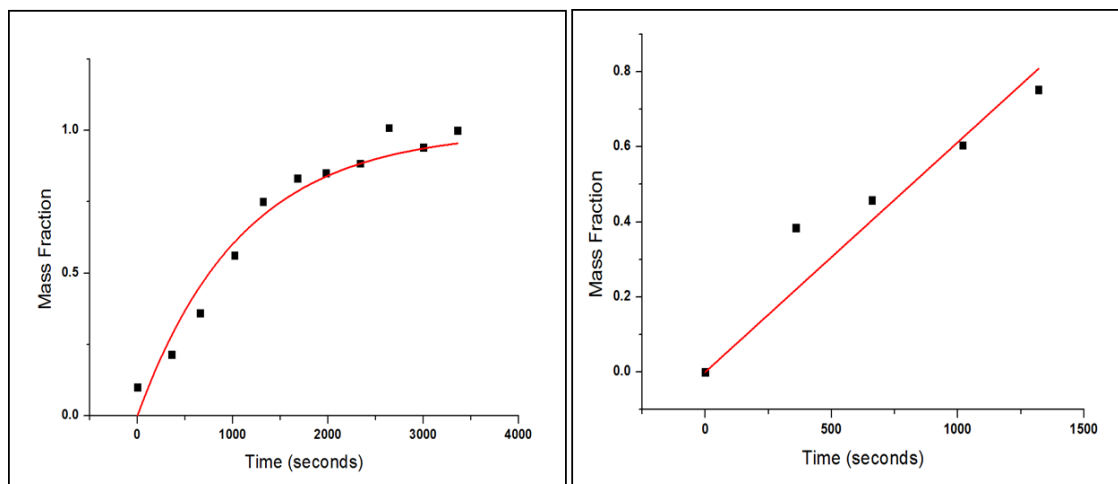
Figure 8-11 Zero order fit to the dissolution data at 30°C (right) and first order fit to the growth data (left).

The fits of the kinetic models to the growth and dissolution profiles for the SMPT of PABA at 30°C are highlighted in Figure 8-11 (left and right respectively). The first order fit of the growth profile and zero order fit of the dissolution profile are shown, from these the calculated values of growth and dissolution rate constants for the respective phases as a function of the isothermal temperature are provided in Table 8-3.

Table 8-3 Calculated values of the dissolution and growth rate constants with the ratio between them for the isothermal temperature experiments

Temperature (°C)	k_{galpha} (wt% s^{-1})	k_{dbeta} (wt% s^{-1})	K_{dbeta} / k_{galpha}
24	2.50E-04	8.17E-05	0.33
26	3.43E-04	1.98E-04	0.58
28	8.11E-04	4.99E-04	0.62
30	1.00E-03	6.80E-04	0.68
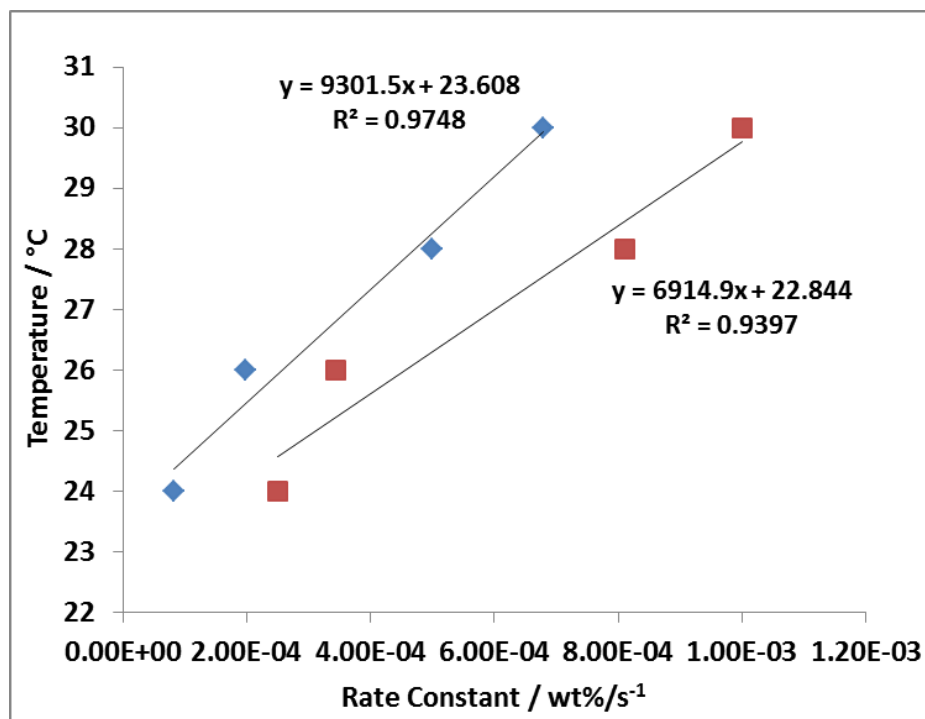
Figure 8-12 Plot of the dissolution (blue diamonds) and growth (red squares)rate constants as a function of temperature to estimate the transition temperature of PABA

The calculated values of the dissolution and growth rate constants from fitting of the rate models were then plotted as a function of the isothermal temperatures of the experiments in Figure 8-12. This allowed an estimation of the polymorphic transition temperature by extrapolation of a linear plot back to a rate constant of 0 wt% / s^{-1}. The linear fits to the data are highlighted in Figure 8-12 which shows the dissolution rate data can be fit with a linear equation of the form y = 9301.5x + 23.068 with a regression value of 0.98 this provides an upper estimate of the transition temperature as 23.6°C. The growth rate data can be fitted to a linear equation of the form y = 6914.9x + 22.844 with a regression value of 0.94, this provides a lower estimate of the transition temperature of 22.8°C. The calculated range of the polymorphic transformation temperature for the enantiotropic system is 22.8 – 23.6 °C.

This result fits reasonably well with previous calculated values of the transition temperature for the PABA system of 25°C and 16°C by Gracin et al and Svard et al

respectively, both of which were calculated from measured solubility data of the two polymorphs[15,16]. The discrepancies between these two values in the literature comes from the proximity of the solubility curves for the two polymorphs which are very close and hence increases the influence of systematic error on these calculations. The study by Hao et al provides a calculated transition temperature, by means of *in-situ* measurement of the solids concentrations of both polymorphic phases by Raman spectroscopy, as 13.8°C. This value is much lower than the calculated value from *in-situ* XRD experiments, this may be due to the timescale of the experiments performed; days in the case of the Raman experiments and hours in the case of the XRD experiment's. This suggests that in the XRD experiments, lower temperatures were not monitored for transformation because the experimental set-up would not allow long data acquisition times. The rates of transformation from the opposite transformation from the alpha to the beta phase were also not measured in this work again due to long transformation times, doing this could provide a more accurate assessment of the transformation temperature.

8.3.4 Reproducibility Testing

The *in-situ* XRD system was also tested for reproducibility regarding calculation of the kinetic parameters for the SMPT of the beta to alpha conversion. Six repetitions of the analysis at the isothermal temperature of 28°C were carried out and the subsequent growth and dissolution rate constants calculated at each repetition to analyse the deviation of the calculated kinetic parameters due to system noise and human error in the experiments.

Table 8-4 Calculated values of the growth and dissolution rate constants from the 6 repeat experiments at 28°C highlighting the standard deviation as a percentage relative to the mean value in each case

Repeat	*k alpha* (wt% s^{-1})	*k beta* (wt% s^{-1})
1	9.93×10^{-4}	4.98×10^{-4}
2	1.01×10^{-3}	5.81×10^{-4}
3	9.72×10^{-4}	4.05×10^{-4}
4	1.19×10^{-3}	8.13×10^{-4}
5	1.11×10^{-3}	4.35×10^{-4}
6	9.60×10^{-4}	4.74×10^{-4}
S.D.	9.11×10^{-5}	6.75×10^{-5}
S.D. %	8.77	12.62

Table 8-4 presents the results of the repeat analysis at 28°C providing the calculated growth rate and dissolution rate constants upon fitting the mass fraction vs time data to first order and zero order models respectively. The data show that the calculated standard deviation for the growth rate constant of the alpha phase is 8.77% and the dissolution rate constant of the beta phase is 12.62%.

The observed higher error in the beta dissolution rate constant can be explained by the variation in peak intensity ratios in the diffraction pattern, which is greater than those observed for the alpha phase. This is likely due to the alpha phase possessing a needle like morphology resulting in preferential orientation along the needle axis upon application of a flow to the crystals.

This could be beneficial for the calibration model as the (103) peak used for concentration calibration is perpendicular to the needle axis and hence will be increased in intensity relative to peaks in the a and c planes. This has the effect of increasing the signal to noise ratio particularly at low concentrations and hence the calibration model and thus the calculated kinetic parameters are less subject to systematic error. The opposite is true for the beta phase which has a more prismatic and isotropic structure which is reflected in its experimental diffraction pattern where the intensity is more evenly distributed between various reflections. This has the

opposite effect where larger systematic errors will be seen for lower concentrations relative to the same case in the alpha phase.

8.3.5 Solution and Solids Composition Analysis

The rate of the overall SMPT process is primarily determined by three components; the nucleation rate of the stable polymorph, the dissolution rate of the meta-stable polymorph and the growth rate of the stable polymorph. So far the composition of the solid state has been determined; now combining the measured transformation profiles with the measured solution supersaturation with respect to the meta-stable phase, an analysis of these three components can be described.
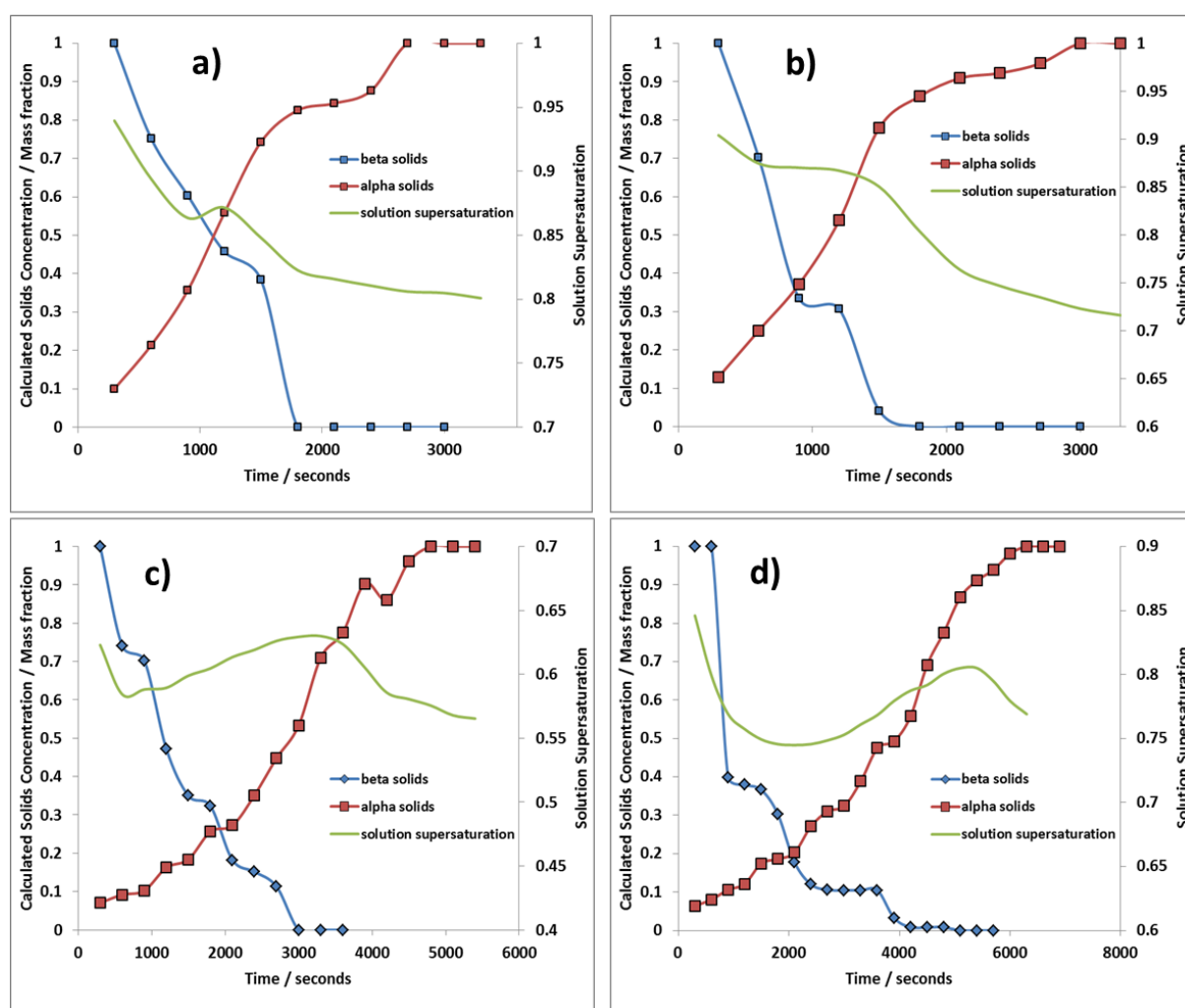

Figure 8-13 SMPT profiles of the beta to alpha phase transformation at a) 30°C, b) 28°C, c) 26°C and d) 24°C, together with the measured solution supersaturation from UV-Vis analysis

Figure 8-13 combines the calculated mass fraction of the solid components of both the alpha and beta forms of PABA from the XRD analysis, with the measured supersaturation profiles with respect to the beta form from UV-Vis analysis. The concentration profiles for all temperatures show that the SMPT proceeds with a very fast reduction in the solids concentration of the beta phase. This highlights that there is no considerable induction time for nucleation to occur; this is unsurprising considering that the solution is saturated with respect to the meta-stable phase and the experiments are seeded with the stable alpha phase. This results in no particular thermodynamic or kinetic barrier to nucleation and hence growth followed by likely secondary nucleation occurs instantly.

The trend in solution concentration relative to the meta-stable beta phase is similar at all 4 isothermal temperatures; whereby the solution de-supersaturates rapidly at the beginning of the SMPT. This precedes the dissolution of the beta phase which occurs generally before any large amount of the stable alpha phase has been produced. This is indicative of a 'dissolution controlled' process (Figure 8-13) whereby the rate at which the stable phase grows out of solution ($\%wt.s^{-1}$) is much greater than the rate at which the meta-stable phase is dissolving ($\%wt.s^{-1}$) to sustain the supersaturation of the solution required for growth.

This conclusion is also supported by the ratio of the dissolution and growth rate constants in Table 4 which highlights that the values at all isothermal conditions are <1. Davey and Cardew[3] showed that this too is indicative of a 'dissolution controlled' process and further supports these results. This rapid decrease in solution concentration is followed by a small plateau region most easily visible in the transformation profile of the 28°C isothermal experiment in Figure 8-13b). This plateau region occurs when most of the beta phase has dissolved and the alpha phase is still growing. This likely indicates when an equilibrium phase is reached due to the fast growth of alpha and the dissolution of beta is becoming increasingly rate limiting.

The intrinsic rate of dissolution ($g/m^2.L.s$) from a molecular point of view is thought to be larger than the intrinsic rate of growth ($g/m^2.L.s$) due to the transport of solute across a boundary layer followed by surface rearrangement and integration to kink sites in the latter. If the rates of dissolution and growth are very similar then the

barrier to the dissolution process maybe due to particle size and particle number differences between the stable and meta-stable phases.

This would suggest that the stable phase will contain a large number of growing crystal nuclei with large solid-liquid interfacial surface area and conversely the dissolving meta-stable phase will have a very small solid-liquid interfacial surface area. This model, if used to explain the observed dissolution controlled process in the PABA beta – alpha transformation, is certainly plausible; the nucleation kinetics of PABA alpha in more dilute solutions such as water tend towards a more progressive mechanism, as highlighted in Chapter 6, which would produce a large number of nuclei, C_0. The experiments in these transformation studies are of course carried out in slurry's compared to cooling crystallisations for the nucleation kinetics experiments; however the correlation is still interesting.
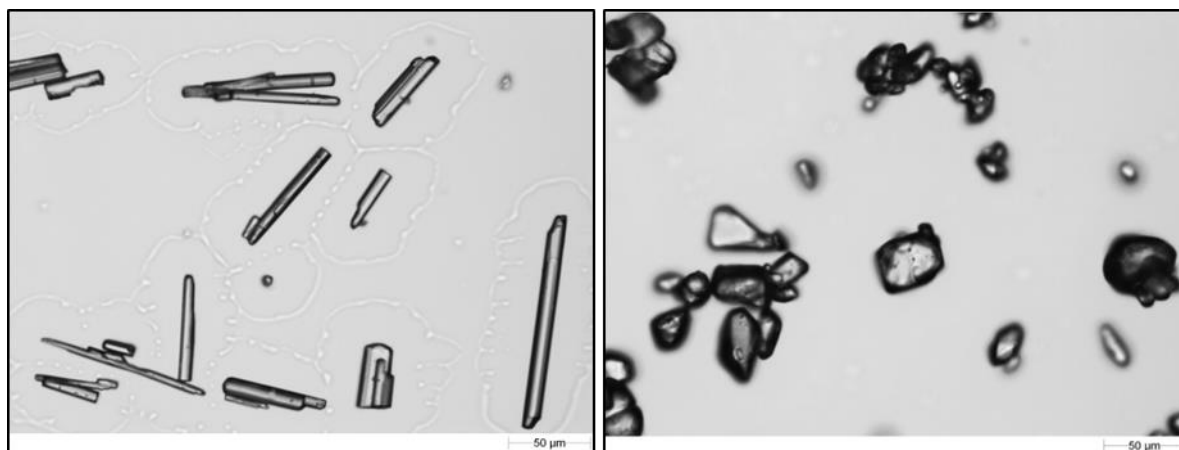
Figure 8-14 Micrographs of the alpha crystals recovered from the transformation experiments (left) and the starting beta phase seeds (right)

The second factor which supports this view are the observed experimental particle morphology's of the two phases, the beta phase is much more isotropic compared to the needle like structure of the alpha phase as seen in the micrographs in Figure 8-14. This could result in a slower dissolution rate of the beta phase due to smaller solid-liquid interface area relative to the very directional growth of the alpha phase which primarily occurs along the b needle axis with a much larger solid-liquid interfacial area. The third factor is that of secondary nucleation, due to a number of seed crystals added at the beginning of the experiments, particle attrition is certainly

likely which would lead to increased secondary nucleation and hence an increased number of crystal nuclei and a larger solid-liquid interface area of the stable phase.

The mechanism of the SMPT of beta – alpha has been shown to be a 'dissolution controlled process', however a number of studies have provided evidence to suggest that a 'growth controlled' process is more likely for most systems due to differences in the intrinsic rates of dissolution and growth expected for organic materials. The example of piracetam form 2 – form 3, glycine alpha to gamma form and l-glutamic acid alpha to beta form all show growth controlled SMPT and the ratios of the dissolution and growth rate constants are much greater than 1[17, 18, 19]. Interestingly, with the exception of glutamic acid, the growth controlled SMPT's of theses polymorphs involve morphological changes from a needle like phase to a prismatic like phase, contrary to the case of PABA. This suggests that the rate limiting factor to these phase transformations is likely a complex combination of the solution thermodynamics and crystallisation kinetics.

8.4 Conclusions

The dissolution and growth processes during the SMPT of PABA beta – alpha have been successfully monitored using *in-situ* XRD using a novel transmission flow through cell in combination with *in-situ* UV-Vis spectroscopy methods, to monitor the solids concentration and solution concentration respectively. It has been found that there is a possible mechanistic change in the transformation process between 28 and 26°C, this is highlighted by the change in growth rate mechanisms of the alpha phase from solids concentration measurements.

Measurement of the solution concentration by UV/Vis spectroscopy shows a fast de-super-saturation indicative of a dissolution controlled process. This was explained by consideration of the measured nucleation kinetics in Chapter 6, where it was found that aqueous solutions contain a large number of nuclei upon nucleation. A further explanation was provided by the observed particle morphologys of the beta and alpha phase where the isotropic particle morphology of the dissolving beta phase slows down this process whereas the fast growth of the alpha phase can be linked to its more directional morphology.

This chapter has provided a combination of flow cell development with combined in-process XRD and spectroscopy results to provide an insight into the factors which direct the dissolution and growth of the final macroscopic crystalline phases during the beta to alpha SMPT process. The results discussed provide kinetic data on the dissolution and growth processes and therefore contribute towards core thesis objective 4.

References

[1] J. Schöll, D. Bonalumi, L. Vicum, M. Mazzotti, M. Müller, *Cryst. Growth Des.* 2006, 6, 881

[2] H. Hao, M. Barrett, Y. Hu, W. Su, S. Ferguson, B. Wood, B. Glennon, *Org. Process Res. Dev.*, 2012, 16, 35

[3] P. T. Cardew, R. J. Davey, *Proc. R. Soc. London,* 1985, *A398*, 415, 28

[4] R. J. Davey, P. T. Cardew, D. Mcewan, D. E. Sadler, *J. Cryst. Growth,* 1986, *79*, 648.

[5] N. Doki, H. Seki, K. Takano, H. Asatani, M. Yokota, N. Kubota, *Cryst. Growth Des.* 2004, 4, 949

[6] G. Févotte, *Int. J. Pharm.,* 2001, 241, 263

[7] E. S. Ferrari, R. J. Davey, *Cryst. Growth Des.* 2001, *4,* 5, 1061

[8] K. Poellaenen, A. Haekkinen, S. Reinikainen, J. Rantanen, M. Karjalainen, M. Louhi-Kultanen, L. Nystroem, *J. Pharm. Biomed. Anal.* 2005, 38*,* 2, 275

[9] T. Ono, J. H. Horst, P. J. Jansens, *J. Cryst. Growth,* 2004, 4*,* 3, 465.

[10] L. E. O'Brien, P. Timmins, A. C. Williams, P. York, *J. Pharm. Biomed. Anal.* 2004, 36, 2, 335

[11] C. Herman, B. Haut, S. Douieb, A. Larcy, V. Vermylen, T. Leyssens *Org. Process Res. Dev.*, 2012, 16, 49

[12] Y. Hu, H. Wikstrom, S. R. Byrn, L. S. Taylor, J. Pharm. Biomed. Anal., 2007, 45, 546

[13] S. Dharmayat, R. B. Hammond, X. Lai, C. Ma, E. Purba, K. J. Roberts, Z. Chen, E. Martin, J. Morris, R. Bytheway *Crystal Growth & Design,* 2008, 8, 7

[14] Z. P. Chen, J. Morris, E. Martin, R. B. Hammond, X. Lai, C. Y. Ma, E. Purba, K. J. Roberts, R. Bytheway, *Anal. Chem.* 2005, *77*, 20, 6563

[15] S. Gracin, A. C. Rasmuson*, Cryst. Growth Des.*, 2004, 4, 1013

[16] M. Svard, F. L. Nordstrom, E. Hoffmann B. Aziz, Å. C. Rasmuson, *CrystEngComm*, 2013,15, 5020

[17] M. A. O'Mahony, A. Maher, D. M. Croker, Å. C. Rasmuson, B. K. Hodnett, *Cryst. Growth Des.* 2012, 12, 1925

[18] X. Yang, J. Lu, X. Wang, C. B. Ching, *J. Raman Spectrosc.*, 2008, 39, 1433

[19] H. Qu, M. Louhi-Kultanen, J. Rantanen, J. Kallas, *Cryst. Growth Des.,* 2006, 6, 2053

Chapter 9 Conclusions and Future Work

Conclusions are drawn together from the results of this thesis together with an assessment of the core thesis objectives and suggestions for future studies

9.1 Introduction

The work presented in the preceding results chapters aimed to extend the knowledge surrounding the structural information regarding the nucleation pathway to formation of a crystalline phase. These aims were based on a lack of fundamental knowledge relating to solution state structure, nucleation clusters and the final macroscopic crystalline phase and the pathway between them.

The chapters presented in this thesis set out to provide a multi-scale approach to understanding the nucleation and subsequent crystallisation of PABA form its saturated solution, with a fundamental molecular approach to explaining this process. The solubility and solution chemistry studies in Chapter 5 were vital for planning the subsequent crystallisation experiments and provided an initial structural link between the solution and solid state assemblies. The poly-thermal and iso-thermal experiments together with the SAXS studies in Chapters 6 and 7 probed nucleation kinetics, thermodynamics and the structural progression of the nucleation process for the PABA system. Chapter 8 provided kinetics information on the solution state polymorphic transformation of the beta to alpha phases.

These studies are concluded in this chapter with a focus on equipment development followed and the link between solution structure, nucleation kinetics and cluster formation. The aims and objectives of the thesis are then reviewed and finally future studies are suggested based on the findings of this work.

9.2 Conclusions of this Study

9.2.1 Development of Instrumentation

An in house built SAXS instrument with a collimated X-ray Micro-source, 2D detector, variable flight tube and adjustable sample stage environment was developed as part of this thesis. The use of this instrument enables *in-situ* characterisation of structural information at the Nano-scale for solid or liquid samples in static or flow environments with complete temperature control. The instrument allows information to be obtained on particle sizes, particle morphology, inter-particle interactions and surface properties from subsequent fractal analysis.

The commissioning experiments summarised in Chapter 7 provided a rigorous test of the instruments capabilities through analysis of known and well-studied standard samples. Analysis of Ludox colloidal silica samples provided a maximum size limitation for detection at the current set-up, which was found to be 23-28.6 nm as a spherical diameter. The minimum sample exposure time was also measured through analysis of the silica Nano-particle samples and found a minimum of 30 minutes was required to obtain a scattering pattern with sufficient structural information above the background scattering.

Further commissioning experiments on micro-emulsion samples provided an estimate of the minimum $\Delta\rho$ required between solute and solution to provide a measurable scattering pattern. This was found to be between 19.2-179 eu/nm^{-3}, this was crucial in planning the future SAXS experiments at synchrotron sources. Additionally the scattering data form the AOT and Triton X100 systems revealed a linear correlation between the water concentration and the measured radius of the water pool. These results provided evidence for the applicability of the instrument in resolving Nano-structural information on a variety of sample types.

The requirement of *in-situ* sample cell environments for this research led to the development of a capillary transmission flow cell, which was utilized during the *in-situ* solution phase transformation studies in Chapter 8. This design has been refined and tested during this research and enables wide angle X-ray diffraction analysis on-line during solution crystallisation experiments. The cell was applied to an online XRD rig together with 100 ml crystallisation vessel with ATR UV/Vis probe, resulting

in a system which can monitor solution and solids concentrations during slurry transformation experiments. The limit of detection of the new cell was found to be 0.5wt% concentration of solids; this is an improvement over previous solution state cells utilised on the same experimental rig.

9.2.2 The Relationship between Solution Chemistry, Nucleation and the Solid State

9.2.2.1 Solution State Characterisation

The solubility of PABA in a variety of solvent systems was determined by UV/Vis, gravimetric and C16 analysis. Further calculations of the enthalpy and entropy of dissolution together with activity coefficients provided evidence of solute-solute interactions from negative deviations away from ideality. The negative deviations from the van't Hoff solubility were rationalised by consideration of the non-polar character of the benzene ring in combination with the polar end groups of PABA. Analysis of the free energy of mixing highlighted negative decreases in entropy of mixing in most solvent systems which further provided evidence of molecular aggregation in solution.

The key structural synthons from the solid state structures of PABA were identified from the crystal structures. FTIR results found the appearance of two carbonyl bands in the solution state spectra, which upon dilution undergo intensity ration variations. This concluded the presence of solution state carboxylic acid dimers which was consistent with the van't Hoff solubility analysis and provided experimental evidence of a link between the alpha phase solid state structural synthon and solution state synthon. Assignment of these IR bands relating to the carbonyl stretching frequencies of the dimerised and solvated structures was supported by MD simulations of the IR spectra for the dimer and monomer species in solution which showed the appearance of the monomer band at higher wavenumber in comparison to the dimer band.

9.2.2.2 Nucleation Kinetics

The isothermal nucleation kinetics studies found that the interfacial tension values calculated in water were 2.36 – 2.60 mJ/m^{-2} which were higher than those in ethanol at 0.85 – 1.31 mJ/m^{-2}. These values were found to be relatively low in comparison to most organic materials and as such the critical nuclei were also low 0.48 – 1.31nm across both solvent systems.

Poly-thermal experiments revealed that the nucleation mechanisms tended toward an instantaneous mechanism at higher concentrations and a progressive mechanism at lower concentrations. This was also observed when comparing between ethanol and water, where water showed a more progressive mechanism. The concentration of nuclei was found to be highest in water and lowest in ethanol, suggesting that attachment frequency was greatest in water and lowest in ethanol, this correlated well with MD simulations of ΔG_{solv} which in combination with previous studies of PABA, suggested that attachment frequency should be highest in water and lowest ethanol.

The interfacial tension values from the KBHR analysis were found to be much larger than those calculated for the higher concentration samples analysed by isothermal analysis. This revealed that as concentration decreases the interfacial tension becomes more rate limiting for nucleation relative to the attachment frequency and explains the more progressive nucleation mechanism. This was found to explain the nucleation mechanism changes between solvents with the solution concentration been the driving factor; this was also supported by the calculated interfacial tension values which were higher in water than in ethanol and hence forcing a more thermodynamically controlled process rather than a kinetic one.

These results provided an interesting conclusion that the nucleation pathway of PABA is concentration dependant and that the solute must stabilise the saturated state at higher concentrations, particularly in ethanoic solutions and to a much lesser extent in water. This correlates well with solubility studies in Chapter 5 where PABA was found to self-associate.

Analysis of the growth exponents of PABA in the three solvents were found to decrease from water to acetonitrile to ethanol, which suggested that a barrier to

growth was present in water solutions which was significantly decreased or not present in ethanol. This was confirmed by optical analysis of the recovered crystallites where the largest crystals, particularly in the needle axis, were found in ethanol solutions followed by acetonitrile solutions and finally water solutions. This was extended to the (00-1) plane which lies in the plane of the needle axis and in combination with published work on PABA which showed that a dimer of PABA would favour attachment at this surface relative to a monomer. This could provide an explanation for the increased growth along the needle axis in the ethanol solutions.

9.2.2.3 Pre-Nucleation Clustering

Small angle scattering results provided a structural probe to the nucleation pathway of PABA. The results showed that from cooling crystallisations of highly saturated ethanolic solutions the R_g value of the high q region increases from the value of a monomer to that of a dimer. This provided further evidence for a population of monomers and dimers in saturated solutions. This correlated well the solubility and FTIR studies in Chapter 5 and provides further confidence in the FTIR solution state spectra.

The iso-thermal and poly-thermal synchrotron SAXS experiments provided evidence for the presence of large highly disordered clusters of PABA in the under-saturated and saturated states. The size and structural order of these clusters increased as the solution driving force increased in both experiments. A fractal model was found to fit these large clusters the best suggesting that the interface between cluster and solution is highly disordered; this was in agreement with the very low interfacial tension values calculated in Chapter 6.

The existence of the large liquid-like clusters in ethanolic PABA solutions provided an explanation for the observed nucleation mechanism change at low concentrations to a more progressive mechanism highlighted in Chapter 6. It was postulated that the large clusters which form, can self-stabilise the PABA solutions and when the critical concentration upon decreasing the solute concentration is reached; the large structures are no longer stable hence the nucleation mechanism change. Although not conclusive this is the first time a link between the nucleation mechanism and SAXS data has been made.

Combining the results of this study a mechanism for the nucleation of PABA was presented whereby the nucleation pathway proceeds through the formation of large disordered clusters of PABA which increase in size and fractal dimensionality through addition of the dimer structure.

9.2.3 Polymorphic Transformation Kinetics

Characterisation of the solution mediated phase transformation of the beta – alpha polymorphs of PABA through *in-situ* XRD and UV/Vis spectroscopy revealed the rate limiting kinetic processes for this phase conversion.

The peak area of polymorph specific Bragg reflections, in combination with a calibration model, allowed calculation of the mass of the two phases of PABA in the slurry. This enabled calculation of the growth and dissolution rate constants of PABA alpha and beta respectively. The ratio of $k_{d\beta}$ and $k_{g\alpha}$ was shown to be <1 at all isothermal temperatures which indicated that the conversion process was dissolution controlled. This was further supported by analysis of the de-supersaturation curves monitored using *in-situ* UV/Vis spectroscopy. The de-supersaturation profiles revealed a fast de-supersaturation of the solution at the start of the transformation process, which precedes the dissolution or growth of the two phases, this indicative of a dissolution controlled process.

This was explained through analysis of the particle morphologies of both phases where by the isotropic prismatic beta phase will have a much lower solid-liquid interfacial area in comparison to the more needle-like morphology of the growing alpha phase. This would result in fast growth of the alpha phase relative to the slower dissolution of the beta phase.

The observation of a dissolution controlled process was also attributed to the derived nucleation mechanism observed in solvents with a lower PABA solubility such as water, presented in Chapter 6. A more progressive mechanism was observed in water which leads to a large number of nuclei forming upon nucleation. A large number of nuclei would result in fast alpha growth and hence fast de-supersaturation of the solution which could be another explanation for the observed dissolution controlled process.

Further to this an estimation of the polymorphic transformation temperature was calculated by plotting the dissolution and growth rate constants as a function of temperature. Extrapolation of the rate constants to 0 wt%/s^{-1} yielded a transition temperature between 22.8 – 23.6 °C.

9.3 Review of Thesis Aims and Objectives

Considering the original core thesis aims and objectives this combination of research has provided a new link between solution state structural synthons and molecular pre-assembly to the solid state structures found in the alpha polymorph of PABA. Poly-thermal and iso-thermal studies have provided a new understanding of the nucleation mechanism and kinetics as a function of solvation environment and concentration of the alpha polymorph. SAXS studies have revealed further evidence for the existence of large liquid-like clusters of PABA along the nucleation pathway.

Combined *in-situ* XRD and UV/Vis experiments provided measurements of growth and dissolution kinetics for the beta to alpha polymorphic transformation of PABA. Combining the results of this work a proposed structural model for the nucleation pathway associated with the crystallisation of alpha PABA from solution was proposed which builds on previous studies in this area.

However some objectives were not met during this research, specifically understanding the structural progression of nano-crystallite formation post-nucleation and relating this to knowledge of the solution state and cluster information gained from the previous work.

Further to this the measured solubility, nucleation parameters and SAXS analysis were all performed specifically on the alpha polymorph of PABA. This is due to the difficulty in directly nucleating the pure beta form which led to a lack of the crystalline material. Planning experimental work, specifically considering scattering experiments, with the beta polymorph is also particularly difficult due to the unstable nature of this polymorph at higher temperatures.

9.4 Suggestions for Future Work

The ultimate aim of this thesis was to improve the understanding of nucleation, with a particular insight into the structural parameters which govern this process. However considering the bigger picture of not only industrial crystallisation but the fundamentals of crystallisation, much more work and technological breakthroughs will be required to move towards the directed assembly of crystalline materials with targeted solid state properties. This can only be achieved through a thorough fundamental understanding of nucleation to the point of predictive process design based on knowledge and understanding of the underlying process chemistry and physics.

A particular focus for the future of nucleation is a further understanding into the building unit of the critical cluster, as self-assembly has been shown to ultimately drive the nucleation of certain polymorphic phases. This will likely involve a multi-disciplinary approach utilising FTIR and Raman spectroscopies together with solution state NMR and neutron scattering experiments to probe the solution state self-assembly of organic materials. This in combination with measured kinetic data on nucleation would enable efficient design of crystallisation processes for certain polymorphic phases by linking the building unit to kinetic parameters which direct the rate of nucleation.

A particular challenge for the future of nucleation research is the structure of the pre-critical and post-critical nano-scale assemblies of solute. There has been a huge step forward in this area of research in past ten to twenty years, identification of large scale clusters of organic materials during nucleation has been particularly interesting due to the questions its asks of classical nucleation theory. The disagreements between CNT and the 2 step model generally hinge on this area and so identifying the structure of the nucleus would be a step change in developing a unified theory of nucleation.

Much work in the arts of dynamic light scattering[1,2,3,4,5,6], X-ray[1,7,8] and neutron[9] scattering, Brownian motion microscopy[1] and cryogenic electron microscopy[2] have so far provided interesting data in this area and a combination of these techniques will be required in order to answer this particularly complex question.

Technological development of synchrotron and neutron sources will be required to provide higher energy, micron-size beams to enhance time and contrast resolution for scattering experiments in order to probe the cluster Nano-structure at sub-second timeframes. This in combination with state of the art molecular modelling of the nucleation pathway will prove vital in explaining whether a system nucleates through monomer addition to an organised nucleus or by addition to a liquid-like pre nucleation cluster.

Focusing these concepts to PABA, further scattering experiments at neutron sources would be required to probe the larger cluster structures reported in Chapter 7. A smaller *q* limit would provide additional *q* space for the larger structures to be analysed, utilising a neutron source would also provide better phase contrast hence yielding further structural information. This would allow a more detailed analysis of the size and fractal dimensions of the reported Nano-sized structures which appear to be liquid-like from this work. Further to this a comprehensive Guinier analysis would reveal the value of I_0 associated with these structures enabling calculation of the concentration of PABA solute contained within these pre-nucleation assemblies.

This analysis would lead to a more complete understanding of the role of these large structures in the nucleation of PABA and possibly similar organic materials. This knowledge is vital in providing information which in combination with complementary experimental and modelling techniques, could lead to identification of the critical cluster structure.

Additionally analysis of the crystallisation process of PABA using *in-situ* synchrotron WAXS would provide information on micro-crystallite structural progression by use of line broadening analysis. This would reveal the structural progression of the micro-crystallites in terms of lattice directions, also the size progression and crystalline disorder could be probed using this technique. The results of such experiments would provide much needed information on the growth of micro-crystallites just after nucleation. This could be linked to the results of neutron scattering experiments to correlate structural similarities or differences in the pathway to crystallisation.

References

[1] A. Jawor-Baczynska, J.Sefcik, B. D. Moore, *Cryst. Growth Des.* 2013, 13, 470

[2] A. Jawor-Baczynska, B.D. Moore, H. S. Lee, A. V. McCormick, J. Sefcik, *Faraday Discuss.*, 2013, 167, 425

[3] Y. Ma, H. Colfen, M. Antonietti, *J. Phys. Chem. B*, 2006, 110, 10822

[4] D. Schwahn, Y. Ma, H. Colfen, *J. Phys. Chem. C*, 2007, 111, 3224

[5] D. D. Medina, Y. Mastai, *Cryst. Growth Des.,* 2008, 8, 3646

[6] H. Colfen, S. Mann*, Angew. Chem., Int. Ed.*, 2003, 42, 2350

[7] S. Chattopadhyay, D. Erdemir, J. M. B. Evans, J. Ilavsky, H. Amenitsch, C. U. Segre, A. S. Myerson, *Cryst. Growth Des.*, 2005, 5, 523

[8] A. Sauter, F. Roosen-Runge, F. Zhang, G. Lotze, R. M. J. Jacobs, F. Schreiber, *J. Am. Chem. Soc.* 2015, 137, 1485

[9] C. A. Koh, R. P. Wisbey, X. P. Wu, R. E. Westacott, A. K. Soper, *J. Chem. Phys.* 2000, 113, 6390

Appendix: Poly-thermal and KBHR Raw Data

1. Raw Turbidometric Data from Poly-Thermal Crystallisation Experiments

Figures 1, 2 and 3 present examples of raw turbidometric data collected on the Crystal 16 apparatus for the 6 g/kg concentration aqueous PABA solution at a range of cooling rates; 0.1, 0.3, 0.5, 0.7 and 1.0 °C/min. These plots allow extrapolation of the crystallisation and dissolution temperatures T_{crys} and T_{dis}.
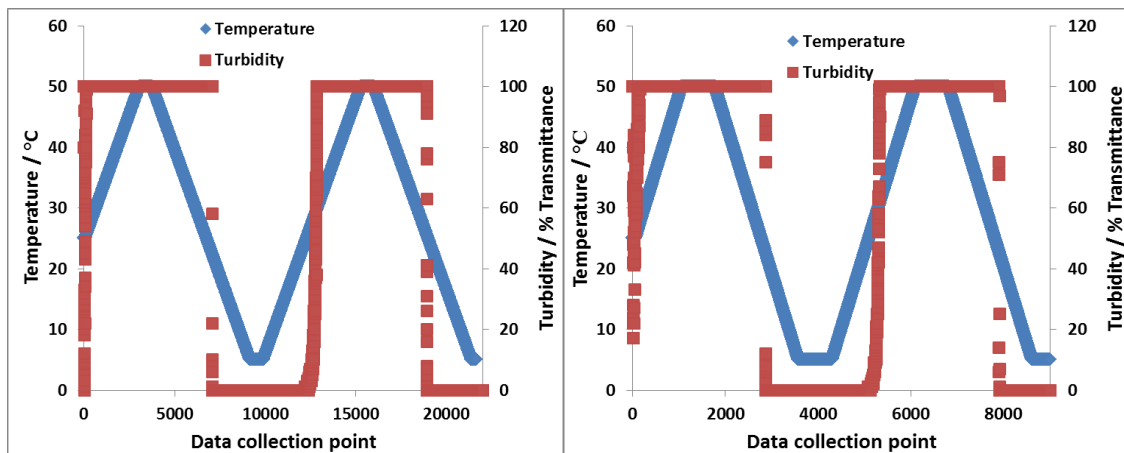

Figure 1: Turbidity vs temperature plot for crystallisation of PABA from 6 g/kg aqueous solution at 0.1left and 0.3 °C / min right
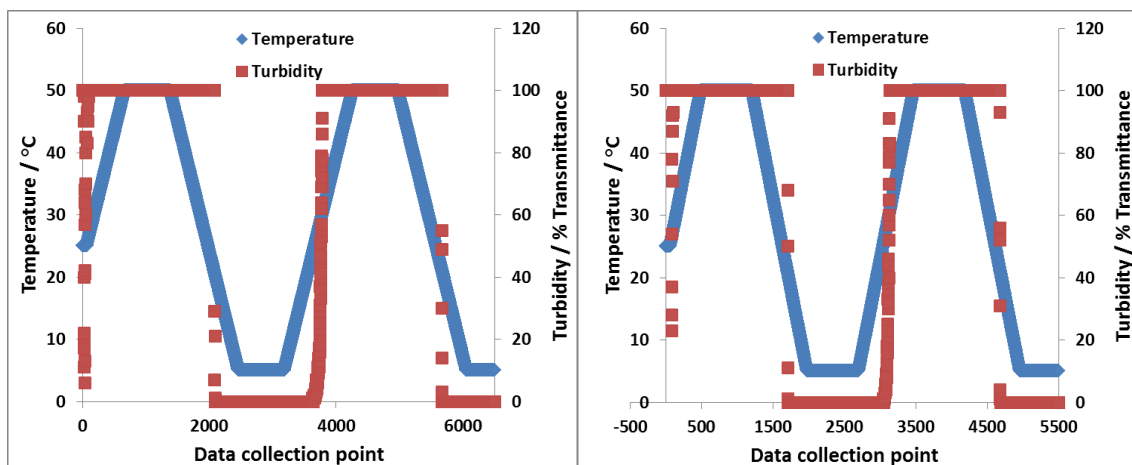

Figure 2: Turbidity vs temperature plot for crystallisation of PABA from 6 g/kg aqueous solution at 0.5 °C / min left and 0.7°C / min right
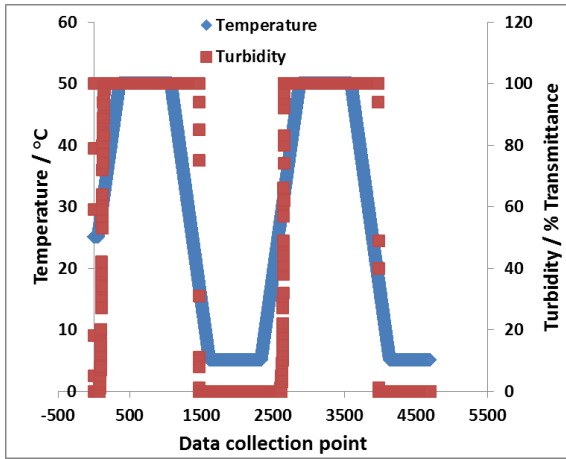
Figure 3: Turbidity vs temperature plot for crystallisation of PABA from 6 g/kg aqueous solution at 1.0°C / min
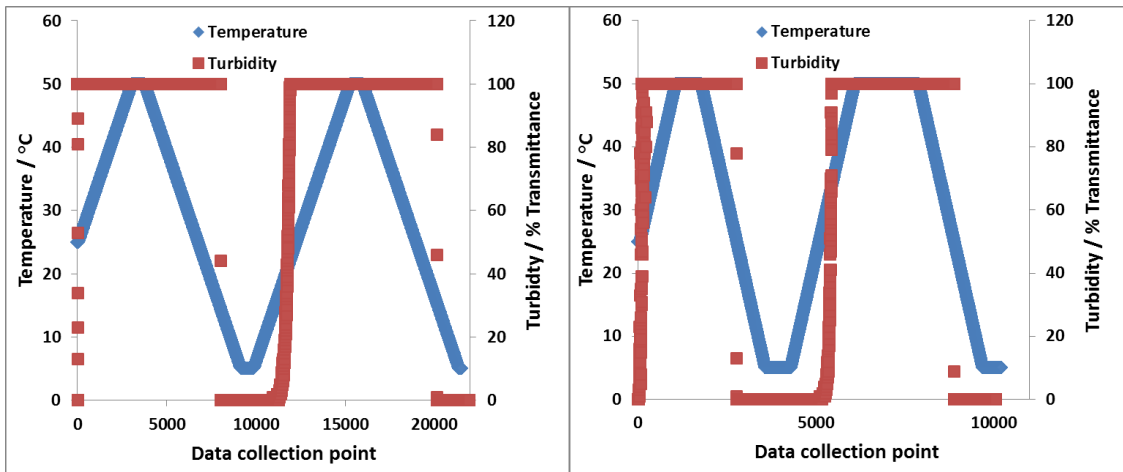

Figure 4: Turbidity vs temperature plot for crystallisation of PABA from 64.8 g/kg acetonitrile solution at 0.1 °C / min left and 0.3°C / min right
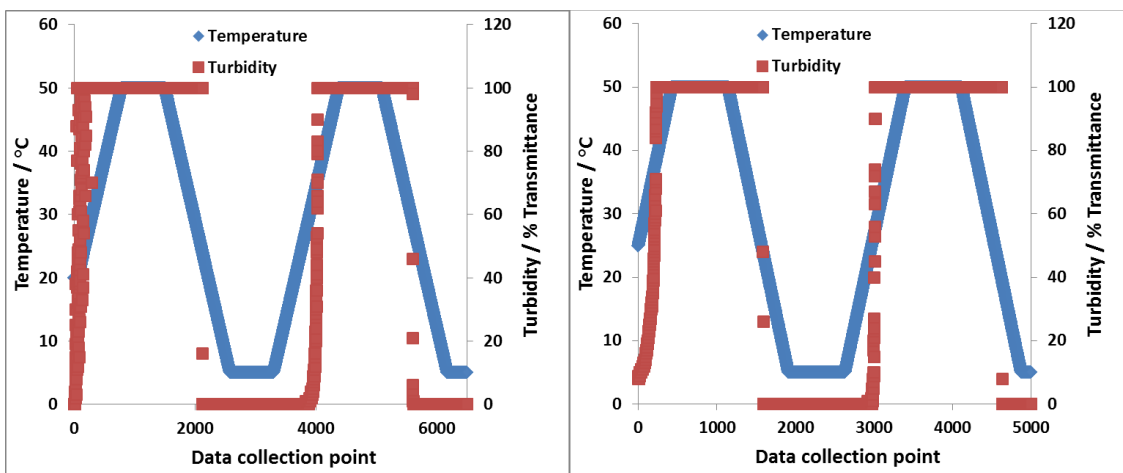

Figure 5: Turbidity vs temperature plot for crystallisation of PABA from 64.8 g/kg acetonitrile solution at 0.5 °C / min left and 0.7°C / min right
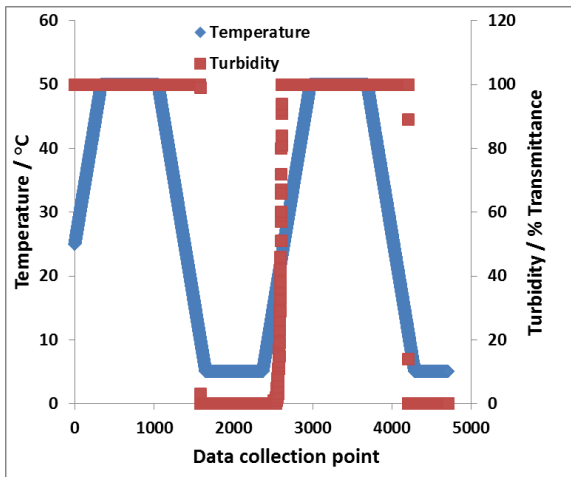
266

Figure 6: Turbidity vs temperature plot for crystallisation of PABA from 64.8 g/kg acetonitrile solution at 1.0 °C / min
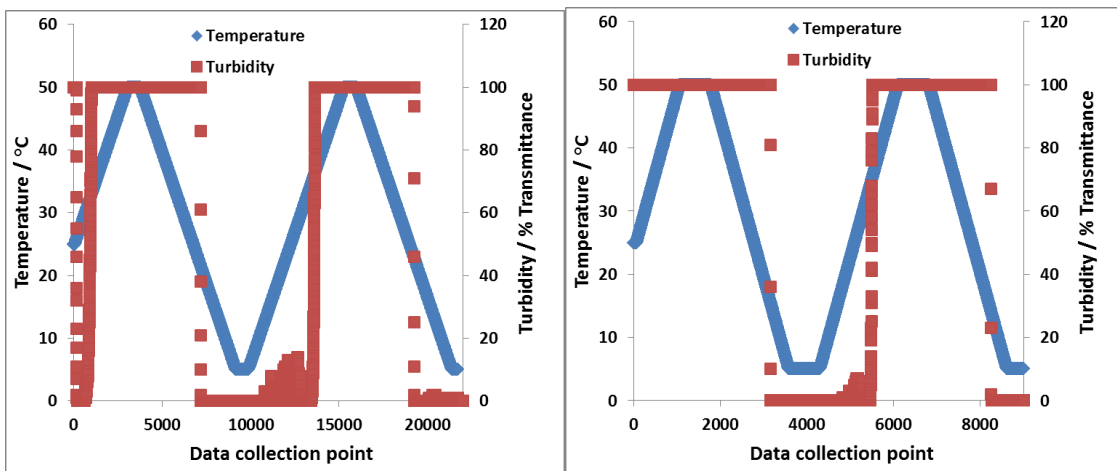

Figure 7: Turbidity vs temperature plot for crystallisation of PABA from 170 g/kg ethanol solution at 0.1 °C / min left and 0.3°C / min right
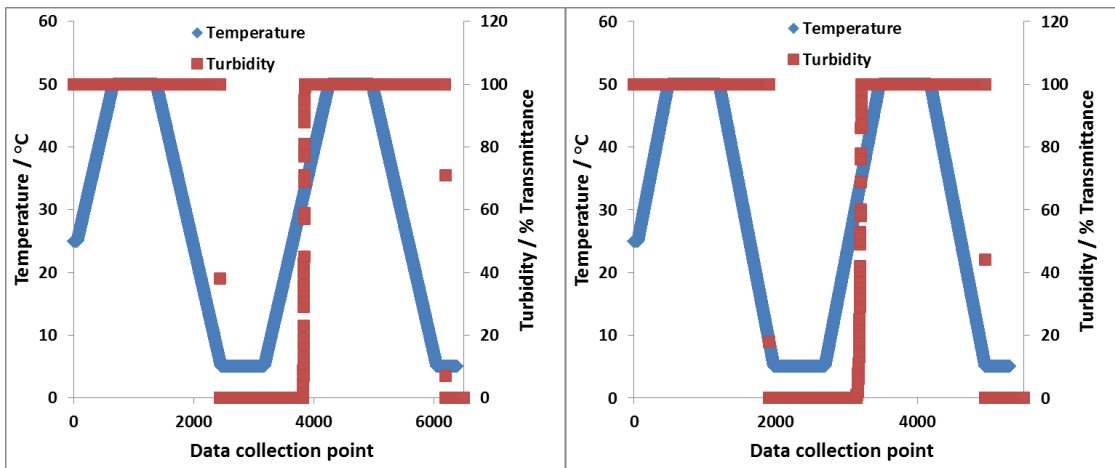
Figure 8: Turbidity vs temperature plot for crystallisation of PABA from 170 g/kg ethanol solution at 0.5 °C / min left and 0.7°C / min right
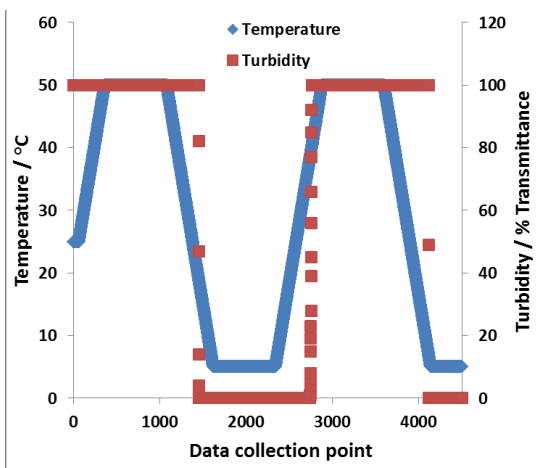
Figure 9: Turbidity vs temperature plot for crystallisation of PABA from 170 g/kg ethanol solution at 1.0 °C / min

2. Recorded Crystallisation Parameters from Turbidometric Data

Table 1 highlights the complete list of all measured crystallisation and dissolution temperatures with standard deviations from repeat measurements in ethanol, acetonitrile and aqueous solutions. The value of the equilibrium dissolution temperature, T_e, is also provided for each concentration from extrapolation of dissolution temperatures to 0°/min cooling rate. The calculated values critical undercooling, ΔTc, is also presented in Table 1 for each cooling rate in the specified solvent system.

Table 1: List of the measured crystallisation and dissolution temperatures together with extrapolated values of the equilibrium dissolution temperature Te and the calculated values of critical undercooling ΔTc for PABA solutions in ethanol, acetonitrile and water at varying concentrations and cooling rates

Ethanol 170g/kg Rate (°C/min^{-1})	$Tdis$ (°C)	T_C (°C)	$ΔTc$
0.1	32.05 ± 0.78	22.40 ± 1.13	6.91
0.3	32.18 ± 0.87	16.10 ± 1.57	13.21
0.5	33.14 ± 1.10	7.85 ± 2.62	21.46
0.7	35.63 ± 1.10	5.40 ± 0.14	23.91
1	41.90 ± 3.42	-0.67 ± 0.32	29.98
	T_e = 29.31		
180g/kg Rate (°C/min^{-1})			
0.1	33.60 ± 1.71	24.58 ± 1.00	7.13
0.3	34.60 ± 1.26	21.67 ± 2.59	10.03
0.5	39.47 ± 0.78	22.15 ± 2.21	9.55
0.7	38.90 ± 0.4	13.53 ± 1.30	18.17
1	45.40 ± 1.21	10.40 ± 1.85	21.30
	T_e = 31.70		
190g/kg Rate (°C/min^{-1})			
0.1	36.17 ± 0.64	29.08 ± 0.91	5.09
0.3	37.20 ± 2.03	24.53 ± 4.11	9.63
0.5	39.85 ± 1.06	26.98 ± 4.21	7.19
0.7	42.93 ± 2.15	27.00 ± 1.87	7.17
1	46.83 ± 2.47	17.60 ± 0.71	16.57
	T_e = 34.17		
200g/kg Rate (°C/min^{-1})			
0.1	40.43 ± 1.40	35.18 ± 0.29	3.81

0.3	42.20 ± 3.19	31.70 ± 1.10	7.28
0.5	42.77 ± 1.92	33.03 ± 1.23	5.95
0.7	46.00 ± 0.42	33.12 ± 1.07	5.86
1	49.35 ± 0.78	25.55 ± 1.20	13.43
	$T_e = 38.98$		

Acetonitrile 54g/kg Rate (°C/min^{-1})	Tdis (°C)	Tcrys (°C)	ΔTc
0.1	14.82 ± 0.49	8.46 ± 0.74	6.81
0.3	16.03 ± 0.21	6.09 ± 1.13	9.18
0.5	18.13 ± 0.54	7.01 ± 1.71	8.26
0.7	17.46 ± 0.27	5.17 ± 0.37	10.10
0.9	17.07 ± 0.23	5.27 ± 0.31	10.00
	$T_e = 15.22$		
64.8g/kg Rate (°C/min^{-1})			
0.1	18.64 ± 0.19	15.53 ± 0.94	3.78
0.3	21.02 ± 1.08	16.12 ± 0.54	3.18
0.5	24.00 ± 0.55	15.73 ± 2.48	3.57
0.7	22.90 ± 0.46	13.85 ± 2.21	5.45
0.9	23.03 ± 0.06	11.55 ± 0.21	7.75
	$T_e = 19.25$		
75.6g/kg Rate (°C/min^{-1})			
0.1	24.62 ± 0.72	21.87 ± 1.84	2.96
0.3	25.62 ± 1.57	21.86 ± 0.73	2.97
0.5	28.56 ± 0.40	22.40 ± 0.20	2.43
0.7	27.84 ± 1.01	20.00 ± 0.48	4.83
0.9	27.68 ± 1.57	19.98 ± 1.93	4.85
	$T_e = 24.78$		
86.4g/kg Rate (°C/min^{-1})			

0.1	29.63 ± 0.17	27.77 ± 0.93	2.19
0.3	29.33 ± 1.50	27.00 ± 0.92	2.96
0.5	34.13 ± 0.82	28.79 ± 1.17	1.17
0.7	31.37 ± 0.21	25.53 ± 2.37	4.44
0.9	30.97 ± 0.91	24.45 ± 1.28	5.51
	$T_e = 29.91$		

Aqueous 6g/kg Rate (°C/min^{-1})	Tdis (°C)	Tcrys (°C)	ΔTc
0.1	29.51 ± 0.83	22.54 ± 0.76	6.56
0.3	29.58 ± 1.74	20.96 ± 0.78	8.14
0.5	30.12 ± 0.83	20.44 ± 0.47	8.66
0.7	31.76 ± 1.09	21.04 ± 1.37	8.06
1	31.46 ± 0.96	18.52 ± 0.53	10.58
	$T_e = 29.10$		
8g/kg Rate (°C/min^{-1})			
0.1	36.10 ± 0.61	30.22 ± 0.89	5.38
0.3	35.92 ± 1.87	28.30 ± 0.93	7.30
0.5	37.12 ± 0.58	27.10 ± 1.17	8.50
0.7	38.02 ± 1.38	29.64 ± 0.94	5.96
1	38.28 ± 0.93	25.62 ± 1.74	9.98
	$T_e = 35.58$		
10g/kg Rate (°C/min^{-1})			
0.1	41.45 ± 1.11	37.28 ± 0.47	3.52
0.3	40.82 ± 2.00	33.68 ± 1.22	7.12
0.5	42.70 ± 0.67	35.10 ± 0.75	5.70
0.7	43.82 ± 1.03	35.10 ± 1.36	5.70
1	43.74 ± 0.88	33.62 ± 1.04	7.18
	$T_e = 40.76$		

12g/kg Rate (°C/min^{-1})			
0.1	46.33 ± 0.36	43.30 ± 1.21	2.60
0.3	45.92 ± 1.80	40.82 ± 1.32	5.08
0.5	47.08 ± 1.21	40.54 ± 1.31	5.36
0.7	48.67 ± 1.39	43.48 ± 1.62	2.42
1	47.82 ± 2.40	39.66 ± 2.01	6.24
	T_e = 45.88		

3. Solubility and Supersolubility Curves

Figure 4 provides the solubility and super-solubility curves of alpha PABA in the three solvents by extrapolation of T_{dis} and T_{crys} to the kinetic limit to obtain the equilibrium solubility and crystallisation temperatures as a function of solution concentration.
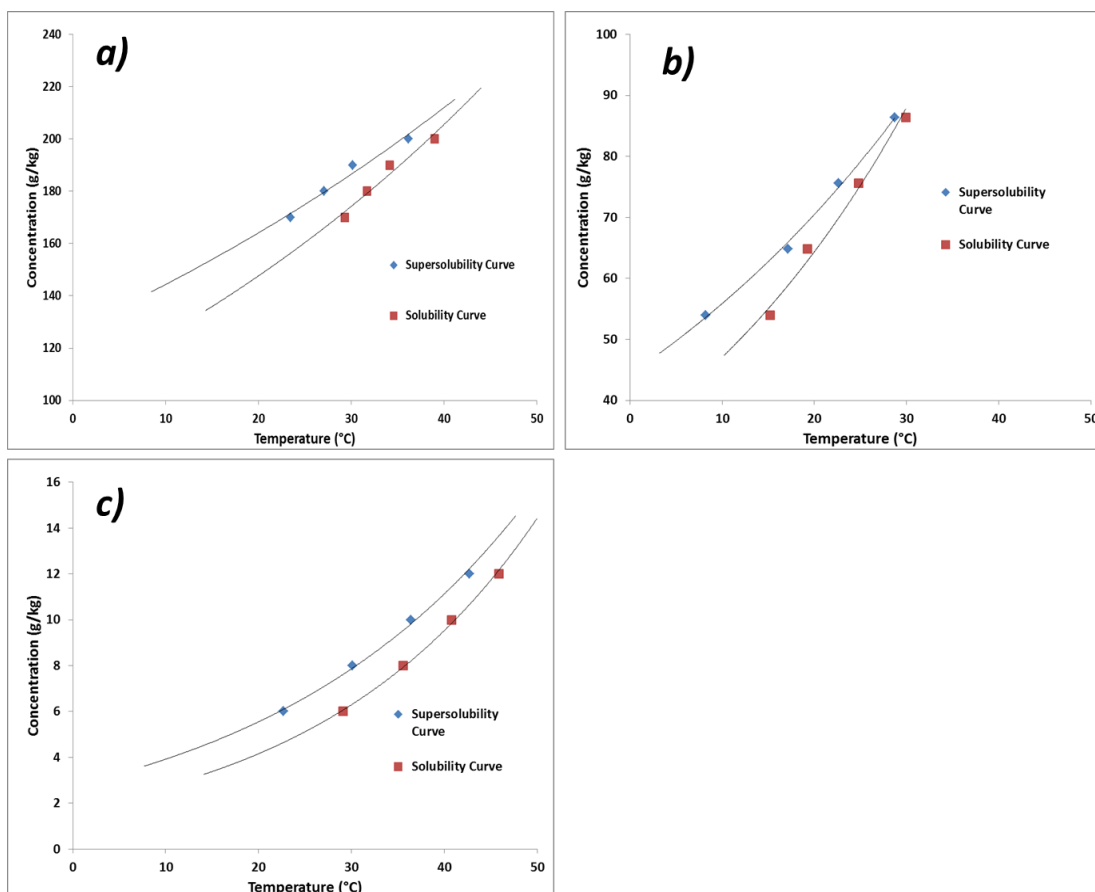

Figure 4: a) Plot of the super-solubility and solubility curves from extrapolation of Te and TC at 0°C/min cooling rate in ethanol b) acetonitrile c) aqueous solutions